

2014-01-01

Mapping Technologically and Economically Important Materials at Lunar and Terrestrial Sites Using Moon Mineralogy Mapper (M3) and Advanced Spaceborne Thermal Emission and Reflection Radiometer (ASTER) Data

Douglas L. Standart

University of Texas at El Paso, dlstandart@miners.utep.edu

Follow this and additional works at: https://digitalcommons.utep.edu/open_etd



Part of the [Geology Commons](#), [Geophysics and Seismology Commons](#), and the [Remote Sensing Commons](#)

Recommended Citation

Standart, Douglas L., "Mapping Technologically and Economically Important Materials at Lunar and Terrestrial Sites Using Moon Mineralogy Mapper (M3) and Advanced Spaceborne Thermal Emission and Reflection Radiometer (ASTER) Data" (2014). *Open Access Theses & Dissertations*. 1356.

https://digitalcommons.utep.edu/open_etd/1356

This is brought to you for free and open access by DigitalCommons@UTEP. It has been accepted for inclusion in Open Access Theses & Dissertations by an authorized administrator of DigitalCommons@UTEP. For more information, please contact lweber@utep.edu.

MAPPING TECHNOLOGICALLY AND ECONOMICALLY IMPORTANT
MATERIALS AT LUNAR AND TERRESTRIAL SITES USING MOON
MINERALOGY MAPPER (M³) AND ADVANCED SPACEBORNE THERMAL
EMISSION AND REFLECTION RADIOMETER (ASTER) DATA

DOUGLAS LAURANCE STANDART

Department of Geological Sciences

APPROVED:

Jose M. Hurtado Jr., Ph.D., Chair

Philip Goodell, Ph.D.

Lin Ma, Ph.D.

Mark Engle, Ph.D.

Ann Q. Gates, Ph.D.

Charles Ambler, Ph.D.
Dean of the Graduate School

Copyright ©

by

Douglas Laurance Standart

2014

Dedication

For my mother.

MAPPING TECHNOLOGICALLY AND ECONOMICALLY IMPORTANT
MATERIALS AT LUNAR AND TERRESTRIAL SITES USING MOON
MINERALOGY MAPPER (M³) AND ADVANCED SPACEBORNE THERMAL
EMISSION AND REFLECTION RADIOMETER (ASTER) DATA

by

DOUGLAS LAURANCE STANDART, B.S.

DISSERTATION

Presented to the Faculty of the Graduate School of

The University of Texas at El Paso

in Partial Fulfillment

of the Requirements

for the Degree of

Doctor of Philosophy

Department of Geological Sciences

THE UNIVERSITY OF TEXAS AT EL PASO

December 2014

ACKNOWLEDGEMENTS

First of all, I want to thank my family for their love and support. I would also like to thank my advisor, Dr. Jose M. Hurtado Jr., for always making time to answer questions and help me work through difficult problems related to my research. Finally, I would like to thank Adam Nazarian and Ana Garcia for helping me compile and process the data that I use in this dissertation. Without these people this dissertation would not be possible.

ABSTRACT

This dissertation comprises three distinct research projects, all of which employ the use of remote sensing and digital image processing methods for the discovery and characterization of mineral resources. Two of the research projects focus on the use of hyperspectral data to identify water and ilmenite on the lunar surface. The third research project involves the use of multispectral data to map alunite in copper porphyry and epithermal silver-gold deposits. Our approach to these problems result in innovative algorithms and geological interpretations that are of use to both planetary science and exploration and the terrestrial mineral industry.

Project I: Towards the late stages of differentiation of the early lunar magma ocean, the remaining material would have been enriched with thorium, water, hydroxyl, and other incompatible species. Using results from the Lunar Prospector Gamma Ray Spectrometer (LP-GRS), we selected thorium (Th) anomalies on the Moon in an effort to detect material rich in KREEP (potassium, rare earth elements, phosphorus) using hyperspectral imagery. Four sites were chosen: Lassell Crater, Hansteen Alpha, Gruithuisen Domes, and Compton-Belkovich Thorium Anomaly (CBTA). Three of these sites are non-mare volcanic features within the Procellarum KREEP Terrane (PKT), while Compton-Belkovich is located on the lunar farside. The Moon Mineralogy Mapper (M³) hyperspectral imager was used to analyze the composition of these locations. The spectra gathered from all four study sites all show pronounced absorptions at $\sim 2.8 \mu\text{m}$, indicating hydroxyl or water. This is significant for three reasons: (1) the strong absorption of hydroxyl/water shown at each of these volcanic sites supports the hypothesis that the lunar mantle is more hydrous than previously thought; (2) it suggests that KREEP may lie, possibly as uncoupled pods, beneath the anorthositic highlands near Compton-

Belkovich as well as underlying other areas outside the previously defined PKT; and (3) it suggests that non-mare silicic volcanic features would have erupted prior to mare basalts due to their increased abundance of magmatic water, consistent with basaltic underplating.

Project II: KREEP material on the Moon is shown to be relatively rich in ilmenite (FeTiO_3). By targeting areas with anomalously high Th signatures, as seen by LP-ThGRS, we attempt to determine if Th hotspots are associated with ilmenite-rich basalts. To map ilmenite, we employ a band depth technique that takes advantage of the fact that the visible-infrared reflectance spectrum of ilmenite exhibits low reflectance and a flat continuum slope. As a result, the spectra of ilmenite-bearing mare basalts will have a reduced 1- μm absorption. We demonstrate this effect by plotting ilmenite concentrations from Apollo basalt samples against the M^3 -derived, 1- μm absorption depths associated with the locations from which the samples were collected. A least-squares regression to the ilmenite vs. 1- μm absorption data is then used to predict ilmenite concentrations of mare basalts from M^3 spectra. Using this methodology, we built ilmenite maps for the following nearside mare: western Mare Imbrium; southern Oceanus Procellarum; eastern Mare Nubium; Mare Serenitatis; and Tranquillitatis. Based on the concentrations of Th and ilmenite associated with the eruptions, we determined that at least three eruption episodes of mare basalts occurred, each with different geochemical signatures. In addition we identified late stage (<3.1 Gya) ilmenite- and Th-rich basalts within the PKT, which we suggest were supplied by the arrival of a KREEP-, and ilmenite-rich plume that formed at the core-mantle boundary after ilmenite-rich and KREEP-rich melts sank into the mantle. However, areas outside of PKT, such as Tranquillitatis and Serenatatis, do not exhibit both high KREEP and high ilmenite concentrations. Instead, early stage basaltic eruptions – consisting of low-Th, ilmenite-rich basalts are present at Mare Tranquillitatis and Th- and ilmenite-poor basalts are

present at Serenitatis. We propose two possible scenarios to explain this. In the first, the Ti-rich but Th-poor mare basalts would have erupted after (or during) a degree-1 downwelling that affected the nearby PKT early in lunar history. The KREEP may have never existed at these locations, or it was removed by the degree-1 downwelling, which redistributed that material and concentrated it in the PKT. In the second scenario, the Ti-rich but Th-poor mare basalts would have erupted prior to the degree-1 downwelling. In this case, the ilmenite-rich cumulates may have existed at the time of melt generation. However, the lack of Th would imply that KREEP did not exist at all at these locations.

Project III: Alunite ($\text{KAl}_3(\text{SO}_4)_2(\text{OH})_6$) is a sulfate mineral that is commonly found in argillic alteration zones of porphyry and epithermal systems, and in other supergene enriched mineral deposits. Using ASTER (Advanced Spaceborne Thermal Emission and Reflection Radiometer) data, we target spectral features associated with hydroxyl (OH^-) and sulfate (SO_4^{2-}). Previous studies have used OH^- absorptions near $2.2\text{ }\mu\text{m}$ to target alunite, but their methods can confuse alunite with carbonates, detrital clays, iron oxides, and jarosite. We use a logical operator approach to increase our confidence in targeting alunite and delineate it from carbonates, detrital clays, iron oxides, and jarosite. The first logical operator targets a doublet absorption near $2.2\text{ }\mu\text{m}$ associated with OH^- in alunite, detrital clays, and carbonates. It also targets the negative spectral slope between 0.8 and $1.65\text{ }\mu\text{m}$, in order to delineate alunite from iron oxide and jarosite. We also develop a second logical operator that targets the $9\text{-}\mu\text{m}$ absorption associated with SO_4^{2-} in alunite, jarosite, and quartz. To test the effectiveness of our logical operator methodology in places where carbonates, detrital clays, limonite, and vegetation not related to porphyry and epithermal systems are present, we conduct a ground truth investigation at Cuprite Hills, Nevada. We show that the alunite identified by our alunite map is

spatially correlative to the regions indicated by AVIRIS mineral maps to contain alunite. Our improved methodology for locating alunite with ASTER data is an inexpensive, easy, and reliable method for discovering new porphyry and epithermal mineral deposits that can be applied to a variety of exploration problems.

TABLE OF CONTENTS

ACKNOWLEDGEMENTS	v
ABSTRACT	vi
TABLE OF CONTENTS	x
CHAPTER 1: INTRODUCTION	1
1 Lunar Water and Ilmenite (Chapters 2 and 3)	1
1.1 Motivation for Study	1
1.2 Goals and Objectives	4
1.3 Research Products and Their Significance	4
2 Terrestrial Mineral Exploration	6
2.1 Motivation for Study	6
2.2 Goals and Objectives	7
2.3 Research Products and Their Significance	8
References	10
Figures	14
CHAPTER 2: DETECTING MAGMATIC OH-H ₂ O AT SITES OF NON-MARE SILCIC VOLCANISM ON THE MOON USING THE MOON MINERALOGY MAPPER (M ³)	18
1 Introduction	20
2 Background.....	22
2.1 Lunar Spectroscopy and Space Weathering	22
2.2 Differentiation of the Moon.....	23
2.3 Silicic Lunar Magmatism	27
2.4 Lunar Water	28
3 Study Areas	30
3.1 Compton/Belkovich Thorium Anomaly	31
3.2 Gruithuisen Domes	32
3.3 Lassell Massif	32
3.4 Hansteen Alpha.....	33
4 Data	33
4.1 Moon Mineralogy Mapper.....	33

4.2 Lunar Reconnaissance Orbiter.....	35
5 Methods	35
5.1 Continuum Removal	36
5.2 Frequency Filter.....	36
5.3 2.8- μ m Band Depth	37
5.4 Hapke Theory	37
5.5 Integrated Molar Absorption Coefficient	39
5.6 Beer-Lambert Law.....	39
5.7 Morphologic Analysis	40
6 Results.....	40
6.1 CBTA	41
6.2 Hansteen Alpha.....	41
6.3 Lassell Massif.....	42
6.4 Gruithuisen Domes	43
7 Discussion	43
7.1 Lunar Water	43
7.2 Nearside Non-mare Volcanics.....	44
7.3 Farside Non-mare Volcanics	45
7.4 Plume or Impact Origin for Nearside Volcanism	46
8 Conclusions.....	47
References.....	50
Tables	62
Figures	65
Appendices.....	79
CHAPTER 3: DELINEATING ILMENITE IN MARE BASALTS USING THE MOON MINERALOGY MAPPER.....	112
1 Introduction	114
2 Background.....	116
2.1 Lunar Spectroscopy and Space Weathering	117
2.2 Differentiation of the Moon.....	118
2.3 Mare Volcanism	122
3 Methods	124
3.1 Moon Mineralogy Mapper.....	124

3.2 Continuum Removal	125
3.3 Frequency Domain Filter	125
3.4 1- μ m Absorption Band Depth	126
3.5 Ilmenite Regression Model	126
3.6 Uncertainty	129
3.7 Ilmenite Map	130
4 Study Areas	132
4.1 Western Mare Imbrium	132
4.2 Mare Serenitatis and Tranquillitatis	133
4.3 Southern Oceanus Procellarum	134
4.4 Eastern Mare Nubium	135
5 Results	135
5.1 Ilmenite Regression Model	135
5.2 Western Mare Nubium	136
5.3 Mare Serenitatis and Tranquillitatis	137
5.4 Southern Oceanus Procellarum	137
5.5 Eastern Mare Nubium	138
6 Discussion	138
7 Conclusions	143
References	146
Tables	158
Figures	160
Appendices	177
CHAPTER 4: TARGETING ALUNITE IN EPITHERMAL AND COPPER PORPHYRY DEPOSITS USING ASTER VNIR, SWIR, AND TIR IMAGERY	191
1 Introduction	193
2 Background	194
2.1 Porphyry Copper Deposits	194
2.2 Epithermal Silver-Gold Deposits	195
2.3 Alteration Assemblages	196
2.4 Hypogene and Supergene Enrichment	197
2.5 Alteration Exploration Using Remote Sensing	198
2.6 Argillic Logical Operators	199

Mineral Mapping Using Hyperspectral Data	202
3 Cuprite Hills, Nevada	203
4 Data	205
5 Methods	206
5.1 ASTER Preprocessing	206
5.2 SO_4^{2-} Logical Operator	207
5.3 OH^- Logical Operator	208
5.4 Alunite Map	209
5.5 Cuprite Hills Field Work	209
5.6 Reflectance Spectroscopy of Cuprite Hills Samples	210
5.7 Analysis of Laboratory Spectra	211
6 Results	211
6.1 SO_4^{2-} Logical Operator	212
6.2 OH^- Logical Operator	212
6.3 Alunite Map	213
6.4 Cuprite Hills Samples	213
7 Discussion	215
7.1 Logical Operator Assessment Using Cuprite Hills Ground Truth	216
7.2 Logical Operator Assessment Using Other Datasets	218
7.3 Implications for Exploration Geology	219
8 Conclusions	222
References	224
Tables	228
Figures	231
Appendices	248
CHAPTER 5: SYNTHESIS	261
1 Lunar Geologic Exploration	261
1.1 Key Research Findings	261
1.2 Broader Implications	264
1.3 Future Research Priorities	266
2 Terrestrial Mineral Exploration	267
2.1 Key Research Findings	268

2.2 Broader Implications.....	268
2.3 Future Research Priorities.....	269
References.....	271
Figures	275
VITA.....	278

CHAPTER 1: INTRODUCTION

This dissertation comprises three research projects presented in the form of manuscripts for submission to professional journals. The author of this dissertation (Douglas Laurance Standart) is the lead author and analyst of each chapter. All three manuscripts employ the use of remote sensing and digital image processing methods for the discovery and characterization of mineral resources. Chapter 2 focuses on the use of hyperspectral data to identify water at the locations of silicic volcanic features on the Moon. Chapter 3 focuses on the use of hyperspectral data to target and estimate the concentration of ilmenite in mare basalts on the nearside of the Moon. Chapter 4 focuses on the use of multispectral data to map the mineral alunite as a proxy for locating copper porphyry and epithermal silver-gold deposits. The approach to these problems has resulted in innovative algorithms and geological interpretations that are of great potential use to planetary science and exploration and also to the terrestrial mineral industry.

1. Lunar Water and Ilmenite (Chapters 2 and 3)

1.1 Motivation for Study

The lunar surface hosts a variety of potentially exploitable resources, and *in-situ* resource utilization (ISRU) of those resources will be a key technology in sustained human exploration of the solar system. ISRU involves using native materials to sustain prolonged activity at a remote site, such as at a lunar outpost (Duke et al., 2006). The discovery and characterization of exploitable water, in the form of molecular water (H₂O) or hydroxyl (OH), and of high concentrations of extractable ilmenite (FeTiO₃), an ore of titanium, is important for the exploration of the lunar surface. A lunar outpost will require water for multiple reasons. The most obvious reason is for drinking, but water can also be broken down to create rocket engine

propellant in the form of oxygen and hydrogen (Duke et al., 2006). The oxygen can also be used for life support, and the hydrogen can be used as consumable in fuel cells and other catalytic reactions (Duke et al., 2006). Due to the high tensile strength, fatigue resistance, and crack resistance of titanium (Duke et al., 2006), it can be used in metal alloys to make spare spaceship parts, spare robot parts, or building materials for the lunar outpost (Duke et al., 2006).

In parallel with the planetary exploration significance of this work, this research also has important scientific implications. Our understanding of lunar water – including its origin, distribution, and abundance – in the form of both OH and H₂O, is also poorly understood. Until recently, the Moon has been thought of as being fairly anhydrous relative to Earth (Klima et al., 2013). However, lunar samples and various remotely-sensed datasets have suggested that the Moon is not as dry as previously thought (Pieters et al., 2009; McCubbin et al., 2010; McCubbin et al., 2011; Klima et al., 2013). Most of this water is attributed to non-magmatic sources, such as solar wind implantation or comet/meteor bombardment (Hodges, 2002). Magmatic water, on the other hand, is water that is intrinsic to the Moon. The presence of magmatic water on the Moon could have major implications for the formation of the lunar crust. Since water lowers the melting point of rocks, water would allow the generation of magmas at lower temperatures than anhydrous material. Because the lunar KREEP (potassium, rare earth elements, phosphorus) is thought to contain water (Elkins-Tanton and Grove, 2011), water may also be a useful indicator of KREEP-enriched lithologies, which can aid in the remote detection of KREEP, and potentially indicate that KREEP is not limited to the Procellarum KREEP terrane (PKT).

In searching for water and titanium, I investigate a fundamental geologic and geochemical asymmetry of the lunar crust. The distribution of basaltic, basin-filling maria (dominantly on the lunar near side) is part of a distinction often referred to as the mare-highland

dichotomy (Zhong et al., 1999; Zhong et al., 2000; Parmentier et al., 2002; Shearer et al., 2006). The abundance of KREEP on the nearside of the Moon could explain the origin of the mare basalts, particularly the large amounts of Th-rich mare basalts within the PKT (Wieczorek and Phillips, 2000). This is because large amounts of radiogenic heat-producing elements may be present in KREEP, and those heat-producing elements would have promoted heating and melting of the mantle, allowing a prolonged volcanic history (Wieczorek and Phillips, 2000).

It is not known whether the KREEP is continuous or discontinuous in the lunar subsurface, since it is not seen at the surface on the farside. A better understanding of the distribution of KREEP will help explain the lunar dichotomy. For example, if KREEP is a continuous layer throughout the lunar subsurface, or if it distributed in places other than the nearside of the Moon, it is possible that it was not the main reason for prolonged volcanism on the nearside. Instead, it is possible that another mechanism was responsible for the prolonged volcanism on the Moon, such as a nearside plume like the one proposed by Andrews-Hanna et al. (2014). Such a plume would drive melting of the lower crust for a prolonged period of time. Those KREEP and Ti- rich melts would then erupt to the surface above the plume. On the other hand, if KREEP were continuous then why don't we see prolonged volcanism elsewhere on the Moon, since radiogenic heat producing elements would encourage melt generation?

The research presented in Chapters 2 and 3 provides evidence for KREEP-enriched lithologies on the lunar farside, challenging the previously accepted extent of KREEP-enriched mare basalts. My results suggest a mechanism for both ilmenite- and KREEP-rich basalt emplacement on the lunar nearside that involves a Ti- and KREEP-rich plume that was created after a dense layer sank to the core-mantle boundary early in lunar history, dragging Ti- and KREEP-rich material with it. Over time, the Ti- and KREEP-rich materials would have mixed

and become thermally buoyant and would have risen back to the base of the crust in the form of a plume (Zhong et al., 2000, Parmentier et al., 2002).

1.2 Goals and Objectives

Chapters 2 and 3 aim to answer the following research questions:

- (1) Why does Th appear to be restricted to the Procellarum KREEP terrane, and does it occur with high concentrations of ilmenite?
- (2) Do useful materials, such as OH⁻, H₂O, REEs and ilmenite, appear in high abundances at Th hotspots? If so, why?
- (3) What constraints can we place on the evolution of the lunar crust using Moon Mineralogy Mapper (M³) data?

The specific objectives that allow these questions to be answered are:

- Implement a methodology for remotely detecting and estimating the abundance of water using hyperspectral data of the lunar surface.
- Produce water abundance maps for areas of suspected high-silica volcanic rocks on the nearside and farside of the Moon.
- Develop a methodology for remotely detecting ilmenite using hyperspectral data of the lunar surface.
- Calibrate the ilmenite-mapping algorithm in order to allow reliable determination of ilmenite concentrations.
- Produce ilmenite abundance maps for a suite of mare on the lunar nearside.

1.3 Research Products and Their Significance

In the process of investigating the asymmetry of the lunar crust using hyperspectral data, I develop ilmenite maps for several maria on the nearside of the Moon and maps showing the possible locations of magmatic water for several non-mare silicic features distributed throughout the Moon.

Chapter 2, “Detecting Magmatic OH/H₂O at Sites of Non-mare Silicic Volcanism on the Moon Using the Moon Mineralogy Mapper (M³)”, is co-authored with Dr. Jose M. Hurtado, Jr. and is in the form of a manuscript to be submitted for peer review to the *Journal of Geophysical Research: Planets*. Chapter 2 focuses on a set of nearside silicic volcanic features – e.g., Lassell Massif, Gruithuisen Domes, Hansteen Alpha (Figure 1) – in an effort to understand the distribution of KREEP and to determine if magmatic water is present in multiple locations on the Moon. I compare the silicic volcanic features to a set of thorium anomalies, including the Compton Belkovich Thorium Anomaly (CBTA), and to mare-type basalts on the lunar farside. In these comparisons I have sought to find compositional relationships between nearside and farside non-mare silicic lithologies, such as the presence of KREEP-related incompatible elements (e.g., Th, OH⁻, H₂O), that can both illuminate the chemical geodynamics of the Moon and aid the discovery of potential resources. For example, I map the spatial relationships of silicic volcanic features with respect to the current boundaries of the PKT (Figure 1) and their water concentrations. This provides insight into the extent of KREEP and, therefore, an idea of how the stages of lunar differentiation may have occurred. I show the first evidence for hydrous KREEP-related incompatible elements at CBTA that indicate a KREEP presence outside the PKT, indicating that KREEP is not only on the nearside, and is possibly a continuous layer or in the form of pods, sills, or dikes on the farside (Figure 2). In addition, the presence of water at the non-mare silicic features has implications for the generation of lunar partial melts, such as

whether basaltic underplating (Hagerty et al., 2006) or silicic liquid immiscibility (Hagerty et al., 2006) is the primary mechanism for generating silicic melts on the Moon.

Chapter 3, “Targeting Ilmenite in Mare Basalts Using the Moon Mineralogy Mapper”, is co-authored with Dr. Jose M. Hurtado, Jr. and is in the form of a manuscript to be submitted for peer review to the journal *Icarus*. KREEP material on the Moon has been shown to contain ilmenite (Shearer et al., 2006), and I target areas with anomalously high Th signatures, and therefore KREEP, (Figure 3) as a proxy for ilmenite-rich basalts. In doing, I map the highest concentrations of ilmenite-rich material on the nearside of the Moon. Geophysical models (Zhong et al., 1999; Parmentier et al., 2002; Shearer et al., 2006) have shown that KREEP- and Ti-rich melts could have mixed during a downwelling early in lunar geologic history and that they may have subsequently reaccumulated at the base of the crust. I do not show any indication of a correlation between Th and ilmenite concentrations in mare basalts in chapter 3. I suggest that an additional factor, such as age, should be considered. In Chapter 3, I show that three stages of eruptions occurred within the PKT, each with a different geochemical signature. Outside of the PKT, the eruption model that I propose is not applicable, possibly because the plume that fed eruptions in the PKT did not affect areas outside of the PKT.

2. Terrestrial Mineral Exploration (Chapter 4)

2.1 Motivation for Study

Regional mineral exploration is a critical first step for junior and major mining companies. The ability to cheaply and quickly find mineral deposits, such as porphyry copper and epithermal silver-gold, would not only help mineral exploration companies find additional deposits, but it would also spark an explosion in regional explorations efforts. For example,

Anglo-American reported that the average cost per kimberlite discovery used to be ~\$1 million, but with multispectral and hyperspectral mapping the cost per kimberlite discovery has been reduced to ~\$300,000 (Toovey, 2011).

Alunite is a hydrothermal clay that is associated with porphyry copper deposits (PCD) and epithermal silver-gold deposits (ESGD) (Guilbert and Park, 2007). Alunite contains several spectral features (i.e. 2.17-2.2 μm OH^- absorption, 9 μm SO_4^{2-} absorption, negative slope between 0.8 and 1.65 μm ; Figure 4) that make it a good remote sensing proxy for PCDs and ESGDs (Mars and Rowan, 2006). However, previous attempts to use remote sensing to map alunite, such as the argillic logical operator developed by Mars and Rowan (2006), cannot distinguish alunite from carbonates, detrital clays, jarosite, and iron oxides. In addition to improving existing methods, there is also a need for a methodology that can map alunite using cheap and easy to use multispectral data and that can yield results with similar accuracy to what is possible with hyperspectral data. Such a methodology would allow mining companies to expand their exploration programs without spending large amounts of their exploration budget on hyperspectral imagery, data which may not be possible to acquire in the first place.

2.2 Goals and Objectives

Chapter 4 aims to answer the following research questions:

- (1) How much can we improve on previous methods of targeting alunite with ASTER data by focusing on spectral features uniquely associated with alunite, such as the 2.17-2.2- μm OH^- absorption, the 9- μm SO_4^{2-} absorption, and the negative spectral slope between 0.8 and 1.65 μm ?

(2) How much more or less effective is ASTER data when used to target alunite? How does the accuracy of ASTER compare to higher spectral and spatial resolution platforms?

The specific objectives that allow these questions to be answered are:

- Implement a methodology that uses ASTER data to remotely detect alunite while also reducing the commission errors associated with carbonates, detrital clays, jarosite and iron oxides.
- Produce alunite maps for areas of suspected hydrothermal alteration at Cuprite Hills, NV.
- Compare the resulting alunite map with mineral maps generated by the Airborne Visible/Infrared Imaging Spectrometer (AVIRIS) hyperspectral instrument, argillic alteration maps created by Ashley and Abrams (1980), and the argillic logical operator map of Mars and Rowan (2006).
- Acquire samples from Cuprite Hills and measure their reflectance spectra to act as ground truth for my logical operator maps.

2.3 Research Products and Their Significance

Chapter 4, “Targeting Alunite in Epithermal and Copper Porphyry Deposits Using ASTER VNIR, SWIR, and TIR Imagery”, is co-authored with Dr. Jose M. Hurtado, Jr. and Dr. Philip C. Goodell and is in the form of a manuscript to be submitted for peer review to the journal *Economic Geology*. The research uses Advanced Spaceborne Thermal Emission and Reflection Radiometer (ASTER) multispectral data to accurately map alunite. The OH⁻ and SO₄²⁻ logical operators that I describe in Chapter 4 have proven to be effective at detecting alunite. By using samples from Cuprite Hills as ground truth, and alunite maps from previous studies (Ashley and Abrams, 1980; Swayze et al., 2014), I was able to show that the alunite map

generated by the logical operators is accurate. In addition, the alunite map spatially correlates with argillic alteration mapped by Ashley and Abrams (1980), and AVIRIS mineral maps by Swayze et al. (2014). The alunite map does not erroneously detect nearly as much detrital clay, carbonate, iron oxide, and jarosite as the argillic logical operator map developed by Mars and Rowan (2006). In Chapter 4 I show that not only is our method for mapping alunite with ASTER effective, but that it is also comparable to the accuracy of high-spatial resolution hyperspectral platforms such as AVIRIS (Green et al., 1998). Cheap ASTER data, along with the reliable methodology I developed in Chapter 4, can usher in a burst of mineral discoveries in areas that are difficult to access, such as the Sierra Madre of Mexico.

References

- Andrews-Hanna, J.C., Besserer, J., Head III, J.W., Howett, C.J.A., Kiefer, W.S., Lucey, P.J., McGovern, P.J., Melosh, H.J., Neumann, G.A., Phillips, R.J., Schenk, P.M., Smith, D.E., Solomon, S.C., and Zuber, M.T., 2014, Structure and evolution of the lunar Procellarum region as revealed by GRAIL gravity data: *Nature*, v. 514, no. 7520, p. 68-71.
- Ashley, R.P. and Abrams, M.J., 1980, *Alteration Mapping Using Multispectral Images – Cuprite Mining District, Esmeralda County, Nevada*: USGS Open-File Report 80-367, p. 17.
- Duke, M.B., Gaddis, L.R., Taylor, J.G., and Schmitt, H.H., 2006, Development of the Moon: *Reviews of Mineralogy and Geochemistry*, v. 60, pp. 597-656.
- Elkins-Tanton, L.T. and Grove, T.L., 2011, Water in the lunar magma ocean: *A Wet Vs. Dry Moon: Exploring Volatile Reservoirs and Implications for the Evolution of the Moon and Future Exploration*, p. 14.
- Green, R.O., Eastwood, M.L., Sarture, C.M., Chrien, T.G., Aronsson, M., Chippendale, B.J., Faust, J.A., Pavri, B.E., Chovit, C.J., Solis, J., Olah, M.R., Williams, O., 1998, Imaging spectroscopy and the Airborne Visible/Infrared Imaging Spectrometer (AVIRIS): *Remote Sensing of Environment*, v. 65, p. 227-248.
- Guilbert, J. M. and Park, C. F., 2007, *The Geology of Ore Deposits*: Waveland Press Inc (Illinois), 985 p.

Hagerty, J.J., Lawrence, D.J., Hawke, B.R., Vaniman, D.T., Elphic, R.C., and Feldman, W.C., 2006, Refined thorium abundances for lunar red spots: Implications for evolved, nonmare volcanism on the Moon: *Journal of Geophysical Research*, v. 111, no. E6, p. 1-20, doi: 10.1029/2005JE002592.

Hodges Jr., R.R., 2002, Ice in the lunar polar regions revisited: *Journal of Geophysical Research*, v. 107, no. E2, p. xxx-xxx.

Klima, R., Cahill, J., Hagerty, J., and Lawrence, D., 2013, Remote detection of magmatic water in Bullialdus Crater on the Moon: *Nature Geoscience*, v. 6, no. 9, p. 737-741, doi: 10.1038/ngeo1909.

Mars, J.C. and Rowan, L.C., 2006, Regional mapping of phyllic- and argillic-altered rocks in the Zagros magmatic arc , Iran , using Advanced Spaceborne Thermal Emission and Reflection Radiometer (ASTER) data and logical operator algorithms: *Geosphere*, v. 2, no. 3, p. 161-186, doi: 10.1130/GES00044.1.

McCubbin, F.M., Steele, A., Hauri, E.H., Nekvasil, H., Yamashita, S., and Hemley, R.J., 2010, Nominally hydrous magmatism on the Moon.: *Proceedings of the National Academy of Sciences of the United States of America*, v. 107, no. 25, p. 11223-11228, doi: 10.1073/pnas.1006677107.

McCubbin, F.M., Jolliff, B.L., Nekvasil, H., Carpenter, P.K., Zeigler, R.A., Steele, A., Elardo, S.M., and Lindsley, D.H., 2011, Fluorine and chlorine abundances in lunar apatite: Implications for heterogeneous distributions of magmatic volatiles in the lunar interior: *Geochimica et Cosmochimica Acta*, v. 75, no. 17, p. 5073-5093, doi: 10.1016/j.gca.2011.06.017.

Parmentier, E.M., Zhong, S., and Zuber, M.T., 2002, Gravitational differentiation due to initial chemical stratification: origin of lunar asymmetry by the creep of dense KREEP?: *Earth and Planetary Science Letters*, v. 201, p. 473-480.

Pieters, C.M., Goswami, J.N., Clark, R.N., Annadurai, M., Boardman, J., Buratti, B., Combe, J. P., Dyar, M. D., Green, R., Head, J.W., Hibbitts, C., Hicks, M., Isaacson, P., and Klima, R., 2009, Character and spatial distribution of OH/H₂O on the surface of the Moon seen by M3 on Chandrayaan-1.: *Science*, v. 326, no. 5952, p. 568-572, doi: 10.1126/science.1178658.

Shearer, C.K., Hess, C.P., Wieczorek, M.A., Pritchard, M.E., Parmentier, E.M., Borg, L.E., Longhi, J., Elkins-Tanton, L.T., Neal, C.R., Antonenko, I., Canup, R.M., Halliday, A.N., Grove, T.L., Hager, B.H., 2006, Thermal and Magmatic Evolution of the Moon: *Reviews in Mineralogy and Geochemistry*, v. 60, no. 1, p. 365-518, doi: 10.2138/rmg.2006.60.4.

- Swayze, G.A., R.N. Clark, A.F.H. Goetz, K.E. Livo, G.N. Breit, F.A. Kruse, S.J. Stutley, L.W. Snee, H.A. Lowers, J.L. Post, R.E. Stoffregen, and R.P. Ashley, 2014, Mapping advanced argillic alteration at Cuprite, Nevada using imaging spectroscopy: *Economic Geology*, v. 109, no. 5, p. 1179-1221. doi:10.2113/econgeo.109.5.1179.
- Toovey, L. M., 2011, *Introduction to Remote Sensing and Mineral Exploration*: <http://goldinvestingnews.com/14571/introduction-to-remote-sensing-and-mineral-exploration.html>. (accessed November, 2014).
- Wieczorek, M.A. and Phillips, R.J., 2000, The “Procellarum KREEP Terrane”: Implications for mare volcanism and lunar evolution: *Journal of Geophysical Research*, v. 105, no. E8, p. 417-420
- Zhong, S., Parmentier, E.M., and Zuber, M.T., 1999, Early Lunar Evolution and the Origin of Asymmetric Distribution of Mare Basalts: *Proceedings of the 30th Lunar and Planetary Science Conference*, p. 1789.
- Zhong, S., Parmentier, E.M., and Zuber, M.T., 2000, A dynamic origin for the global asymmetry of lunar mare basalts: *Earth and Planetary Science Letters*, v. 177, no. 3-4, p. 131-140, doi: 10.1016/S0012-821X(00)00041-8.

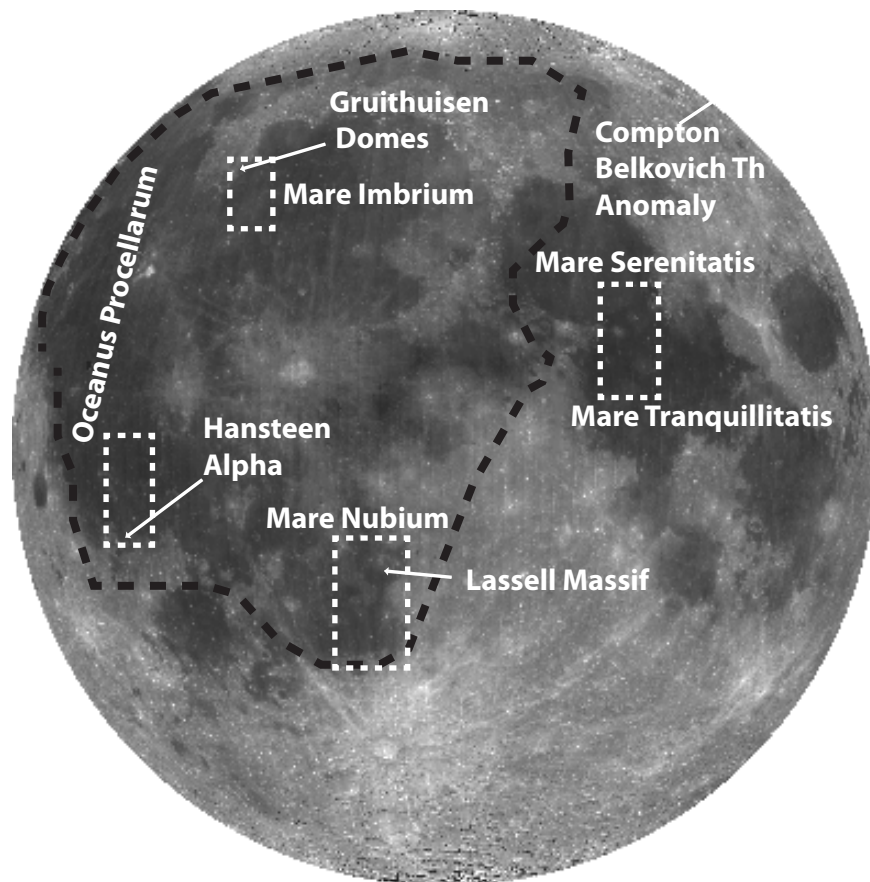


Figure 1: Clementine global albedo image showing target sites (labeled with white text and white dashed boxes). The Procellarum KREEP Terrane boundary is shown by the black dashed polygon. From Lunar and Planetary Institute (<http://www.lpi.usra.edu/lunar/missions/clementine/images/>).

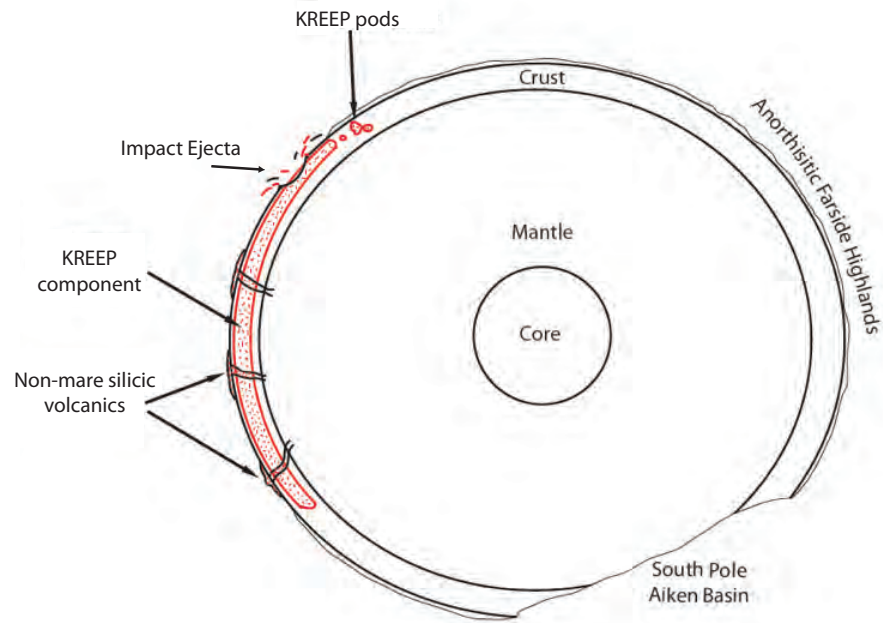


Figure 2: Schematic cross-section of the showing the spatial extent of KREEP within the lunar crust ~1-3 billion years ago. Modified from Wieczorek et al. (2006). Mare basalts on the nearside could possibly have been enriched by KREEP as their melts were mixed with the KREEP layer.

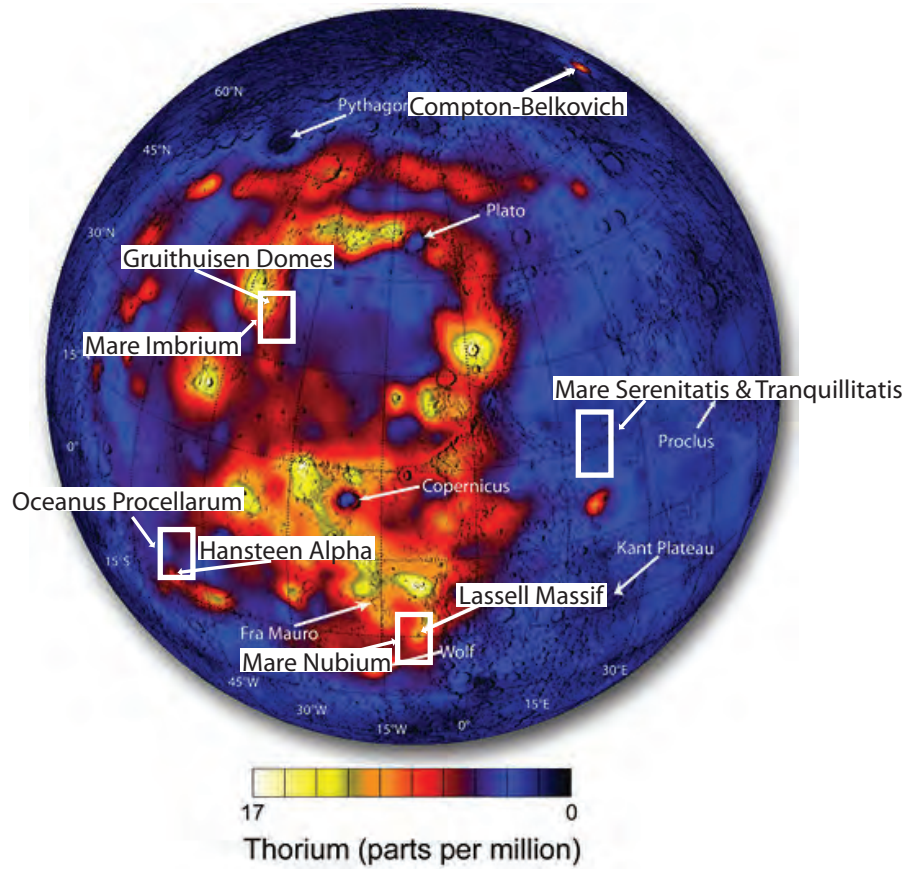


Figure 3: LP-ThGRS data showing nearside thorium concentrations. White boxes indicate target sites: Southern Oceanus Procellarum and Hansteen Alpha(lower left), West Mare Nubium and Lassell Massif (lower right), West Mare Imbrium and the Gruithuisen Domes (upper left), Mare Tranquillitatis and Serenitatis(middle right), and Compton-Belkovich Thorium Anomaly (upper right). From Lawrence et al. (2007).

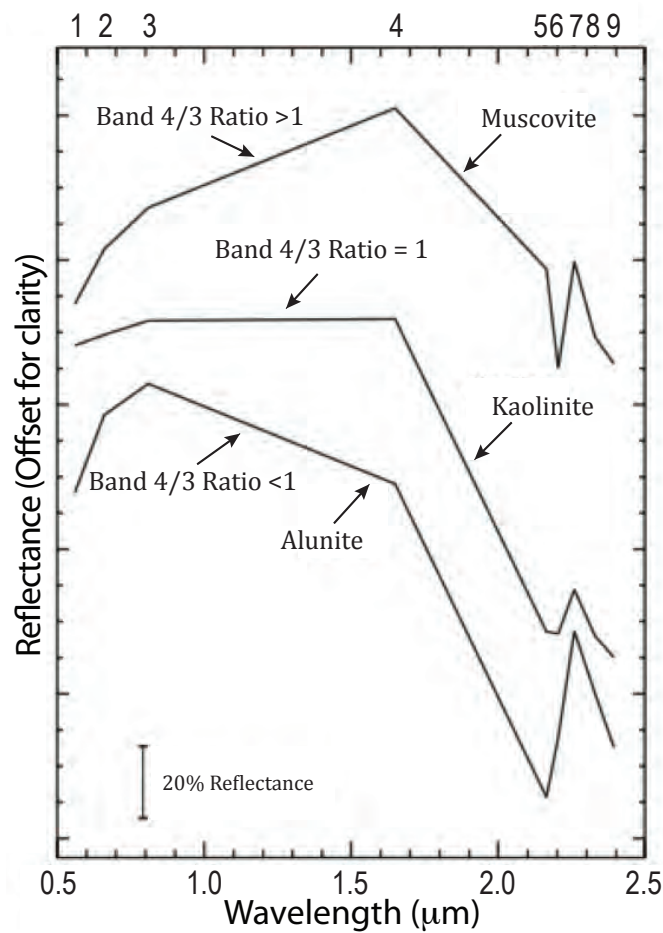


Figure 4: Laboratory reflectance spectra of alunite, kaolinite, and muscovite. The spectra have been resampled to ASTER bandpasses. Numbers across the top indicate ASTER band center positions. The spectral slopes estimated using the ASTER band 4/3 ratio shows how a band threshold can be determined from ASTER spectra. These spectral slopes allow us to distinguish minerals from one another. Modified from Mars and Rowan (2006).

CHAPTER 2: DETECTING MAGMATIC OH-H₂O AT SITES OF NON-MARE SILICIC VOLCANISM ON THE MOON USING THE MOON MINERALOGY MAPPER (M³)

Standart, D. L. and Hurtado, J. M. (Jr.)

Department of Geological Sciences, The University of Texas at El Paso, 500 West University Avenue, El Paso, Texas 79968

Abstract: Towards the late stages of differentiation of the early lunar magma ocean, the remaining layer was enriched with thorium (Th), water (H₂O), hydroxyl (OH⁻), and other incompatible materials. Therefore, locations that show high concentrations of Th and hydroxyl-water (OH-H₂O) may indicate assimilation of or interaction with KREEP (potassium, rare earth elements, phosphorus). Using results from the Lunar Prospector Gamma Ray Spectrometer (LP-GRS), we selected high Th anomalies on the Moon in an effort to detect KREEP-rich material using hyperspectral imagery. Four sites were chosen: Lassell Crater, Hansteen Alpha, Gruithuisen Domes, and Compton-Belkovich Thorium Anomaly. Three of these sites are non-mare volcanic features within the KREEP Terrane, while Compton-Belkovich is located on the lunar farside. The Moon Mineralogy Mapper (M³) hyperspectral imager was used to analyze the OH-H₂O composition of these locations. The spectra gathered from the volcanic domes all show pronounced absorptions at ~2.8 μm, indicating the presence of OH-H₂O. The presence of OH-H₂O in the non-mare silicic features in this study is significant for three reasons: (1) the strong absorption of hydroxyl/water shown at each of these volcanic features supports the hypothesis that the lunar mantle is more hydrous than previously thought; (2) it suggests that KREEP may lie, possibly as uncoupled pods, beneath the anorthositic highlands near Compton-Belkovich as

well as underlying other areas outside the previously defined Procellarum KREEP Terrane; and (3) it suggests that non-mare volcanic features would have erupted prior to mare basalts due to their increased abundance of magmatic water, consistent with basaltic underplating.

Keywords: Moon Mineralogy Mapper, lunar water, non-mare silicic features, Compton Belkovich Thorium Anomaly, basaltic underplating

1. Introduction

There is more abundant, relatively recent (ca. 400 Ma to 4.2 Ga; Schultz and Spudis, 1983; Wieczorek et al., 2006) basaltic volcanic activity on the nearside of the Moon compared to the farside. This distribution of basaltic, basin-filling maria is part of a distinction often referred to as the mare-highland dichotomy (Zhong et al., 1999; Zhong et al., 2000; Parmentier et al., 2002; Shearer et al., 2006). Volcanic activity on the nearside has produced mare basalts, which erupted 100-400 Ma after the crust was thinned by large impactors (Arkani-Hamed and Pentecost, 2001). The thinned crust promoted decompression melting of the mantle and also formed faults that allowed those melts to later escape (Warren, 2001; Wieczorek et al., 2006). The lunar farside, on the other hand, exhibits a long history of inactivity compared to the nearside, and the crust there is dominated by ancient (~4.5 Ga) anorthosite highlands, which are thought to be representative original crust of the Moon (Wieczorek et al., 2006).

The origin of this asymmetry is still poorly understood, but many attribute it to the abundance of heat-producing elements that have been concentrated in a geochemical reservoir known as KREEP (“potassium, rare earth elements, and phosphorus”) (Wieczorek and Phillips, 2000; Wieczorek et al., 2006; Shearer et al., 2006). KREEP is enriched in incompatible species, including thorium (Th), potassium (K), rare earth elements (REE), phosphorus (P), OH⁻, H₂O, uranium, etc., and it is hypothesized to represent the final ~2% melt fraction that remained during the final stages of fractional crystallization of the lunar magma ocean (LMO; Warren, 1985; Snyder and Taylor, 1991; Wieczorek and Phillips, 2000). Large amounts of radiogenic heat-producing elements would be found in the KREEP, and its abundance on the nearside of the Moon could explain the origin of the mare basalts, particularly the voluminous, Th-rich mare basalts (Wieczorek and Phillips, 2000). The heat-producing elements in the KREEP would have

promoted heating and melting of the mantle, allowing a prolonged volcanic history (Wieczorek and Phillips, 2000).

The Procellarum KREEP Terrane (PKT) comprises Oceanus Procellarum, Mare Imbrium, Mare Frigoris, and western Mare Serenatatis (Figure 1). More than 60% of all the mare basalts on the Moon are located within this region (Wieczorek et al., 2006), which has a relatively young volcanic history compared to other sites on the Moon. The youngest mare volcanism is within Oceanus Procellarum and dates to ~400 Ma (Wieczorek et al., 2006). The maria in the PKT also differ from those in other regions because of the large amounts of incompatible species they contain. The PKT maria contain more than 5 wt% TiO_2 and an average of 12-13 ppm Th, which is much higher than the average 2 ppm Th in mare elsewhere (Wieczorek et al., 2006). These high concentrations of Th within PKT indicate that some mechanism, which is not apparent on the farside, was involved in bringing evolved magmas enriched in incompatible species, including water or hydroxyl ($\text{OH-H}_2\text{O}$), to the nearside. Interestingly, Th maps obtained from lunar orbit (Figure 2) do show a large Th anomaly on the farside of the Moon, outside of the PKT boundary. The presence of KREEP on the farside would suggest that this layer extends beyond the PKT boundary.

Previously, the Moon has been thought of as being fairly anhydrous relative to Earth (Klima et al., 2013). Recently, however, lunar samples and various remotely-sensed datasets have suggested that the Moon is not as water-poor as previously thought (Pieters et al., 2009; McCubbin et al., 2010; McCubbin et al., 2011; Klima et al., 2013). Most of the water seen at the lunar surface is attributed to sources such as solar wind implantation or comet/meteor bombardment (Hodges, 2002). Magmatic water, on the other hand, is water that is inherent to the Moon, but, until recently (Klima et al., 2013), it had not been identified at the lunar surface

using remote sensing techniques. In this paper, we use spectral data from the Moon Mineralogy Mapper (M^3) to show additional evidence for a magmatic source of water from several non-mare silicic volcanic features on the Moon. Non-mare silicic volcanics are evolved lunar lithologies similar to granite (Jolliff et al., 2011). We focus on several nearside and farside non-mare silicic volcanic sites (Figure 1) in order to determine if they are enriched in OH-H₂O. We show evidence for the first hydrous KREEP feature on the farside of the Moon and provide insight into how and when non-mare silicic features erupted on the Moon. Understanding the geochemistry of non-mare silicic features on the nearside and farside will lead to an understanding of how they formed, and the manner in which KREEP is distributed in the lunar subsurface.

2. Background

In this study, we seek to understand the distribution of KREEP and water (herein referred to as “OH-H₂O”) on the Moon, in order to interpret how, and when, non-mare silicic features could have erupted onto the surface of the Moon. We do this using hyperspectral remote sensing to determine the presence of OH-H₂O at non-mare silicic features. The following sections serve as an introduction to these topics.

2.1 Lunar Spectroscopy and Space Weathering

At short wavelengths – in the near-infrared, visible, and ultraviolet – molecular vibrations result in absorption features in reflectance spectra of geologic materials (Jensen, 2005). The various vibrational modes of molecular species, such as OH and H₂O, require specific, quantized amounts of energy to excite (Jensen, 2005). The exact amount of energy depends on the number of atoms in the molecule and the strength of its bonds (Jensen, 2005). OH and H₂O, for example,

both have a vibrational mode that produces an absorption feature at 2.8 μm (Figure 3) (Pieters et al., 2009; McCord et al., 2011; Klima et al., 2013).

Because there is no atmosphere on the Moon, micrometeorites and solar and cosmic rays constantly bombard the lunar regolith and slowly alter the surface, both physically and chemically, in a process called space weathering. The resulting geochemical effects have a strong influence on the absorption spectra for lunar materials (Isaacson et al., 2011). For example, space weathering of the lunar regolith reduces particle size and coats particle surfaces with a thin veneer of vapor deposited, nanophase iron (Lucey et al., 2006; Isaacson et al., 2011). Over time, the amount of nanophase iron increases and causes the slope of reflectance spectra to increase, an effect referred to as “reddening” (Figure 4). The reddening preferentially increases the reflectance of the spectrum at longer wavelengths, and can also shift the center wavelength of absorption features towards longer (e.g. “redder”) wavelengths. Redder lunar material is described as being “optically mature”, whereas material exposed at the surface for shorter times is described as being “optically immature” (Isaacson et al., 2011). Without accounting for the effects of space weathering, it is difficult to compare lunar spectra to spectra for analogous terrestrial samples that have not undergone space weathering processes (Isaacson et al., 2011).

2.2 Differentiation of the Moon

The Moon is thought to have formed when a Mars-sized giant impactor hit the early proto-Earth at ~ 4.5 Ga (Wasserburg, 1987; Allègre et al., 1995; Touboul et al., 2007). Most of the debris from the impact would have rapidly coalesced in orbit around Earth, forming the Moon within the span of decades (Canup and Asphaug, 2001). Approximately 60-74% of the material in orbit would have originated from the impactor, although the impactor’s dense core

would have been assimilated into the Earth's mantle upon impact (Hiesinger and Head III, 2006; Touboul et al., 2007). The rest of the material came from the crust and upper mantle of proto-Earth (Hiesinger and Head III, 2006; Touboul et al., 2007).

Initially, the early Moon would have been mostly, if not completely, molten due to the immense amount of energy of the giant impact (Touboul et al., 2007). As the molten moon cooled and underwent fractional crystallization, it gravitationally differentiated. Anorthosite and olivine were the first to crystallize, and, due to its lower density (2.7 g/cm^3 ; Shearer et al., 2006), the anorthosite would have floated to the surface while the olivine and pyroxene would have sunk into the mantle. A relict of this anorthosite-rich floatation crust is represented by the farside anorthositic highlands (FAH) that we see today. The FAH consists of ~87% plagioclase, lacks incompatible elements, and almost completely lacks mare volcanism (Wieczorek et al., 2006).

As differentiation continued, a near-surface, 10-100 km thick shell of magma, also known as the lunar magma ocean (LMO), formed (Warren, 1985). As the LMO underwent fractional crystallization, and the primordial anorthosite crust grew, the LMO progressively became a thinner layer, possibly non-existent in some places (Figure 5; Warren, 1985). Towards the end of this fractional crystallization period (~4.42 Ga; Nemchin et al., 2009), only magmas enriched with incompatible species (e.g., OH^- , H_2O , Th, U, REE, K, and P) remained (Warren, 1985). These residual magmas of the LMO are known as urKREEP (Warren, 1985; Wieczorek et al., 2000). The urKREEP would eventually mix with mantle-derived magnesian melts to form KREEP-basalts (Wieczorek et al., 2006).

Many workers (e.g., Warren, 1985; Wieczorek and Phillips, 2000; Wieczorek et al., 2006) have suggested that the presence of abundant mare basalts on the nearside and the

dominance of FAH on the farside (i.e. the mare-highlands dichotomy) is due to a higher abundance of radiogenic heat producing elements (Th, U, and K) associated with KREEP beneath the nearside crust. The nearside enrichment of radiogenic heat producing elements could have prolonged magma production due to elevated heat production in the subsurface. It is still disputed, however, as to whether the KREEP on the nearside (let alone on the farside, if it exists there at all) is a continuous layer (Snyder and Taylor, 1991) or if it is discontinuous in the form of dikes, sills, or pods (Wieczorek and Phillips, 2000). For example, the Compton Belkovich Thorium Anomaly (CBTA) lies outside the PKT and shows signs of relatively recent volcanic activity (Jolliff et al., 2011) and high Th content (Figure 2; Lawrence et al., 2003), which are consistent with the presence of KREEP at this site. The presence of KREEP material outside of the PKT boundary could indicate that KREEP extends beyond the nearside.

A hypothesis for the large concentration of KREEP in the PKT is the effect of large impacts during pre-Nectarian lunar history (4.5-3.9 Ga) (Warren, 2001; Wieczorek et al., 2006). Large, pre-Nectarian, basin-forming impacts excavated material and thinned the lunar crust, particularly on the nearside (Warren, 2001; Wieczorek et al., 2006). The presence of thinner crust on one side of the Moon may have caused a hydrostatic pressure differential that forced urKREEP-rich melts to pool underneath the thinner crust (Figure 6; Arkani-Hamed and Pentecost, 2001; Shearer et al., 2006). The debated Procellarum impact on the nearside between 4.5 Ga and 4 Ga (Wieczorek et al., 2006; Zuber et al., 2012), may have been the large impact responsible for the crustal thinning and subsequent urKREEP-rich magma accumulation (Figure 5; Arkani-Hamed and Pentecost, 2001; Warren, 2001; Wieczorek et al., 2006).

An alternative hypothesis for the origin of the PKT considers the effect that downwelling of ilmenite-enriched material could have had on the differentiating early Moon (Zhong et al.,

1999; Parmentier et al., 2002; Shearer et al., 2006). In this model, Rayleigh-Taylor instabilities in the differentiating LMO would have developed, ultimately resulting in a degree-1 downwelling of Ti-enriched, dense material into the mantle before the “main phase” of mare volcanism (before 4 Ga) (Parmentier et al., 2002; Shearer et al., 2006). This degree-1 downwelling could have either occurred spontaneously, given enough time, or it could have been triggered by an event, such as a large impact (Parmentier, et al., 2002; Shearer et al., 2006). Regardless of the trigger, the degree-1 downwelling would likely have carried urKREEP material along with the Ti-rich material, including radiogenic heat-producing elements that would have subsequently heated the mantle near the core-mantle boundary to produce melts rich in both urKREEP and Ti (Parmentier et al., 2002; Shearer et al., 2006). Zhong et al. (2000) show that such a degree-1 downwelling would have later resulted in the hemispherical dichotomy now seen in the distribution of KREEP material. According to their model, a portion of the downwelling would thermally expand due to radiogenic heating (Zhong et al., 2000). This thermal expansion would cause Ti- and urKREEP-rich cumulates to become less dense than the overlying mantle and allow them to buoyantly rise and accumulate below the nearside crust (Zhong et al., 2000). The non-uniform accumulation of radiogenic heat producing elements and Ti-rich melts at the base of the crust would help produce the increased volcanic activity on the nearside as well as the Ti-rich mare basalts present in the PKT.

Recently, the Gravity Recovery and Interior Laboratory (GRAIL) mission has discovered a semi-rectangular array of fractures in the PKT region that may present a mechanism for the eruption of mare basalts (Andrews-Hanna et al., 2014). They argue that the observed semi-rectangular array of fractures is not the pattern that would be expected if a basin-forming impact were responsible for the mare basalts on the nearside. Rather, a basin forming impact would be

elliptical in shape, and the observed rectilinear pattern may instead be consistent with a large plume below the lunar crust (Andrews-Hanna et al., 2014). Such a plume could have formed as a product of the ilmenite downwelling discussed previously (Zhong et al., 2000; Parmentier et al., 2002; Shearer et al., 2006). This plume would have generated a large heat gradient in the crust, forcing the crust to flex and fracture (Andrews-Hanna et al., 2014). These fractures would later act as conduits for magmas to reach the surface (Andrews-Hanna et al., 2014).

2.3 Silicic Lunar Magmatism

Silicic volcanism is much less common than basaltic mare volcanism on the Moon and may be the result of one or more mechanisms that include silicate liquid immiscibility (SLI; Weiblen and Roeder, 1973; Rutherford and Hess, 1973; Hess, 1989) and basaltic underplating (Hildreth, 1981; Bergantz, 1989; McCarthy and Patiño-Douce, 1997; Barboza and Bergantz, 1998; Huppert and Sparks, 1998). While SLI is considered to not be significant on Earth (Hagerty et al., 2006), both SLI and underplating have been shown, through natural and experimental studies, to be applicable to the Moon (Hagerty et al., 2006).

SLI will take place after ~90-98% crystallization of a basaltic magma (Hagerty et al., 2006). At this point, the temperature, pressure, and composition of the magma changes and two immiscible melts develop (Hagerty et al., 2006). One melt is silica-poor and-iron rich (basalt) while the other is silica-rich and contains alkali elements (granite/rhyolite) (Hagerty et al., 2006). Basaltic underplating, on the other hand, involves the emplacement of basaltic magmas under the crust (Hagerty et al., 2006). The basaltic magmas melt the crustal country rock, potentially yielding silicic partial melts. The resulting silicic melts are less dense than the country rock, which leads to the rise of silica-rich magmas to the surface (Hagerty et al., 2006). Of the two

mechanisms, basaltic underplating is generally more accepted as the primary mechanism for developing silicic melts on the Moon, as shown in natural and experimental studies (Hildreth, 1981; Bergantz, 1989; McCarthy and Patiño-Douce, 1997; Barboza and Bergantz, 1998; Huppert and Sparks, 1998). However, both SLI and underplating could act together to produce silicic volcanism on the Moon (Hagerty et al., 2006).

2.4 Lunar Water

There are several potential mechanisms for emplacement of water (OH-H₂O) on the surface of the Moon: implantation of solar wind hydrogen nuclei (protons) into the lunar regolith (Pieters et al., 2009); impacts of water-rich asteroids and comets (Greenwood et al., 2011); and exhumation of water endogenous to the Moon in the form of primordial water incorporated into minerals such as apatite (Klima et al., 2013). In this study we refer to primordial water as “magmatic” OH-H₂O.

Some of the OH-H₂O seen at the lunar surface could have been deposited by impacting meteors and comets (Arnold, 1979; Hodges, 2002; Pieters et al., 2009; Klima et al., 2013). These objects may have brought 2-3% (by mass) of the total lunar water (Hodges, 2002), but it is uncertain how much of the water in an impactor would be preserved after the impact (Hodges, 2002). The energy generated during an impact should cause all but a small fraction of the water to vaporize or escape lunar gravity (Hodges, 2002). The efficient loss of water due to vaporization during impacts suggests that the majority of the OH-H₂O signature seen in reflectance spectroscopy of the lunar surface may be attributed to either solar-wind implanted water or to magmatic water.

Previous studies (Pieters et al., 2009) have shown that a relatively large amount of solar wind implanted OH-H₂O is present at the lunar poles, with modeled abundances as high as 770 ppm (Pieters et al., 2009). Solar wind protons, however, bombard the entire surface of the Moon, where they interact with surface silicates and form OH-H₂O, with the highest production rates at the lunar equator (Pieters et al., 2009; McCord et al., 2011; Klima et al., 2013). During the lunar day, solar heating causes the loosely bound OH-H₂O to migrate through ballistic lateral flow (Hodges, 2002; Klima et al., 2013), until it is eventually sequestered by “cold traps” such as the permanently shadowed craters at the poles or, potentially, in shadowed cavities such as lava tubes during the lunar day (Crider and Vondrak, 2003; Pieters et al., 2009; Hibbitts et al., 2011; Klima et al., 2013). As solar heating of the lunar surface ceases during lunar the night, solar wind implanted OH-H₂O could re-bind to surface silicates and be remobilized during the next lunar day (Pieters et al., 2009; Klima et al., 2013). During the lunar dawn and dusk, the 2.8 μ m absorption associated with OH-H₂O is heavily affected by solar wind implanted OH-H₂O. Because solar wind implanted OH-H₂O is expected to be the most mobile during the warmest part of the lunar day, we can observe the Moon during lunar mid-day to obtain the best estimates of the concentration of magmatic OH-H₂O that is strongly bound within lunar rocks.

Recent mass spectrometer studies of Apollo samples (e.g., Saal et al., 2008; McCubbin et al., 2010; Boyce et al., 2010; Greenwood et al., 2011; Hauri et al., 2011; Hurwitz and Head, 2011; Klima et al., 2013; Hui et al., 2013) have shown that lunar magmas are significantly more hydrous than previously thought. Magmatic OH-H₂O on the Moon could have originated from the proto-Earth, prior to the giant impact that formed the Moon, as well from as the giant impactor itself (Greenwood et al., 2011). Magmatic OH-H₂O has been difficult to find on the lunar surface using remote sensing methods, but such evidence of magmatically-sourced OH-

H₂O was recently found in the central peak of Bullialdus Crater (Klima et al., 2013). Klima et al. (2013) used M³ hyperspectral imagery obtained close to lunar dawn and close to lunar mid-day to determine if the 2.8 μ m absorption associated with OH-H₂O persisted. Persistent 2.8- μ m absorptions were interpreted by Klima et al. (2013) to indicate that the absorption could not be attributed to solar wind implanted OH-H₂O, which mobilizes during the lunar day, and that it may instead be magmatic OH-H₂O (Klima et al., 2013). We utilize a similar method in this study to investigate the presence of magmatic OH-H₂O at sites where there is an even greater potential for volatile-enriched rocks than at Bullialdus Crater.

3. Study Areas

Th is radioactive, and the characteristic gamma rays emitted as the element decays can be remotely sensed. Because of its presence in KREEP-rich material, Th is one of the best remote indicators of KREEP on the Moon. The Gamma Ray Spectrometer that was on board the Lunar Prospector mission (LP-GRS) was designed with the intention of mapping Th and other key surface elements (H, U, K, O, Si, Mg, Fe, Ti, Al, and Ca) in order to develop global compositional maps of the Moon (Binder, 1998). Previous studies (e.g., Lawrence et al., 2000; Lawrence et al., 2003; Jolliff et al., 2012) have used data collected from the LP-GRS to locate Th hotspots in order to better understand the distribution of KREEP on the Moon (Figure 2). Lawrence et al. (2007) showed that the PKT has the highest concentration of Th-rich material on the Moon (Lawrence et al., 2000; Lawrence, 2003; Lawrence et al., 2007). The only regions showing any signs of Th enrichment on the lunar farside are the South Pole Aitken Basin (SPAB) (Hagerty et al., 2011) and the CBTA (Jolliff et al., 2011), indicating that material enriched in incompatible species are potentially present at these locations. The evolved

lithologies present at these potential sites of KREEP could also contain OH-H₂O, suggesting to us that Th may also be a good proxy for locating magmatic OH-H₂O sources. Since KREEP is enriched in both Th and magmatic OH-H₂O we can target non-mare volcanic features with high Th signatures, and determine if these evolved lithologies are enriched in OH-H₂O, and, if so, by how much.

Using the LP-GRS Th maps developed by Lawrence et al. (2007) (Figure 2), we chose four high-Th sites, inferred to mark KREEP-enriched locations, to explore for OH-H₂O. The Th “hot spots” chosen for this study are: Compton/Belkovich; the Gruithuisen Domes; Lassell Massif; and Hansteen Alpha. Each of these locations possesses an anomalously high Th concentration consistent with granitic Th concentrations here on Earth (Hawke et al., 2003; Lawrence et al., 2003; Garrick-Bethell et al., 2005; Hagerty et al., 2006; Greenhagen et al., 2010; Jolliff et al., 2011), and most exhibit 8- μ m spectral signatures (Christiansen features) that are consistent with silica- and/or alkali feldspar-rich rocks as shown by results from the DIVINER instrument (Jolliff et al., 2011; Wilson and Head, 2003; Hawke et al., 2003; Hagerty et al., 2006; Greenhagen et al., 2010). All four study sites also display rough, mounded morphologies, suggesting viscous lavas, seen in high resolution imagery (Wilson and Head, 2003; Jolliff et al., 2011).

3.1 Compton/Belkovich Thorium Anomaly

The Compton/Belkovich Th anomaly (CBTA) is located on the farside of the moon (61.1° N, 99.5° E; Figure 1) and covers a ~25 km by ~35 km area. Imagery from the Lunar Reconnaissance Orbiter Near Angle Camera (LRO-NAC) shows morphologies, including domes and vents, and textures, including large boulders and rough terrain that are similar to terrestrial

felsic volcanics (Jolliff et al., 2011). In contrast, mare volcanism will, at scales visible in orbital imagery and digital topography, show different, smoother textures and landforms (Figure 7). Th concentrations at CBTA as measured by LP-GRS are greater than 9 ppm (Figure 2; Jolliff et al., 2011), possibly indicating lunar granites, which have high Th concentrations (Hagerty et al., 2006). CBTA has a crater retention age of ~ 1 Gy (Jolliff et al., 2012), making it much younger than other the nearside non-mare features in this study. This is interesting considering its geographic location on the farside.

3.2 Gruithuisen Domes

The Gruithuisen Domes are located on the lunar nearside on the western border of Mare Imbrium, and consists of two domes: Gruithuisen Gamma and Gruithuisen Delta (36° N, 40° W; Figure 1). Gruithuisen Gamma, a 1200-m high, flat-topped dome covering an area of ~ 24 km by ~ 18 km, has Th concentrations up to 43 ppm (Hagerty et al., 2006). Previous studies (Chevrel et al., 1999; Wilson and Head, 2003) have shown that the morphologies and rough surface textures of the Gruithuisen Domes are indicative of highly viscous lava such as in terrestrial dacite and rhyolitic domes. Stratigraphic relationships show these domes to be Late Imbrium in age (3.2-3.8 Gya; Chevrel et al., 1999).

3.3 Lassell Massif

Lassell Massif is located at the northern end of Mare Nubium (15° S, 8° W; Figure 1). This ~ 30 km by ~ 15 km, mottled, rectangular massif contains Th concentrations of 53 ppm (Hagerty et al., 2006). This massif is embayed by Imbrium age mare deposits, giving it a pre-Imbrium age ($\sim > 3.8$ Ga; Ashley et al., 2013).

3.4 Hansteen Alpha

Hansteen Alpha, located in the southern portion of Oceanus Procellarum (12°S, 50°W; Figure 1), is a triangular mound measuring ~25 km on each side. There are linear depressions on top of the mound, which are interpreted to be probable volcanic vents (McCauley, 1973). The concentrations as high as 19.5 ppm were found at Hansteen Alpha by Hagerty et al. (2006). The impact ejecta from nearby craters, Billy and Hansteen, do not drape this feature indicating that it was emplaced after these two impacts (~3.8 Ga; Hawke et al., 2003). However, Hansteen Alpha is embayed by the mare basalts adjacent to it, indicating that it is older than the basalts (Hawke et al., 2003), which are ~3.0-3.8 Ga (Hiesinger et al., 2003).

4. Data

4.1 Moon Mineralogy Mapper

Moon Mineralogy Mapper (M^3) is an imaging spectrometer that was on board India's Chandrayaan-1 spacecraft (Boardman et al., 2011). It had a spectral range from 0.43 μm to 3.0 μm , spanning 85 bands with 20-40 nm spectral resolution (Boardman et al., 2011). In this study we use the M^3 data to measure the depth of 2.8- μm absorptions and use those measurements to calculate OH-H₂O concentrations. The images used in this study were acquired from the NASA Planetary Data System (PDS) Imaging Node (<http://ode.rsl.wustl.edu/moon>). Preprocessing done by the M^3 science team includes thermal correction, photometric correction, and statistical polishing (for more detail on calibration and preprocessing techniques see Lundeen et al. [2011]). In addition, the images available on the PDS have already been converted to reflectance

using the I/F method (Lundeen et al., 2011). Once downloaded from the PDS, the M³ data were ready for processing and interpretation using ENVI software as well as using MATLAB codes specifically written for the purposes of this study (Appendix 1).

M³ imagery was obtained during four different optical periods during the life of the Chandrayaan-1 mission (Boardman et al., 2011). The data used in this study came from two of those optical periods. Optical period 1B (OP1B) has solar zenith angles (~53°-61°) consistent with lunar dawn or dusk (Boardman et al., 2011). Images acquired during OP1B have better spatial resolutions (140 m) than those acquired during later optical periods because the Chandrayaan-1 spacecraft was in a lower (100 km) orbit during OP1B (Boardman et al., 2011) (Table 1). Optical period 2C (OP2C) has solar zenith angles consistent with lunar mid-day (~14°-18°), but, because Chandrayaan-1 was in a higher (200 km) orbit, these images have lower spatial resolutions (280 m) than those acquired during other optical periods (Boardman et al., 2011).

During the times the OP1B imagery was acquired, it is expected that surface materials would be affected by a relatively large amount of solar wind implanted OH-H₂O, which would increase the strength of the 2.8-μm absorption (Pieters et al., 2009; Klima et al., 2013). OP2C imagery is better suited to our purposes because it was obtained close to lunar noon. This is when loosely-bound solar wind implanted OH-H₂O would be mobilized as the surface warms during the lunar day and would have the smallest effect on the 2.8 μm absorption attributed to magmatic OH-H₂O (Klima et al., 2013). If the OH-H₂O signature is magmatic, instead of being implanted by solar wind, then the 2.8-μm absorption feature would be expected to persist in OP2C images as compared to OP1B images (Figure 8).

4.2 Lunar Reconnaissance Orbiter

In this study we use digital terrain models (DTMs) and high resolution imagery to identify geomorphologies consistent with volcanism, such as volcanic vents, ridges, or domes. The Lunar Reconnaissance Orbiter (LRO) has two cameras on board, both with the ability to generate DTMs. The Narrow-Angle Camera (NAC) is a high-resolution camera with a band-center at 550 nm and a spatial resolution of 0.5 m (Chin et al., 2007). The Wide-Angle Camera (WAC) is a multispectral camera that has a spatial resolution of 100 m per pixel in visible light (Chin et al., 2007). WAC DTMs are utilized in areas that NAC DTMs are not available. The high-resolution LROC images and the NAC and WAC DTMs used in this study were acquired from the LRO DTM viewer (<http://lroc.sese.asu.edu>) (Table 2). We use the high-resolution imagery and DTMs to determine if volcanic landforms with bouldery textures that are consistent with silica-rich volcanism are present at sites we identify as having high concentrations of potentially magmatic OH-H₂O.

5. Methods

In M³ imagery, OH-H₂O enriched minerals exhibit a 2.8- μ m absorption that we can use to calculate OH-H₂O concentrations. Increasing amounts of OH-H₂O deepens the 2.8- μ m absorption, but to convert the absorption depth to concentration we must take into account the radiative transfer physics that quantitatively relate water abundance to spectral absorption depth. We do this by using Hapke radiative transfer theory (Hapke, 2012) and the Beer-Lambert law (Libowitzky and Rossman, 1997). Using a methodology similar to that of Klima et al. (2013), we can determine the concentration of OH-H₂O in lunar rocks. In order to demonstrate that the

OH-H₂O signatures that we see in OP2C images are not entirely attributed to solar wind, we compare available M³ images from OP1B and OP2C at Hansteen Alpha.

5.1 Continuum Removal

The 2.8- μ m absorption is difficult to measure due to the effect of slope reddening (Issacson et al., 2011). To correct for slope reddening, a linear fit to the continuum slope at the shoulders of the 2.8- μ m absorption is performed (Figure 9). The original spectrum is then divided by the continuum slope, which flattens the spectrum (Issacson et al., 2011). With the flattened spectrum we can accurately measure the width and depth of the 2.8 μ m absorption, which tells us the relative amount of OH-H₂O present (Pieters et al., 2009; Klima et al., 2013).

5.2 Frequency Filtering

After continuum removal, a number of the images exhibited vertical striping that is the result of instrument and sensor defects (Boardman et al., 2011). Pixels associated with this striping noise show reflectances that are not consistent with the actual surface reflectance, making the unfiltered data difficult to use. To remove the striping, we apply a frequency domain filter. The filter is applied by first computing the Fast Fourier transform (FFT) of the M³ image (Jensen, 2005). A mask, with tapered edges (Figure 10), is then applied to the M³ image in the frequency domain in order to remove frequency components that create vertical striping (Jensen, 2005). The frequency components associated with the striping are identified as anomalously high power (bright spots or lines) frequencies that are outside the high frequency center (Figure 10). The resulting filtered M³ image is then converted from the frequency domain back to the spatial domain using an inverse Fast Fourier transform (IFFT) (Jensen, 2005). The result is a

filtered M^3 image that has less vertical striping than the unfiltered image, and is, therefore, easier to interpret.

5.3 2.8- μm Band Depth

The filtered M^3 data is used to calculate the depth of the 2.8- μm absorption associated with OH-H₂O. We calculate the band depth by subtracting the minimum reflectance of the 2.8- μm absorption (b_{min}) from the left shoulder reflectance value ($b_{shoulder}$) (Figure 9):

$$b_{shoulder} - b_{min} = \Delta R \quad (1),$$

where ΔR is the change in reflectance from absorption shoulder to minimum (i.e. band depth). Equation (1) is applied to each pixel in the filtered M^3 image to yield a band depth image that we contour. The contoured band depth image highlights pixels with large OH-H₂O absorptions that we then investigate in detail to measure OH-H₂O concentrations using Hapke radiative transfer equations (Hapke, 2012) and the Beer-Lambert law (Libowitzky and Rossman, 1997).

5.4 Hapke Theory

We quantify the OH-H₂O concentration associated with the 2.8- μm absorption band depth by converting reflectance spectra extracted from the original M^3 images into absorption coefficient (α) spectra following the method of Klima et al. (2013). This requires first determining the appropriate albedo factor (γ) and then the equivalent single scattering albedo (ω) (Hapke, 2012). The albedo factor is obtained using the following equations (Hapke, 2012):

$$\gamma = \frac{[(\mu_0 + \mu)^2 \Gamma_L^2 + (1 + 4\mu_0 \mu \Gamma_L)(1 - \Gamma_L)]^{1/2} - (\mu_0 + \mu) \Gamma_L}{1 + 4\mu_0 \mu \Gamma_L} \quad (2)$$

$$\Gamma_L = 4 \frac{\mu_0 + \mu}{\mu_0} \frac{1}{(1 + 2\mu_0)(1 + 2\mu)} \frac{I}{F} \quad (3),$$

where Γ_L is the reflectance relative to a Lambert surface, μ_0 is the cosine of the viewing angle, μ is the cosine of the zenith angle of incidence, and I/F is the pre-processed M³ imagery that is provided by the M³ science team. The albedo factor is then converted to single scattering albedo using (Hapke, 2012):

$$\omega = 1 - \gamma^2 \quad (4).$$

With the single scattering albedo we can now calculate the absorption coefficient using the following equations (Hapke, 2012):

$$\alpha = -\frac{1}{D} \ln \left(\frac{\omega - S_e}{1 - S_e - S_i + S_i \omega} \right) \quad (5)$$

$$S_e = 0.058 + 0.8543R(0) + 0.0870R(0)^2 \quad (6)$$

$$S_i = 1 - \frac{1}{n_r^2} [0.9413 - 0.8543R(0) - 0.0870R(0)^2] \quad (7)$$

$$R(0) = \frac{(n_r - 1)^2 + n_i^2}{(n_r + 1)^2 + n_i^2} \quad (8),$$

where D is the particle size (45 μm ; Klima et al., 2013); S_e is the exterior surface reflection coefficient of an irregular particle; S_i is internal reflection coefficient of an irregular particle; $R(0)$ is the normal specular reflection coefficient; n_r is the real refractive index for pyroxene (0.75; Klima et al., 2013); and n_i is the imaginary refractive index for pyroxene. Since n_i is proportional to α , we iteratively determine n_i and α using Equations (5)-(8) and the following relationship (Hapke, 2012):

$$\alpha(\lambda) = \frac{4\pi n_i}{\lambda} \quad (9),$$

where λ is wavelength. Klima et al. (2013) found no significant difference in absorption coefficient values, and the resulting water abundances (see Sections 5.5 and 5.6), calculated

using refractive indices for pyroxene, quartz, and anorthite. Therefore, we use the refractive index of pyroxene (0.75) to be consistent with Klima et al. (2013) methodology. Klima et al. (2013), however, show that absorption coefficient is strongly dependent on particle size. Klima et al. (2013) found that a grain size of 15 μm yields water abundances 20% higher than those obtained assuming a grain size of 45 μm , whereas a grain size of 150 μm yields water abundances 20% lower.

5.5 Integrated Molar Absorption Coefficient

To determine the integrated molar absorption coefficient (ϵ_i), required to calculate OH-H₂O concentrations, we first must flatten the absorption coefficient spectrum. To perform the flattening, we estimate the continuum slope of the absorption spectrum similar to the way described in Section 5.1. The original spectrum is then divided by the continuum slope, thus flattening the absorption coefficient spectrum (Figure 9). We then fit a Gaussian curve to the flattened absorption coefficient spectrum and determine the wavenumber ($\bar{\nu}$) of the center of the absorption coefficient maximum associated with the ~ 2.8 μm OH-H₂O feature (Klima et al., 2013). With $\bar{\nu}$ we can calculate ϵ_i (in cm^{-2} per mol H₂O/L) using the following equation (Libowitzky and Rossman, 1997):

$$\epsilon_i = 246.6(3753 - \bar{\nu}) \quad (10).$$

5.6 Beer-Lambert Law

We use ϵ_i to calculate OH-H₂O concentration (c ; in ppm) using the Beer-Lambert law (Libowitzky and Rossman, 1997; Klima et al., 2013):

$$c = \frac{A_i}{D \times \rho \times \epsilon_i} \times 1.8e5 \quad (11),$$

where ρ is density (in g/cm^3) and D is grain size (in cm). Due to the silicic composition of the non-mare volcanic features in this study, we assume ρ to be 2.7 g/cm^3 (approximate ρ for anorthosite and quartz). A_i (in cm^{-1}) is the area under the Gaussian curve fit to the flattened absorption coefficient spectrum and is computed by numerical integration.

5.7 Morphologic Analysis

In addition to calculating OH-H₂O concentrations, we determine if the highs in the M³ band depth contour image (i.e. locations of pronounced OH-H₂O signatures) coincide with morphologies consistent with volcanic activity, such as vents or domes. This is done by draping the high-resolution LRO-NAC imagery onto DTMs derived from LRO-NAC or LRO-WAC images (Figure 11). If the filtered M³ images show OH-H₂O signatures and volcanic features in the same locations, it increases our confidence that the OH-H₂O absorptions are magmatic signatures. Both mafic and silicic volcanism will show morphologic features such as vents, ridges, and domes. However, silicic magmatism is typically associated with distinct bouldery textures compared to the smoother textures seen in terrestrial mafic examples (Figure 7).

6. Results

The following sections report the magmatic OH-H₂O concentrations calculated from each study site (Figure 12). Although the OP2C images from which these concentrations were calculated were obtained near lunar noon, and should exhibit the minimum amount of solar wind influence, it is possible that some amount of solar wind implanted water may remain. Therefore, the water concentrations we report should be considered maxima. The study sites were given the following abbreviations (Table 3; Appendix 2): Compton-Belkovich Thorium Anomaly (CBTA),

Hansteen Alpha (HAN), Lassell Massif (LASS), and Gruithuisen Domes (GRUITH). Numbers following these abbreviations indicate the specific locations at those sites from which the spectra were extracted (Figure 12).

6.1 CBTA

Large OH-H₂O concentrations were found in the OP2C M³ imagery that was available for CBTA (Table 1 and 3; Figure 12 and 13), with concentrations ranging from 82±20 ppm to 274±47 ppm OH-H₂O (CBTA1-3, 6; Table 3; Figure 12). By contrast, the FAH surrounding CBTA have much lower concentrations of 16±7 ppm to 46±17 ppm OH-H₂O (CBTA4 and 5; Table 3; Figure 12).

In the NAC/WAC DTMs we see dome-like features at the locations of large OH-H₂O concentrations (CBTA1; Figure 11). In NAC imagery these features have rounded morphologies and bouldery textures that are suggestive of silicic volcanic features (CBTA1; Figure 11). Just south of these domes (between CBTA1 and CBTA3), Jolliff et al. (2011) identified irregular depressions that they suggest are collapse features associated with volcanism (Jolliff et al., 2011). These also are associated with large 2.8-μm absorptions (Figure 13).

6.2 Hansteen Alpha

High OH-H₂O signatures at Hansteen Alpha (HAN4) appear to align with topographically high, ridge-like features seen in the NAC imagery (Figure 11). The OH-H₂O concentrations at Hansteen Alpha range from 82±22 ppm to 127±21 ppm (HAN1-4; Table 3; Figure 12). The bouldery ridge in the northeast (HAN4; Figure 11 and 12) shows OH-H₂O concentrations of 84±23 ppm (Table 3). The highest concentration at Hansteen Alpha (127±21

ppm; Table 3) is located at HAN2, which is a topographically high feature, with a shape consistent with a volcanic dome (Figure 11).

A comparison of spectra extracted from a ~ 1 km area in the OP2C and OP1B images of HAN4 (Figure 8) illustrates the expected influence of solar wind implanted water. The depth of the $2.8\text{-}\mu\text{m}$ absorption feature is shallower in the OP2C spectrum than in the OP1B spectrum, consistent with the expected mobility of solar wind implanted water during the lunar day. This supports our assumption that OP2C imagery will give the best estimate for the magmatic water concentration.

6.3 Lassell Massif

In NAC DTMs, WAC DTMs, and NAC imagery for Lassell Massif, Ashley et al. (2013) see negative relief features (at LASS2), possibly collapse or explosive pits, that could have been created by relatively recent volcanic activity. Our results show that these features are associated with moderately deep $2.8\text{-}\mu\text{m}$ absorptions and a water concentration of 19 ± 62 ppm. Within Lassell Massif proper, the magmatic OH-H₂O concentrations range from 19 ± 62 ppm to 42 ± 106 ppm (Table 3), but we do not consider these concentrations reliable due to the large uncertainties. The large uncertainties result from the fact that the Lassell Massif images in the vicinity of LASS1-3 are heavily affected by striping (see Section 5.2), even after frequency filtering.

Spectra extracted from a high albedo feature (LASS4) and a crater (LASS5), both ~ 40 km west of Lassell Massif, show OH-H₂O concentrations of 263 ± 20 ppm and 323 ± 54 ppm, respectively (Figure 12; Table 3). These large OH-H₂O concentrations could be attributed to the fresh impact crater west of the massif and LASS4 and LASS5. A water-rich impactor may have

produced it, or, more likely, the impact may have exposed magmatic OH-H₂O rich material in the subsurface, thus, resulting in a large 2.8- μ m absorption at these sites (Figure 12).

6.4 Gruithuisen Domes

Gruithuisen Domes exhibits the largest OH-H₂O concentrations (Figure 13), as high as 294 \pm 74 ppm OH-H₂O at GRUITH1 (Table 3; Figure 12). Unfortunately, the only M³ data we were able to analyze were OP1B images, making it difficult to determine how much of the OH-H₂O signature is attributed to solar wind implantation and how much is actually magmatic in origin (see Section 7.1).

7. Discussion

7.1 Lunar Water

Recent studies of lunar apatites from Apollo samples have shown that pre-eruption magmas on the Moon would have contained ~100 ppm water (Robinson and Taylor et al., 2014) with a minimum water concentration of 64 ppb to 21 ppm (McCubbin et al., 2010). In addition, Klima et al. (2013) have shown that the central peak of Bullialdus crater contains 45-125 ppm of presumably magmatic water. Here we have shown that Lassell Massif contains moderate water concentrations (~42 \pm 106 ppm; Table 3), Hansteen Alpha contains high water concentration (~82-127 ppm; Table 3), and CBTA contains concentrations as high as 274 \pm 47 ppm (CBTA6; Table 3). Unfortunately we were unable to confidently determine if magmatic OH-H₂O was present at Gruithuisen Domes.

Higher concentrations of water at non-mare silicic features, such as Hansteen Alpha and CBTA, could indicate that they were formed from melts heavily enriched in urKREEP material, since KREEP is thought to contain large amounts of water (Elkins-Tanton and Grove, 2011). In addition, the presence of magmatic OH-H₂O within the non-mare silicic features in this study indicates that the melts that produced them may have had a low melting point. Therefore, the melts may have formed and migrated to the surface sooner than other melts (i.e. mare basalts). This is consistent with the relative timing of volcanic events on the nearside, where mare basalts embay non-mare silicic features, indicating the non-mare features were erupted prior to the maria. CBTA is an interesting case because it is located on the farside and overlies the FAH (Jolliff et al., 2011), suggesting it had erupted after the FAH formed. The presence of magmatic OH-H₂O and Th at CBTA may have promoted prolonged melt generation and migration through the thick farside crust.

7.2 Nearside Non-mare Volcanism

Hansteen Alpha shows persistent 2.8- μ m absorptions throughout the lunar day, as well as morphologies consistent with a magmatic OH-H₂O source, as seen in NAC/WAC imagery. The large Th concentrations at Hansteen Alpha, as well as the boulder fields and volcanic features (ridges, domes, etc.; Figure 11), suggest that these features are similar to granite/rhyolite features here on Earth. Here we have also shown that these boulder fields may also be enriched in magmatic water. The abundance of water could have created a lower melting point for the magmas at Hansteen Alpha and allowed the melts to reach the surface sooner than mare basalt material. It has been thought that the non-mare silicic features could have formed due to silicate liquid immiscibility or basaltic underplating (Hagerty et al., 2006). However, the fact that these

non-mare silicic volcanics erupted within their respective impact basins before mare basalts is contradictory to SLI (Hagerty et al., 2006). While SLI could produce non-mare silicic features, it would only do so after a majority of the mafic melts were produced (Hagerty et al., 2006). Our suggestion that Hansteen Alpha melts formed prior to the mare basalts melts, is consistent with the cross-cutting geologic relationships that we observe at Hansteen Alpha, where mare basalts appear to embay Hansteen Alpha, indicating that Hansteen Alpha is older than the maria adjacent to it (Hawke et al., 2003).

7.3 Farside Non-mare Volcanism

The high Th and OH-H₂O concentrations at CBTA on the farside of the Moon are consistent with the silica- and water-rich evolved lithologies seen on the nearside at Hansteen Alpha, and Lassell Massif. While these signatures are consistent with KREEP, the location of CBTA on the farside is problematic because it is such a large distance away from the currently recognized PKT boundary (Figure 1). Our work here suggests that CBTA could be geochemically related to the nearside non-mare silicic features, despite the fact it is spatially separated. This geochemical relationship indicates that CBTA could be a product of the same process that created the nearside non-mare features.

CBTA could have been produced from partial melts that were isolated as the LMO crystallized early in the Moon's geologic history (Figure 4). The last of the melts from the LMO could have been rich in Th and OH-H₂O (Elkins-Tanton and Grove, 2011), yielding spectral signatures consistent with what we see at Hansteen and CBTA. However, since CBTA is on the farside, these melts would have had a much thicker anorthositic crust to migrate through, compared to the thin nearside crust. This thicker crust would require more time for CBTA

magmas to migrate through, which would explain the younger age (~1 Gya) of CBTA, relative to the nearside non-mare features (3-4 Gya) (Jolliff et al., 2012). High concentrations of Th and magmatic OH-H₂O at CBTA suggest that the CBTA was produced from the KREEP, which could imply that the KREEP extends beyond the recognized PKT boundary on the nearside. However, it is uncertain how much further beyond CBTA the KREEP layer extends. At places like CBTA the KREEP could be present in the form of a dike, sill, or pod. Alternatively, KREEP could be present on the farside in the form of a global, continuous layer. If KREEP is global in extent, then one place one would expect it to see it at the South Pole Aiken Basin.

7.4 Plume or Impact Origin for Nearside Volcanism

The recent GRAIL gravity gradient maps produced by Andrews-Hanna et al. (2014) show that Hansteen Alpha and Lassell Massif are near, or are in close proximity to, fractures that may have been created by a potential nearside plume (Andrew-Hanna et al., 2014). This plume could have been responsible for most of the mare basalt volcanism on the nearside, which created the mare-highland dichotomy (Andrews-Hanna et al., 2014). Aided by lowered melting points, due to elevated water and radiogenic heat producing element concentrations, the Hansteen Alpha and Lassell Massif silicic melts could have formed and reached the surface prior to mare basalts using fractures created by the rising plume (Figure 14; Andrews-Hanna et al., 2014). However, the GRAIL gravity maps show that the Gruithuisen Domes are not near the fractures identified by Andrews-Hanna et al. (2014). Instead, the Gruithuisen Domes are located on the rim of the Imbrium basin, suggesting that those magmas reached the surface through ring fractures generated by the Imbrium impact (Figure 14).

This work suggests that Hansteen Alpha and CBTA are geochemically related to one another due to their high concentrations of Th (>10 ppm; Lawrence et al., 2007) and magmatic OH-H₂O (>100 ppm; this study). The presence of magmatic OH-H₂O would lower the melting point of subsurface rock, potentially heated by the plume suggested by Andrews-Hanna et al. (2014), leading to the eruption of the non-mare silicic material prior to the eruption of mare basalts. This is inconsistent with non-mare silicic feature formation induced by SLI, and is consistent with basaltic underplating. We would not expect to see silicic non-mare features forming sooner than mare basalts based on SLI. SLI produces silica-rich melts after 90-98% of the basaltic melt has formed (Hagerty et al., 2006). Basaltic underplating, on the other hand, predicts that silicic melts could be formed if the country rock it melts is enriched in silica. Basaltic underplating doesn't require a majority of the mafic melts to crystallize before silica-rich melts can be formed. Therefore, basaltic underplating is the likely mechanism for generating these non-mare silicic features. It is also possible that CBTA is a product of the nearside plume proposed by Andrews-Hanna et al. (2014). Since the nearside non-mare silicic features seem to be geochemically related to CBTA in that they are all KREEP- and OH-H₂O-rich, it is also possible that CBTA could be the product of a secondary plume head that was formed off the primary nearside plume proposed by (Zhong et al., 2000)..

8. Conclusions

Our band depth contour images allow us to easily identify large 2.8- μ m absorptions attributed to OH-H₂O at a set of non-mare silicic features on both the nearside and the farside of the Moon. With the band depth contour images, we were able to locate features within Hansteen Alpha and CBTA with high OH-H₂O concentrations as well as identify volcanic morphologies

with LRO NAC imagery and DTMs. By targeting some of the largest Th anomalies on the Moon, we were able to locate areas that are enriched in OH-H₂O. In this study we were able to identify the largest concentrations of water yet seen at non-polar latitudes on the nearside, with magmatic OH-H₂O concentrations as high as 127±21 ppm. Furthermore, we found more than double the water concentration (274±47 ppm) at CBTA on the farside. The water concentrations that we report here are exciting and suggest that the Moon is much wetter than we previously thought.

We have determined that CBTA and Hansteen Alpha likely host hydrous evolved lithologies. Using M³ hyperspectral images obtained near lunar dawn (OP1B) and at lunar mid-day (OP2C), we were able to determine if the 2.8 μm absorption associated with OH-H₂O persisted into lunar mid-day. Persistent 2.8-μm absorptions were observed at Hansteen Alpha, indicating that the absorption was not attributed to solar wind implanted OH-H₂O, which mobilizes during the lunar day, and that the 2.8-μm absorptions instead may be magmatic OH-H₂O (Klima et al., 2013). In addition, CBTA and Lassell Massif contain significant 2.8-μm absorptions in lunar mid-day imagery, which suggests that the absorptions there are also attributed to magmatic water. Gruithuisen Domes appear to have a hydrous signature, given their large OH-H₂O concentrations, but without proper OP2C imagery, we are unable to confidently determine if they contained magmatic OH-H₂O. However, the large difference in OH-H₂O concentrations inside and outside of Gruithuisen Domes (Figure 12; Table 3) suggests that at least some of the water within the non-mare silicic features is magmatic.

Our results suggest that OH-H₂O-rich melts would have promoted melt generation, with the heat supplied by a nearside plume (Andrews-Hanna et al., 2014). Increased magmatic OH-H₂O could lead to formation of the non-mare silica features at an earlier time than mare basalts.

It is currently debated that whether basaltic underplating or SLI are responsible for the generation of non-mare silicic features (Hagerty et al., 2006). The SLI mechanism for generating the silica-rich melts, however, is incompatible with our interpretation that hydrous non-mare silicic features formed prior to the mare basalts adjacent to them. Therefore, we suggest that basaltic underplating is the primary mechanism for generating hydrous non-mare silicic features on the Moon. More importantly, CBTA is the only known hydrous evolved lithologic feature on the lunar farside. The geochemical signature of CBTA is consistent with nearside non-mare features, such as Hansteen Alpha, suggesting that it was also formed by urKREEP-rich partial melts through basaltic underplating. The geochemical signature at CBTA suggests that KREEP may be present outside of the previously accepted boundary within the PKT.

References

- Allégre, C.J., Manhés, G., and Göpel, C., 1995, The Age of the Earth: *Geochimica et Cosmochimica Acta*, v. 59, no. 8, p. 1445-1456.
- Andrews-Hanna, J.C., Besserer, J., Head III, J.W., Howett, C.J.A., Kiefer, W.S., Lucey, P.J., McGovern, P.J., Melosh, H.J., Neumann, G.A., Phillips, R.J., Schenk, P.M., Smith, D.E., Solomon, S.C., and Zuber, M.T., 2014, Structure and evolution of the lunar Procellarum region as revealed by GRAIL gravity data: *Nature*, v. 514, no. 7520, p. 68-71.
- Arkani-hamed, J. and Pentecost, A., 2001, On the Source Region of the Lunar Mare Basalt: *Journal of Geophysical Research*, v. 106, p. 14691-14700.
- Arnold, J. R., 1979, Ice in the lunar polar regions: *Journal of Geophysical Research*, v. 84, p. 5659-5668.
- Ashley, J. W., Robinson, M. S., Stopar, J. D., Glotch, T. D., Hawke, B. R., Lawrence, S. J., Greenhagen, B. T., and Paige, D. A., 2013, The Lassell Massif – Evidence for complex volcanism on the Moon: *Proceedings of the 44th Lunar and Planetary Science Conference*. p. 2504.
- Barboza, S. A. and Bergantz, G. W., 1998, Rheological transitions and the progress of melting of crustal rocks: *Earth and Planetary Science Letters*, v. 158, p. 19-29.

- Bergantz, G. W., 1989, Underplating and partial melting: implications for melt generation and extraction: *Science*, v. 245, p. 1093-1095.
- Binder, A.B., 1998, Lunar Prospector: Overview: *Science*, v. 281, p. 1475-1476.
- Boardman, J.W., Pieters, C.M., Green, R.O., Lundeen, S.R., Varanasi, P., Nettles, J., Petro, N., Isaacson, P., Besse, S., and Taylor, L.A., 2011, Measuring moonlight: An overview of the spatial properties, lunar coverage, selenolocation, and related Level 1B products of the Moon Mineralogy Mapper: *Journal of Geophysical Research*, v. 116, p. 1-15, doi: 10.1029/2010JE003730.
- Boyce, J.W., Liu, Y., Rossman, G.R., Guan, Y., Eiler, J.M., Stolper, E.M., and Taylor, L.A., 2010, Lunar apatite with terrestrial volatile abundances: *Nature*, v. 466, p. 466-469.
- Canup, R.M. and Asphaug, E., 2001, Origin of the Moon in a giant impact near the end of the Earth's formation: *Nature*, v. 412, no. 6848, p. 708-712, doi: 10.1038/35089010.
- Chevrel, S.D., Pinet, P.C., and Head, J.W., 1999, Gruithuisen domes region: A candidate for an extended non-mare volcanism unit on the Moon: *Journal of Geophysical Research*, v. 104, no. E7, p. 16515-16529, doi: 10.1029/1998JE900007.
- Chin, G., Brylow, S., Foote, M., Garvin, J., Kasper, J., Keller, J., Litvak, M., Mitrofanov, I., Paige, D., Raney, K., Robinson, M., Sanin, A., Smith, D., Spence, H., 2007, Lunar

Reconnaissance Orbiter Overview: The Instrument Suite and Mission: *Space Science Reviews*, v. 129, p. 391-419, doi: 10.1007/s11214-007-9153-y.

Crider, D. H. and Vondrak, R. R., 2003, The solar wind as a possible source of lunar polar hydrogen deposits: *Journal of Geophysical Research*, v. 105, 26773-26782.

Elkins-Tanton, L.T. and Grove, T.L., 2011, Water in the lunar magma ocean: *A Wet Vs. Dry Moon: Exploring Volatile Reservoirs and Implications for the Evolution of the Moon and Future Exploration*, p. 14.

Garrick-Bethell, I. and Zuber, M.T., 2005, An indigenous origin for the South Pole Aitken basin thorium anomaly: *Geophysical Research Letters*, v. 32, no. 13, p. 1-5, doi: 10.1029/2005GL023142.

Greenhagen, B.T., Lucey, P.G., Wyatt, M.B., Glotch, T.D., Allen, C.C., Arnold, J.A., Bandfield, J.L., Bowles, N.E., Donaldson Hanna, K.L., Hayne, P.O., Song, E., Thomas, I.R., and Paige, D.A., 2010, Global silicate mineralogy of the Moon from the Diviner lunar radiometer: *Science*, v. 329, no. 5998, p. 1507-1509, doi: 10.1126/science.1192196.

Greenwood, J.P., Itoh, S., Sakamoto, N., Warren, P., Taylor, L., Yurimoto, H., 2011, Hydrogen Isotope Ratios in Lunar Rocks Indicate Delivery of Cometary Water to the Moon: *Nature Geoscience*, v. 4, p. 79-82.

Hagerty, J.J., Lawrence, D.J., Hawke, B.R., Vaniman, D.T., Elphic, R.C., and Feldman, W.C., 2006, Refined thorium abundances for lunar red spots: Implications for evolved, nonmare volcanism on the Moon: *Journal of Geophysical Research*, v. 111, no. E6, p. 1-20, doi: 10.1029/2005JE002592.

Hagerty, J.J., Lawrence, D.J., and Hawke, B.R., 2011, Thorium abundances of basalt ponds in South Pole-Aitken basin: Insights into the composition and evolution of the far side lunar mantle: *Journal of Geophysical Research*, v. 116, no. E6, doi: 10.1029/2010JE003723.

Hapke, B., 2012, *Theory of Reflectance and Emittance Spectroscopy*: Cambridge University Press, 528 p.

Hauri, E.H., Weinreich, T., Saal, A.E., Rutherford, M.C., and Van Orman, J.A, 2011, High pre-eruptive water contents preserved in lunar melt inclusions: *Science*, v. 333, no. 6039, p. 213-215, doi: 10.1126/science.1204626.

Hawke, B.R., Lawrence, D.J., Blewett, D.T., Lucey, P.G., Smith, G.A., Spudis, P.D., and Taylor, G.J., 2003, Hansteen Alpha: A volcanic construct in the lunar highlands: *Journal of Geophysical Research*, v. 108, no. E7, doi: 10.1029/2002JE002013.

Hess, P. C., 1989, *Origins of Igneous Rocks*: Harvard University Press (Cambridge, MA), 344 p.

- Hibbitts, C. A., Grieves, G. A., Poston, M. J., Dyar, M. D., Alexandrov, A. B., Johnson, M. A., and Orlando, T. M., 2011, Thermal stability of water and hydroxyl on the surface of the Moon from temperature-programmed desorption measurements of lunar analog materials: *Icarus*, v. 213, no. 1, p. 64-72.
- Hiesinger, H., Head III, J.W., Wolf, U., Jaumann, R., and Neukum, G., 2003, Ages and stratigraphy of mare basalts in Oceanus Procellarum, Mare Nubium, Mare Cognitum, and Mare Insularum: *Journal of Geophysical Research*, v. 108, no. E7, doi: 10.1029/2002JE001985.
- Hiesinger, H. and Head III, J.W., 2006, New Views of Lunar Geoscience: An Introduction and Overview: *Reviews in Mineralogy and Geochemistry*, v. 60, p 1-81.
- Hildreth, W., 1981, Gradients in silicic magma chambers: Implications for lithospheric magmatism: *Journal of Geophysical Research*, v. 86 (B11), p. 10,153–10,192.
- Hodges Jr., R. R., 2002, Ice in the lunar polar regions revisited: *Journal of Geophysical Research*, v. 107, no. E2, p. 6-1 – 7-1.
- Hui, H., Peslier, A.H., Zhang, Y., and Neal, C.R., 2013, Water in lunar anorthosites and evidence for a wet early Moon: *Nature Geoscience*, v. 6, no. 3, p. 177–180, doi: 10.1038/ngeo1735.

Huppert, H. E. and Sparks, R. S., 1988, The generation of granitic magmas by intrusion of basalt into continental crust: *Journal of Petrology*, v. 29, p. 599-624.

Hurwitz, D.M. and Head, J.W., 2011, Implications of volatiles within lunar basalts for the origin of sinuous rille source depressions: *A Wet Vs. Dry Moon: Exploring Volatile Reservoirs and Implications for the Evolution of the Moon and Future Exploration*, p. 27.

Isaacson, P., Besse, S., Petro, N., and Nettles, J., 2011a, M³ overview and working with M³ data: *Proceedings of the 42nd Lunar and Planetary Science Conference*, p. 1-62.

Jensen, J.R., 2005, *Introductory Digital Image Processing: A Remote Sensing Perspective* (3rd ed.): Pearson Prentice Hall (New Jersey), 526 p.

Jolliff, B.L., Wiseman, S.A., Lawrence, S.J., Tran, T.N., Robinson, M.S., Sato, H., Hawke, B. R., Scholten, F., Oberst, J., Hiesinger, H., van der Bogert, C.H., Greenhagen, B.T., Glotch, T.D., and Paige, D.A., 2011, Non-mare silicic volcanism on the lunar farside at Compton–Belkovich: *Nature Geoscience*, v. 4, no. 8, p. 566-571, doi: 10.1038/ngeo1212.

Jolliff, B.L., Zanetti, M., Shirley, K.A., Accardo, N.J., Lauber, C., Robinson, M.S., and Greenhagen, B. T., 2012, Compton-Belkovich Volcanic Complex: *Proceedings of the 43rd Lunar and Planetary Science Conference*, p. 2097.

- Klima, R., Cahill, J., Hagerty, J., and Lawrence, D., 2013, Remote detection of magmatic water in Bullialdus Crater on the Moon: *Nature Geoscience*, v. 6, no. 9, p. 737-741, doi: 10.1038/ngeo1909.
- Lawrence, D.J., Feldman, W.C., Barraclough, B.L., Binder, A.B., Elphic, R.C., Maurice, S., Miller, M.C., and Prettyman, T.H., 2000, Thorium abundances on the lunar surface: *Journal of Geophysical Research*, v. 105, no. E8, p. 20307-20331, doi: 10.1029/1999JE001177.
- Lawrence, D.J., 2003, Small-area thorium features on the lunar surface: *Journal of Geophysical Research*, v. 108, no. E9, doi: 10.1029/2003JE002050.
- Lawrence, D.J., Puetter, R.C., Elphic, R.C., Feldman, W.C., Hagerty, J.J., Prettyman, T.H., and Spudis, P.D., 2007, Global spatial deconvolution of Lunar Prospector Th abundances: *Geophysical Research Letters*, v. 34, no. 3, p. 1-5, doi: 10.1029/2006GL028530.
- Libowitzky, E. and Rossman, G., 1997, An IR absorption calibration for water in minerals: *American Mineralogist*, v. 82, p. 1111-1115.
- Lucey, P., Korotev, R.L., Gillis, J.J., Taylor, L.A., Lawrence, D., Campbell, B.A., Elphic, R., Feldman, B., Hood, L.L., Hunten, D., Mendillo, M., Noble, S., Papike, J.J., Reedy, R.C., Lawson, S., Prettyman, T., Gasnault, O., and Maurice, S., 2006, Understanding the Lunar

Surface and Space-Moon Interactions: *Reviews in Mineralogy and Geochemistry*, v. 60, p. 83-219.

Lundeen, S., McLaughlin, S., and Alanis, R., 2011, Moon Mineralogy Mapper data product (JPL D-39032): Jet Propulsion Laboratory, p. 1-111, http://pds-imaging.jpl.nasa.gov/documentation/M3_DPSIS.PDF.

McCarthy, T.C., and Patiño-Douce, A.E., 1997, Experimental evidence for high temperature felsic melts formed during basaltic intrusion of deep crust: *Geology*, v. 25, p. 463-466.

McCauley, J. F., 1973, Geologic map of the Grimaldi quadrangle of the Moon: *United States Geological Survey Miscellaneous Investigations Series*, Map I-740.

McCord, T.B., Taylor, L.A., Combe, J.-P., Kramer, G., Pieters, C.M., Sunshine, J.M., and Clark, R.N., 2011, Sources and physical processes responsible for OH/H₂O in the lunar soil as revealed by the Moon Mineralogy Mapper (M³): *Journal of Geophysical Research*, v. 116, doi: 10.1029/2010JE003711.

McCubbin, F.M., Steele, A., Hauri, E.H., Nekvasil, H., Yamashita, S., and Hemley, R. J., 2010, Nominally hydrous magmatism on the Moon: *Proceedings of the National Academy of Sciences of the United States of America*, v. 107, no. 25, p. 11223-11228, doi: 10.1073/pnas.1006677107.

- McCubbin, F.M., Jolliff, B.L., Nekvasil, H., Carpenter, P.K., Zeigler, R. a., Steele, A., Elardo, S.M., and Lindsley, D.H., 2011, Fluorine and chlorine abundances in lunar apatite: Implications for heterogeneous distributions of magmatic volatiles in the lunar interior: *Geochimica et Cosmochimica Acta*, v. 75, no. 17, p. 5073-5093, doi: 10.1016/j.gca.2011.06.017.
- Nemchin, A., Timms, N., Pidgeon, R., Geisler, T., Reddy, S., and Meyer, C., 2009, Timing of crystallization of the lunar magma ocean constrained by the oldest zircon: *Nature Geoscience*, v. 2, p. 133-136, doi: 10.1038/ngeo417.
- Parmentier, E.M., Zhong, S., and Zuber, M.T., 2002, Gravitational differentiation due to initial chemical stratification: origin of lunar asymmetry by the creep of dense KREEP?: *Earth and Planetary Science Letters*, v. 201, p. 473-480.
- Pieters, C.M., Goswami, J.N., Clark, R.N., Annadurai, M., Boardman, J., Buratti, B., Combe, J. P., Dyar, M.D., Green, R., Head, J. W., Hibbitts, C., Hicks, M., Isaacson, P., Klima, R., 2009, Character and spatial distribution of OH/H₂O on the surface of the Moon seen by M³ on Chandrayaan-1: *Science*, v. 326, no. 5952, p. 568-572, doi: 10.1126/science.1178658.
- Rutherford, M. J. and Hess, P. C., 1973, Origin of lunar granites as immiscible liquids: *Proceedings of the 6th Lunar and Planetary Science Conference*. p. 696.

- Saal, A.E., Hauri, E.H., Cascio, M.L., Van Orman, J.A., Rutherford, M.C., and Cooper, R.F., 2008, Volatile content of lunar volcanic glasses and the presence of water in the Moon's interior: *Nature*, v. 454, no. 7201, p. 192-195, doi: 10.1038/nature07047.
- Schultz, P.H. and Spudis, P.D., 1983, Beginning and end of lunar mare volcanism: *Nature*, v. 302, no. 5905, p. 233-236.
- Shearer, C.K., Hess, C.P., Wieczorek, M.A., Pritchard, M.E., Parmentier, E.M., Borg, L.E., Longhi, J., Elkins-Tanton, L.T., Neal, C.R., Antonenko, I., Canup, R. M., Halliday, A. N., Grove, T.L., and Hager, B.H., 2006, Thermal and Magmatic Evolution of the Moon: *Reviews in Mineralogy and Geochemistry*, v. 60, no. 1, p. 365-518, doi: 10.2138/rmg.2006.60.4.
- Snyder, G.A. and Taylor, L.A., 1991, In Search of the urKREEP Reservoir: Trapped Residual Lunar Magma Ocean Liquid in the interstices of Upper Mantle Cumulates: *Proceedings of the 22nd Lunar and Planetary Science Conference*, p. 1287.
- Staid, M.I., Pieters, C.M., Besse, S., Boardman, J., Dhingra, D., Green, R., Head, J.W., Isaacson, P., Klima, R., Kramer, G., Mustard, J.M., Runyon, C., Sunshine, J., and Taylor, L.A., 2011, The mineralogy of late stage lunar volcanism as observed by the Moon Mineralogy Mapper on Chandrayaan-1: *Journal of Geophysical Research*, v. 116, p. 1-15, doi: 10.1029/2010JE003735.

- Touboul, M., Kleine, T., Bourdon, B., Palme, H., and Wieler, R., 2007, Late formation and prolonged differentiation of the Moon inferred from W isotopes in lunar metals: *Nature*, v. 450, no. 7173, p. 1206-1209, doi: 10.1038/nature06428.
- Warren, P.H., 1985, The Magma Ocean Concept and Lunar Evolution: *Annual Reviews of Earth and Planetary Sciences*, v. 13, p. 201-240.
- Warren, P.H., 2001, Early lunar crustal genesis: The ferroan anorthosite epsilon-neodymium paradox as a possible result of crustal overturn: *64th Annual Meteoritical Society Meeting*, p. 5391.
- Wasserburg, G.J., 1987, Isotopic abundances: inferences on solar system and planetary evolution: *Earth and Planetary Science Letters*, v. 86, p. 129-173.
- Weiblen, P.W. and Roedder, E., 1973, Petrology of silicate melt inclusions, Apollo 11 and Apollo 12 and terrestrial equivalents: *Proceedings of the 2nd Lunar and Planetary Science Conference*, p. 507-528.
- Wieczorek, M.A. and Phillips, R.J., 2000, The “Procellarum KREEP Terrane”: Implications for mare volcanism and lunar evolution: *Journal of Geophysical Research*, v. 105, no. E8, p. 417-420.

- Wieczorek, M.A., Jolliff, B.A., Khan, A., Pritchard, M E., Weiss, B.P., Williams, J.G., Hood, L.L., Richter, K., Neal, C.R., Shearer, C.K., McCallum, I.S., Tompkins, S., Hawke, B.R., Peterson, C., Gillis, J.J., and Bussey, B., 2006, The Constitution and Structure of the Lunar Interior: *Reviews in Mineralogy and Geochemistry*, v. 60, p. 221-364, doi: 10.2138/rmg.2006.60.3.
- Wilson, L. and Head, J.W., 2003, Lunar Gruithuisen and Mairan domes: Rheology and mode of emplacement: *Journal of Geophysical Research*, v. 108, no. E2, p. 1-7, doi: 10.1029/2002JE001909.
- Zhong, S., Parmentier, E.M., and Zuber, M.T., 1999, Early Lunar Evolution and the Origin of Asymmetric Distribution of Mare Basalts: *Proceedings of the 30th Lunar and Planetary Science Conference*, p. 1789.
- Zhong, S., Parmentier, E.M., and Zuber, M.T., 2000, A dynamic origin for the global asymmetry of lunar mare basalts: *Earth and Planetary Science Letters*, v. 177, no. 3-4, p. 131-140, doi: 10.1016/S0012-821X(00)00041-8.
- Zuber, M.T., Smith, D.E., Watkins, M.M., Asmar, S.W., Konopliv, A.S., Lemoine, F.G., Melosh, H.J., Neumann, G. a, Phillips, R.J., Solomon, S.C., Wieczorek, M. a, Williams, J.G., Goossens, S.J., and Kruizinga, G., 2013, Gravity field of the Moon from the Gravity Recovery and Interior Laboratory (GRAIL) mission: *Science*, v. 339, no. 6120, p. 668-671, doi: 10.1126/science.1231507.

TABLE 1. SUMMARY OF M ³ DATA						
Image	Target Feature	Optical Period	Date Acquired	Altitude (km)	Resolution (m/pixel)	Solar Zenith Angle (deg.)
M3G20090531T215442	CBTA	OP2C	5/31/09	200	280	18
M3G20090208T175211	Gruithuisen Domes	OP1B	2/8/09	100	140	61
M3G20090418T190900	Hansteen Alpha	OP2A	4/18/09	100	140	58
M3G20090612T101600	Hansteen Alpha	OP2C	6/12/09	200	280	14
M3G20090206T092112	Lassell Massif	OP1B	2/6/09	100	140	53
M3G20090609T095022	Lassell Massif	OP2C	6/9/09	200	280	17
<i>Optical Period 1A (OP1A): Nov 18-Jan 24, 1 of 2 star sensors.</i> <i>Optical Period 1B (OP1B): Jan 25-Feb 14, 1 of 2 star sensors .</i> <i>Optical Period 2A (OP2A): Apr 15-Apr 27, 1 of 2 star sensors.</i> <i>Optical Period 2B (OP2B): May 13-May 16, 0 of 2 star sensors, orbit raised.</i> <i>Optical Period 2C (OP2C): May 20-Aug 16, 0 of 2 star sensors, variable conditions (Boardman et al., 2011.).</i>						

TABLE 2. SUMMARY OF LUNAR RECONASSIANCE ORBITER DATA			
Image	Target Feature	Data Type*	Resolution (m/pixel)
NAC_DTM_CMPTNBELK_M154590204_60CM	CBTA	NAC	0.6
NAC_DTM_CMPTNBELK3_M156958414_60CM	CBTA	NAC	0.6
NAC_DTM_CMPTNBELK_M139238146_50CM	CBTA	NAC	0.5
NAC_DTM_COMPTONBELK	CBTA	NAC DTM	1
NAC_DTM_CMPTNBELK2	CBTA	NAC DTM	1
NAC_DTM_CMPTNBELK3	CBTA	NAC DTM	1
WAC_GLD100_P900N0000_100M	CBTA	WAC DTM	100
NAC_DTM_HANSTEENAL_MOSAIC_50M	Hansteen Alpha	NAC	0.5
NAC_DTM_HANSTEENAL_MOSAIC_100CM	Hansteen Alpha	NAC DTM	1
* - NAC – Near Angle Camera. * - WAC – Wide Angle Camera. * - DTM – Digital Terrain Model			

TABLE 3. QUANTITATIVE OH ⁻ /H ₂ O RESULTS FOR SPECTRA GATHERED FROM SELECTED LUNAR SITES					
Spectrum**	$\bar{\nu}^{\circ\circ}$ (cm ⁻¹)	ϵ_i° x10 ⁴ (l/mol•cm ²)	$A_i^{\dagger\dagger}$ (cm ⁻¹)	Gaussian Fit RMS* x10 ⁻²	OH ⁻ /H ₂ O [†] (ppm)
CBTA1	3590	4.02	6.14	2.4	226±42
CBTA2	3578	4.31	5.91	2.0	203±34
CBTA3	3574	4.41	2.43	0.9	82±20
CBTA4	3551	4.99	0.54	0.4	16±7
CBTA5	3551	4.97	1.53	0.7	46±17
CBTA6	3586	4.11	7.60	2.5	274±47
HAN1	3592	3.96	2.71	1.1	102±76
HAN2	3598	3.82	2.27	1.2	127±21
HAN3	3599	3.81	2.10	0.9	82±22
HAN4	3593	3.95	2.23	0.9	84±23
HAN5	3708	1.10	0.04	0.1	5±14
HAN6	3551	4.99	0.29	0.4	9±3
LASS1	3708	1.10	0.31	24	42±106
LASS2	3654	2.44	0.31	20	19±62
LASS3	3654	2.44	0.63	0.3	38±11
LASS4	3720	8.10	1.77	0.8	323±54
LASS5	3722	7.71	1.37	0.7	263±20
GRUITH1	3595	3.90	7.74	0.2	294±74
GRUITH2	3551	4.99	0.58	0.9	17±94
** - Locations of the spectra shown in Figure 14. ^{°°} - $\bar{\nu}$ - mean wavenumber of the Gaussian curve fit to the absorption coefficient spectrum. [°] - ϵ_i is the integrated molar absorption coefficient. ^{††} - A_i is the area under the fit Gaussian curve. * - Root Mean Square (RMS) of the Gaussian curve fit. [†] - 1- σ Uncertainty.					

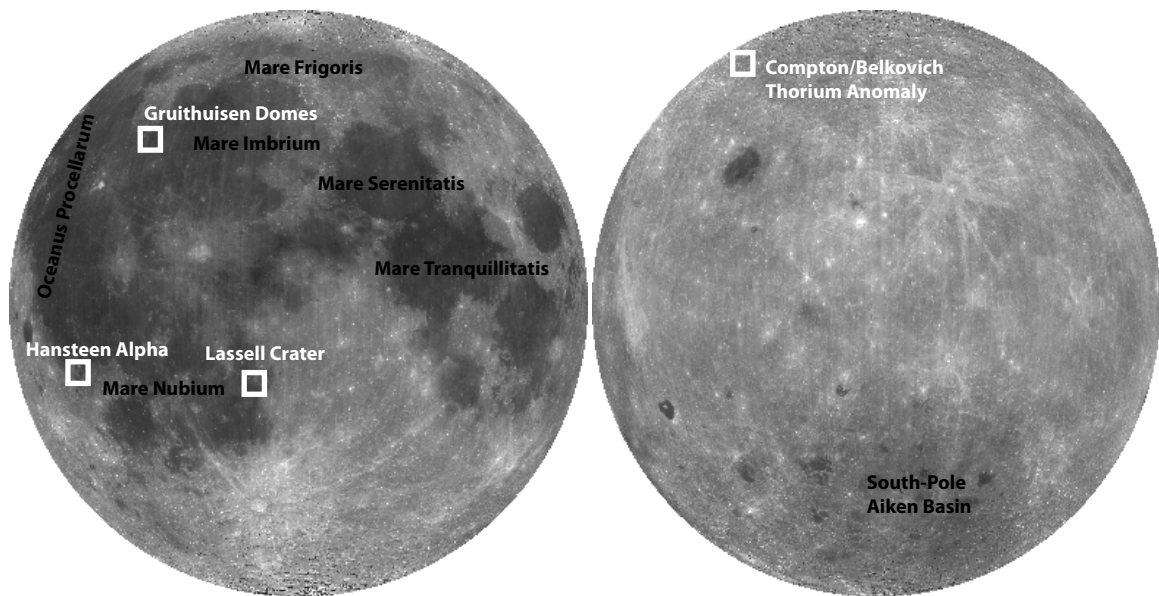


Figure 1: Clementine global albedo image showing target sites (labeled with white boxes and text). Black text refers to notable lunar basins. From Lunar and Planetary Institute (<http://www.lpi.usra.edu/lunar/missions/clementine/images/>).

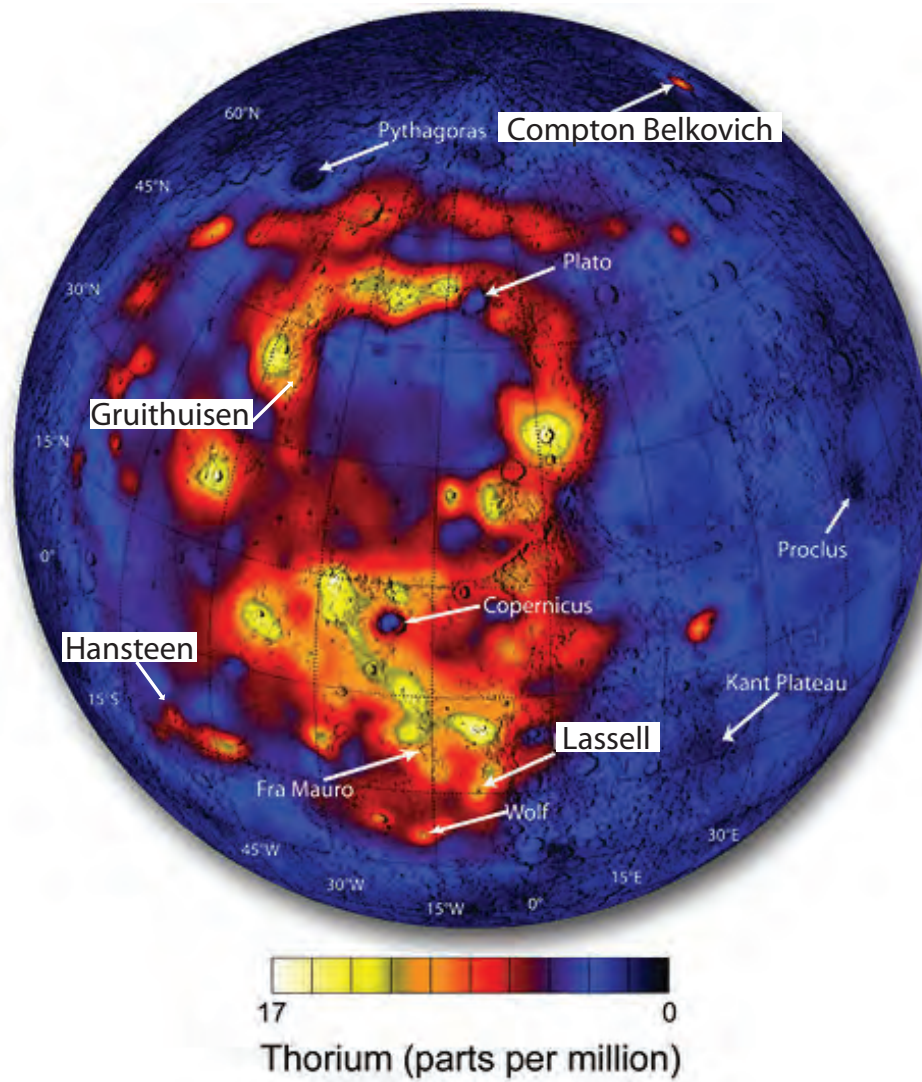


Figure 2: LP-ThGRS data showing nearside thorium concentrations. Hansteen Alpha (lower left), Lassell Crater (lower right), Gruithuisen Domes (upper left), and CBTA (upper right). From Lawrence et al. (2003).

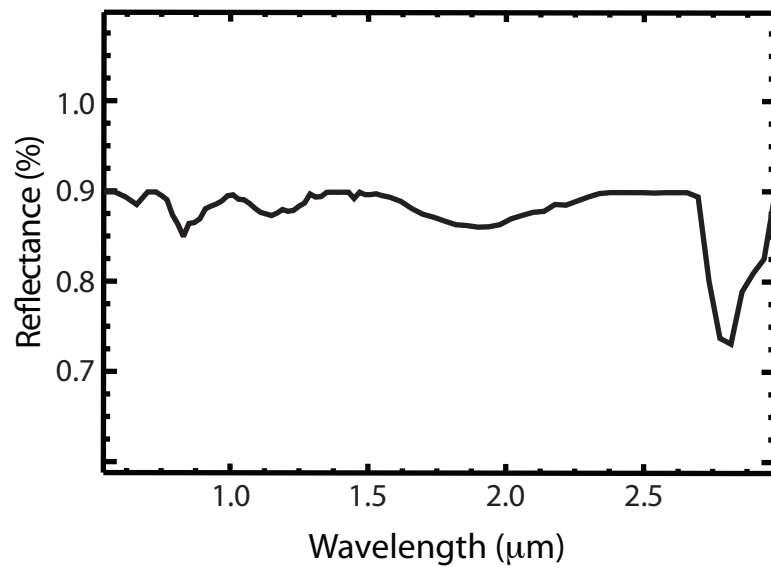


Figure 3: Reflectance spectra obtained from Compton Belkovich Thorium Anomaly showing a deep water absorption at $\sim 2.8 \mu\text{m}$.

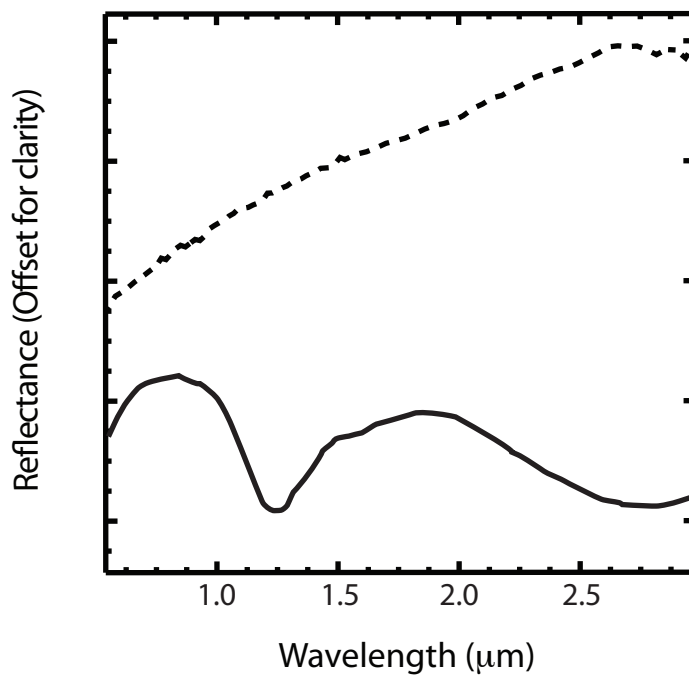


Figure 4: M³ reflectance spectra from Mare Imbrium basalts on the nearside. Solid line represents mare basalt spectrum without “reddening” effect. Dashed line shows mare basalt spectrum with the “reddening” effect. Notice the increased slope in the dashed spectrum, compared to the solid spectrum.

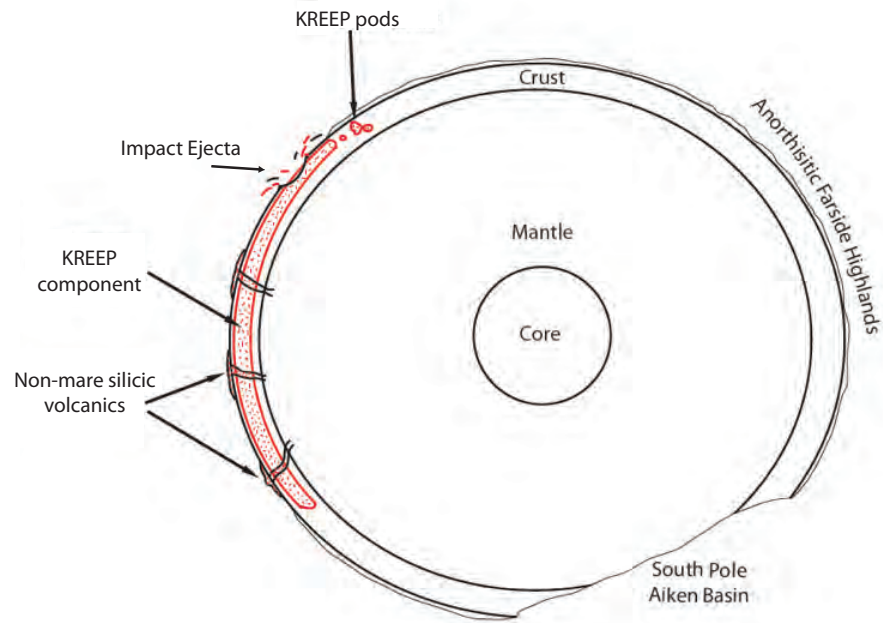


Figure 5: Schematic cross-section showing the spatial extent of KREEP within the lunar crust ~1-3 billion years ago. Mare basalts on the nearside could possibly have been enriched by KREEP as their melts were mixed with the KREEP layer. Modified from Wieczorek et al. (2006).

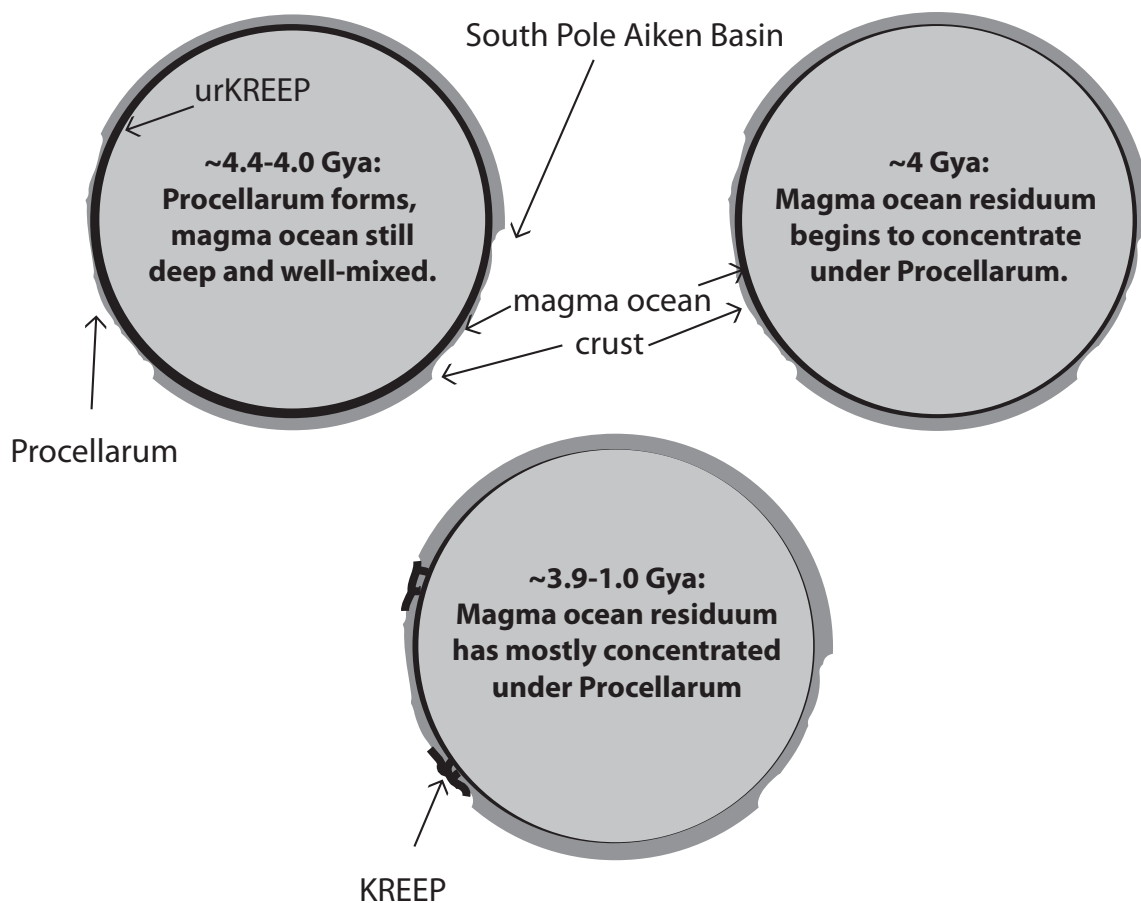


Figure 6: Progressive development of the lunar magma ocean. By the time the South Pole Aitken Basin impact occurred (Time 1), most of the lunar magma ocean had already accumulated under the thinner crust on the nearside. From Shearer et al. (2006).

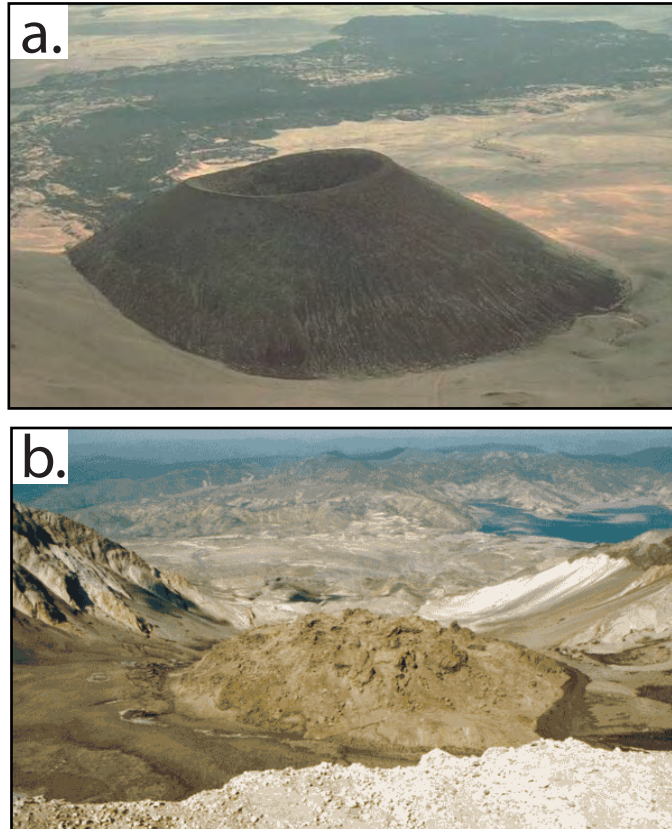


Figure 7: Terrestrial examples of volcanic textures and morphologies. (a) SP Crater is a cinder cone in Arizona, and shows the smooth texture of a mafic volcanic feature. (b) An example of the rough, bouldery textures of felsic volcanics can be seen in the resurgent dome of Mt. St. Helens. Photos from <http://www.asu.edu/courses/gph111>.

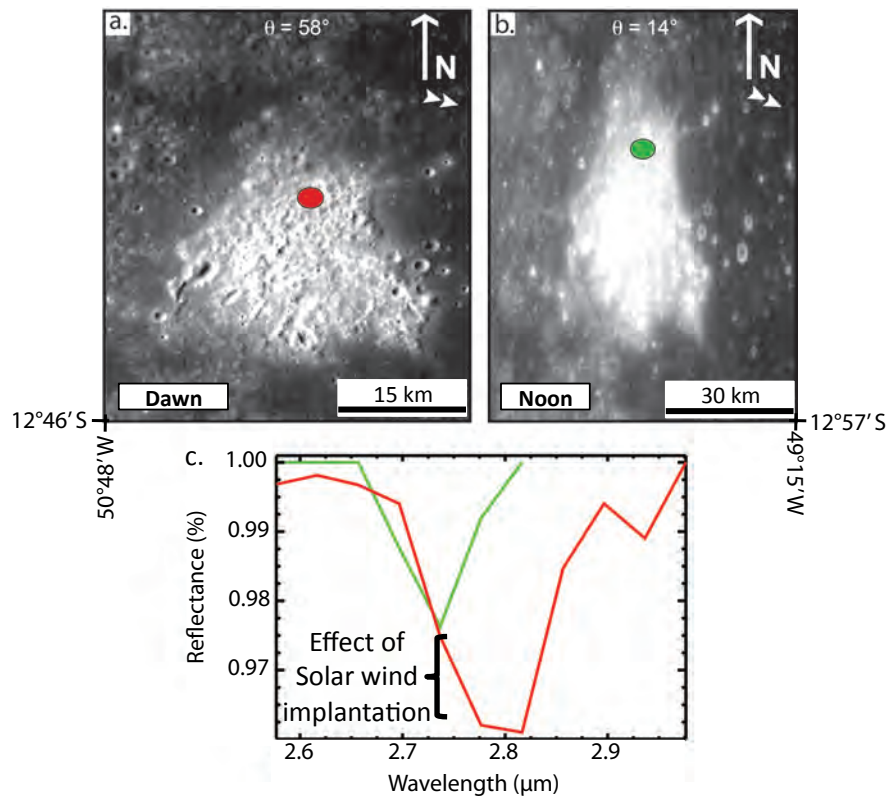


Figure 8: Comparison of spectra from optical period 1B (a) and optical period 2C (b) at Hansteen Alpha. (c) Spectra illustrating how solar wind implanted OH/H₂O adds to the 2.8- μm absorption associated with OH/H₂O. Optical period 1B spectrum is shown in red, and optical period 2C spectrum is shown in green. Illumination direction shown with white double arrows in upper right of (a) and (b).

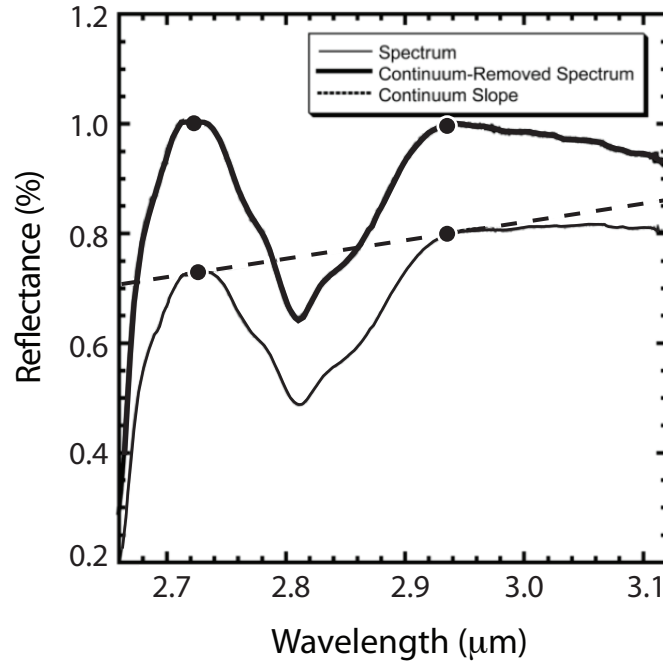
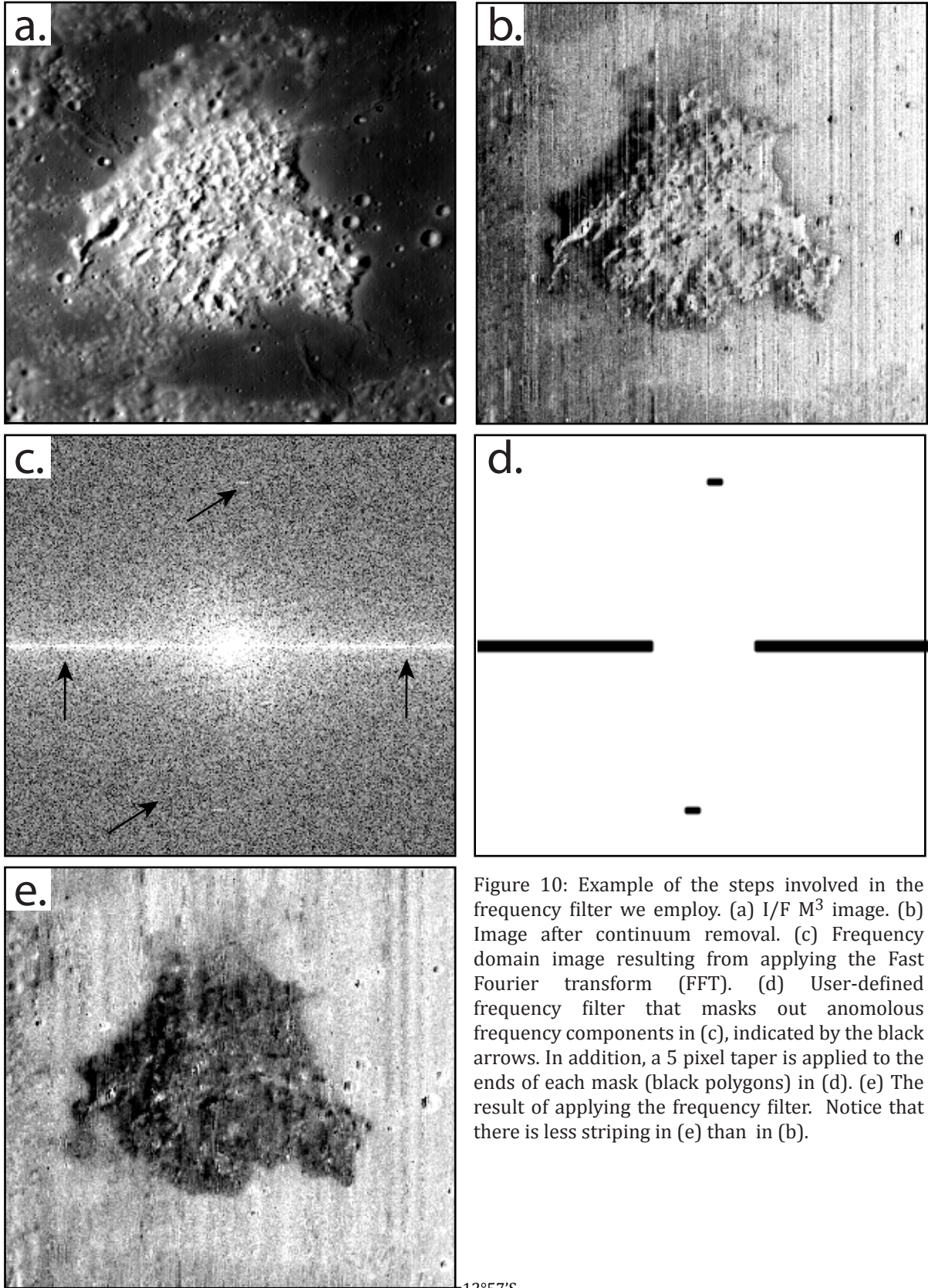


Figure 9: Continuum slope removal process. The thin, solid line shows the original spectrum of hydrous non-mare material before continuum removal. The dashed line is the continuum slope defined by the line connecting the band shoulders (solid dots) of the ca. 2.8 μm absorption. The continuum slope is then used to produce a continuum-removed spectrum by dividing the original spectrum by the continuum slope. The bold, solid line shows the resulting continuum-removed spectrum. Modified from Isaacson et al. (2011).



12°57'S
49°27'W

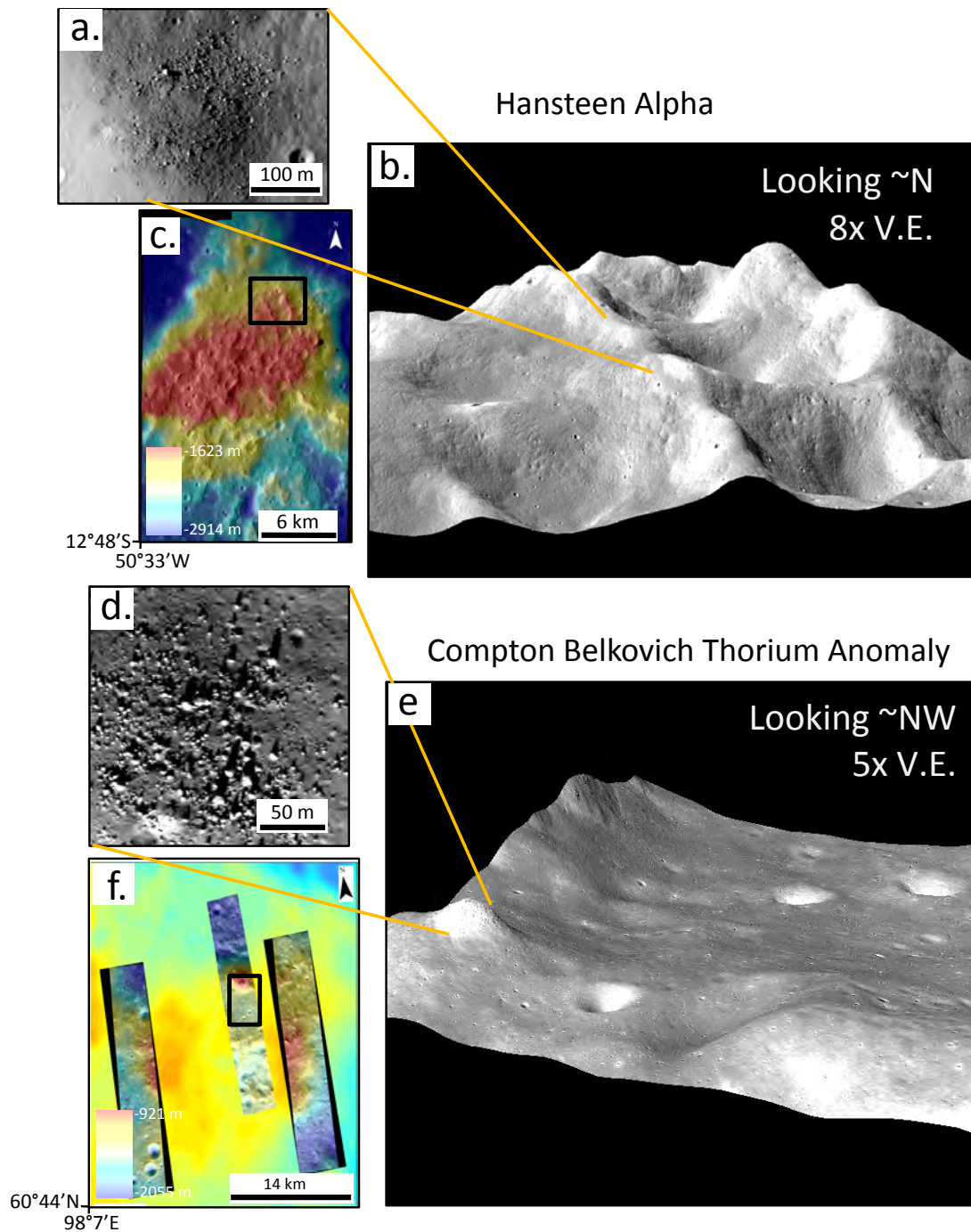


Figure 11: (a) Hansteen Alpha 0.5 m/pixel NAC image showing a boulder field. (b) Oblique view of the NAC image overlain on the NAC DTM of Hansteen Alpha. (c) Hansteen Alpha NAC 0.5 m/pixel images overlain on NAC-derived DEM with elevation color map applied. (d) CBTA NAC 0.5 m/pixel image showing a boulder field. (e) Oblique view of the NAC image overlain on the NAC DTM of CBTA. (f) CBTA NAC 0.5 m/pixel images overlain on NAC- and WAC-derived DEMs with elevation color map applied.

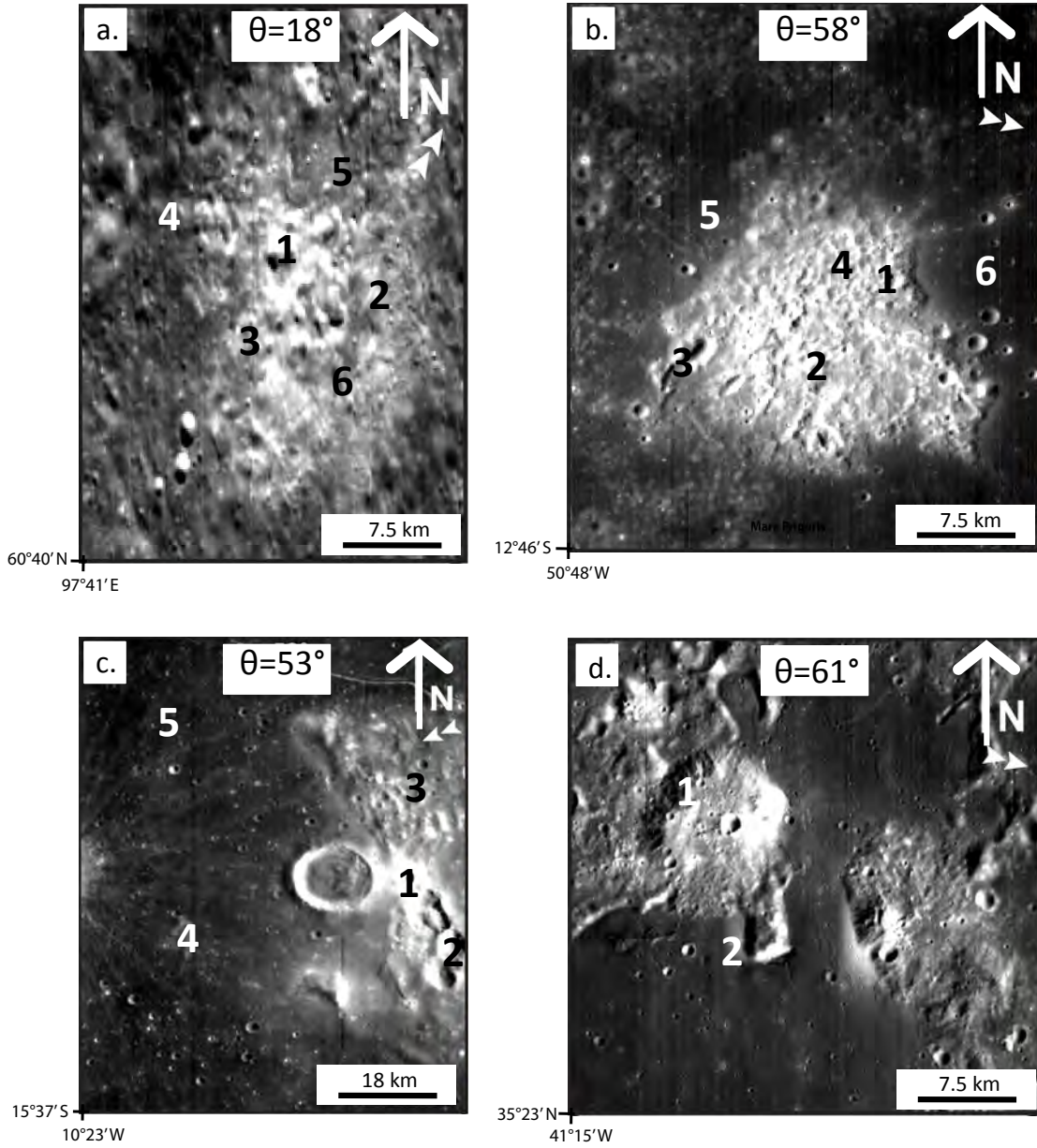


Figure 12: M³ imagery of sites of interest (see Figure 1) showing where spectra were extracted for analysis. Black and white numbers indicate the extracted spectra locations, with the water concentrations shown in Table 1. θ is illumination angle. White arrows show illumination direction. (a) Compton Belkovich Thorium Anomaly (CBTA), (b) Hansteen Alpha (HAN), (c) Lassell Massif (LASS), (d) Gruithuisen Domes (GRUITH).

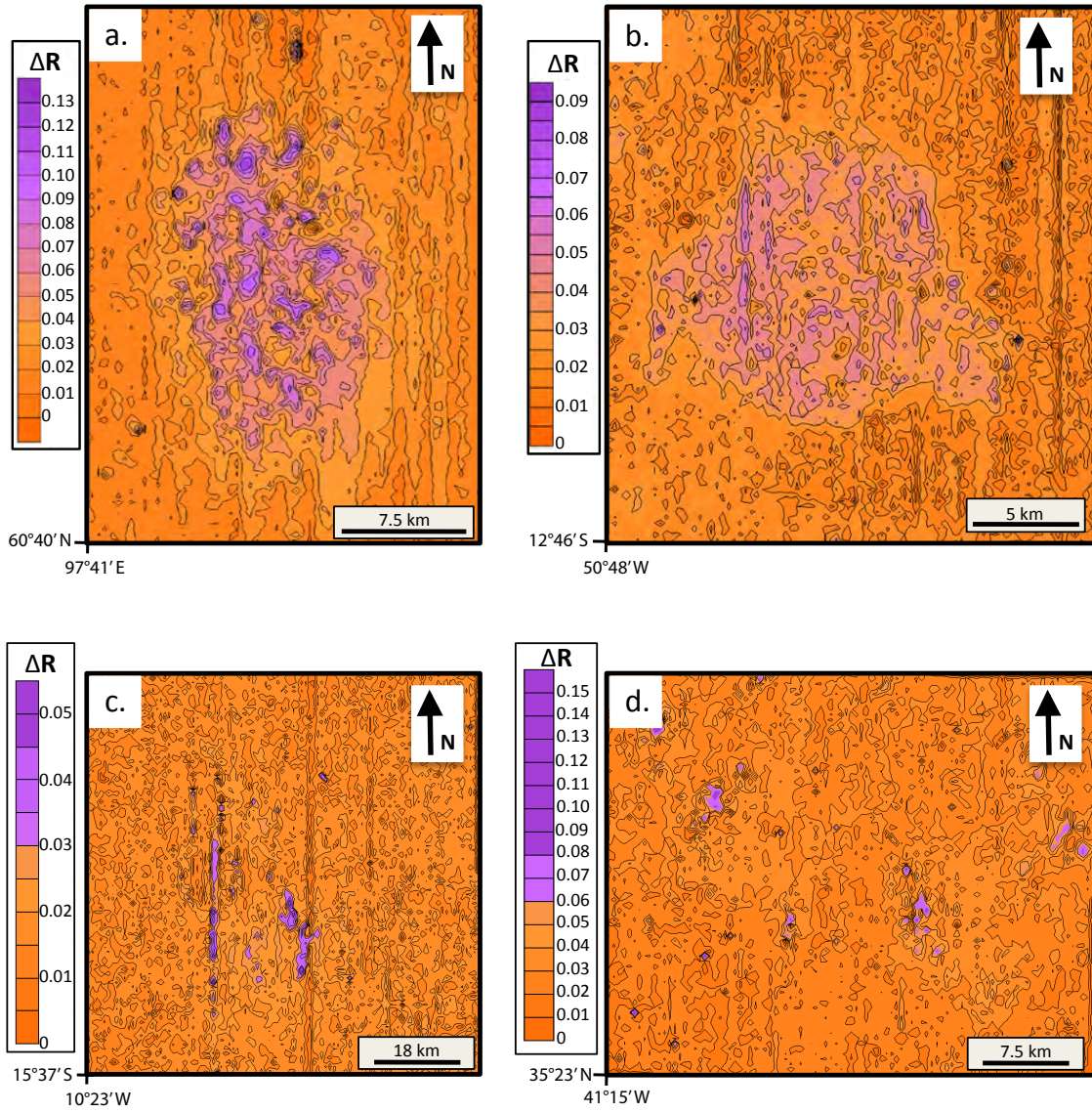


Figure 13: Contoured M^3 band depth images showing absorption depths (ΔR). Purples mark locations with large 2.8- μ m absorptions. Oranges indicate small absorptions. (a) Compton Belkovich Thorium Anomaly (CBTA), (b) Hansteen Alpha (HAN), (c) Lassell Massif (LASS), (d) Gruithuisen Domes (GRUITH).

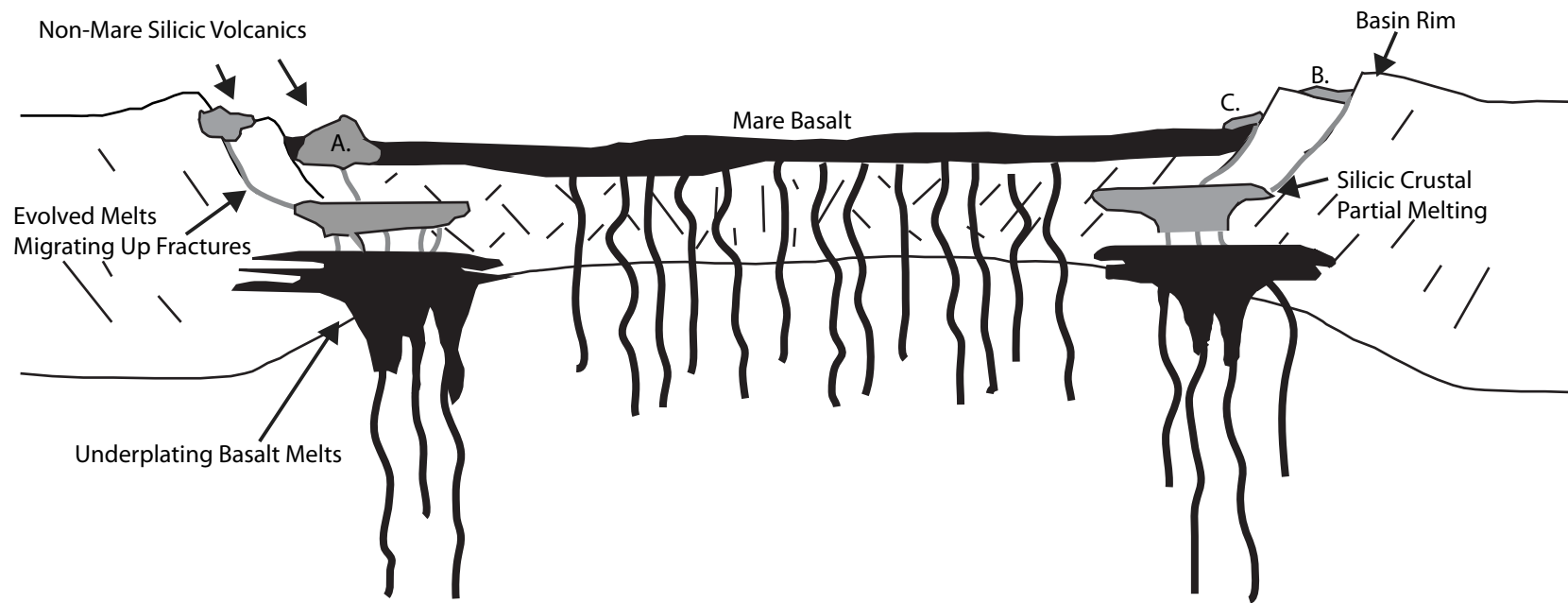


Figure 14: Conceptual model of basaltic underplating of the lunar crust. Partial melting of the pre-existing crust creates silica- and Th-rich melts that would be thermally and compositionally buoyant. Fractures, produced by either an impact or plume, serve as conduits for magmas to reach the surface. The addition of OH-H₂O to crustal rocks would decrease their melting point and generate silicic melts sooner than mafic melts. The earlier generation of silicic melts would allow more time for the melts to migrate to the surface before mafic melts. Photogeologically, the would non-mare silicic features would be embayed by mare basalts (eg. A). This is exactly what we see at several hydrous non-mare features, such as Hansteen Alpha, Gruithuisen Domes, and Lassell Massif. The hydrous silicic crustal melts that produced CBTA (i.e. B) would also have a lower melting point, however they have a much longer migration path to the surface, compared to nearside melts, due to thier position in the farside anorthositic highlands. Non-mare features produced by silicate liquid immiscibility on the other hand would be generated after most of the basaltic melts are crystallized. These melts would then begin migrating to the surface, but would overlie all pre-existing mare basalts (i.e. C). Modified from Hagerty et al. (2006).

APPENDIX 1: CALCULATING WATER CONCENTRATIONS USING THE BEER-LAMBERT LAW

We quantify the concentration associated with 2.8- μm absorption features in M^3 imagery by converting reflectance spectra into absorption coefficient (α) spectra following the method of Hapke (2012). This requires first determining the appropriate albedo factor (γ) and then the equivalent single scattering albedo (ω) (Hapke, 2012). The single scattering albedo is used to calculate the absorption coefficient, and is dependent on assumed variables such as refractive indices for pyroxene (n_i), grain size (D), and mineral density (ρ). Klima et al. (2013) found no significant difference in α values, and the resulting water abundances, calculated using refractive indices for pyroxene, quartz, and anorthite. Therefore, we use the refractive index of pyroxene (0.75) to be consistent with Klima et al. (2013) methodology.

The first part of the code (lines 52-113) involves selecting a “region of interest” from the band depth contour image to measure the reflectance spectra from. Note, however, that even though we select the region of interest from the band depth contour image, the reflectance spectra is extracted from the frequency-domain filtered M^3 image (lines 77-89). The second part of the code (lines 116-154) defines the shoulders of the 2.8- μm absorption in the filtered M^3 reflectance spectrum. After defining the shoulders, the code (lines 143-154) extracts the same wavelength range from the unfiltered M^3 image. The unfiltered spectra will be used in the remainder of the code to determine the absorption coefficient.

The next step in the code (lines 164-182) converts the unfiltered M^3 (`ioverf`; line 178) into reflectance relative to a Lambert surface (`biggamma`; line 178) using Equation 3 (Section 5.4). This Lambertian reflectance is then used to calculate the single scattering albedo (`littlegamma`; lines 179-181) using Equation 2 (Section 5.4). Line 186 then converts the

single scattering albedo into albedo factor (`littleomega`) using Equation 4.

The next step in the code (lines 188-207) involves calculating the absorption coefficient (`littlealpha`) using Equations 5-8 (Section 5.4). Lines 231-247 flatten the absorption coefficient by fitting a line to the ends of the spectrum, then dividing that line from the spectrum. The result is a flattened absorption coefficient spectrum that we can easily measure the area and band center. To measure the area and mean wavenumber of the absorption spectrum, we fit a Gaussian curve to the spectrum (lines 272-296; Equation 10 in Section 5.5). Finally, we use the Beer-Lambert Law (lines 307-323; Equations 11 in Section 5.6) to obtain water concentrations from the absorption coefficient spectrum.

The code was designed using MATLAB version 7.12.0. The input images are in ENVI format and the output plots are in MATLAB format. The MATLAB plots can be saved as TIFF files. A digital copy of the MATLAB code can be found in the CD provided with this dissertation in the file *gaussian_fit.m*.

References

Hapke, B., 2012, *Theory of Reflectance and Emittance Spectroscopy*: Cambridge University Press, 528 p.

Klima, R., Cahill, J., Hagerty, J., and Lawrence, D., 2013, Remote detection of magmatic water in Bullialdus Crater on the Moon: *Nature Geoscience*, v. 6, no. 9, p. 737-741, doi: 10.1038/ngeo1909.

Libowitzky, E. and Rossman, G., 1997, An IR absorption calibration for water in minerals:
American Mineralogist, v. 82, p. 1111-1115.

```

% Code for taking M3 I/F spectra (and some derived products) and computing
% single-scattering albedo, absorption coefficient, and ppm water
% concentrations using Hapke radiative transfer equations and Beer-Lambert
%Law

%Hapke, B., 2012, Theory of Reflectance and Emittance Spectroscopy: Cambridge
%University Press, 528 p.

%Libowitzky, E. and Rossman, G., 1997, An IR absorption calibration for water
%in minerals: American Mineralogist, v. 82, p. 1111-1115.

% Jose M. Hurtado, Jr. and Douglas L. Standart 05/09/14
% updated 08/29/14

clear
clc
clf

%DATA PREPARATION

% define some constants
columns = 168 ;
rows = 246 ;
bands = 10 ;
wavelengths = [ 2576.959961, 2616.879883, 2656.810059, 2696.729980,
2736.649902, 2776.580078, 2816.500000, 2856.429932, 2896.350098,
2936.270020];
wavelengthspacing = 40 ;
wavenumberspacing = 1 ./ ( wavelengthspacing ./ 10000000 ) ;
bandtoshow = 2 ;
D = 45 ; % path length in microns
nr = 0.75 ; % real refractive index (for pyroxene)
density = 2.7; % density for anorthosite in g/cm3

% load ENVI continuum-removed and FFT-processed M3 image cube
imagecontFFT = multibandread( '101600_sub_contremove75to84_FFT_usercut1_IFFT'
, [ rows , columns , bands ] , 'float' , 0 , 'bsq' , 'ieee-le' ) ;

% load raw M3 image cube
image = multibandread( '101600_subsub_75to84' , [ rows , columns , bands ] ,
'float' , 0 , 'bil' , 'ieee-le' ) ;

% load ENVI band-depth image
fid1 = fopen( '101600_sub_contremove75to84_FFT_usercut1_IFFT_OHL075to81' ,
'r' , 'l' ) ;
imagecontour = fread( fid1 , [ columns , rows ] , 'float' ) ;
fclose( fid1 ) ;
imagecontour = imagecontour' ;

% load "to m3 zenith" angle file
fid2 = fopen( '101600_M3Zenith_subsub' , 'r' , 'l' ) ;
tom3zenith = fread( fid1 , [ columns , rows ] , 'float' ) ;
fclose( fid2 ) ;
tom3zenith = tom3zenith' ;
mew = cosd( tom3zenith ) ;

```



```

% load "to sun zenith" angle file
fid3 = fopen( '101600_SunZenith_subsub' , 'r' , 'l' ) ;
tosunzenith = fread( fid2 , [ columns , rows ] , 'float' ) ;
fclose( fid3 ) ;
tosunzenith = tosunzenith' ;
mewnot = cosd( tosunzenith ) ;

% plot image
figure( 1 )
colormap( bone )
hold off
imagesc( imagecontour( : , : ) )
axis image
hold on
set(gca, 'FontSize', 15);
title( 'Band Depth Contour Image' )
xlabel( 'column' )
ylabel( 'row' )
colorbar( 'vert' )
saveas(gcf, 'Fig_BandDepthImg_LocX.fig');
saveas(gcf, 'Fig_BandDepthImg_LocX.tif');

% select area for analysis
disp( ' Select a rectangular region of interest by clicking the four corner
      points. ' )
figure( 1 )
[ u , v ] = ginput( 4 ) ;

figure( 1 )
plot( u , v , 'r*' )

minu = floor( min( u ) ) ;
minv = floor( min( v ) ) ;
maxu = ceil( max( u ) ) ;
maxv = ceil( max( v ) ) ;

% extract and plot average spectrum for subset area
imagesubsetcontFFT = imagecontFFT( minv : maxv , minu : maxu , : ) ;
imagesubset = image( minv : maxv , minu : maxu , : ) ;
mewsubset = mew( minv : maxv , minu : maxu , : ) ;
mewnotsubset = mewnot( minv : maxv , minu : maxu , : ) ;
imagecontsubset = imagecontour( minv : maxv , minu : maxu ) ;
for i = 1 : bands
    reflectancescontFFT = imagesubsetcontFFT( : , : , i ) ;
    reflectances = imagesubset( : , : , i ) ;
    averagereflectancecontFFT( i ) = mean( reflectancescontFFT( : ) ) ;
    averagereflectance( i ) = mean( reflectances( : ) ) ;
end

figure( 100 )
colormap( bone )
hold off
imagesc( imagecontsubset( : , : ) )
axis image
hold on
title( 'Band Depth Contour Image' )

```

```

xlabel( 'column' )
ylabel( 'row' )
colorbar( 'vert' )

averagemew = mean( mewsubset( : ) ) ;
averagemewnot = mean( mewnotsubset( : ) ) ;

[ numsubrows , numsubcols , numsubbands ] = size( imagesubset ) ;

figure( 2 )
hold on
plot( wavelengths , averagereflectancecontFFT , 'b+' )
plot( wavelengths , averagereflectancecontFFT , 'b-' )
set(gca, 'FontSize', 15);
title( 'Average Spectrum for Continuum-Removed M3 Image' )
xlabel( 'Wavelength in Nanometers' )
ylabel( 'Reflectance' )
saveas(gcf, 'Fig_ContRemoveFFTM3spectra_LocX.fig');
saveas(gcf, 'Fig_ContRemoveFFTM3spectra_LocX.tif');

% select spectral interval for analysis
disp( ' Select the spectral interval for analysis by clicking the minimum and
maximum wavelengths to consider. ' )
figure( 2 )
[ uu , vv ] = ginput( 2 ) ;

minuu = floor( min( uu ) ) ;

for j = 1 : length( wavelengths )
    diff1( j ) = abs( wavelengths( j ) - minuu ) ;
end
sortdiff1 = sort( diff1 ) ;
whereismin = find( diff1 == sortdiff1( 1 ) ) ;
minuuvloc = whereismin ;

maxuu = ceil( max( uu ) ) ;

for k = 1 : length( wavelengths )
    diff2( k ) = abs( wavelengths( k ) - maxuu ) ;
end
sortdiff2 = sort( diff2 ) ;
whereismax = find( diff2 == sortdiff2( 1 ) ) ;
maxuuvloc = whereismax ;

figure( 2 )
plot( minuu , averagereflectancecontFFT( minuuvloc ) , 'r*' )
plot( maxuu , averagereflectancecontFFT( maxuuvloc ) , 'r*' )

% extract and plot spectral interval
spectralsubset = averagereflectance( minuuvloc : maxuuvloc ) ;
wavelengthrange = wavelengths( minuuvloc : maxuuvloc ) ;
numsubbands = length( wavelengthrange ) ;

figure( 3 )

```

```

hold on
plot( wavelengthrange , spectralsubset , 'b+' )
plot( wavelengthrange , spectralsubset , 'b-' )
set(gca, 'FontSize', 15);
title( 'Average Raw M3 Spectrum For Region of Interest' )
xlabel( 'Wavelength in Nanometers' )
ylabel( 'Reflectance' )
saveas(gcf, 'Fig_RawM3spectra_LocX.fig');
saveas(gcf, 'Fig_RawM3spectra_LocX.tif');

%HAPKE ANALYSIS FOR OBTAINING SINGLE-SCATTERING ALBEDO AND ABSORPTION
COEFFICIENT

% calculate absorption coefficient using method of Klima (and Hapke)

ioverf = spectralsubset ; % M3 documentation says their reflectance is I/F!

% convert I/F to albedo factor (littlegamma)
% use eq. 14.6a in Hapke (p. 377)
mew = averagemew ;
mewnot = averagemewnot ;

% FINDING LITTLE GAMMA USING HAPKE EQUATION 14.6A
littlegamma = zeros( 1 , numsubbands ) ;
for l = 1 : numsubbands
    biggamma( l ) = ( 4 .* ( ( mewnot + mew ) ./ mewnot ) ) .* ( 1 ./ ( ( 1 +
        ( 2 .* mewnot ) ) .* ( 1 + ( 2 .* mew ) ) ) ) .* ioverf( l ) ;
    littlegammdown( l ) = 1 + ( 4 .* mewnot .* mew .* biggamma( l ) ) ;
    littlegammaup( l ) = sqrt( ( ( ( mewnot + mew ) .* ( mewnot + mew ) ) .*
        ( biggamma( l ) .* biggamma( l ) ) ) + ( littlegammdown( l ) .* ( 1
        - biggamma( l ) ) ) ) - ( ( mewnot + mew ) .* biggamma( l ) ) ) ;
    littlegamma( l ) = littlegammaup( l ) ./ littlegammdown( l ) ;
end

% convert littlegamma to single-scattering albedo (littleomega)
% use eq. 14.3 in Hapke (p. 376)
littleomega = 1 - ( littlegamma .* littlegamma ) ;

% convert littleomega to absorption coefficient (littlealpha)
% we will do this iteratively
nistart = zeros( numsubbands ) ;
criterion = 1e-3 ; % tolerance for difference between guess value and final
value; test for ending while loop
diff = 1000 ; % difference between guess value and final value; test for
ending while loop

for m = 1 : numsubbands
    ni = nistart( m ) ;
    while diff >= criterion
        Rnot = ( ( ( nr - 1 ) .* ( nr - 1 ) ) + ( ni .* ni ) ) ./ ( ( ( nr +
            1 ) .* ( nr + 1 ) ) + ( ni .* ni ) ) ; % Hapke p. 125
        Se = 0.0587 + ( 0.8543 .* Rnot ) + ( 0.0870 .* Rnot .* Rnot ) ; %
            Hapke p. 125
        Si = 1 - ( ( 1 ./ ( nr .* nr ) ) .* ( 0.9413 - ( 0.8543 .* Rnot ) - (

```

```

        0.087 .* Rnot .* Rnot ) ) ) ; % eq. 6.23 Hapke p. 127
    littlealpha = ( -1 ./ ( D ./ 10000 ) ) .* log( ( littleomega( m ) -
        Se ) ./ ( 1 - Se - Si + ( Si .* littleomega( m ) ) ) ) ; % eq
        14.21 Hapke p. 396
    alpha_ni_now = ( 4 .* pi * ni ) ./ ( wavelengthrange( m ) ./ 10000000
        ) ; % note proportionality between ni and littlealpha
    diff = abs( littlealpha - alpha_ni_now ) ;
    ni = ( littlealpha .* ( wavelengthrange( m ) ./ 10000000 ) ) ./ ( 4
.* pi ) ;
    end
    alpha( m ) = littlealpha ;
    diff = 1000 ;
end

% convert wavelengths in nanometers to wavenumber in cm-1
wavenumber = 1 ./ ( wavelengthrange ./ 10000000 ) ;

figure( 4 )
hold on
plot( wavenumber , littleomega , 'b+' )
plot( wavenumber , littleomega , 'b-' )
set(gca, 'FontSize', 15);
title( 'Single Scattering Albedo' )
xlabel( 'Wavenumber in cm-1' )
ylabel( 'Single Scattering Albedo' )
saveas(gcf, 'Fig_SingleScatteringAlbedo_LocX.fig');
saveas(gcf, 'Fig_SingleScatteringAlbedo_LocX.tif');

figure( 5 )
hold on
plot( wavenumber , alpha , 'b+' )
plot( wavenumber , alpha , 'b-' )
set(gca, 'FontSize', 15);
title( 'Absorption Coefficient Spectrum' )
xlabel( 'Wavenumber in cm-1' )
ylabel( 'Absorption Coefficient' )
saveas(gcf, 'Fig_AbsorptionCoeff_LocX.fig');
saveas(gcf, 'Fig_AbsorptionCoeff_LocX.tif');

% baseline removal (essentially a continuum removal)

% do linear fit to the spectral interval
x1 = wavenumber( 1 ) ;
y1 = alpha( 1 ) ;
x2 = wavenumber( length( wavenumber ) ) ;
y2 = alpha( length( alpha ) ) ;
XX = [ x1 , x2 ] ;
YY = [ y1 , y2 ] ;
PP = polyfit( XX , YY , 1 ) ;
baseline = polyval( PP , wavenumber ) ;

flatalpha = alpha - baseline ;

%check for negative values in flattened spectrum and remove them

```

```

for mmmmm = 1 : numsubbands
    if flatalpha( mmmmm ) < 0
        flatalpha( mmmmm ) = 0.0001 ;
    end
end

figure( 6 )
hold on
plot( wavenumber , flatalpha , 'b+' )
plot( wavenumber , flatalpha , 'b-' )
set(gca, 'FontSize', 15);
title( 'Baseline-Removed Absorption Coefficient Spectrum' )
xlabel( 'Wavenumber in cm-1' )
ylabel( 'Absorption Coefficient' )
saveas(gcf, 'Fig_AbsorptionCoeffBaselineRemove_LocX.fig');
saveas(gcf, 'Fig_AbsorptionCoeffBaselineRemove_LocX.tif');

%CONVERT ABSORPTION COEFFICIENT TO ABSORBANCE
flatalpha = flatalpha .* ( D ./ 10000 ) ;

%GAUSSIAN CURVE FIT
gaussfit = fit(wavenumber.', flatalpha.', 'gauss1')
gausscoeffvalues = coeffvalues(gaussfit);
factor = gausscoeffvalues(1)
mu = gausscoeffvalues(2)
sigma = gausscoeffvalues(3)
wavenumberaxis = [ min( wavenumber ) : 1 : max( wavenumber ) ] ;
fitspectrum = factor .* exp ( - ( ( wavenumberaxis - mu ) ./ sigma ) .^2 );

%calculate RMS value
flatalphamodel = factor .* ( 1 ./ ( sigma .* sqrt( 2 .* pi ) ) ) .* exp( -0.5
.* ( ( ( wavenumber - mu ) ./ sigma ) .* ( ( wavenumber - mu ) ./ sigma ) ) )
;
en = length( wavenumber );
for kk = 1 : en
    differencessquared = ( abs( flatalpha - flatalphamodel ) ) .^ 2 ;
end
sumdiffsquare = sum ( differencessquared ) ;
RMS = sqrt( sumdiffsquare ./ en )

figure( 7 )
hold on
plot( wavenumber , flatalpha , 'b+' )
plot( wavenumberaxis , fitspectrum , 'r-' )
set(gca, 'FontSize', 15);
title( 'Fit Baseline-Removed Absorption Coefficient Spectrum' )
xlabel( 'Wavenumber in cm-1' )
ylabel( 'Absorption Coefficient' )
saveas(gcf, 'Fig_FitAbsorptionCoeff_LocX.fig');
saveas(gcf, 'Fig_FitAbsorptionCoeff_LocX.tif');

%CALCULATE AREA

```

```

areaundercurve = trapz( fitspectrum )

integratedabsorptionintensity = areaundercurve

%BEERS LAW CALCULATION TO OBTAIN PPM WATER

% pick wavenumber of center of absorption coefficient feature

wavenumbermiddle = mu ;

% use Libowitzcky 1997 to determine epsilon value from wavenumber (in cm-2
per mol H2O/L

epsilon = 246.6 .* ( 3753 - wavenumbermiddle )

% use areaundercurve, epsilon, D, and density in Beers Law to get ppm water

concentration = ( areaundercurve .* 1.8 ) ./ ( ( D ./ 10000 ) .* density .*
    epsilon ) % in wt percent H2O
concentrationppm = concentration .* 10000

```

APPENDIX 2: SINGLE SCATTERING AND ABSORPTION COEFFICIENT SPECTRA

In this Appendix are single scattering albedo and absorption coefficient spectra from Compton Belkovich Th Anomaly (CBTA), Hansteen Alpha (HAN), Lassell Massif (LASS), Gruithuisen Domes (GRUITH) transformed to absorption coefficient spectra. The absorption coefficient spectra are used to calculate water abundance using the method of Klima (2013). Calculated concentrations for each site are shown in Table 2.

On the following pages are figures illustrating each step in converting reflectance spectra into absorption coefficient spectra. In each figure:

- A. Shows the average subset spectrum, derived from multiple spectra extracted from the area being measured from the continuum-removed M^3 image;
- B. Shows the spectrum obtained from the I/F M^3 image, which is the original M^3 image provided by the M^3 science team;
- C. Shows the single scattering albedo spectrum obtained from B using Equations 2-4 (Appendix 1);
- D. Shows the absorption coefficient spectrum obtained from C using Equations 5-8 (Appendix 1);
- E. Shows the baseline-removed absorption coefficient spectrum obtained from D; and
- F. Shows the Gaussian curve that is fit to E.

The RMS for the Gaussian fit, the area under the curve (A_i ; cm^{-1}), the mean wavenumber of the absorption coefficient spectrum ($\bar{\nu}$; cm^{-1}), the integrated molar absorption coefficient (e_i ; $\text{l/mol}\cdot\text{cm}^2$), and the OH-H₂O concentrations are shown in (F).

References

Klima, R., Cahill, J., Hagerty, J., and Lawrence, D., 2013, Remote detection of magmatic water in Bullialdus Crater on the Moon: *Nature Geoscience*, v. 6, no. 9, p. 737-741, doi: 10.1038/ngeo1909.

CBTA1

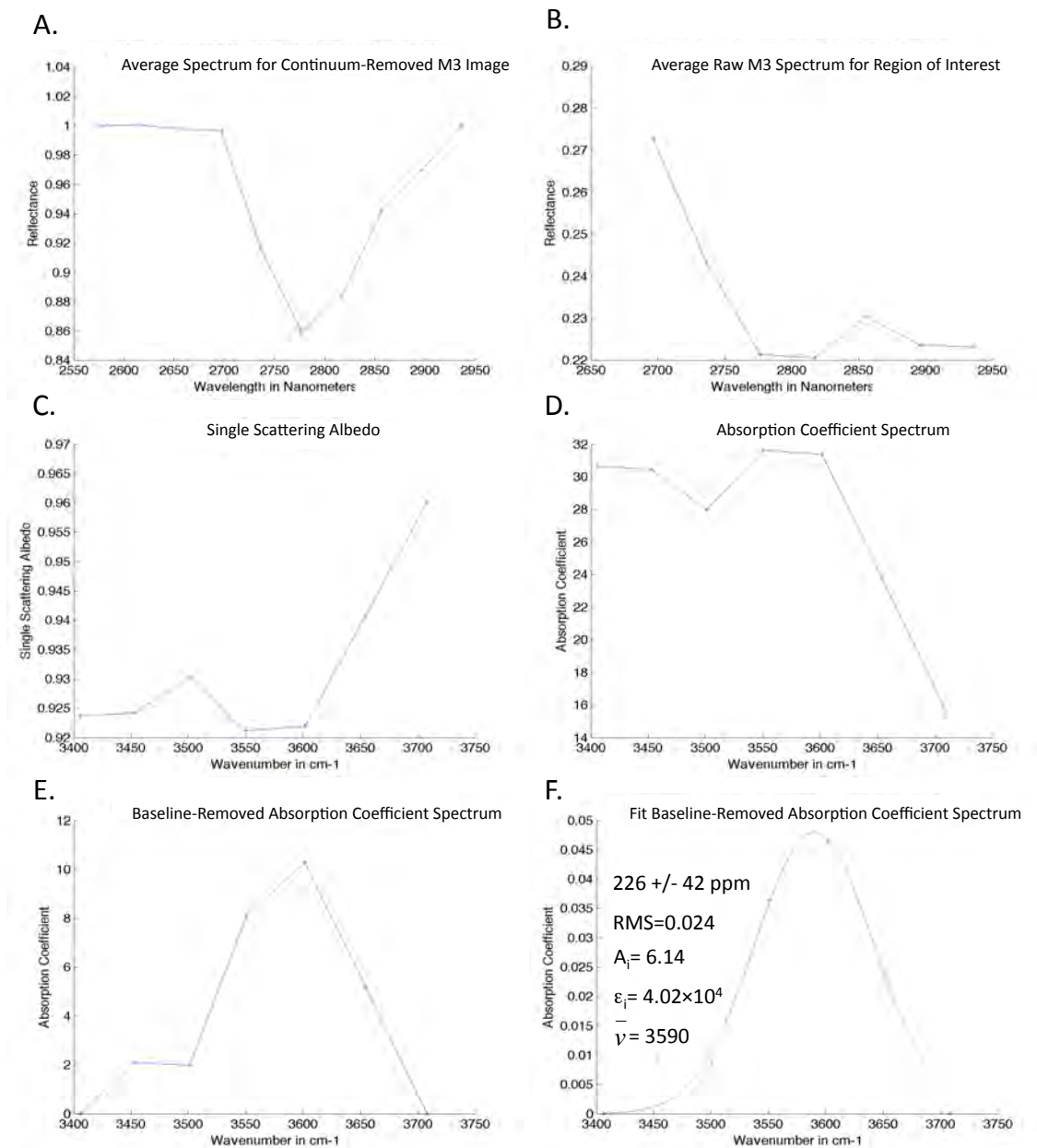


Figure A1: Results from CBTA1

CBTA2

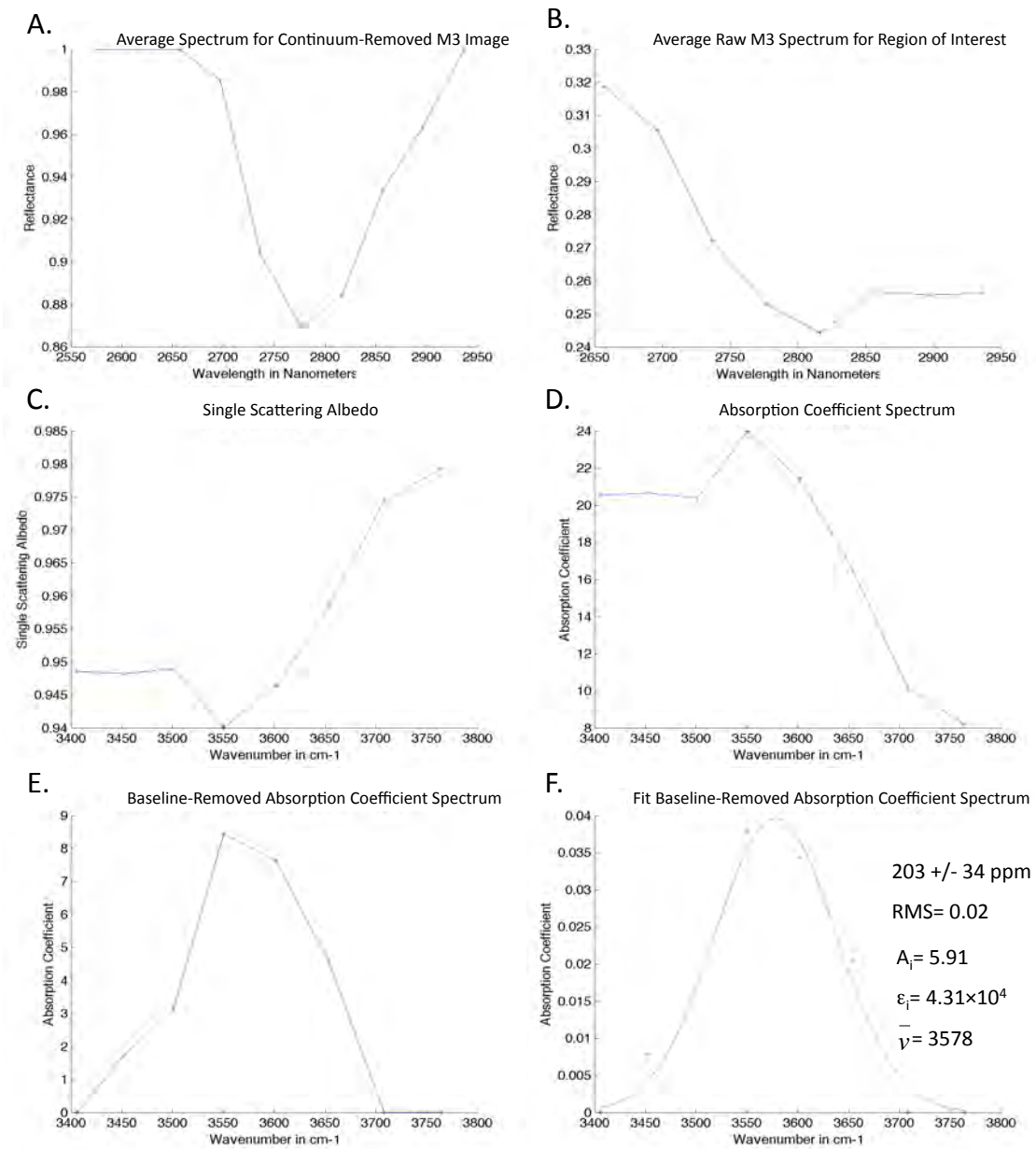


Figure A2: Results from CBTA2

CBTA3

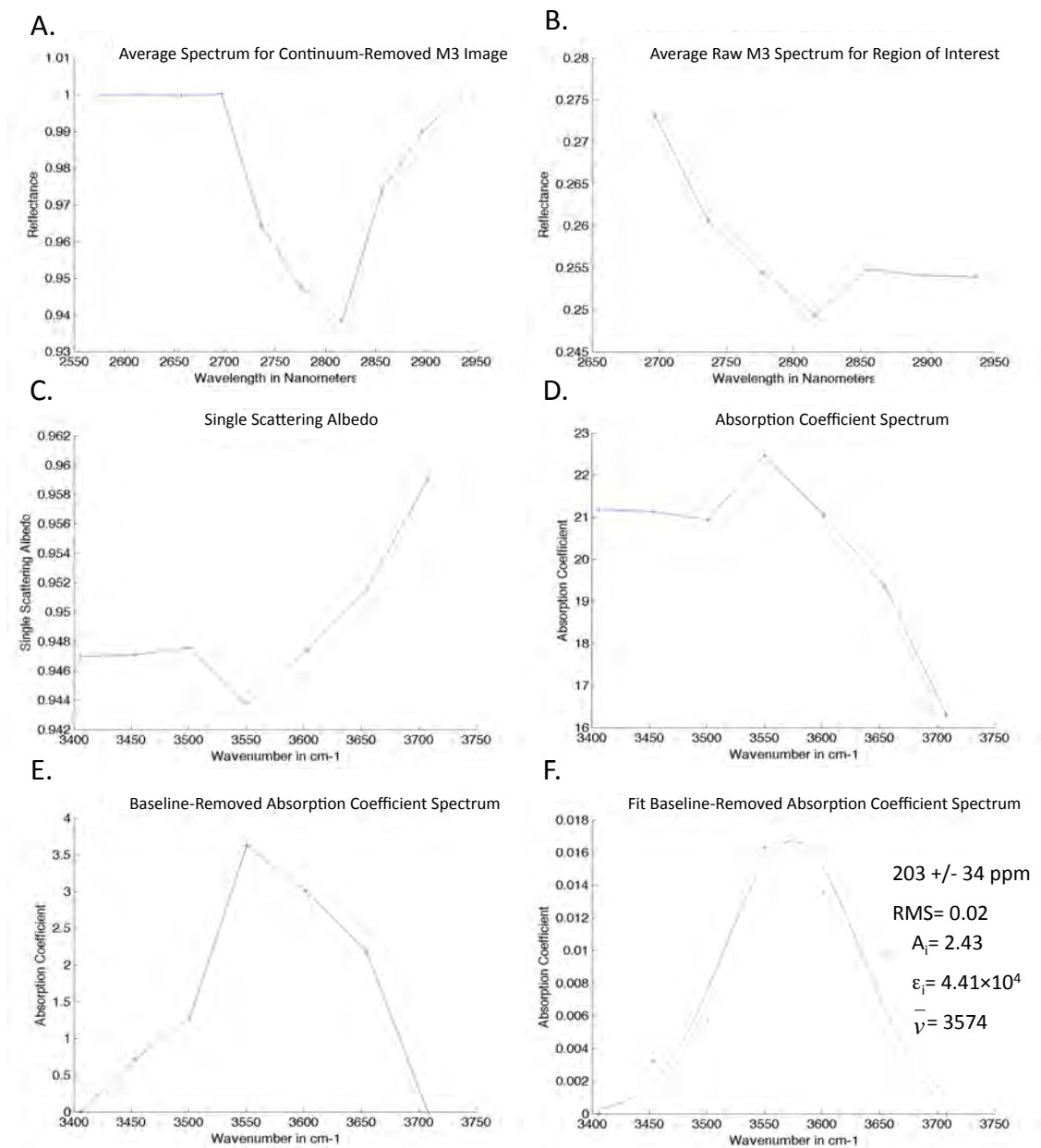


Figure A3: Results from CBTA3

CBTA4

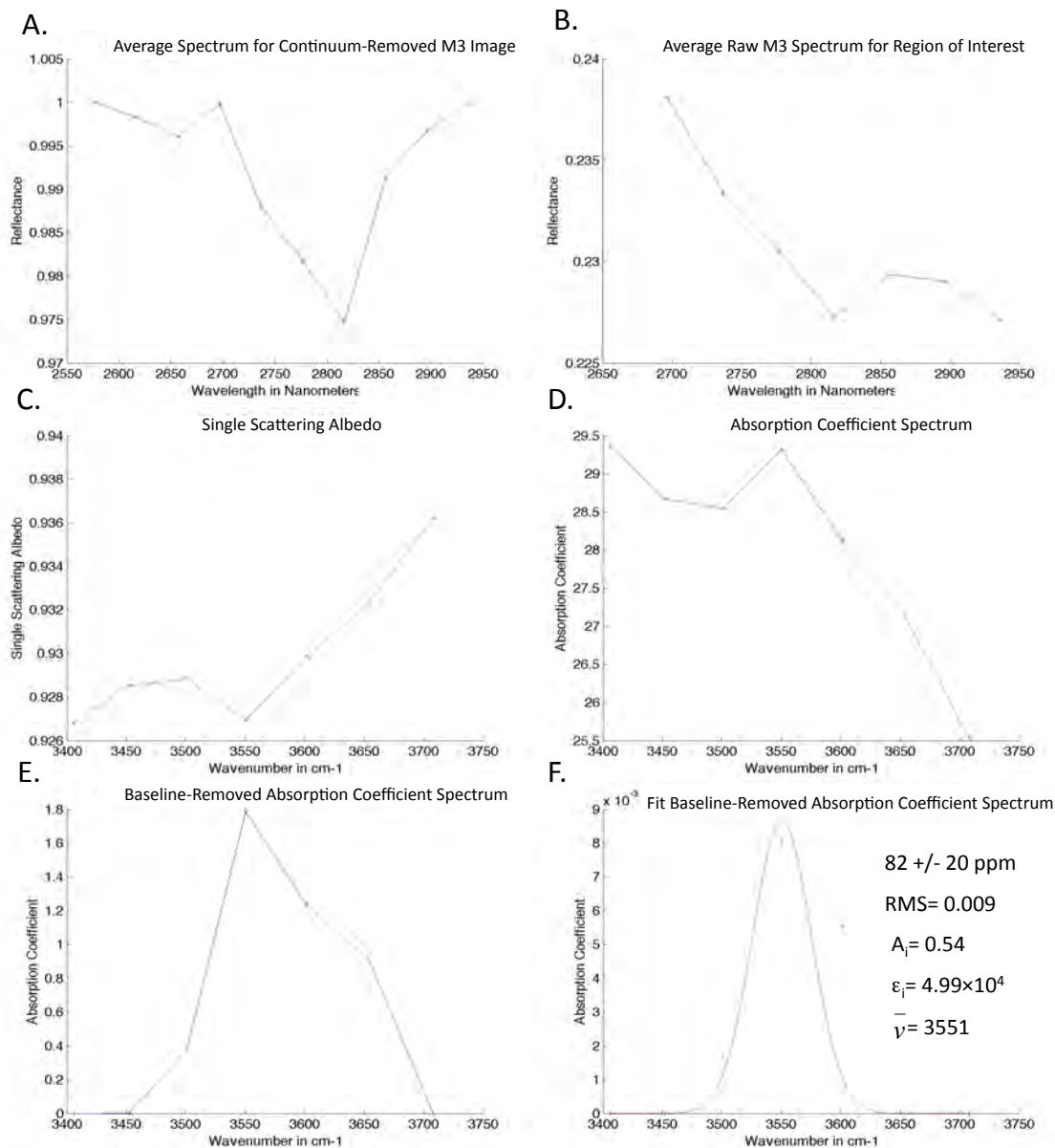


Figure A4: Results from CBTA4

CBTA5

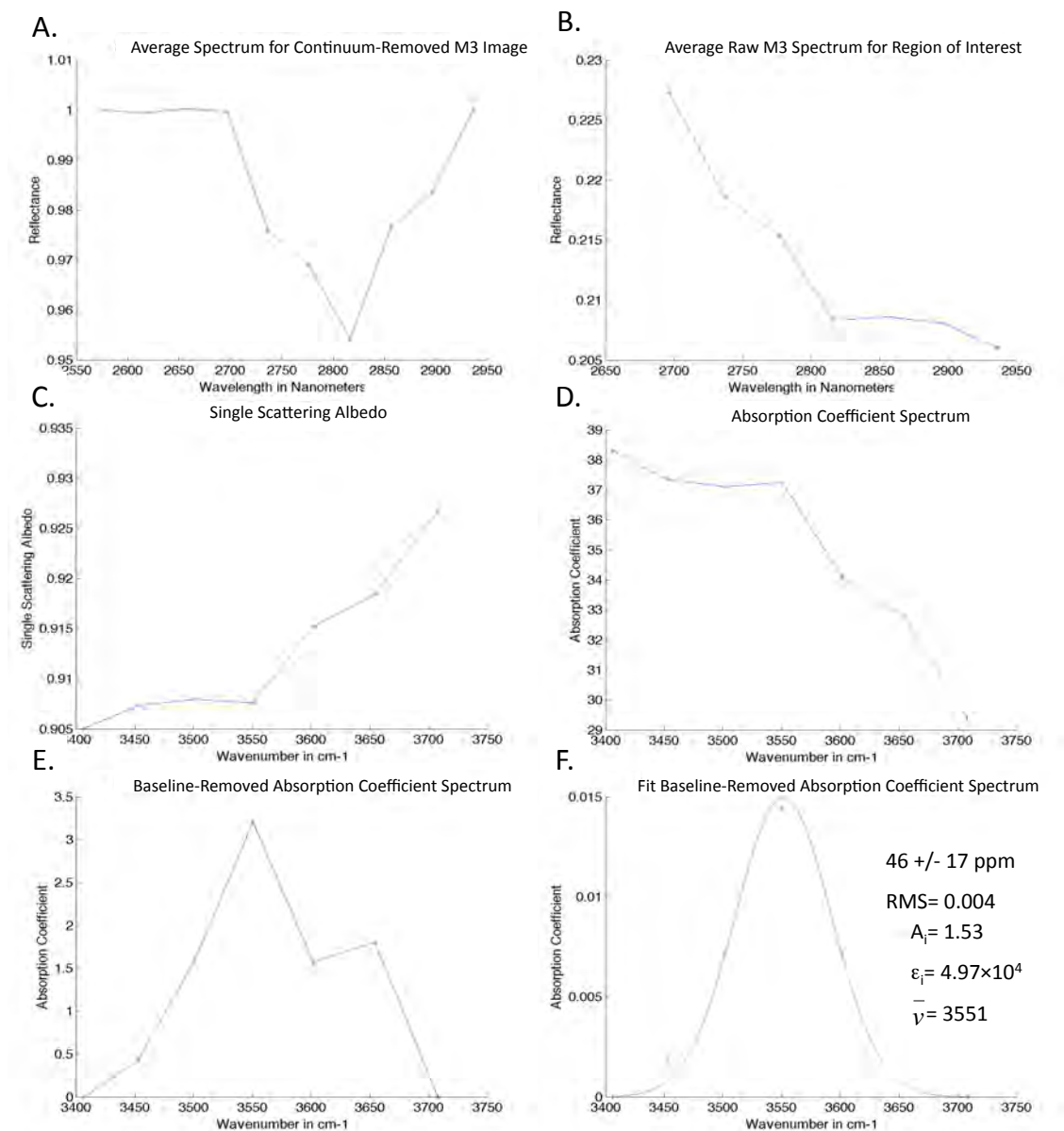


Figure A5: Results from CBTA5

CBTA6

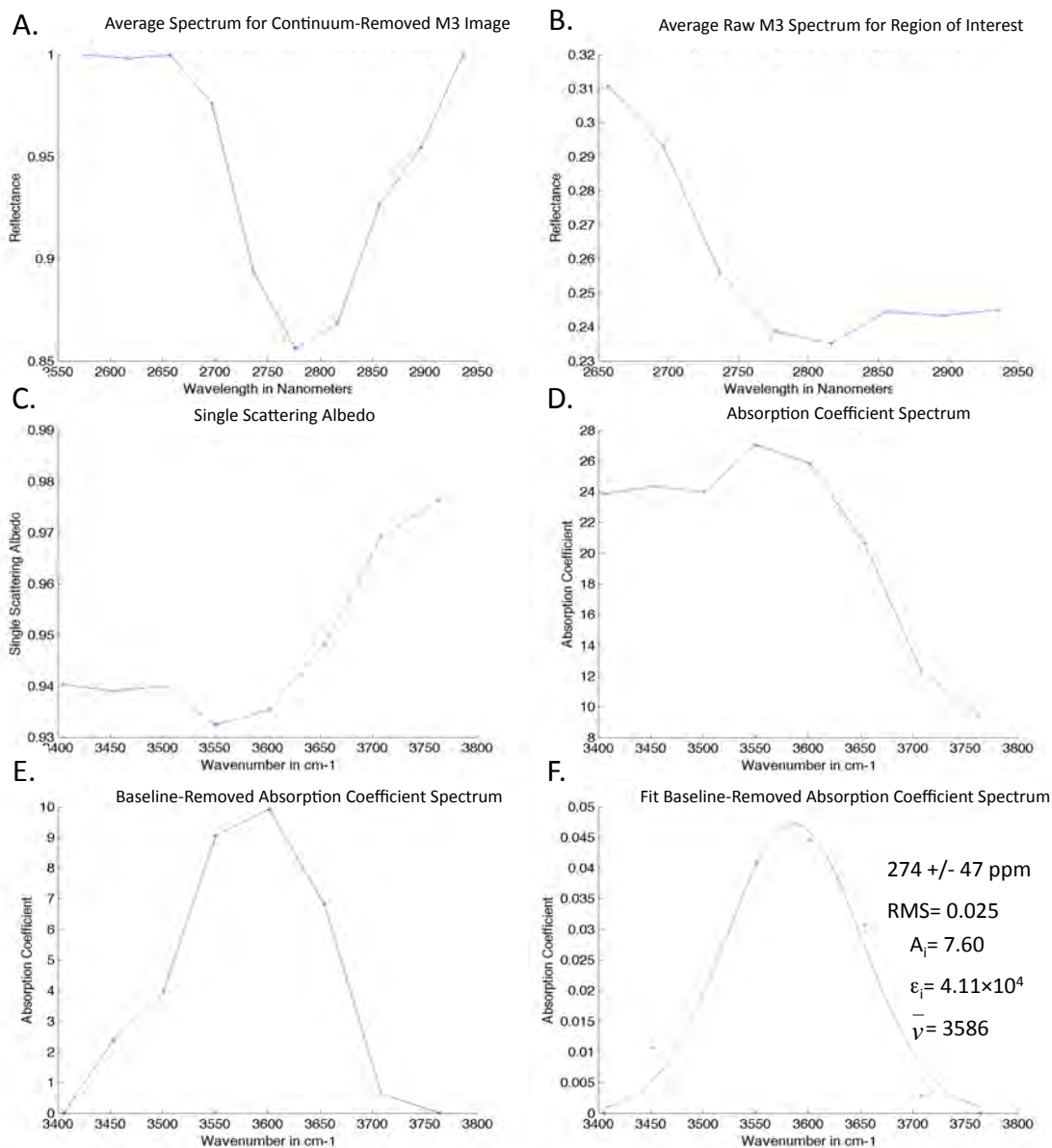


Figure A6: Results from CBTA6

HAN1

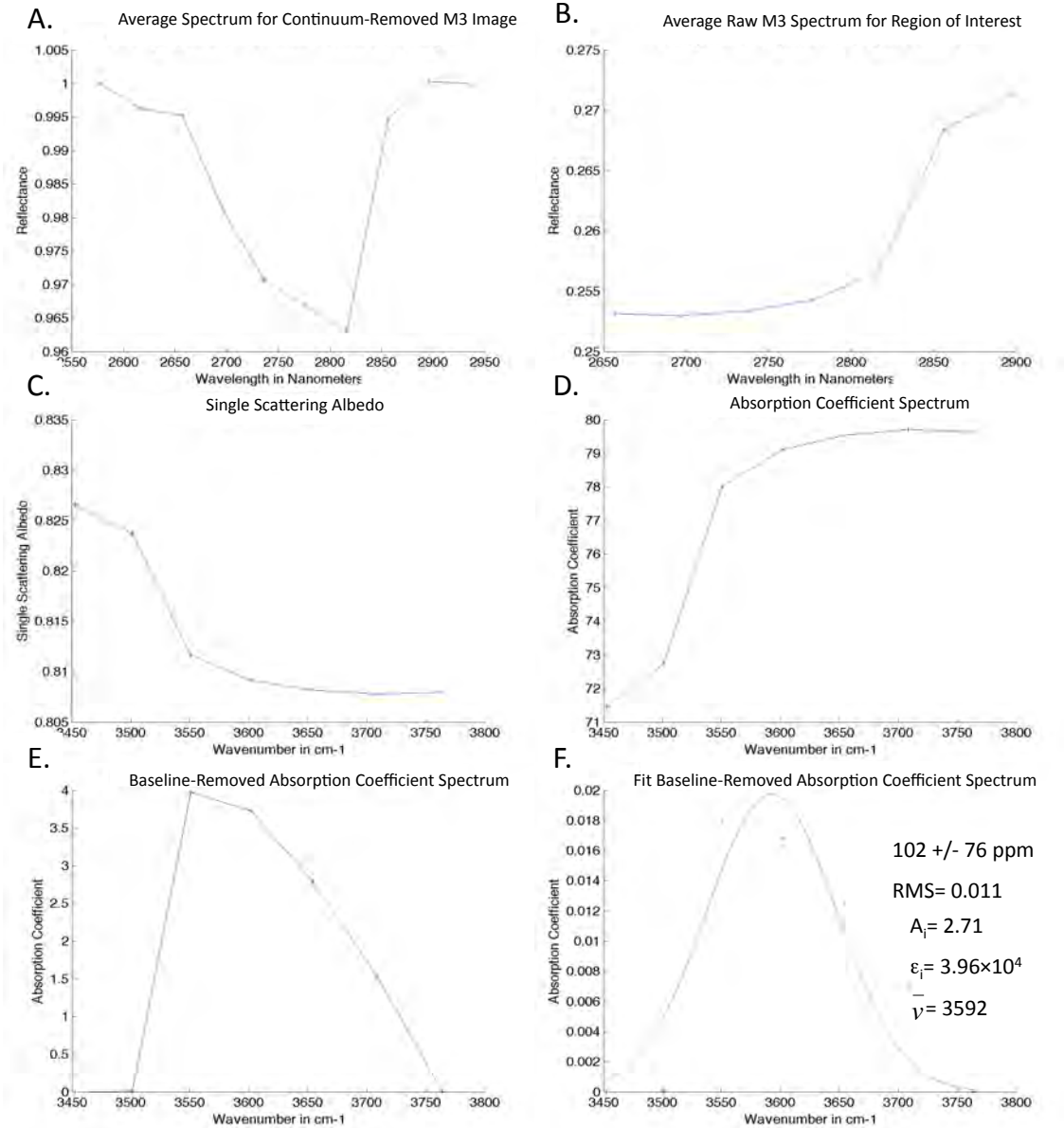


Figure A7: Results from HAN1

HAN2

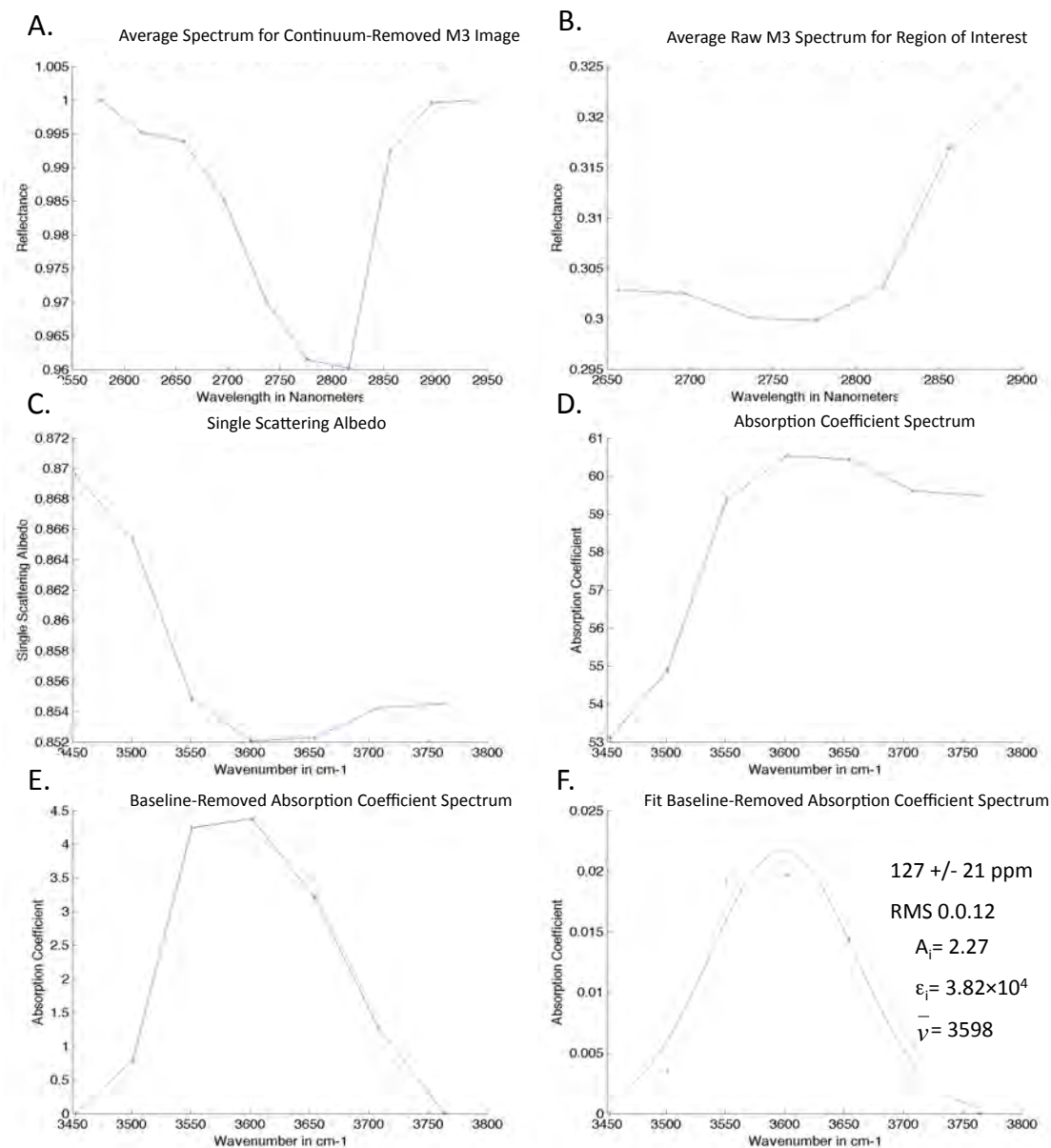


Figure A8: Results from HAN2

HAN3

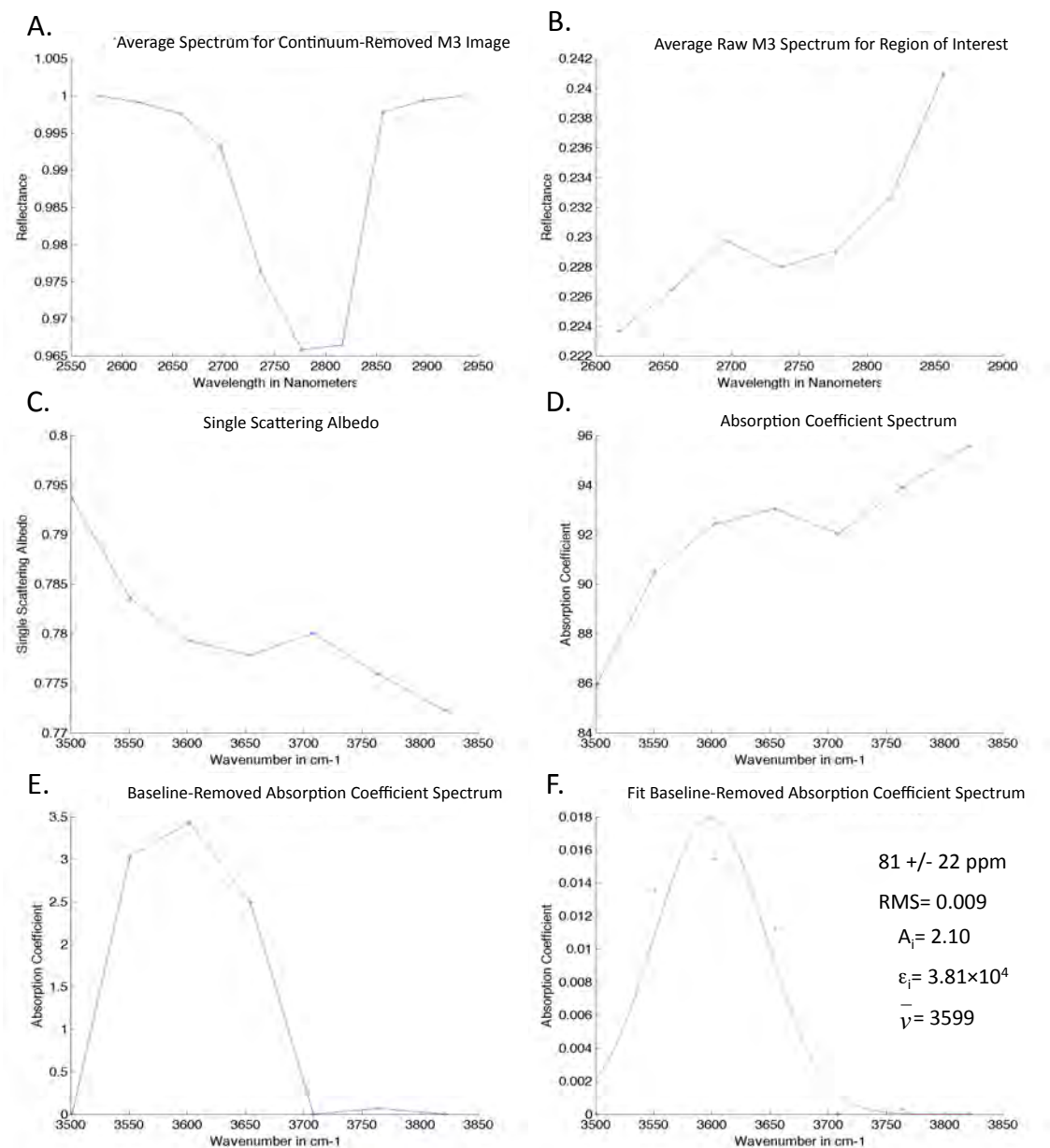


Figure A9: Results from HAN3

HAN4

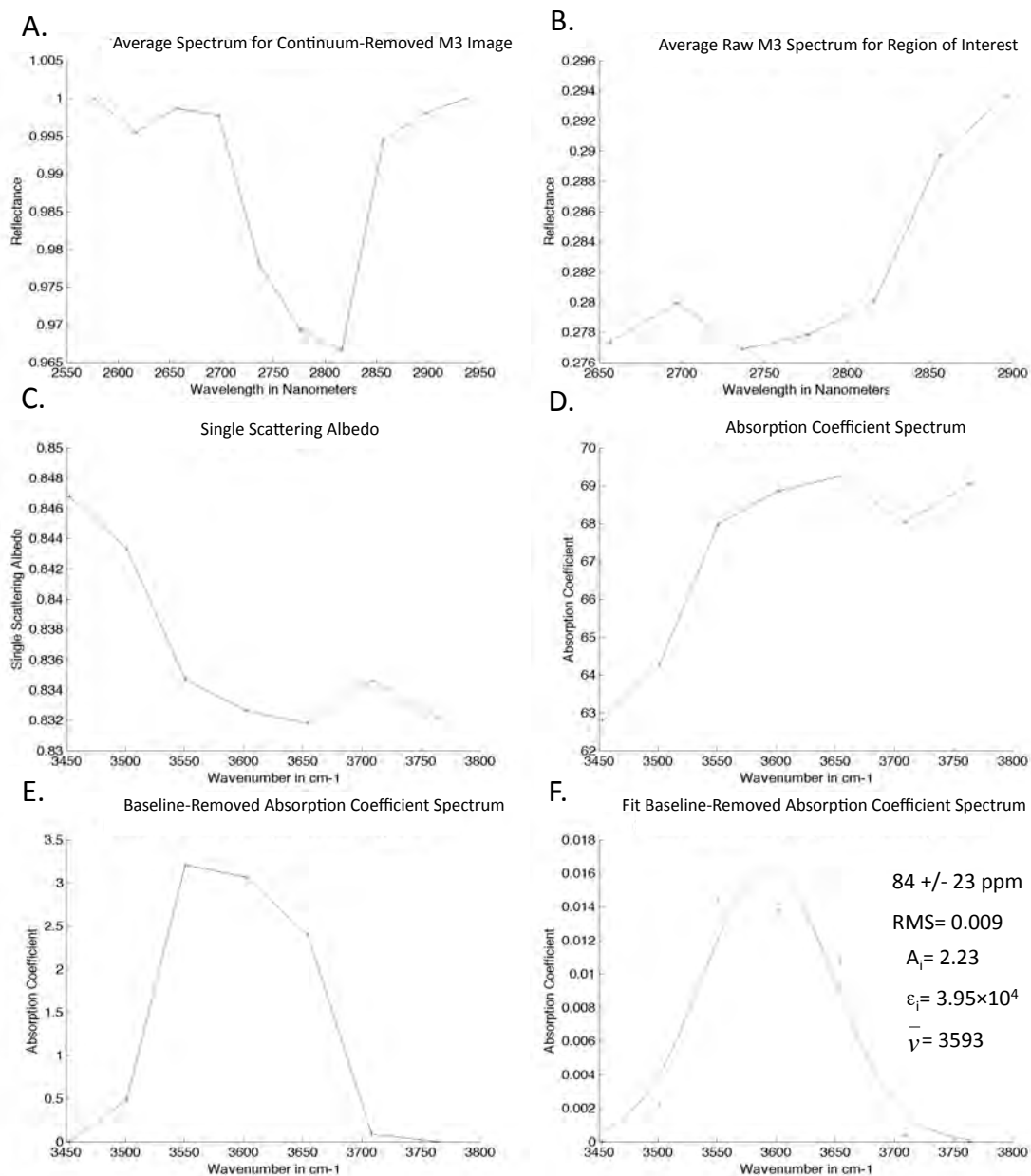


Figure A10: Results from HAN4

HAN5

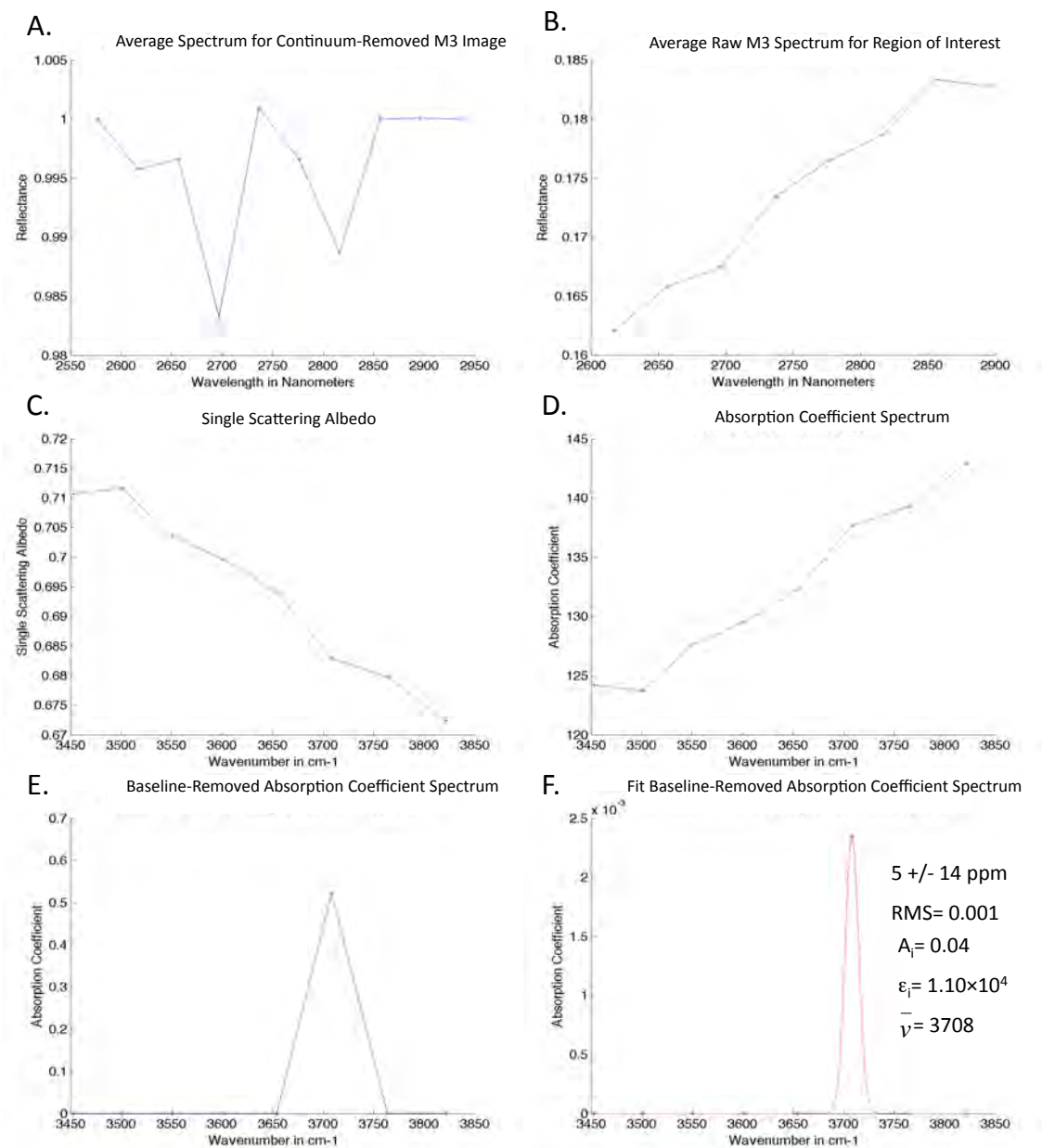


Figure A11: Results from HAN5

HAN6

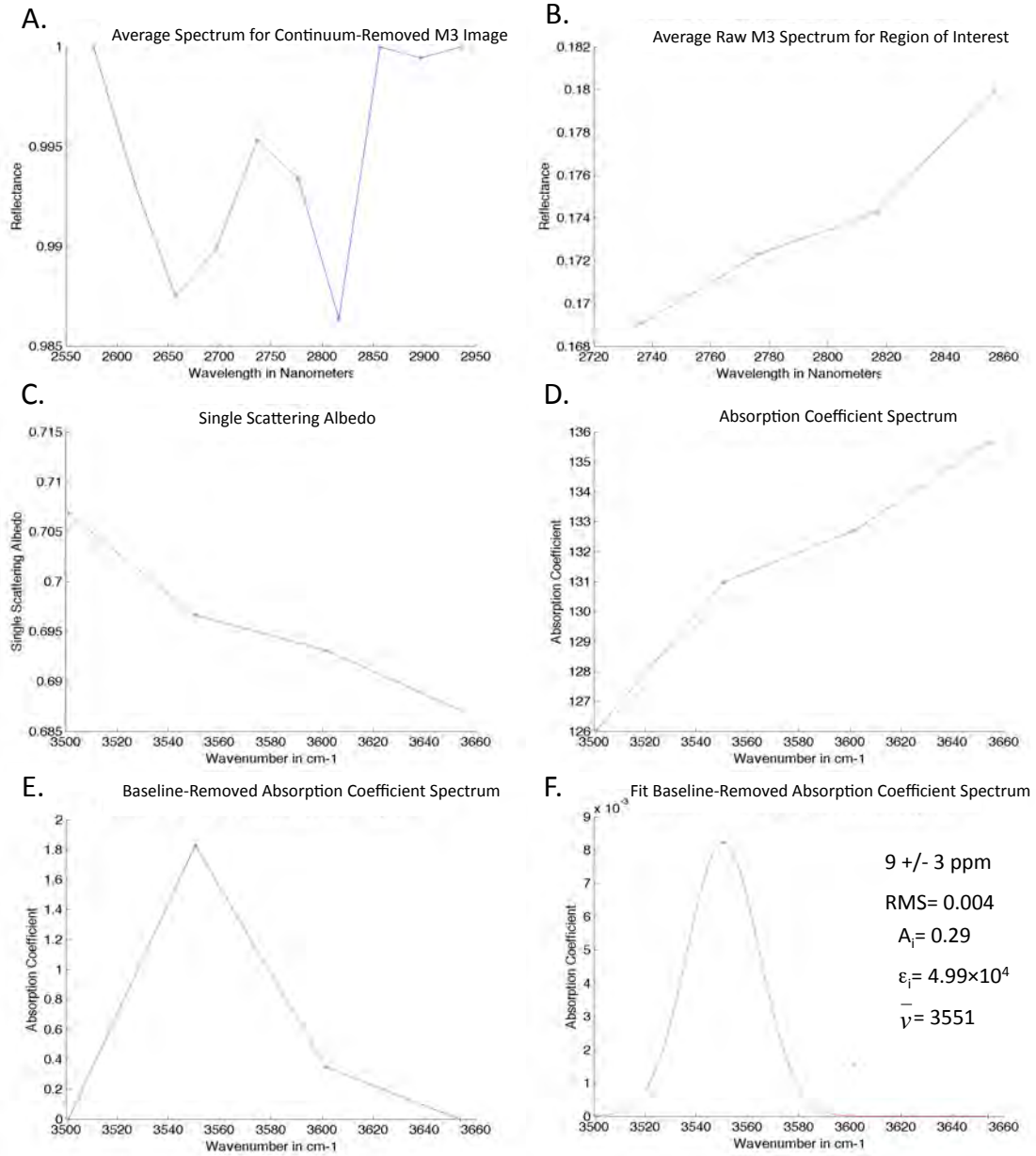


Figure A12: Results from HAN6

LASS1

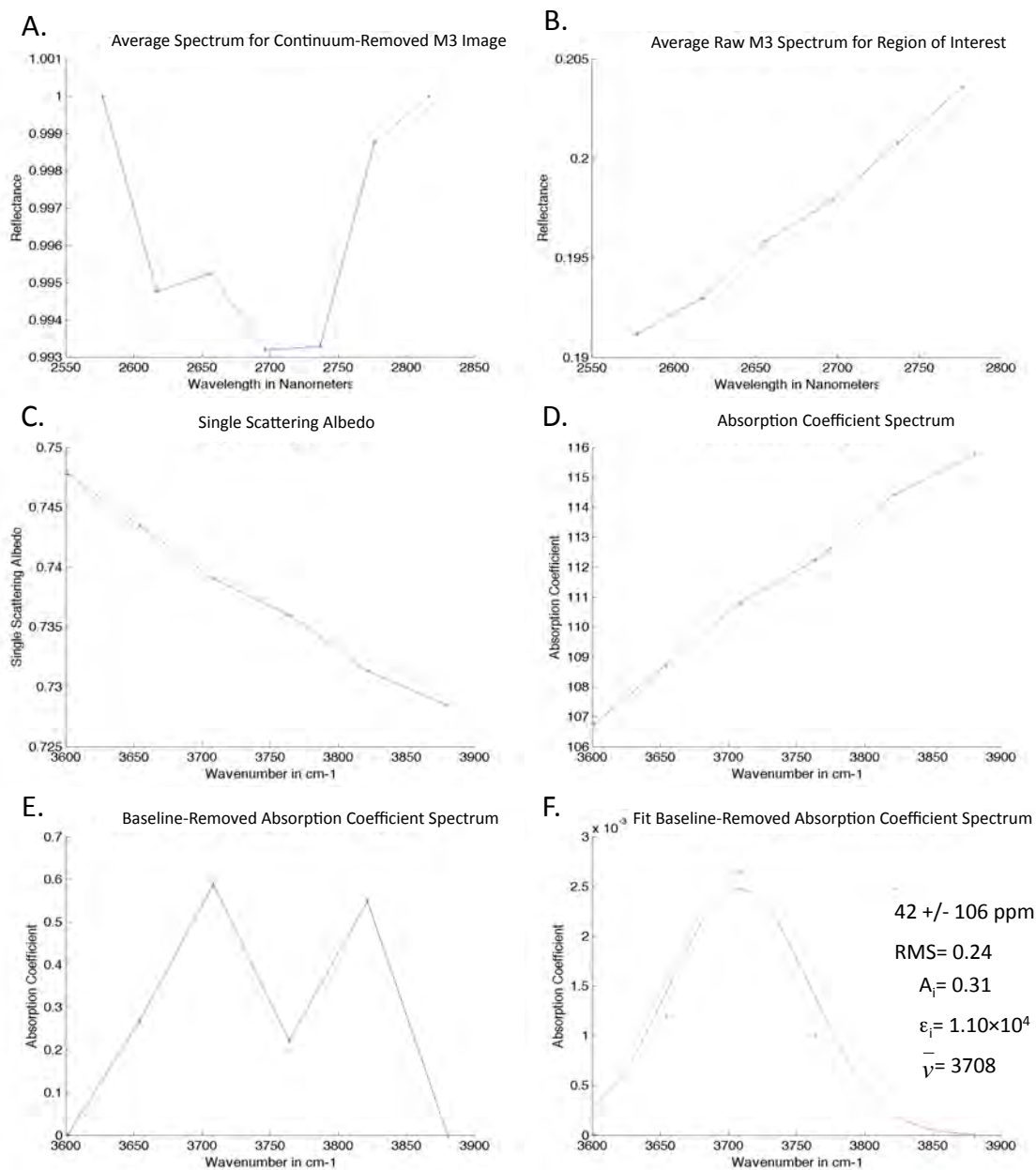


Figure A13: Results from LASS1

LASS2

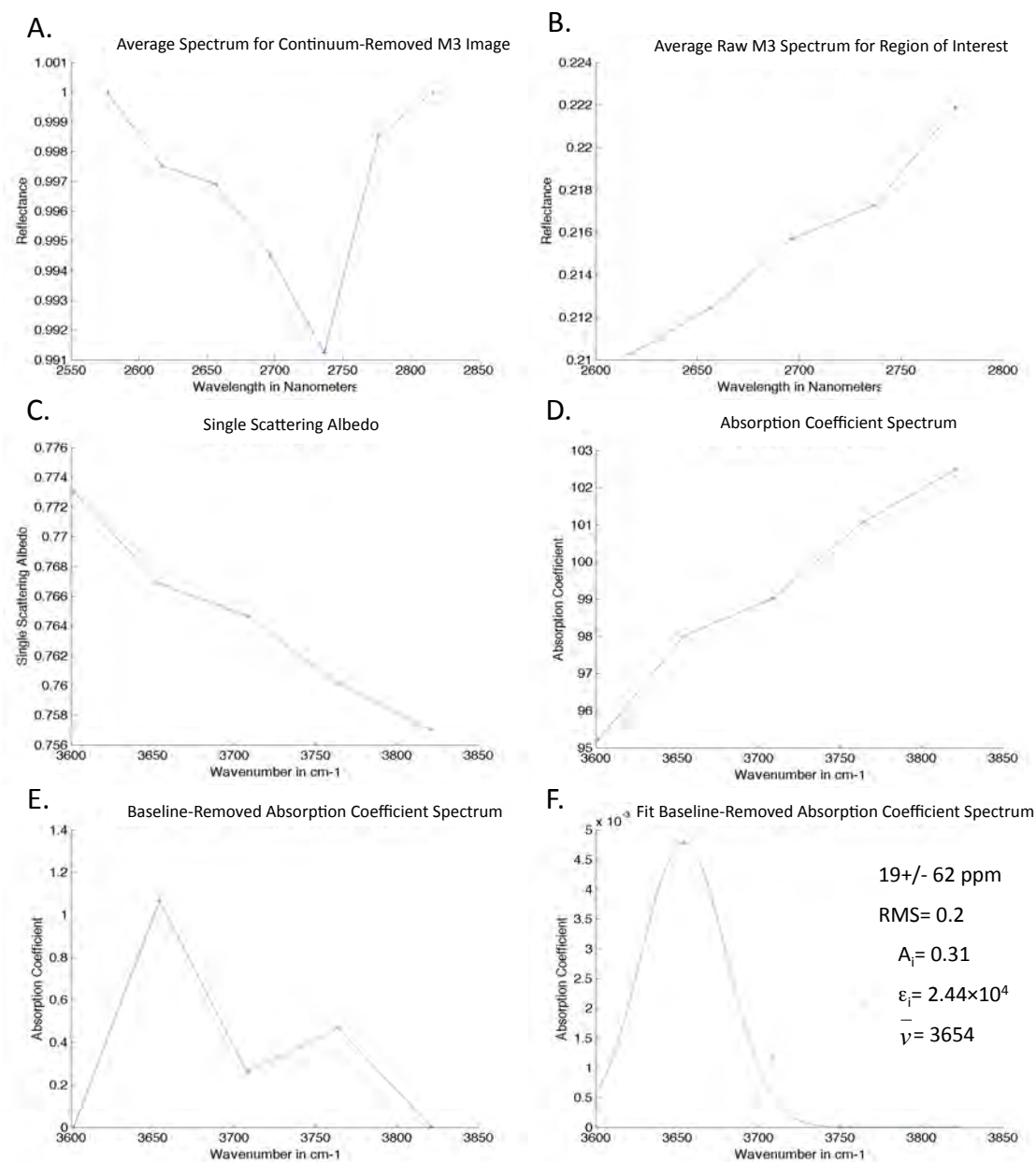


Figure A14: Results from LASS2

LASS3

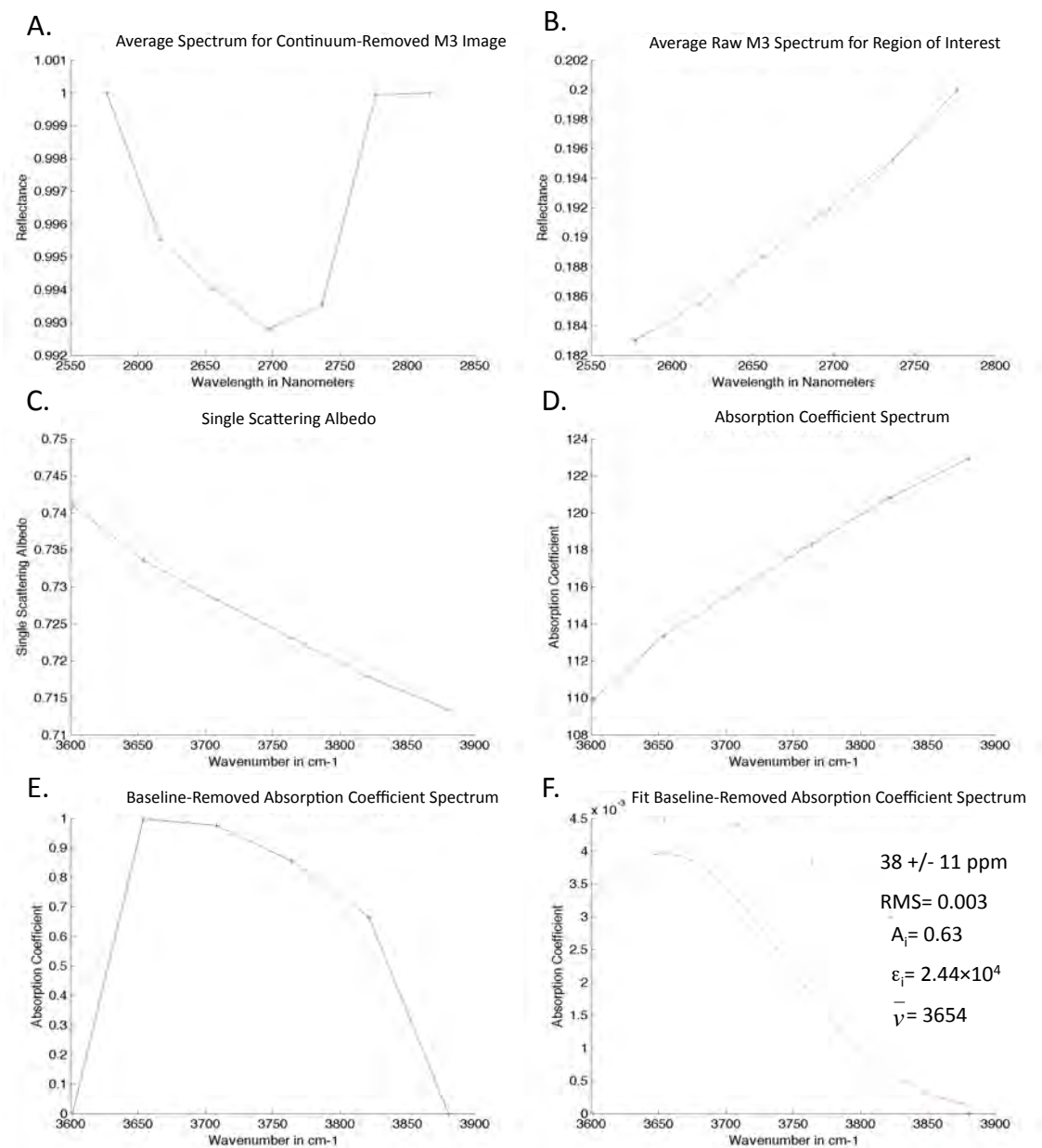


Figure A15: Results from LASS3

LASS4

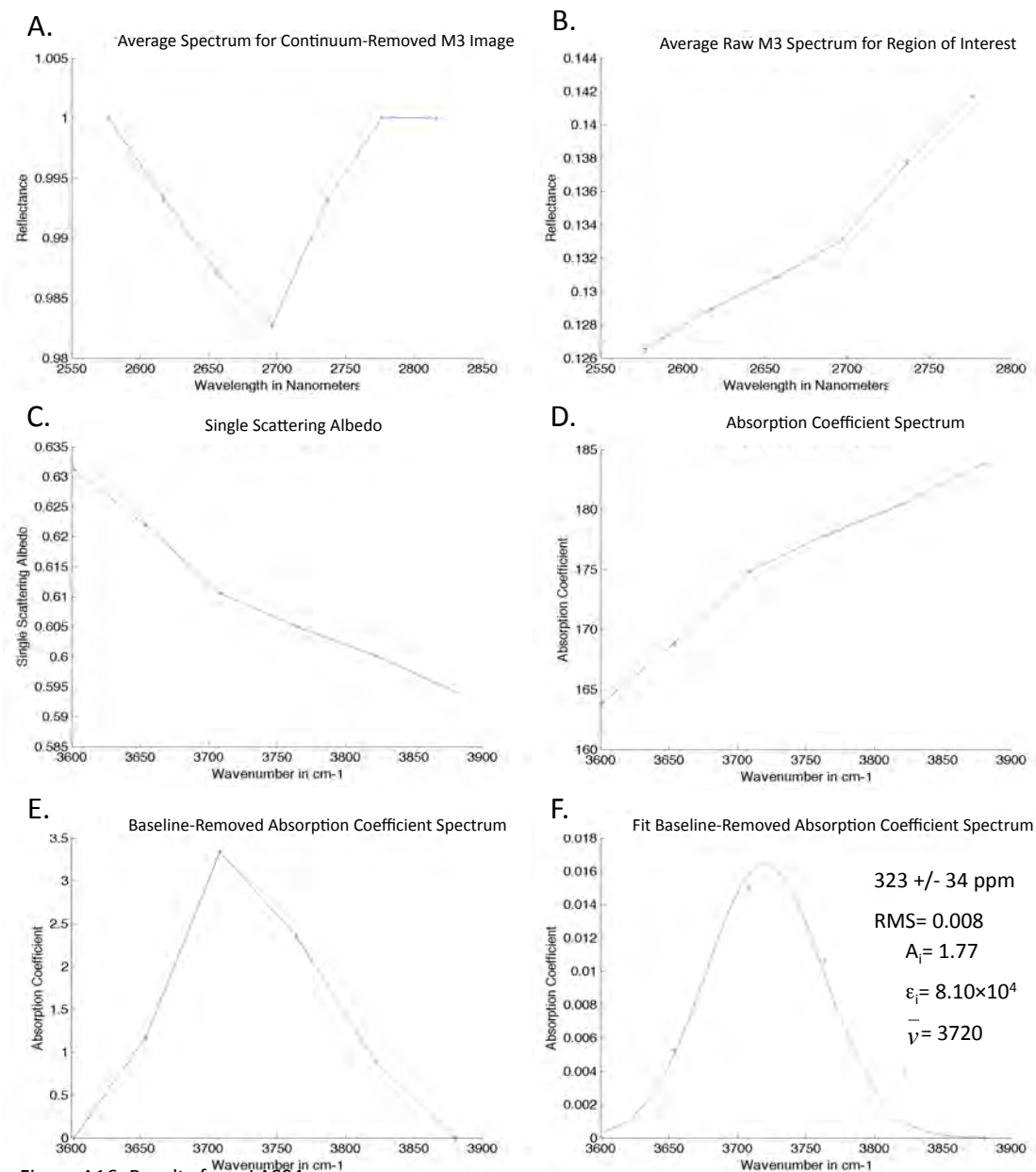


Figure A16: Results from LASS4

LASS5

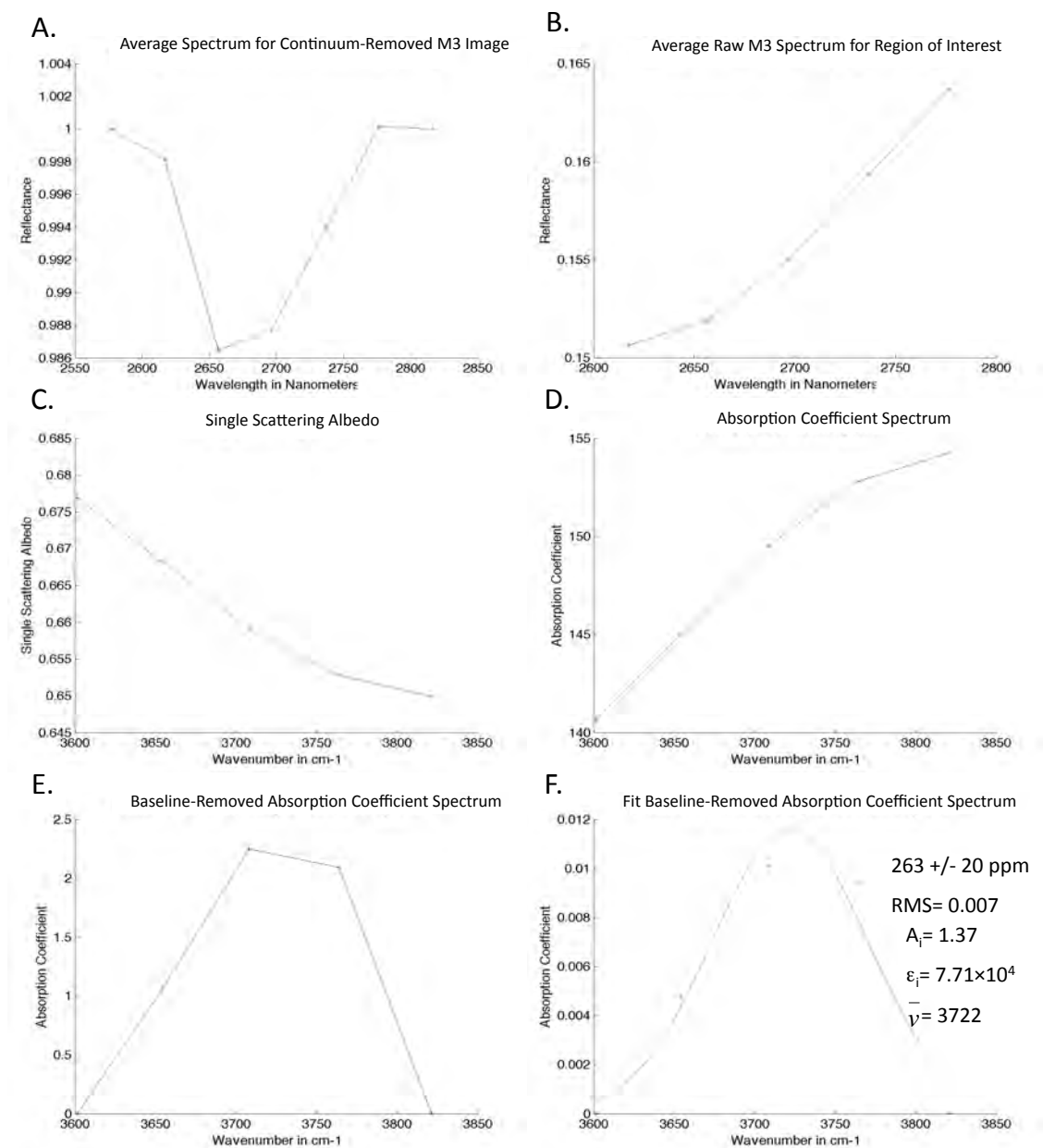


Figure A17: Results from LASS5

GRUITH1

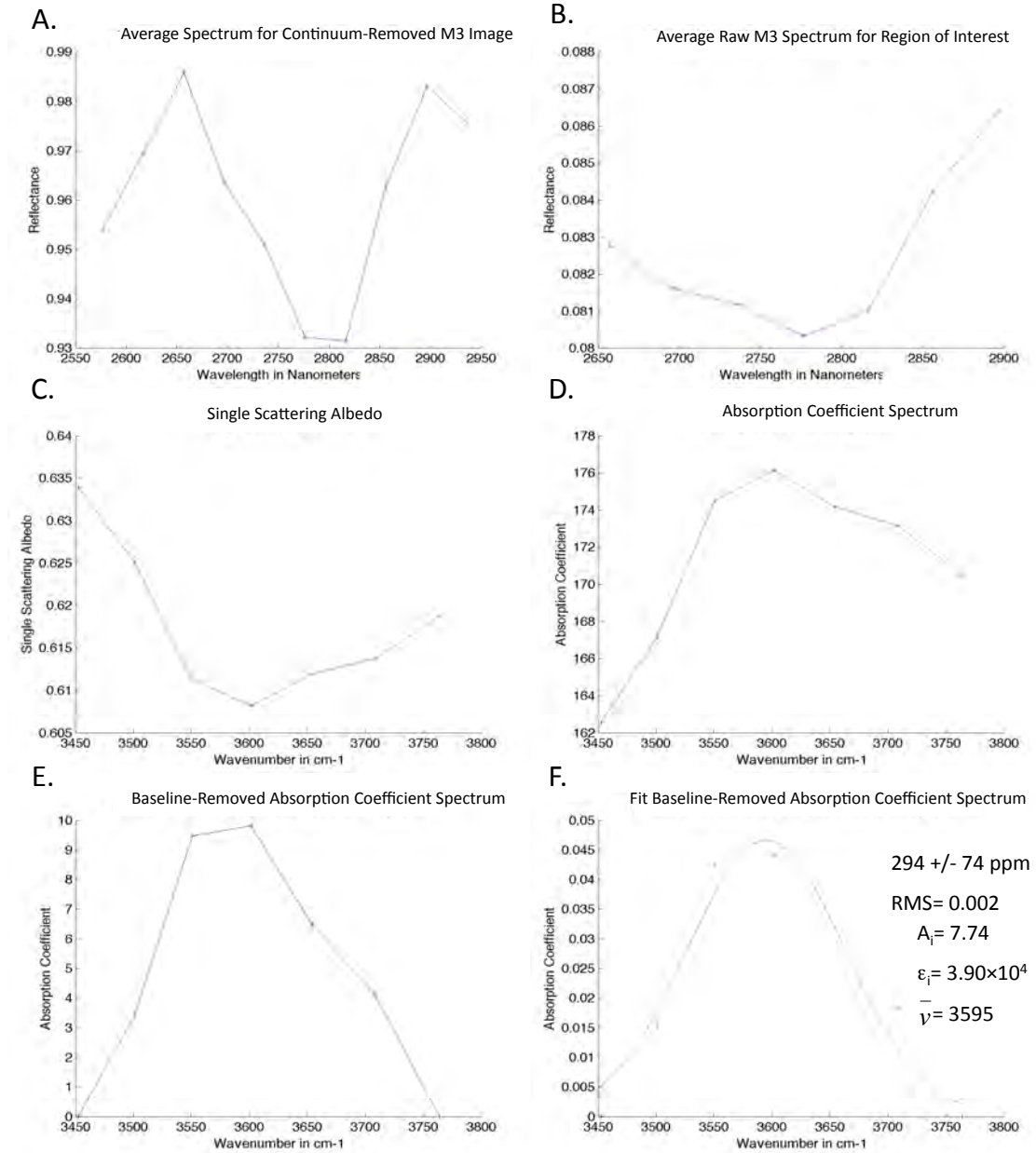


Figure A18: Results from GRUITH1.

GRUITH2

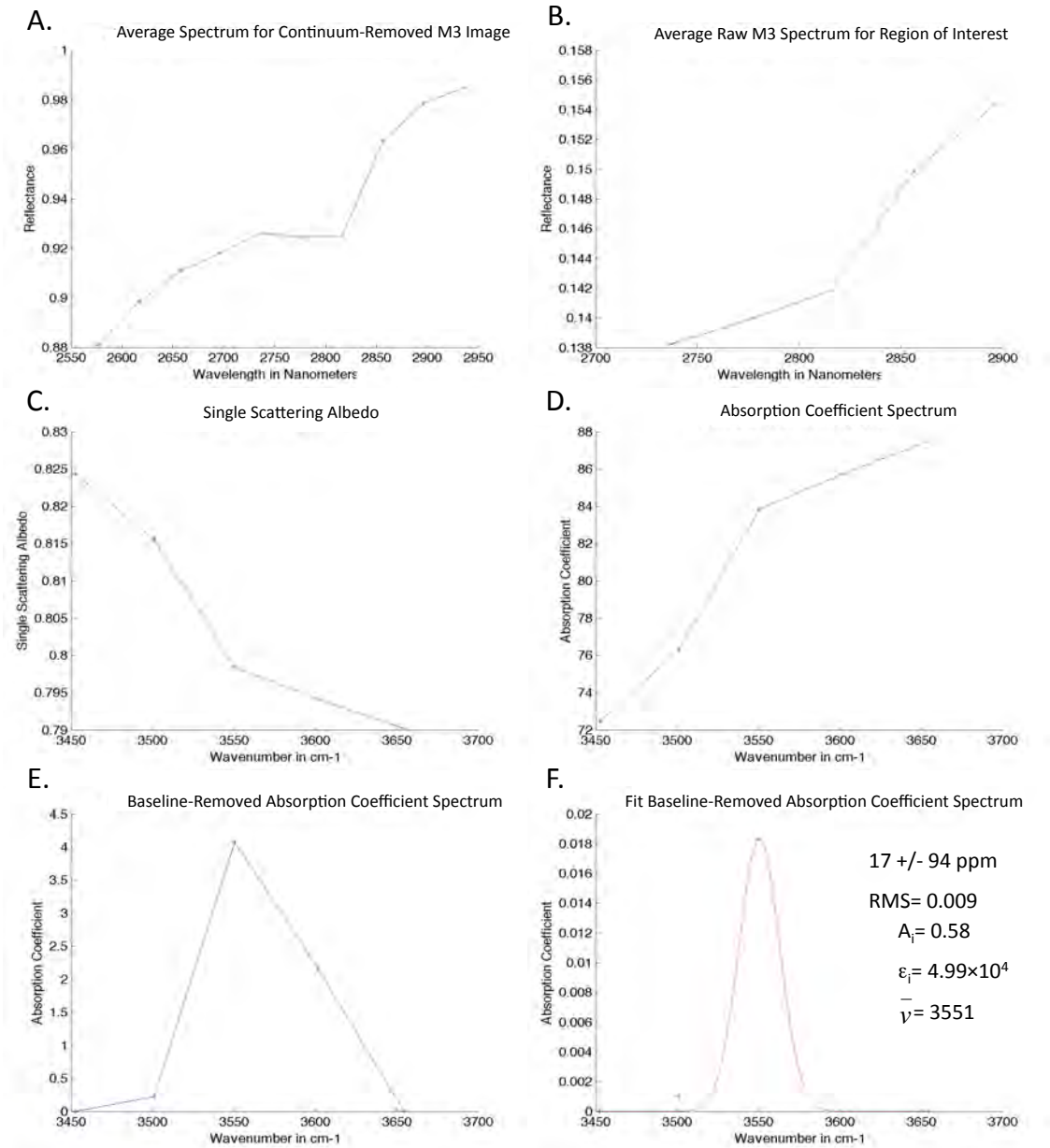


Figure A19: Results from GRUITH2

APPENDIX 3: MONTE CARLO METHOD FOR PROPAGATING UNCERTAINTY

The MATLAB code in this appendix propagates the error in the variables of the Beer-Lambert law (Equation 11; Section 5.6) using a Monte Carlo Simulation and calculates the $1\text{-}\sigma$ uncertainty of water concentration. The code was developed in MATLAB version 7.12.0. The first part of the code (lines 10-28) involves inputting the mean and standard deviation for each variable in Equations A3.1 and A3.2. The next part of the code (lines 30-42) involves running the Monte Carlo simulation through 100,000 iterations of Equations A3.1 and A3.2. Line 45 converts the concentrations in parts per million (ppm), and then a water concentration mean and uncertainty is output (lines 47-49). The user manually enters the variables in the code. The result is stated in the main MATLAB window and must be manually entered into a table in order to be preserved. A digital copy of the MATLAB code can be found in the CD provided with this dissertation in the file *montecarlo.m*.

```

%Monte Carlo Simulation of the Beers Law to calculate the error in OH/H2O
%concentrations.

%updated 10/20/2014 Douglas L. Standart

clear
clc

%how many iterations for the Monte Carlo to simulate.
iter = 100000;

%input the mean and standard deviation for each variable in the equation
%that is being simulated.
%means and standard deviations are given in Table 1.
vmean = 3708;
vSTD = 6;
%epsilon is dependent on v, so we can calculate random v's and then
%calculate random epsilons for each iteration (lines 30-31).
densitymean = 2.7;
densitySTD= 0.1;
%D is the grain size, we use a large standard deviation for grain size since
alpha is heavily dependent on it (Klima et al., 2013).
Dmean = 45;
DSTD = 45;
%areaundercurve is the area under the curve calculated by the MATLAB code
%in appendix 2
areaundercurve = 0.0396;
areaSTD = 0.01;

%create an array of random concentration values after generating a random
%value for each variable in the Beers Law.
%normrnd = ( mu , sigma , M , N ), which returns a random M by N array with
values based on the mu and sigma you specify.
concentrations = zeros ( 1 , iter );
for m = 1 : iter;
    v = normrnd ( vmean, vSTD , 1 , 1 );
    epsilon = 246.6 .* ( 3753 - v );
    %epsilon = normrnd ( epsilonmean , epsilonSTD , 1 , 1 );
    density = normrnd ( densitymean, densitySTD , 1 , 1 );
    D = normrnd ( Dmean, DSTD , 1 , 1 );
    area = normrnd ( areaundercurve , areaSTD , 1 , 1 );
    concentrations (m) = ( area .* 1.8 ) ./ ( ( D ./ 10000 ) .* density .*
epsilon ); % in wt percent H2O
end

%convert concentrations to ppm.
concentrations = concentrations .* 10000;

%output the mean and standard deviation of the values in concentrations
mu = mean(concentrations)
sigma = std(concentrations)

```

CHAPTER 3: DELINEATING ILMENITE IN MARE BASALTS USING THE MOON MINERALOGY MAPPER

Standart, D. L. and Hurtado, J. M. (Jr.)

Department of Geological Sciences, The University of Texas at El Paso, 500 West University
Avenue, El Paso, Texas 79968

Abstract: KREEP (Potassium, Rare Earth Elements, Phosphorus) material on the Moon has been shown to be relatively rich in ilmenite and other useful materials. By targeting areas with anomalously high Thorium (Th) signatures, as seen by Lunar Prospector Th gamma ray spectroscopy (LP-ThGRS), we attempt to determine if younger maria are both Ti- and Th-rich. To map Ti, we target ilmenite (FeTiO_3) by employing a band depth technique that takes advantage of the fact that the visible-infrared reflectance spectrum of ilmenite exhibits low reflectance and a flat continuum slope, so the spectra of ilmenite-bearing mare basalts will have a reduced 1- μm absorption. In order to do this, we plot ilmenite concentrations from Apollo basalt samples against the 1- μm absorption depths associated with the locations the samples were collected. A least-squares fit to the ilmenite vs. 1- μm absorption data is used to predict ilmenite concentrations of mare basalts from spectra obtained from the Moon Mineralogy Mapper. With this method, we build ilmenite maps for the following nearside mare: western Mare Imbrium; southern Oceanus Procellarum; eastern Mare Nubium; Mare Serenitatis; and Mare Tranquillitatis. We determine that multiple eruption episodes with different geochemical signatures occurred based on the concentrations of Th and ilmenite associated with the eruptions. We observe <3.1 Gya ilmenite- and Th-rich eruptions within the PKT, which we expected to

occur after Th-rich urKREEP and Ti were pulled into the mantle by a downwelling, and subsequently rose back to the base of the lunar crust in the form of a plume early in lunar history. However, areas outside of PKT, such as Tranquillitatis and Serenatatis, do not exhibit both high KREEP and ilmenite concentrations. We propose two possible scenarios to explain this. In the first, the Ti-rich but Th-poor mare basalts would have erupted after (or during) a degree-1 downwelling that affected the nearby PKT early in lunar history. The KREEP may have never existed at these locations, or it was removed by the degree-1 downwelling which redistributed that material and concentrated it in the PKT. In the second scenario, the Ti-rich but Th-poor mare basalts would have erupted prior to the degree-1 downwelling. In this case, the Ti-rich cumulates may have existed at the time of melt generation. However, the lack of Th would imply that KREEP did not exist at all at these locations.

Keywords: lunar mare-highland dichotomy; ilmenite; mare basalt; KREEP; Moon Mineralogy Mapper

1. Introduction

There is more abundant, relatively recent (ca. 400 Ma to 4.2 Ga; Schultz and Spudis, 1983; Wieczorek et al., 2006) volcanic activity on the nearside of the Moon compared to the farside. Much of the older volcanic activity on the nearside produced mare basalts, which erupted 100-400 Ma after the crust was thinned by large impactors (Arkani-Hamed and Pentecost, 2001). These basin-forming impacts promoted decompression melting of the mantle and formed structures (e.g. faults) that allowed those melts to later escape (Warren, 2001; Wieczorek et al., 2006). The farside, on the other hand, exhibits a long history of inactivity compared to the nearside, and the crust there is dominated by ancient (~4.5 Ga) farside anorthositic highlands (FAH), which are thought to be representative original crust of the Moon (Wieczorek et al., 2006). The distribution of basaltic, basin-filling maria and FAH is part of a distinction often referred to as the mare-highland dichotomy (Zhong et al., 1999; Zhong et al., 2000; Parmentier et al., 2002; Shearer et al., 2006).

The Procellarum KREEP Terrane (PKT), on the lunar nearside, comprises Oceanus Procellarum, Mare Imbrium, Mare Frigoris, and western Mare Serenatatis (Figure 1). More than 60% of all the mare basalts on the Moon are located within this region (Wieczorek et al., 2006). The maria here differ from those in other regions on the Moon because of the large amounts of incompatible species they contain. For example, the PKT maria contain more than 5 wt% TiO_2 and an average of 12-13 ppm Th, which is much higher than the average 2 ppm Th contained in other mare (Wieczorek et al., 2006). The high concentrations of Th and Ti within PKT indicate that the mechanism involved in bringing Ti- and urKREEP-enriched magmas to the surface may have operated on the nearside but not the farside. The PKT also has a relatively young volcanic

history compared to other regions of the Moon. For example, the youngest mare volcanism is within Oceanus Procellarum and dates to ~400 Ma (Wieczorek et al., 2006).

The origin of the mare-highlands dichotomy is still poorly understood, but many attribute it to the abundance of heat-producing elements that have been concentrated in the KREEP (“potassium, rare earth elements, and phosphorus”) (Wieczorek and Phillips, 2000; Wieczorek et al., 2006; Shearer et al., 2006). urKREEP is a geochemical reservoir on the Moon that is enriched in incompatible species [thorium (Th), potassium (K), rare earth elements (REE), phosphorus (P), OH, H₂O, uranium (U), etc.] compared to other geochemical reservoirs on the Moon. urKREEP is hypothesized to represent the ~2% melt fraction that remained during the final stages of fractional crystallization of the lunar magma ocean (LMO) (Warren, 1985; Snyder and Taylor, 1991; Wieczorek and Phillips, 2000; Elkins-Tanton and Bercovici, 2014). Large amounts of radiogenic heat-producing elements may be present in the urKREEP, and the abundance of KREEP on the nearside of the Moon could explain the origin of the mare basalts, particularly the large amounts of Th-rich mare basalts (Wieczorek and Phillips, 2000). The heat-producing elements in the urKREEP would have promoted heating and melting of the mantle, allowing a prolonged volcanic history (Wieczorek and Phillips, 2000). However, it is debatable whether the KREEP is continuous or discontinuous in the lunar subsurface (Warren, 1985; Wieczorek and Phillips, 2000).

KREEP material on the Moon has been shown to contain ilmenite (FeTiO₃) and incompatible elements (Shearer et al., 2006). By targeting areas with anomalously high Th signatures, we attempt to map the highest concentrations of ilmenite-rich material on the nearside of the Moon. To map ilmenite, we employ a band depth technique that takes advantage of the fact that the visible-infrared reflectance spectrum of ilmenite exhibits low reflectance and a flat

continuum slope (Figure 2; Issacson et al., 2011a). These effects may obscure spectral absorption features indicative of other minerals, such as pyroxene, within the host rock. Specifically, we predict that the presence of ilmenite in mare basalt will reduce the depth of the 1- μ m absorption associated with pyroxene and olivine in a way that is proportional to the amount of ilmenite. In order to determine if ilmenite does reduce the depth of 1- μ m absorptions in mare basalts, we use Moon Mineralogy Mapper (M³) images and mineralogical data from Apollo basalt samples to determine if there is a correlation between 1- μ m absorption strength and ilmenite abundance. Such a correlation can be used to ground-truth ilmenite maps made from remotely-sensed data. In this work, we use such ilmenite maps to investigate a potential association between high Ti concentrations and high Th concentrations in lunar maria. Geophysical models (Zhong et al., 2000; Parmentier et al., 2002; Khan et al., 2014) have shown that urKREEP- and Ti-rich melts could have mixed during a downwelling of dense material early in lunar geologic history. These models (Zhong et al., 2000; Parmentier et al., 2002) also predict that this material would later rise as a plume and accumulate at the base of the crust. If this is correct, we should see a correlation between Th and Ti concentrations in mare basalts. If incorrect, then KREEP- and Ti-rich basalts could be associated with specific time periods of mare volcanism. Such a pattern has important implications for the thermal and chemical geodynamical history of the Moon.

2. Background

This work relies on the use of remotely-sensed data sets to study the mineralogy of the lunar surface to gain insight into lunar differentiation and the distribution of elements such as Ti on the Moon. This section serves as an introduction to these topics.

2.1 Lunar Spectroscopy and Space Weathering

At short wavelengths – in the near-infrared, visible, and ultraviolet – electronic transitions within single atoms result in absorption features in reflectance spectra. As with the excitation of molecular bonds, the excitation of electrons to higher-energy states requires specific, quantized amounts of energy. The specific amount of energy depends on the atom, its valence, and the resulting electropotential field of the surrounding atoms in the crystal lattice of the material (Jensen, 2005). One type of electronic transition is charge transfer in which an electron is swapped between two cations with different valences, for example between Fe^{2+} and Fe^{3+} (Adams, 1974). This process results in a strong absorption at $\sim 1\ \mu\text{m}$ in the reflectance spectra of mafic minerals such as pyroxene and olivine (Figure 3; Isaacson et al., 2011b). By comparison, because ilmenite is an opaque mineral, it exhibits very low reflectance at short, visible wavelengths, except for a small reflection at $1\ \mu\text{m}$, and a low spectral slope between 0.4 to $3\ \mu\text{m}$ (Figure 2; Isaacson et al., 2011b). These characteristics can weaken the $1\text{-}\mu\text{m}$ Fe absorption feature in the spectra of olivine and pyroxene, common minerals in lunar basalts, if ilmenite is present.

Due to the lack of atmosphere on the Moon, micrometeorites and solar and cosmic rays constantly bombard the lunar regolith and slowly alter the surface, both physically and chemically, in a process called space weathering (Isaacson et al., 2011c). The geochemical effects of space weathering have a strong influence on the reflectance spectra of lunar materials (Isaacson et al., 2011c), and, if space weathering is not accounted for, reflectance measurements can be inaccurate or misleading. For example, space weathering processes on regolith reduce particle size and create a thin veneer of vapor deposited, nanophase iron on exposed surfaces

(Lucey et al., 2006; Isaacson et al., 2011c). Finer particle sizes make absorptions shallower and increase the overall reflectance of spectra (Pieters, 1983; Cooper and Mustard, 1999). As the regolith matures, the amount of nanophase iron increases, which causes regolith spectra to exhibit increased reflectance at longer wavelengths and creates steep spectral continuum slopes, an effect referred to as “reddening” (Figure 4). The reddening effectively shallows visible-near infrared/shortwave infrared (VNIR/SWIR) absorptions, and it can also skew the center wavelength of absorption features towards longer (e.g. “redder”) wavelengths. The longer material is exposed to the surface space weathering environment the steeper the continuum slope of reflectance spectra will become.

Without accounting for space weathering effects, it is difficult to compare lunar spectra to spectra for analogous terrestrial samples that have not undergone space weathering processes (Isaacson et al., 2011c). In this study, we incorporate spectral processing methods to take into account the effects of space weathering in order to detect ilmenite-rich basalts on the lunar nearside.

2.2 Differentiation of the Moon

The Moon is thought to have formed when a Mars-sized giant impactor hit the early proto-Earth at ~4.5 Ga (Wasserburg, 1987; Allègre et al., 1995; Touboul et al., 2007). Most of the debris from the impact would have rapidly coalesced in orbit around Earth, forming the Moon within the span of decades (Canup and Asphaug, 2001). Approximately 60-74% of the material in orbit would have originated from the impactor, except its dense core, which was assimilated into the Earth’s mantle upon impact (Canup and Asphaug, 2001). The rest of the

debris came from the crust and upper mantle of proto-Earth (Hiesinger and Head III, 2006; Touboul et al., 2007).

Initially, the early Moon would have been mostly, if not completely, molten due to the immense amount of energy of the giant impact (Touboul et al., 2007). As the molten moon cooled and underwent fractional crystallization, it gravitationally differentiated. Anorthosite and olivine were the first to crystallize, and, due to its lower density (2.7 g/cm^3), the anorthosite would have floated to the surface while the olivine and pyroxene would have sunk into the mantle (Shearer et al., 2006). A relict of this original anorthosite-rich floatation crust is represented in the FAH that we see today. The FAH consists of ~87% plagioclase, lacks incompatible elements, and almost completely lacks mare-type volcanism (Wieczorek et al., 2006).

As differentiation continued, a 10-100 km thick shell of magma, called the lunar magma ocean (LMO), coalesced below the crust (Warren, 1985). As the LMO underwent fractional crystallization, and the primordial anorthosite crust grew, the LMO progressively became a thinner layer, possibly non-existent in some places (Figure 5; Warren, 1985). Towards the end of this fractional crystallization period (~4.42 Ga; Nemchin et al., 2009), only magmas enriched with incompatible species (e.g., OH^- , H_2O , Th, U, REE, K, and P) would have remained (Warren, 1985; Elkins-Tanton and Grove, 2011). These residual magmas of the LMO are known as urKREEP (Warren, 1985; Wieczorek et al., 2000). The urKREEP would eventually mix with mantle-derived magnesian melts to form KREEP-basalts (Wieczorek et al., 2006).

Many workers (e.g., Warren, 1985; Wieczorek and Phillips, 2000; Wieczorek et al., 2006) believe that the presence of abundant mare basalts on the nearside and the dominance of FAH (i.e. the mare-highlands dichotomy) is due to a higher abundance of radiogenic heat

producing elements (i.e., Th, U, and K) associated with KREEP beneath the nearside crust. The KREEP-enriched region on the nearside is known as the Procellarum KREEP Terrane (PKT; Figure 1). The radiogenic heat producing elements in urKREEP could have prolonged magma production beneath the PKT due to elevated heat production in the subsurface.

A hypothesis for the large concentration of KREEP in the PKT is the effect of large impacts during pre-Nectarian lunar history (4.5-3.9 Ga) (Warren, 2001; Wieczorek et al., 2006). Large, pre-Nectarian, basin-forming impacts excavated material and thinned the lunar crust, particularly on the nearside (Warren, 2001; Wieczorek et al., 2006). The presence of thinner crust on one side of the Moon may have caused a hydrostatic pressure differential that forced urKREEP-rich melts to pool underneath the thinner crust (Figure 6; Arkani-Hamed and Pentecost, 2001; Shearer et al., 2006). The debated Procellarum impact on the nearside between 4.5 Ga and 4 Ga (Wieczorek et al., 2006; Zuber et al., 2012), may have been the large impact responsible for the crustal thinning and subsequent urKREEP-rich magma accumulation (Figure 5; Arkani-Hamed and Pentecost, 2001; Warren, 2001; Wieczorek et al., 2006).

An alternative hypothesis for the origin of the PKT considers the effect that downwelling of ilmenite-enriched material could have had on the differentiating early Moon (Zhong et al., 1999; Parmentier et al., 2002; Shearer et al., 2006). In this model, Rayleigh-Taylor instabilities in the differentiating LMO would have developed, ultimately resulting in a degree-1 downwelling of Ti-enriched, dense material into the mantle before the “main phase” of mare volcanism (before 4 Ga) (Parmentier et al., 2002; Shearer et al., 2006). This degree-1 downwelling could have either occurred spontaneously, given enough time, or it could have been triggered by an event, such as a large impact (Parmentier, et al., 2002; Shearer et al., 2006). Regardless of the trigger, the degree-1 downwelling would likely have carried urKREEP

material along with the Ti-rich material, including radiogenic heat-producing elements that would have subsequently heated the mantle near the core-mantle boundary to produce melts rich in both urKREEP and Ti (Parmentier et al., 2002; Shearer et al., 2006). Zhong et al. (2000) show that such a degree-1 downwelling would have later resulted in the hemispherical dichotomy now seen in the distribution of KREEP material. According to their model, a portion of the downwelling would thermally expand due to radiogenic heating (Zhong et al., 2000). This thermal expansion would cause Ti- and urKREEP-rich cumulates to become less dense than the overlying mantle and allow them to buoyantly rise and accumulate below the nearside crust (Zhong et al., 2000). The non-uniform accumulation of radiogenic heat producing elements and Ti-rich melts at the base of the crust would help produce the increased volcanic activity on the nearside as well as the Ti-rich mare basalts present in the PKT.

Recently, the Gravity Recovery and Interior Laboratory (GRAIL) mission has discovered a semi-rectangular array of fractures in the PKT region that may present a mechanism for the eruption of mare basalts (Andrews-Hanna et al., 2014). They argue that the observed semi-rectangular array of fractures is not the pattern that would be expected if a basin-forming impact were responsible for the mare basalts on the nearside. Rather, a basin forming impact would be elliptical in shape, and the observed rectilinear pattern may instead be consistent with a large plume below the lunar crust (Andrews-Hanna et al., 2014). Such a plume could have formed as a product of the ilmenite downwelling discussed previously (Zhong et al., 2000; Parmentier et al., 2002; Shearer et al., 2006). This plume would have generated a large heat gradient in the crust, forcing the crust to flex and fracture (Andrews-Hanna et al., 2014). These fractures would later act as conduits for magmas to reach the surface (Andrews-Hanna et al., 2014).

It is still debated if the KREEP on the nearside (let alone on the farside, if it exists there at all) is a continuous layer (Snyder and Taylor, 1991) or if it is discontinuous in the form of dikes, sills, or pods (Wieczorek and Phillips, 2000). For example, the Compton Belkovich Thorium Anomaly (CBTA) lies outside the PKT, yet it shows signs of relatively recent volcanic activity (Jolliff et al., 2011) and high Th content (Figure 7; Lawrence et al., 2007), both of which are consistent with the presence of KREEP. The possible presence of KREEP material outside of the PKT, at sites like CBTA, could indicate either a global or near-global KREEP layer or the existence of KREEP pods, dikes, or sills that extend beyond the nearside and into the farside of the Moon.

The distribution of KREEP on the nearside and farside has also been investigated by Standart and Hurtado (2012; see Chapter 1). They studied non-mare silicic features on the nearside, as well as at CBTA on the farside, in order to determine the presence of water and also to determine if KREEP exists outside the PKT. Since KREEP is predicted to be Th- and water-rich (Warren, 1995; Elkins-Tanton and Grove, 2011), lithologies containing an abundance of Th and water are likely to be associated with KREEP. Standart and Hurtado (2012) used 2.8- μm absorptions in M^3 reflectance spectra to calculate water concentrations, and they show that CBTA is potentially associated with KREEP and hydrous, evolved lunar magmas (see Chapter 1).

2.3 Mare Volcanism

There are four processes that may be involved in the generation of melts: decompression melting; adiabatic melting; volatile-related melting; and temperature-induced melting. Decompression melting can occur when a large impactor excavates crustal material, thereby

reducing lithostatic pressure (Warren, 2001; Wieczorek et al., 2006). Isostatic uplift of material below the impact would also occur, warping isotherms upwards, causing pressure to decrease faster than temperature, and induce adiabatic melting. Whereas decompression melting is capable of producing large amounts of partial melt (~98%) (Whitten et al., 2011), adiabatic melting can only account for ~2% of the total melt created during lunar basin formation (Whitten et al., 2011). Melts can also be generated by increasing the amount of available volatiles, such as water or carbon dioxide, which reduce the melting point of rocks in the crust (Schmincke, 2004). The KREEP layer is thought to be highly enriched in water (Elkins-Tanton and Grove, 2011), which could reduce the melting point of the lunar crust and form volatile-related partial melts. Finally, partial melting of the lower crust can also occur during asthenospheric upwelling in the form of a plume, which increases temperatures at the base of the crust, forming temperature-induced partial melts, and will also induce a larger amount of adiabatic melting (Schmincke, 2004; Andrews-Hanna et al., 2014). The consensus in the literature is that the melts responsible for mare volcanism were generated from decompression melting after large impacts (Warren, 2001; Wieczorek et al., 2006), however recent studies (Andrews-Hanna et al., 2014) have suggested that adiabatic melting and temperature-induced melting in a plume may have been important.

The mare basalts that formed on the nearside did so in two stages: an early stage, and a late stage. Early stage (3.9-3.1 Gya; Staid et al., 2011) mare basalts are low in Ti and contain more pyroxene than olivine, the latter of which exhibits strong 1- and 2- μm absorptions in visible-infrared reflectance spectra (Staid et al., 2011). Late stage (3.1-1.1 Gya; Staid et al., 2011) mare basalts have higher concentrations of Ti and contain more olivine than pyroxene, the

latter of which exhibits a strong 1 μm absorption and a less pronounced 2 μm absorption than does pyroxene (Staid et al., 2011).

3. Methods

We use Moon Mineralogy Mapper (M^3) data to measure the depth of the 1- μm absorption attributed to pyroxene and olivine in mare basalts. We hypothesize that M^3 pixels with reduced 1- μm absorptions may contain higher amounts of ilmenite, and we use this effect to quantify the amount of ilmenite present in lunar basalts. We test this hypothesis, and quantify the relationship between ilmenite abundance in mare basalts and the 1- μm absorption depth, by comparing the ilmenite concentrations of Apollo samples with M^3 spectra from the stations from which they were collected. From this comparison we derive a model for predicting ilmenite concentrations from M^3 spectra. We use that model to test our hypotheses for the origins of KREEP- and Ti-enriched mare basalts.

3.1 Moon Mineralogy Mapper

Moon Mineralogy Mapper (M^3) is an imaging spectrometer that was on board the Indian Chandrayaan-1 spacecraft (Boardman et al., 2011). M^3 measured radiance at wavelengths from 0.43 μm to 3.0 μm , spanning 85 bands with 20-40 nm spectral resolution (Boardman et al., 2011). The images used in this study were acquired from the NASA Planetary Data System (PDS) Imaging Node (<http://ode.rsl.wustl.edu/moon>). Preprocessing done by the M^3 science team included thermal correction, photometric correction, and statistical polishing (for more detail on calibration and preprocessing techniques see Lundeen et al. (2011)). In addition, M^3 images available on the PDS, including the ones used in this study, have already been converted

to reflectance using the I/F method (Lundeen et al., 2011). Once downloaded from the PDS, the M³ data were ready for processing and interpretation using ENVI software. Table 1 summarizes the M³ imagery used in this study.

3.2 Continuum Removal

The 1- μ m absorption in mare basalt can be difficult to measure in lunar spectra due to the effect of slope reddening (Issacson et al., 2011a). To correct for slope reddening, a linear fit to the shoulders of the 1- μ m absorption is performed to define the continuum slope (Figure 8). The original spectrum is then divided by the continuum slope, which flattens the spectrum (Issacson et al., 2011a). With the flattened spectrum we can accurately measure the depth of the 1- μ m absorption.

3.3 Frequency Domain Filtering

After continuum removal, a number of the M³ images exhibited vertical striping that is the result of instrument and sensor defects (Boardman et al., 2011) that are made more apparent by removing the continuum slope. These artifacts make the images difficult to use for further spectral processing. To remove the striping, we apply a frequency domain filter. The filter is applied by first computing the Fast Fourier Transform (FFT) of the continuum-removed M³ image (Jensen, 2005). A mask, with tapered edges (Figure 9), is then applied to the image in the frequency domain to remove the frequency components that create the vertical striping (Jensen, 2005). The frequency components associated with the striping are identified as anomalously high power frequencies (bright spots or lines) that are outside the zero frequency center of the frequency domain image (Figure 9). The resulting filtered image is then converted from the

frequency domain back to the spatial domain using an inverse Fast Fourier Transform (IFFT) (Jensen, 2005). The result is a filtered, continuum-removed M^3 image that has less vertical striping than the unfiltered image and is, therefore, suitable for further image processing.

3.4 1- μm absorption Band Depth

To determine the amount of ilmenite present, we calculate 1- μm band depth by subtracting the minimum of the 1- μm absorption (b_{min}) from the $\sim 0.75 \mu\text{m}$ shoulder reflectance value ($b_{shoulder}$) (Figure 8):

$$b_{shoulder} - b_{min} = \Delta R \quad (1),$$

where ΔR is the change in reflectance from absorption shoulder to minimum (i.e. the band depth). Equation (1) is applied to each pixel in the continuum-removed and filtered M^3 image to yield a 1- μm band depth image.

3.5 Ilmenite Regression Model

In order to use the ΔR values obtained with Equation (1) to determine ilmenite abundance, we compare the ilmenite concentrations from returned Apollo samples to the M^3 reflectance spectra of where they were collected on the Moon.

We obtain ilmenite concentrations from modal mineralogies reported for Apollo 11, 12, 15, and 17 basalt samples (Meyer, 2012). Some samples contained multiple modal mineralogies that were calculated in different studies (Meyer, 2012). In order to obtain single, representative ilmenite concentrations for those samples, we calculated the mean and the standard deviation of the reported values (Appendix 1).

Apollo 11 landed in the southwest section of Mare Tranquillitatis ($\sim 0.7^\circ$ N, 23.5° E) (Shoemaker et al., 1969), and analyses of the samples collected there yielded ilmenite concentrations from 19 mare basalt samples (Meyer, 2012) (Appendix 1). Apollo 12 landed in the eastern section of Oceanus Procellarum ($\sim 23.4^\circ$ W, 3.2° E) (Shoemaker et al., 1970) and provided ilmenite concentrations from 41 mare basalt samples (Meyer, 2012) (Appendix 1).

Apollo 15 landed near Hadley Rille in the eastern section of Mare Imbrium ($\sim 3.6^\circ$ E, 26.5° N) (Swann et al., 1972). Three extravehicular activities (EVAs) were performed during which a total of 10 stations were visited along 3 rover-assisted traverses (Swann et al., 1972). The mobility of the rover allowed the astronauts to cover a larger area than was possible on previous missions (Swann et al., 1972). The Apollo 15 crew collected 29 mare basalt samples at 4 stations (Stations 3, 4, 7, and 9) from which ilmenite concentrations were later determined (Meyer, 2012) (Appendix 1). We chose not to use the mare basalt samples from Station 7 due to the proximity of this site to the Apennine Mountain front, which is composed of highland material.

Apollo 17 landed in a narrow valley surrounded by anorthositic highland material at the eastern section of Serenatis basin ($\sim 20.2^\circ$ N, 30.8° E) (Muehlberger et al., 1973). The Apollo 17 astronauts conducted 3 rover-assisted EVAs, and obtained 71 mare basalt samples from which ilmenite concentrations were later determined (Meyer, 2012) (Appendix 1). These basalt samples came from 10 stations: Stations 1, 2, 5, 8, and 9; the lunar module station (LM); the Apollo Lunar Surface Experiment Package (ALSEP) station; traverse station LRV-2; traverse station LRV-3; and traverse station LRV-12. The three LRV traverse stations were unplanned and un-numbered stops along their respective traverse segments. Only 29 of the mare basalt samples (from Stations 5, 8, 9, LM, ASLEP and LRV-12) were used because these samples were

from areas that were not in close proximity to highlands materials. Station 1 was not used because of its proximity to Steno Crater and its ejecta blanket (Muehlberger et al., 1973).

We extract ΔR values from the areas in the band depth-images (Table 2) associated with the Apollo sampling stations. The Apollo stations were located using M^3 images co-registered with the band-depth images, but, because of the relatively low-resolution of the M^3 data (~ 140 m/pixel), it was only possible to locate individual stations for Apollo 15 and 17 to within an area (“region-of-interest”) of 3-4 pixels (Appendix 1). For each station, the average ΔR was calculated from the pixels in the region-of-interest, and this value was associated with the ilmenite concentration for the rocks collected at that station. Because of their small extents, it was only possible to locate the entire areas of the Apollo 11 and 12 traverses (Figure 10) to within 5 and 3 pixels, respectively, in the M^3 images (Appendix 1). Therefore, all the Apollo 11 samples are associated with the same average ΔR value, as is the case with the Apollo 12 samples (Figure 10; Appendix 1). Averaging the ilmenite concentrations for Apollo 11 and 12 basalt samples does not affect the accuracy of the measurements because the sample regions were small enough that 2-4 pixels were used to obtain an average ΔR . In addition, the ΔR values for the pixels associated with the landing sites were nearly equivalent.

Samples from Apollo 14, which visited the Fra Mauro region, ($\sim 3.6^\circ$ S, 17.5° W; Swann et al., 1971) and Apollo 16, which visited the Descartes Highlands ($\sim 9^\circ$ S, 15.5° E; Muehlberger et al., 1972), were not used because these landing sites were in highland areas. Similarly, because the ~ 140 -m/pixel resolution of the M^3 imagery limits our ability to measure the spectra of a mare basalt site that is directly adjacent to anorthositic highland material, we chose to omit certain sampling sites from the other missions in our analysis (see above). For example, the Apollo sites near highland material (e.g., Apollo 17 stations 6, 7, and 8) (Figure 10) might

include anorthositic rocks, which, at the resolution of the M^3 images, would yield a mixed image spectrum that is hard to reconcile with the mineralogy of the mare basalt samples collected there. Recall that our methodology for detecting ilmenite in mare basalt uses shallowing of the 1- μm absorption as a proxy. It is, however, only applicable to basalt. Therefore, if we extract image spectra from an area with anorthositic material, which has no significant 1- μm absorption (Figure 2), we could incorrectly interpret these highland materials to be mare basalts containing large concentrations of ilmenite. Therefore, we chose not to include Apollo basalt samples that were collected from stations near anorthositic highland material in our study.

We plot the ΔR values for the Apollo sample sites ($N = 53$) against the corresponding ilmenite concentrations (in wt%) and use the statistical tools in MATLAB (Appendix 2) to regress the data with a least-squares estimation method (York, 1969; York and Evenson, 2004), which takes into account the uncertainties in both ΔR and the ilmenite concentrations (x). The result is a linear equation in the form of:

$$\Delta R = mx + b \quad (2),$$

where m is the slope and b is the y-intercept of the linear fit. If the 1- μm absorption in mare basalt indeed becomes shallower with increasing ilmenite concentration (Figure 2; Isaacson et al., 2011b), we should expect to see a negative correlation between ΔR and x . The regression model can then be used to predict the ilmenite abundances for mare basalts based on M^3 spectra.

3.6 Uncertainty

Uncertainties in the ΔR values obtained from the M^3 imagery, in the ilmenite concentrations from Apollo basalt samples, and in the regression model are all explicitly propagated to yield uncertainties in the ilmenite concentrations we determine using Equation (2).

ΔR uncertainties for each Apollo station are obtained from the statistics – mean and 1-sigma standard deviation ($\sigma_{\Delta R}$) – of the ΔR values extracted from the region-of-interest around that station in the band depth images. Because the reported modal mineralogies do not include uncertainties, we required an alternative way to determine the uncertainties of the ilmenite concentrations obtained from the Apollo samples. We focused on the samples for which several alternative modal mineralogies are reported, and calculated the mean and standard deviation of the ilmenite concentrations listed for the samples with multiple modal mineralogies. We then determined the average standard deviation for these samples and assumed this standard deviation in ilmenite concentration for all the Apollo samples (Appendix 1).

The least-squares estimation method (York, 1969; York and Evenson, 2004; Appendix 2) was used to determine the goodness-of-fit parameters for the regression described in Section 3.5. Among these parameters are the 1-sigma uncertainty (σ_m) on the slope and the 1-sigma uncertainty (σ_b) on the y-intercept of the linear fit. With these parameters we can formally calculate the 1-sigma uncertainty (σ_x) on the predicted ilmenite concentration values using the error-propagation formulae of Davis and Sampson (2002):

$$\sigma_x = \sqrt{\left(\frac{\Delta R - b}{m}\right)^2 \left(\frac{\sqrt{\sigma_{\Delta R}^2 + \sigma_b^2}}{(\Delta R - b)^2} + \frac{\sigma_m^2}{m^2} \right)} \quad (3).$$

3.7 Ilmenite Map

Equation (2) is used to calculate ilmenite concentration (in wt%) maps derived from the M^3 data using a MATLAB code (Appendix 3). The striping noise in the M^3 images will sometimes produce band depth images with ΔR values ≤ 0 , and, therefore, can result in erroneous ilmenite concentrations. In order to avoid the effect of striping on calculated ilmenite

concentrations, the MATLAB code assigns a concentration of 33.7 ± 1.8 wt% to pixels that have ΔR values less than 0 (Appendix 3). This value for the upper limit of ilmenite concentration we can reliably detect (see below) was determined by solving Equation (2) for a ΔR value of 0. The corresponding uncertainty was determined with Equation (3).

A shallow or absent 1- μm absorption can also occur for reasons other than striping. For example, anorthosite and non-mare silicic features can have shallow or absent 1- μm absorptions (Issacson et al., 2011b). To avoid erroneous interpretations of such features, we mask them out of the ilmenite maps (Figures 11-14). Another way of producing shallow or absent 1- μm absorptions is the effect of large amounts of ilmenite on spectra. Pure ilmenite has small reflection at 1 μm (Figure 2). While exposures of pure ilmenite on the lunar surface may be unlikely, extremely ilmenite-enriched basalts may be possible. Such basalts may have so much ilmenite that the 1- μm absorption due to olivine and/or pyroxene may be absent. In this way, the 33.7 ± 1.8 wt% value calculated above is the upper limit of ilmenite abundance detectable with our method. Alternatively, the spectral effect of ilmenite in such rocks may saturate such that, even at extremely high ilmenite concentrations, a $\Delta R > 0$ will remain. Future work will be needed to determine which is the case.

Similarly, pixels with ΔR values greater than 0.084 may give erroneous (i.e. negative) ilmenite concentrations. Using Equation (2) we can determine what ΔR value is consistent with 0 wt% ilmenite. Essentially the y-intercept (0.084) is where we see ilmenite concentrations at 0 wt%. In order to avoid this, the MATLAB code assigns a concentration of 0 wt% ilmenite to pixels with ΔR values greater than 0.084 (Appendix 3). Such pixels can be interpreted as mare basalt with no ilmenite, in which the depth of the olivine and/or pyroxene spectral feature at 1 μm is not being modified.

4. Study Areas

If the ilmenite downwelling hypothesis for the development of KREEP is correct (Zhong et al., 1999; Parmentier et al., 2002; Shearer et al., 2006), we may expect to see areas with high concentrations of ilmenite – and, therefore, Ti – in close proximity to areas with high Th concentrations. Th is radioactive, and the gamma rays emitted as the element decays can be remotely sensed. Because of this, and due to its presence in KREEP-rich material, Th is one of the best remote indicators of KREEP on the Moon. Previous studies (e.g., Lawrence et al., 2000; Lawrence et al., 2003; Jolliff et al., 2012) have used data collected from the Lunar Prospector Gamma Ray Spectrometer (LP-GRS; Binder, 1998) to locate Th “hotspots” in order to better understand the distribution of KREEP on the Moon (Figures 7). LP-GRS Th data shows that the PKT has the highest concentration of Th-rich material on the Moon (Lawrence et al., 2000; Lawrence, 2003). The only regions showing any signs of Th enrichment on the lunar farside are the South Pole Aitken Basin (SPAB) (Hagerty et al., 2011) and the Compton-Belkovich Th anomaly (Jolliff et al., 2011), suggesting that material enriched in incompatible species may also be present at these locations. We use the published results of Lawrence et al. (2007) to locate and select the largest Th concentrations for study. These Th anomalies may be good places to test for a spatial correlation between Ti and Th.

4.1 Western Mare Imbrium

Mare Imbrium, located on the nearside and within the PKT (~35° N, 17° W; Figure 1), is the largest mare on the Moon. The Imbrium basin has a diameter of 1160 km (Hiesinger et al., 2000). LP-GRS data (Lawrence et al., 2007) from the western Mare Imbrium show ~5-11 Th

ppm in the basalt flows (Figure 7). Regions in the center of Mare Imbrium show low Th concentrations (<5 ppm) (Figure 7).

Previous workers have determined that Mare Imbrium is 3.91 ± 0.1 Ga in age (Neukum and Ivanov, 1994). Subsequent mare basalt flows have ages between 2 Ga and 3.6 Ga, as determined by crater counting within the respective basalt flows (Hiesinger et al., 2000). In western Mare Imbrium ($\sim 36^\circ$ N, 40° W; Figure 1) there are multiple basalt flows that have an age range of 3.2-3.5 Ga. (Hiesinger et al., 2000).

Clementine RGB images (Eliason et al., 1999) from the western Mare Imbrium show basalt flows enriched in Ti (Figure 15). However, to the southwest of Gruithuisen Domes (Figure 15), Clementine RGB images show a mix of Ti-rich and ilmenite-poor mare basalts (Figure 15; Eliason et al., 1999).

4.2 Maria Serenitatis and Tranquillitatis

Mare Serenitatis is a multi-ring impact basin on the nearside, but it lies outside the PKT (26° N, 18° E; Figure 1). The rings of the Serenitatis basin have diameters from 410 km to 1800 km (Hiesinger et al., 2000). LP-GRS data (Lawrence et al., 2007) from Mare Serenitatis show ~ 3 Th ppm in the basalt flows (Figure 7). Regions near the western rim (outside the area we focus on here) show moderate Th concentrations (~ 8 ppm) (Figure 7).

Previous studies using crater counting have derived an age for the Serenitatis impact of 3.98 ± 0.05 Ga (Neukum and Ivanov, 1994). Basin-filling events took place in the 2.44-3.81 Ga interval (Hiesinger et al., 2000). The southern rim of Mare Serenitatis ($\sim 19^\circ$ N, 26° E; Figure 1) contains mare basalts that were erupted at 2.84-3.81 Ga (Hiesinger et al., 2000).

The prominent impact basin south of Mare Serenitatis is called Tranquillitatis (7° N, 30° E), and contains two basin rings with 700 km and 900 km diameters (Hiesinger et al., 2000). LP-GRS data (Lawrence et al., 2007) from Mare Tranquillitatis show ~3 Th ppm in the basalt flows (Figure 7). A relatively high Th concentration (~10 ppm) relative to the rest of Tranquillitatis occurs near the southwest rim of the basin (Figure 7).

Crater counting has been used to derive 3.39-3.80 Ga ages for the Mare Serenitatis basin-filling basalt flows (Hiesinger et al., 2000). In this study, we focus on the northern region of Mare Tranquillitatis (~19° N, 26° E; Figure 1) where mare basalts have ages of 3.42-3.76 Ga (Hiesinger et al., 2000).

A study within Mare Tranquillitatis by Staid et al. (2011) showed that Ti abundances in the mare there have increased with time. The oldest basalts have between 3 and 5 wt% TiO₂ (Staid et al., 2011). Younger basalts, however, show TiO₂ concentrations of 5-10 wt% (Staid et al., 2011). Clementine RGB imagery (Eliason et al., 1999) shows that Mare Serenatatis is Ti-poor and Mare Tranquillitatis is Ti-rich (Figure 15).

4.3 Southern Oceanus Procellarum

Oceanus Procellarum is a large, elongate expanse of mare basalt on the western nearside (Figure 1). This basin is thought to have been created by a large impact on the nearside, within the PKT (Hiesinger et al., 2003). LP-GRS data (Lawrence et al., 2007) from southern Oceanus Procellarum show ~3-8 Th ppm in the basalt flows (Figure 7).

Based on crater counts, the age of the mare basalts in Oceanus Procellarum is 1.2-3.93 Ga (Hiesinger et al., 2003). The southern region of Oceanus Procellarum (10° S, 50° W; Figure 1) shows ages between 1.33 Ga and 3.74 Ga (Hiesinger et al., 2003).

The Clementine RGB imagery indicates that the mare basalts in Oceanus Procellarum just north of Hansteen Alpha, a non-mare silicic feature (see Chapter 1), show mid- to high-Ti concentrations (Figure 15) (Eliason et al., 1999). Farther north of Hansteen Alpha, there are lower-Ti mare basalts (Figure 15).

4.4 Eastern Mare Nubium

Mare Nubium, located south of Mare Imbrium (21° S, 15° W; Figure 1), is also within the PKT. This basin has a diameter of ~690 km (Hiesinger et al., 2003). LP-GRS data (Lawrence et al., 2007) from eastern Mare Nubium show ~7-15 Th ppm in the basalt flows (Figure 7). Small circular regions of high Th (~11 ppm) occur in the southwest section of Mare Nubium (outside of the area we focus on here) (Figure 7). These could be small impact basins that exposed Th-rich material below the surface (Figure 7).

Crater counting yields a 2.77-3.85 Ga age for the basalt flows filling the Nubium basin (Hiesinger et al., 2003). The mare basalts in the eastern region of Mare Nubium (~15° S, 8° W; Figure 1) are between 3.09 Ga and 3.79 Ga in age (Hiesinger et al., 2003).

In eastern Mare Nubium, Clementine RGB imagery (Nozette et al., 1994; Eliason et al., 1999) shows several large patches of high-Ti mare basalts that are west and southwest of the Lassell Massif feature (Figure 15). Directly north of these high-Ti basalt flows is a large low-Ti basalt flow (Figure 15).

5. Results

5.1 Ilmenite Regression Model

The Apollo mare basalt sample dataset (Appendix 1) shows the expected negative correlation between ilmenite concentration (wt%) and the depth of the 1- μ m absorption in continuum-removed and filtered M³ imagery (Figure 16):

$$\Delta R = -0.0025x + 0.0842 \quad (4).$$

The model accounts for ~93% of the variance ($R^2 = 0.93$) in the data ($N = 53$) with a mean square weighted deviation (*MSWD*) of 0.67 (Figure 16). With this model, we can calculate ilmenite concentrations from the basalts at the high-Th study sites (Table 2) using the ΔR values obtained from the M³ band depth images (Figures 11-14). The persistent vertical striping in all the filtered M³ imagery increases the uncertainty of the ilmenite concentrations we obtain from the M³ data, particularly in Southern Oceanus Procellarum. Our model can predict ilmenite concentrations between 0 and 33.7 ± 1.8 wt%. There is an upper limit on detectable ilmenite abundance because the spectrum for mare basalts containing more than 33.7 ± 1.8 wt% ilmenite is indistinguishable from the spectrum of pure ilmenite.

5.2 Western Mare Imbrium

The band depth image of western Mare Imbrium indicates a mixture of ilmenite-rich and ilmenite-poor basalts (Figure 11). The mare basalt in the eastern portion of the image has ΔR values consistent with 13.1 ± 0.9 to 14.0 ± 0.9 wt% ilmenite (Table 2; Figure 11). South of the highlands, in the northern portion of the image, the mare basalts show zero or trace ilmenite concentrations, except for a couple of flows that have ΔR values consistent with moderate ilmenite concentrations of 7.2 ± 0.9 wt%. The locations of the high-ilmenite and moderate-ilmenite basalts coincide with the high- and low-Ti basalts, respectively, seen in the Clementine

RGB imagery (Eliason et al., 1999) (Figures 11 and 15). Western Mare Imbrium shows moderate-high Th concentrations (~ 5 -11 ppm; Lawrence et al., 2007; Figure 7).

5.3 Mare Serenitatis and Tranquillitatis

Mare Serenitatis is almost entirely devoid of ilmenite except for a few traces (Figure 12). One prominent exception is a basalt flow along the eastern rim of Serenitatis that has 17.0 ± 1.0 wt% ilmenite (Table 2; Figure 12). Mare Tranquillitatis, on the other hand, shows an abundance of ilmenite-rich basalts (Figure 12). Spectra from within Tranquillitatis show ΔR values consistent with 20.5 ± 1.2 to 26.4 ± 1.5 wt% ilmenite (Table 2; Figure 12). The high-ilmenite basalts in Tranquillitatis and along the eastern rim of Serenatatis coincide with the high-Ti basalts seen in Clementine RGB imagery (Eliason et al., 1999) (Figures 12 and 15). Similarly, the low-ilmenite basalts in Serenatatis coincide with the low-Ti basalts seen in Clementine RGB imagery (Eliason et al., 1999) (Figures 12 and 15). Both Mare Tranquillitatis and Serenitatis show low Th concentrations (~ 3 ppm; Lawrence et al., 2007; Figure 7).

5.4 Southern Oceanus Procellarum

The M^3 imagery from southern Oceanus Procellarum still has a large amount of vertical striping, even after applying the frequency filter (Figure 13). Nevertheless, the northern portion of Southern Oceanus Procellarum has ΔR values consistent with low amounts (< 3 wt%) of ilmenite (Figure 13). However, one flow from which spectra were gathered shows a high ilmenite concentration of 13.5 ± 1.0 wt% (Table 2; Figure 13). Farther south, there are basalts with lower ilmenite concentrations (7.4 ± 1.4 to 8.4 ± 1.1 wt%; Figure 13; Table 2). Both the band depth image of southern Oceanus Procellarum and the Clementine RGB image indicate the

presence of low-ilmenite basalts in the same areas (Eliason et al., 1999) (Figures 13 and 15). Southern Oceanus Procellarum shows low-moderate Th concentrations (3-9 ppm; Lawrence et al., 2007; Figure 7).

5.5 Eastern Mare Nubium

Spectra obtained from the northern portion of eastern Mare Nubium, near Lassell Massif, indicate ilmenite-poor basalts with concentrations of 6.6 ± 1.1 wt% ilmenite (Table 2; Figure 14). Farther south, there are higher ilmenite concentrations, ranging from 11.2 ± 0.8 to 15.3 ± 0.9 wt% (Table 2; Figure 14). An expansive basalt flow that appears to be ilmenite-rich lies in the southeast Mare Nubium adjacent to anorthositic highlands material. Spectra from this flow are consistent with ilmenite concentrations of 15.3 ± 0.9 wt% (Table 2; Figure 14). The high-ilmenite basalts in the band depth image coincide with the high-Ti basalts in the Clementine RGB imagery (Eliason et al., 1999) (Figures 14 and 15). Eastern Mare Nubium shows moderate-high Th concentrations (~ 7 -15 ppm; Lawrence et al., 2007; Figure 7).

6. Discussion

The ilmenite concentrations obtained from modal mineralogies of a suite of Apollo basalt samples have shown a good correlation with ΔR values obtained from processed M^3 spectra of the Apollo sampling sites (Figures 10 and 16). This correlation has allowed us to remotely identify locations that contain ilmenite-rich and ilmenite-poor basalts (Figures 11-14). We find that the locations of high-ilmenite basalts spatially correlate with the locations of high-Ti basalts in Clementine RGB imagery, suggesting that our hypothesis for the effect of ilmenite on the 1- μm absorption in basalt is correct (Figures 11-14 and Figure 15).

Interestingly, it appears that there is no direct correlation between Th concentrations from LP-GRS (Figure 7; Lawrence et al., 2007) and the locations of ilmenite-rich basalts we have identified within our study areas. This suggests that the hypothesis that Th concentration correlates with Ti concentration in mare basalts is incorrect or incomplete. We propose that time is the additional factor that needs to be taken into account in order to completely understand the relationships between Th and Ti concentrations in mare basalts. For example, Staid et al. (2011) report that older (3.9-3.1 Gya) mare basalts have low Ti and that younger (3.1-1 Gya) mare basalts have high Ti. Based on this, we suspect that the correlation between high Th and high Ti concentrations should systematically become stronger through time, at least within the PKT, due to the arrival of a Ti- and urKREEP-rich plume at the base of the crust (Zhong et al., 2000, Andrews-Hanna et al., 2014). We argue that such a temporal pattern is evident in our results in the form of a series of eruptive episodes with distinct ilmenite and Th abundances that occurred between 3.74 Gya and 2.62 Gya (Hiesinger et al., 2000; Hiesinger et al., 2003) (Table 2):

- Eruptive episode 1 occurred outside of the PKT, at northern Mare Tranquillitatis (3.74 ± 0.04 to 3.55 ± 0.07 Gya; Hiesinger et al., 2003) (Figure 12). The erupted basalts are low in Th (~ 3 ppm; Lawrence et al., 2007; Figure 7) and rich in ilmenite (20.5 ± 1.2 to 26.4 ± 1.5 wt%; Table 2). The high ilmenite concentrations at this time are inconsistent with the Staid et al. (2011) model.
- Eruptive episode 2 occurred at eastern Mare Nubium (3.49 ± 0.08 to 3.48 ± 0.07 Gya; Hiesinger et al., 2000) (Figure 14). The erupted basalts are high in Th (~ 7 -15 ppm; Lawrence et al., 2007; Figure 7) but contain low to moderate ilmenite concentrations (1.0 ± 0.8 to 6.6 ± 1.1 wt%; Table 2). The low ilmenite concentrations are consistent with the pattern reported by Staid et al. (2011), but the single flow (Figure 14) with

moderate ilmenite concentration is not consistent with the Ti-poor mare basalts expected at this time.

- Eruptive episode 3 occurred at eastern Mare Nubium (3.32 ± 0.11 Gya; Hiesinger et al., 2000) (Figure 14). This group of basalts have high Th (~ 7 -15 ppm; Lawrence et al., 2007; Figure 7) and moderate-to-high ilmenite concentrations (12.2 ± 0.8 to 15.3 ± 0.9 wt%; Table 2). The ilmenite concentrations at this time are inconsistent with the Staid et al. (2011) model.
- Eruptive episode 4 occurred outside of the PKT, at southern Mare Serenitatis, along the eastern rim of the basin (2.99 ± 0.14 Gya; Hiesinger et al., 2003) (Figure 12). These basalts show low Th (~ 3 ppm; Lawrence et al., 2007; Figure 7) and high ilmenite (17.0 ± 1.0 wt%; Table 2) concentrations. Older (3.28 - 3.44 Gya; Hiesinger et al., 2000) mare basalts in southeast Serenitatis, closer to the basin center, show low Th (~ 3 ppm; Lawrence et al., 2007; Figure 7) and low ilmenite concentrations (0 - 3.0 ± 0.2 wt%; Figure 12). Ilmenite concentrations at Mare Serenitatis are consistent with the Staid et al. (2011) model.
- Eruptive episode 5 occurred at Mare Nubium (2.77 ± 0.24 Gya; Hiesinger et al., 2000) (Figure 14). These basalts show high Th (~ 7 -15 ppm; Lawrence et al., 2007; Figure 7) and moderate-to-high ilmenite concentrations (11.2 ± 0.8 wt%; Table 2). The ilmenite concentrations at this time are consistent with the Staid et al. (2011) model.
- Eruptive episode 6 occurred at western Mare Imbrium (2.62 ± 0.17 Gya; Hiesinger et al., 2003) (Figure 11). This episode erupted basalts with high Th (~ 5 -11 ppm; Lawrence et al., 2007; Figure 7) and high ilmenite concentrations (13.1 ± 0.9 to

14.0±0.9 wt%; Table 2). The ilmenite concentrations at this time are consistent with the Staid et al. (2011) model.

The occurrence of two distinct stages of mare volcanism, as suggested by Staid et al. (2011), indicates that a mechanism for supplying Ti-rich mare basalts to the lunar nearside was not active in the early history of the Moon. This is consistent with our results for the PKT and the eruptive episodes described above. However, our results suggest that a transition stage occurred, one that is not part of the Staid et al. (2011) model. The three magmatic stages we propose are defined by their geochemistry, and occurred only within the PKT. The first magmatic stage, similar to the first stage of the Staid et al. (2011) model, would have erupted melts that were depleted in Ti. The second magmatic stage is a transition stage that is suggested by the increase from low to moderate ilmenite concentrations seen in mare basalts within the PKT at ~3.32 Gya. The third magmatic stage, similar to the second stage of Staid et al. (2011), is when Ti- and urKREEP-rich material rose back to the base of the crust in the form of a plume (Zhong et al., 2000; Andrews-Hanna et al., 2014), causing eruption of mare basalts containing larger amounts of Th and ilmenite.

The first magmatic stage within the PKT is associated with low-Th and low-ilmenite mare basalts from Mare Nubium that erupted ~3.5 Gya (Hiesinger et al., 2000). The low-ilmenite concentrations in the Nubium mare basalts are consistent with Staid et al. (2011) who suggested early stage low-Ti basalts erupted between 3.9 and 3.1 Gya. The low-Th and low-Ti abundances in these basalts may be due to sequestration of Ti- and urKREEP-rich material into the degree-1 downwelling proposed by Zhong et al. (2000) (Figure 17).

The second magmatic stage, or the “transition stage”, within the PKT is associated with moderate ilmenite concentrations in western Mare Imbrium basalts which erupted ~3.32 Gya

(Hiesinger et al., 2000). The increase in ilmenite abundance, from low to moderate, suggests that Ti- and urKREEP-rich precursor plumes had begun to arrive at the base of the crust by 3.32 Ga (Figure 17). These precursor plumes presaged the arrival of Ti- and Th-rich melts, associated with the main plume (Zhong et al., 2000; Khan et al., 2014).

The third magmatic stage within the PKT is associated with high-Th and high-ilmenite mare basalts from Mare Nubium and Imbrium that erupted after 3.32 Gya (Hiesinger et al., 2000). Our determination of high ilmenite abundances for these basalts is consistent with Staid et al. (2011) who show that late stage high-Ti basalts erupted between 3.1 and 1 Gya. The geochemistry of these basalts suggest that the main plume, enriched in Ti- and urKREEP-rich material, arrived at the base of the crust from the core-mantle boundary at this time. The rising plume would have generated most melts through adiabatic melting. In addition, the plume would have supplied heat that would have also contributed to the generation of enriched partial melts that subsequently erupted at the surface (Figure 17).

It is important to note, however, that these three magmatic episodes are not applicable to areas outside of the PKT. This is illustrated by our results for Tranquillitatis, which lies outside the PKT. At Tranquillitatis, we show that high-ilmenite basalts were erupted at ~3.8 Gya (Hiesinger et al., 2003), at a time when low-ilmenite basalts were being erupted in the PKT. In addition, at eastern Serenitatis and Tranquillitatis, low-Th basalts were erupted during the time of our third magmatic stage, rather than the high-Th basalts that erupted in the PKT. The presence of old, Ti-rich but Th-poor mare basalts at Tranquillitatis and eastern Serenitatis suggests that there was little or no interaction with urKREEP, but that there was interaction with Ti-rich material.

We propose two possible scenarios to explain this. In the first, the Ti-rich but Th-poor mare basalts would have erupted after (or during) the degree-1 downwelling (Zhong et al., 2000; Parmentier et al., 2002; Khan et al., 2014) that affected the nearby PKT. In this case, the Ti originated from interaction with Ti-rich urKREEP that was not completely removed by the downwelling and that remained at the base of the crust. The urKREEP may have never existed at these locations, or it was removed by the degree-1 downwelling, redistributing that material and concentrating it at the PKT. In the second scenario, the Ti-rich but Th-poor mare basalts would have erupted prior to the degree-1 downwelling. In this case, while the Ti-rich urKREEP may eventually have been partially or completely removed by the downwelling, it existed in the subsurface at the time of melt generation. However, the lack of Th would imply that urKREEP did not exist at all at Tranquillitatis and eastern Serenitatis. These hypotheses are testable if both the timing of mare basalt volcanism and the degree-1 downwelling can be constrained. While the former is known (3.9-1 Gya; Hiesinger et al., 2000; Hiesinger et al., 2003), the latter is not.

7. Conclusions

We have mapped ilmenite concentrations in mare basalts using remote sensing techniques and M^3 data for the first time. Using Apollo basalt samples, we were able to develop a linear regression model that accurately predicts the ilmenite concentrations of mare basalts based on remotely sensed spectra. The effectiveness of the linear regression is seen in the high R^2 value (93%), and by low 1-sigma uncertainties in the slope and y-intercept.

Ilmenite-rich mare basalts are primarily concentrated on the nearside of the Moon. By comparing the occurrence of Th-rich and Th-poor mare basalts with ilmenite concentrations obtained from those basalts using remote sensing, we have determined that several eruptive

episodes, each with different geochemical signatures, occurred. These episodes can be grouped into three stages. Within the PKT, the first magmatic stage consisted of ilmenite- and Th-poor mare basalts within Mare Nubium. The lack of Ti and Th can be explained by a downwelling of these materials early in lunar history (Zhong et al., 2000; Parmentier et al., 2002; Khan et al., 2014). Starting at ~3.32 Gya, however, we see the transition from low to high ilmenite concentrations, as well as the transition from low Th concentrations to high Th concentrations within the PKT. This transition stage could indicate that pre-cursor plumes rich in both Ti and urKREEP were arriving at the base of the lunar crust at this time. The third magmatic stage consisted of ilmenite- and Th-rich mare basalts within Mare Nubium and Imbrium. The mechanism for the source and timing of these ilmenite- and Th-rich eruptions could be the return of Ti- and urKREEP-rich material in the form of a plume rising to the base of the lunar crust (Zhong et al., 2000; Parmentier et al., 2002; Shearer et al., 2006; Khan et al., 2014).

Areas outside of the PKT, including Mare Serenitatis and Tranquillitatis, however, do not fit this history. The presence of ilmenite-rich basalts at Tranquillitatis suggests that a source for the ilmenite-rich basalts must have been present prior to the arrival of the plume (~3.32 Gya). In addition, Mare Serenitatis contains low-Th basalts that were erupted at the time when basalts rich in Th and ilmenite were being erupted elsewhere. We propose two possible scenarios. In the first, the Ti-rich but Th-poor mare basalts would have erupted after (or during) the degree-1 downwelling (Zhong et al., 2000; Parmentier et al., 2002; Khan et al., 2014) that affected the nearby PKT. In this case, the Ti originated from interaction with Ti-rich material that was not completely removed by the downwelling and that remained at the base of the crust. In the second scenario, the Ti-rich but Th-poor mare basalts would have erupted prior to the degree-1 downwelling. The lack of Th would imply that KREEP did not exist at all at these locations.

This would explain why we see ilmenite-rich basalts at Mare Tranquillitatis and eastern Serenitatis while the other sites show low-to-moderate ilmenite concentrations.

The results shown here suggest a more complicated eruption history than that proposed by Staid et al. (2011). However, because our study only sampled a relatively small area of the nearside, the eruption history may be even more complicated than what we propose here. A larger study of all the nearside maria that considers the occurrence of both Ti and Th as a function of age is required to accurately determine how many eruption episodes occurred and if a relationship exists between Th and Ti concentrations in younger mare basalts. Such a study could determine where and when Ti-rich melts pooled at the base of the crust, like the Ti-rich melts we suggest were associated with Tranquillitatis.

References

- Adams, J.B., 1974, Visible and near-infrared diffuse reflectance spectra of pyroxenes as applied to remote sensing of solid objects in the solar system: *Journal of Geophysical Research*, v. 79, no. 32, p. 4829-4836, doi: 10.1029/JB079i032p04829.
- Allégre, C.J., Manhés, G., and Göpel, C., 1995, The Age of the Earth: *Geochimica et Cosmochimica Acta*, v. 59, no. 8, p. 1445-1456.
- Andrews-Hanna, J.C., Besserer, J., Head III, J.W., Howett, C.J.A., Kiefer, W.S., Lucey, P.J., McGovern, P.J., Melosh, H.J., Neumann, G.A., Phillips, R.J., Schenk, P.M., Smith, D.E., Solomon, S.C., and Zuber, M.T., 2014, Structure and evolution of the lunar Procellarum region as revealed by GRAIL gravity data: *Nature*, v. 514, no. 7520, p. 68-71.
- Arkani-hamed, J. and Pentecost, A., 2001, On the Source Region of the Lunar Mare Basalt: *Journal of Geophysical Research*, v. 106, p. 14691-14700.
- Binder, A.B., 1998, Lunar Prospector: Overview: *Science*, v. 281, p. 1475-1476.
- Boardman, J.W., Pieters, C.M., Green, R.O., Lundeen, S.R., Varanasi, P., Nettles, J., Petro, N., Isaacson, P., Besse, S., and Taylor, L.A., 2011, Measuring moonlight: An overview of the spatial properties, lunar coverage, selenolocation, and related Level 1B products of the Moon Mineralogy Mapper: *Journal of Geophysical Research*, v. 116, p. 1-15, doi: 10.1029/2010JE003730.

- Canup, R.M. and Asphaug, E., 2001, Origin of the Moon in a giant impact near the end of the Earth's formation: *Nature*, v. 412, no. 6848, p. 708-712, doi: 10.1038/35089010.
- Cooper, C.D. and Mustard, J.F., 1999, Effects of Very Fine Particle Size on Reflectance Spectra of Smectite and Palagonitic Soil: *Icarus*, v. 142, p. 557-570.
- Davis, J.C. and Sampson, R.J., 2002, *Statistics and Data Analysis in Geology (Vol. 3)*: Wiley (New York). 656 p.
- Eliason, E.M., McEwen, A.S., Robinson, M.S., Lee, E.M., Becker, T.L., Gaddis, L., Weller, L.A., Isbell, C.E., Shinaman, J.R., Duxbury, T., and Malaret, E., 1999, Clementine: A Global Multi-Spectral Map of the Moon from the Clementine UVVIS Imaging Instrument: *Proceedings of the 30th Lunar and Planetary Science Conference*, p. 1933-1934.
- Elkins-Tanton, L.T. and Grove, T.L., 2011, Water in the lunar magma ocean: *A Wet Vs. Dry Moon: Exploring Volatile Reservoirs and Implications for the Evolution of the Moon and Future Exploration*, p. 14.
- Elkins-Tanton, L.T. and Bercovici, D., 2014, Contraction or expansion of the Moon's crust during magma ocean freezing?: *Proceedings of the 45th Lunar and Planetary Science Conference*, p. 1128.

- Hagerty, J.J., Lawrence, D.J., and Hawke, B.R., 2011, Thorium abundances of basalt ponds in South Pole-Aitken basin: Insights into the composition and evolution of the far side lunar mantle: *Journal of Geophysical Research*, v. 116, no. 6, doi: 10.1029/2010JE003723.
- Hiesinger, H., Jaumann, R., Neukum, G., and Head III, J.W., 2000, Ages of mare basalts on the lunar nearside: *Journal of Geophysical Research*, v. 105, p. 239-275.
- Hiesinger, H., Head III, J.W., Wolf, U., Jaumann, R., and Neukum, G., 2003, Ages and stratigraphy of mare basalts in Oceanus Procellarum, Mare Nubium, Mare Cognitum, and Mare Insularum: *Journal of Geophysical Research*, v. 108, no. E7, doi: 10.1029/2002JE001985.
- Hiesinger, H. and Head III, J.W., 2006, New Views of Lunar Geoscience: An Introduction and Overview: *Reviews in Mineralogy and Geochemistry*, v. 60, p 1-81.
- Isaacson, P., Besse, S., Petro, N., and Nettles, J., 2011a, M³ overview and working with M³ data: *Proceedings of the 42nd Lunar and Planetary Science Conference*, Conference Workshop.
- Isaacson, P.J., Pieters, C.M., Hiroi, T., Liu, Y., Dhingra, D., Klima, R.L., and Taylor, L.A., 2011b, Reflectance Spectroscopy of Ilmenite: New Constraints from Apollo Sample Measurements: *Proceedings of the 42nd Lunar and Planetary Science Conference*, p. 2130.

Isaacson, P.J., Pieters, C.M., Besse, S., Clark, R.N., Head, J.W., Klima, R.L., Mustard, J.F., Petro, N.E., Staid, M.I., Sunshine, J.M., Taylor, L.A., Thaisen, K.G., and Tompkins, S., 2011c, Remote compositional analysis of lunar olivine-rich lithologies with Moon Mineralogy Mapper (M³) spectra: *Journal of Geophysical Research*, v. 116, p. 1-17, doi: 10.1029/2010JE003731.

Jensen, J.R., 2005, *Introductory Digital Image Processing: A Remote Sensing Perspective* (3rd ed.): Pearson Prentice Hall (New Jersey), 526 p.

Jolliff, B.L., Wiseman, S.A., Lawrence, S.J., Tran, T.N., Robinson, M.S., Sato, H., Hawke, B.R., Scholten, F., Oberst, J., Hiesinger, H., van der Bogert, C.H., Greenhagen, B.T., Glotch, T.D., and Paige, D.A., 2011, Non-mare silicic volcanism on the lunar farside at Compton–Belkovich: *Nature Geoscience*, v. 4, no. 8, p. 566-571, doi: 10.1038/ngeo1212.

Jolliff, B.L., Zanetti, M., Shirley, K.A., Accardo, N.J., Lauber, C., Robinson, M.S., and Greenhagen, B. T., 2012, Compton-Belkovich Volcanic Complex: *Proceedings of the 43rd Lunar and Planetary Science Conference*, p. 2097.

Khan, A., Connolly, A.D., Pommier, A., and Noir, J., 2014, Geophysical evidence for melt in the deep lunar interior and implications for lunar evolution: *Journal of Geophysical Research Planets*, v. 119, doi:10.1002/2014JE004661.

- Klima, R., Cahill, J., Hagerty, J., and Lawrence, D., 2013, Remote detection of magmatic water in Bullialdus Crater on the Moon: *Nature Geoscience*, v. 6, no. 9, p. 737-741, doi: 10.1038/ngeo1909.
- Lawrence, D.J., Feldman, W.C., Barraclough, B.L., Binder, A.B., Elphic, R.C., Maurice, S., Miller, M.C., and Prettyman, T.H., 2000, Thorium abundances on the lunar surface: *Journal of Geophysical Research*, v. 105, no. E8, p. 20307-20331, doi: 10.1029/1999JE001177.
- Lawrence, D.J., 2003, Small-area thorium features on the lunar surface: *Journal of Geophysical Research*, v. 108, no. E9, doi: 10.1029/2003JE002050.
- Lawrence, D.J., Puetter, R.C., Elphic, R.C., Feldman, W.C., Hagerty, J.J., Prettyman, T.H., and Spudis, P.D., 2007, Global spatial deconvolution of Lunar Prospector Th abundances: *Geophysical Research Letters*, v. 34, no. 3, p. 1-5, doi: 10.1029/2006GL028530.
- Lucey, P., Korotev, R.L., Gillis, J.J., Taylor, L.A., Lawrence, D., Campbell, B.A., Elphic, R., Feldman, B., Hood, L.L., Hunten, D., Mendillo, M., Noble, S., Papike, J.J., Reedy, R.C., Lawson, S., Prettyman, T., Gasnault, O., and Maurice, S., 2006, Understanding the Lunar Surface and Space-Moon Interactions: *Reviews in Mineralogy and Geochemistry*, v. 60, p. 83-219.

Lundeen, S., McLaughlin, S., and Alanis, R., 2011, Moon Mineralogy Mapper data product (JPL D-39032): Jet Propulsion Laboratory, p. 1-111, http://pds-imaging.jpl.nasa.gov/documentation/M3_DPSIS.PDF.

Meyer, C., 2012, *The Lunar Sample Compendium* <http://curator.jsc.nasa.gov/lunar/lsc/index.cfm>.

Muehlberger, W.R., Batson, R.M., Boudette, E.L., Duke, C.M., Eggleton, R.E., Elston, A.W., England, A.W., Freeman, V.L., Hait, M.H., Hall, T.A., Head, J.W., Hodges, C.A., Holt, H.E., Jackson, E.D., Jordan, J.A., Larson, K.B., Milton, D.J., Reed, V.S., Rennilson, J.J., Schaber, G.G., Schafer, J.P., Silver, L.T., Stuart-Alexander, D., Sutton, R.L., Swann, G.A., Tyner, R.I., Ulrich, G.E., Wilshire, H.G., Wolfe, E.W. and Young, J.W., 1972, Preliminary Geologic Investigation of the Apollo 16 Landing Site, In: *Apollo 16 Preliminary Science Report*: National Aeronautics and Space Administration. p. 6-1-7-1.

Muehlberger, W. R., Batson, R. M., Cernan, E. A., Freeman, V. L., Hait, M. H., Holt, H. E., Howard, K. A., Jackson, E. D., Larson, K. B., Reed, V. S., Rennilson, J. J., Schmitt, H. H., Scott, D. H., Sutton, R. L., Stuart-Alexander, D., Swann, G. A., Trask, N. J., Ulrich, G. E., Wilshire, H. G., and Wolfe, E. W., 1973, Preliminary Geologic Investigation of the Apollo 17 Landing Site, In: *Apollo 17 Preliminary Science Report*: National Aeronautics and Space Administration. p. 6-1-7-1.

- Nemchin, A., Timms, N., Pidgeon, R., Geisler, T., Reddy, S., and Meyer, C., 2009, Timing of crystallization of the lunar magma ocean constrained by the oldest zircon: *Nature Geoscience*, v. 2, p. 133-136, doi: 10.1038/ngeo417.
- Neukum, G. and Ivanov, B. A., 1994, Crater size distributions and impact probabilities on Earth from lunar, terrestrial planets, and asteroid cratering data, In: *Hazards Due to Comets and Asteroids*: University of Arizona Press (Tucson), p. 359-416.
- Nozette, S., Rustan, P., Pleasance, L.P., Kordas, J.F., Lewis, I.T., Park, H.S., Priest, R.E., Horan, D.M., Regeon, P., Lichtenberg, C.L., Shoemaker, E.M., Eliason, E.M., McEwen, A.S., Robinson, M.S., 1994, The Clementine Mission to the Moon: Scientific Overview: *Science*, v. 266 , no. 5192 , p. 1835-1839, doi: 10.1126/science.266.5192.1835 .
- Parmentier, E.M., Zhong, S., and Zuber, M.T., 2002, Gravitational differentiation due to initial chemical stratification: origin of lunar asymmetry by the creep of dense KREEP?: *Earth and Planetary Science Letters*, v. 201, p. 473-480.
- Pieters, C.M., 1983, Strength of mineral absorption features in the transmitted component of near-infrared reflected light: First results from RELAB. *Journal of Geophysical Research*, v. 88, p. 9534-9544.
- Salisbury, J. W., Walter, L. S., Vergo, N., and D'Aria, D. M., 1991, *Infrared (2.1- 25 micrometers) Spectra of Minerals*: Johns Hopkins University Press, 294 p.

Schminke, H-U., 2004, *Volcanism*: Springer-Verlag (Berlin/Heidelberg), 324 p.

Schultz, P.H. and Spudis, P.D., 1983, Beginning and end of lunar mare volcanism: *Nature*, v. 302, no. 5905, p. 233-236.

Shearer, C.K., Hess, C.P., Wieczorek, M.A., Pritchard, M.E., Parmentier, E.M., Borg, L.E., Longhi, J., Elkins-Tanton, L.T., Neal, C.R., Antonenko, I., Canup, R. M., Halliday, A. N., Grove, T.L., Hager, B.H., 2006, Thermal and Magmatic Evolution of the Moon: *Reviews in Mineralogy and Geochemistry*, v. 60, no. 1, p. 365-518, doi: 10.2138/rmg.2006.60.4.

Shoemaker, E. M., Bailey, N. G., Batson, R. M., Dahlem, D. H., Foss, T. H., Grolier, M. J., Goddard, E. N., Hoit, M. H., Holt, H. E., Larson, K. B., Rennilson, J. J., Schaber, G. G., Schleicher, D. L., Schmitt, H. H., Sutton, R. L., Swann, G. A., Waters, A. C., and West, M. N., 1969, Geologic Setting of the Lunar Samples Returned by the Apollo 11 Mission, In: *Apollo 11 Preliminary Science Report*: National Aeronautics and Space Administration, p. 41-84.

Shoemaker, E.M., Batson, R.M., Bean, A.L., Conrad, Jr., C., Dahlem, D.H., Goddard, E.N., Hoit, M.H., Larson, K.B., Schaber, G.G., Schleicher, D.L., Sutton, R.L., Swann, G.A., and Waters, A.C., 1970, Preliminary Geologic Investigation of the Apollo 12 Landing

Site, In: *Apollo 12 Preliminary Science Report*: National Aeronautics and Space Administration, p. 113-156.

Snyder, G.A. and Taylor, L.A., 1991, In Search of the urKREEP Reservoir: Trapped Residual Lunar Magma Ocean Liquid in the interstices of Upper Mantle Cumulates: *Proceedings of the 22nd Lunar and Planetary Science Conference*, p. 1287.

Staid, M.I., Pieters, C.M., Besse, S., Boardman, J., Dhingra, D., Green, R., Head, J.W., Isaacson, P., Klima, R., Kramer, G., Mustard, J.M., Runyon, C., Sunshine, J., and Taylor, L.A., 2011, The mineralogy of late stage lunar volcanism as observed by the Moon Mineralogy Mapper on Chandrayaan-1: *Journal of Geophysical Research*, v. 116, p. 1-15, doi: 10.1029/2010JE003735.

Standart, D.L. and Hurtado, J.M., 2012, Non-Polar Lunar OH and Water Using the Moon Mineralogy Mapper: *EOS* (Proceedings of the 2012 Fall Meeting AGU Meeting, San Francisco, CA, December 3-7, 2012), abstract #P53A-2058.

Swann, G.A., Bailey, N.G., Batson, R.E., Eggleton, R.E., Hait, M.H., Holt, H.E., Larson, K.B., McEwen, M.C., Mitchell, E.D., Schaber, G.G., Schafer, J.B., Shepard, A.B., Sutton, R. L., Trask, N.J., Ulrich, G.E., Wilshire, H.G., and Wolfe, E.W., 1971, Preliminary Geologic Investigations of the Apollo 14 Landing Site, In: *Apollo 14 Preliminary Science Report*: National Aeronautics and Space Administration. p. 39-86.

Swann, G.A., Bailey, N.G., Batson, R.M., Freeman, V.L., Hait, M.H., Head, J.W., Holt, H.E., Howard, K.A., Irwin, J.B., Larson, K.B., Muehlberger, W.R., Reed, V.S., Rennilson, J.J., Schaber, G.G., Scott, D.R., Silver, L.T., Sutton, R.L., Ulrich, G.E., Wilshire, H.G., and Wolfe, E. W., 1972, Preliminary Geologic Investigation of the Apollo 15 Landing Site, In: *Apollo 15 Preliminary Science Report*: National Aeronautics and Space Administration. p. 5-1-6-1.

Touboul, M., Kleine, T., Bourdon, B., Palme, H., and Wieler, R., 2007, Late formation and prolonged differentiation of the Moon inferred from W isotopes in lunar metals: *Nature*, v. 450, no. 7173, p. 1206-1209, doi: 10.1038/nature06428.

Warren, P.H., 1985, The Magma Ocean Concept and Lunar Evolution: *Annual Reviews of Earth and Planetary Sciences*, v. 13, p. 201-240.

Warren, P.H., 2001, Early lunar crustal genesis: The ferroan anorthosite epsilon-neodymium paradox as a possible result of crustal overturn: 64th Annual *Meteoritical Society Meeting*, p. 5391.

Wasserburg, G.J., 1987, Isotopic abundances: inferences on solar system and planetary evolution: *Earth and Planetary Science Letters*, v. 86, p. 129-173.

Whitten, J., Head, J.W., Staid, M., Pieters, C.M., Mustard, J., Clark, R., Nettles, J., Klima, R.L., and Taylor, L., 2011, Lunar mare deposits associated with the Orientale impact basin:

New insights into mineralogy, history, mode of emplacement, and relation to Orientale Basin evolution from Moon Mineralogy Mapper (M³) data from Chandrayaan-1: *Journal of Geophysical Research*, v. 116, no. E00G09, doi: 10.1029/2010JE003736.

Wieczorek, M.A. and Phillips, R.J., 2000, The “Procellarum KREEP Terrane”: Implications for mare volcanism and lunar evolution: *Journal of Geophysical Research*, v. 105, no. E8, p. 417-420

Wieczorek, M.A., Jolliff, B.A., Khan, A., Pritchard, M.E., Weiss, B.P., Williams, J.G., Hood, L.L., Richter, K., Neal, C.R., Shearer, C.K., McCallum, I.S., Tompkins, S., Hawke, B. R., Peterson, C., Gillis, J.J., and Bussey, B., 2006, The Constitution and Structure of the Lunar Interior: *Reviews in Mineralogy and Geochemistry*, v. 60, p. 221-364, doi: 10.2138/rmg.2006.60.3.

York, D., 1969, Least-squares fitting of a straight line: *Earth Planetary Science Letters*, v. 5, p. 320-324.

York, D., Evenson, N., Martinez, M., and Delgado, J., 2004, Unified equations for the slope, intercept, and standard errors of the best straight line: *American Journal of Physics*. v. 72 no. 3. p. 367-375.

Zhong, S., Parmentier, E.M., and Zuber, M.T., 1999, Early Lunar Evolution and the Origin of Asymmetric Distribution of Mare Basalts: *Proceedings of the 30th Lunar and Planetary Science Conference*, p. 1789.

Zhong, S., Parmentier, E.M., and Zuber, M.T., 2000, A dynamic origin for the global asymmetry of lunar mare basalts: *Earth and Planetary Science Letters*, v. 177, no. 3-4, p. 131-140, doi: 10.1016/S0012-821X(00)00041-8.

Zuber, M.T., Smith, D.E., Watkins, M.M., Asmar, S.W., Konopliv, A.S., Lemoine, F.G., Melosh, H.J., Neumann, G. a, Phillips, R.J., Solomon, S.C., Wieczorek, M. a, Williams, J.G., Goossens, S.J., and Kruizinga, G., 2013, Gravity field of the Moon from the Gravity Recovery and Interior Laboratory (GRAIL) mission: *Science*, v. 339, no. 6120, p. 668-671, doi: 10.1126/science.1231507.

TABLE 1. SUMMARY OF M ³ DATA				
Region	Image	Date Acquired	Resolution* (m)	Optical Period*
Mare Serenitatis & Tranquillitatis	M3G20090107T011405	01/07/2009	140	OP1A
	M3G20090107T130225	01/07/2009	140	OP1A
	M3G20090203T135512	02/03/2009	140	OP1B
	M3G20090203T160452	02/03/2009	140	OP1B
	M3G20090203T175131	02/03/2009	140	OP1B
	M2G20090203T200051	02/03/2009	140	OP1B
Eastern Mare Nubium	M3G20090206T065053	02/06/2009	140	OP1B
	M3G20090206T050647	02/06/2009	140	OP1B
	M3G20090206T105850	02/06/2009	140	OP1B
	M3G20090206T092112	02/06/2009	140	OP1B
	M3G20090206T124510	02/06/2009	140	OP1B
	M3G20090206T145451	02/06/2009	140	OP1B
	M3G20090206T164110	02/06/2009	140	OP1B
	M3G20090206T185403	02/06/2009	140	OP1B
Southern Oceanus Procellarum	M3G20090418T151350	04/18/2009	280	OP2A
	M3G20090516T040653	05/16/2009	280	OP2B
	M3G20090418T190900	04/18/2009	280	OP2A
	M3G20090418T172221	04/18/2009	280	OP2A
Western Mare Imbrium	M3G20090208T114652	02/08/2009	140	OP1B
	M3G20090208T135610	02/08/2009	140	OP1B
	M3G20090208T160125	02/08/2009	140	OP1B
	M3G20090208T175211	02/08/2009	140	OP1B
	M3G20090208T194335	02/08/2009	140	OP1B
	M3G20090208T214811	02/08/2009	140	OP1B

* From Boardman et al. (2011).

TABLE 2. QUANTIFIED ILMENITE RESULTS			
Region	Location*	Mean ΔR^{**}	Ilmenite (wt%) [†]
Mare Serenitatis & Tranquillitatis	1	0.042±0.012	17.0±1.0
	2	0.026±0.014	23.4±1.3
	3	0.018±0.020	26.4±1.5
	4	0.033±0.017	20.5±1.2
Eastern Mare Nubium	1	0.056±0.016	11.2±0.8
	2	0.068±0.017	6.6±1.1
	3	0.046±0.008	15.3±0.9
	4	0.054±0.014	12.2±0.8
Southern Oceanus Procellarum	1	0.050±0.023	13.5±1.0
	2	0.054±0.015	12.2±0.8
	3	0.066±0.024	7.4±1.4
	4	0.063±0.020	8.4±1.1
Western Mare Imbrium	1	0.049±0.017	14.0±0.9
	2	0.052±0.017	13.1±0.9
	3	0.066±0.015	7.2±0.9
	4	0.066±0.015	7.2±0.9

* - Locations correspond to white numbers in Figure 11-14.

** - ΔR -band depth of 1- μm absorption in M^3 imagery (Equation 1).

† - wt%-weight percentage.

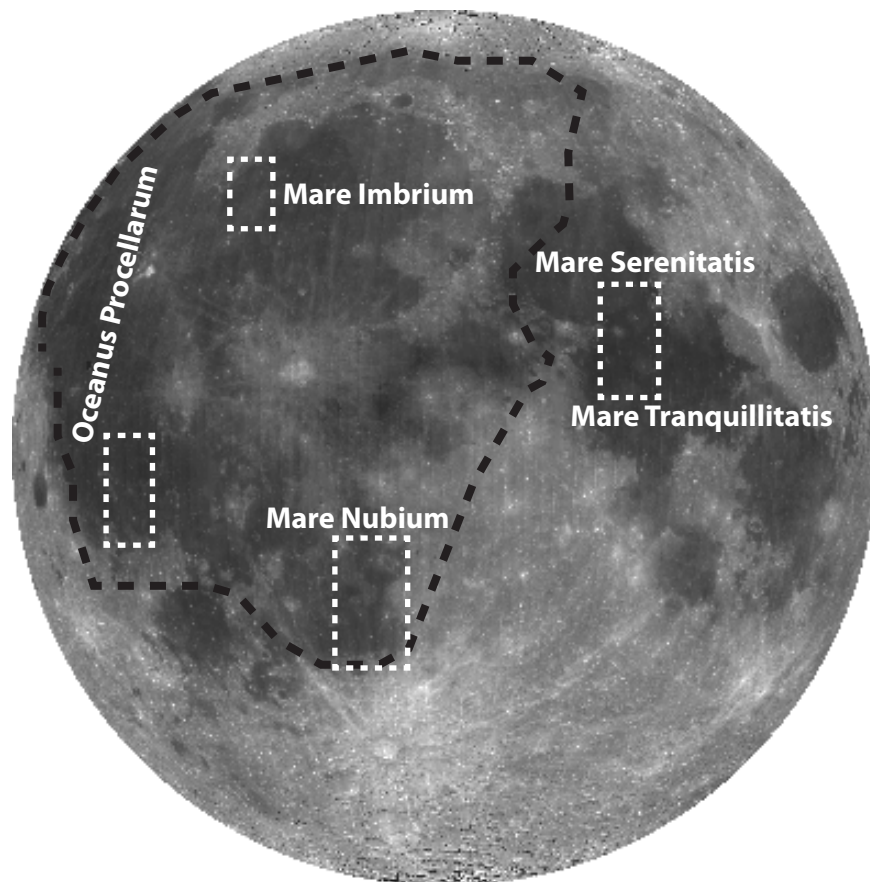


Figure 1: Clementine global albedo image showing target sites (labeled with white text and white dashed boxes). The Procellarum KREEP Terrane boundary is shown by the black dashed polygon. From Lunar and Planetary Institute (<http://www.lpi.usra.edu/lunar/missions/clementine/images/>).

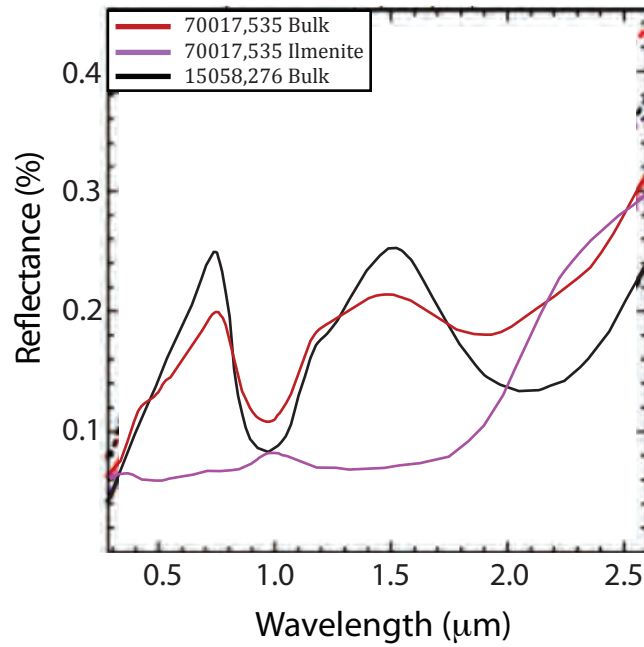


Figure 2: Bidirectional reflectance spectra of bulk Apollo samples and coarse- and fine-grained ilmenite separates. Ilmenite-rich basalt samples shown in red, ilmenite-poor basalt shown in black, and pure ilmenite is shown in purple. Notice that the 1- μm absorption in the basalt samples (black vs. red) becomes shallower when more ilmenite is in the basalt sample. From Isaacson et al. (2011b).

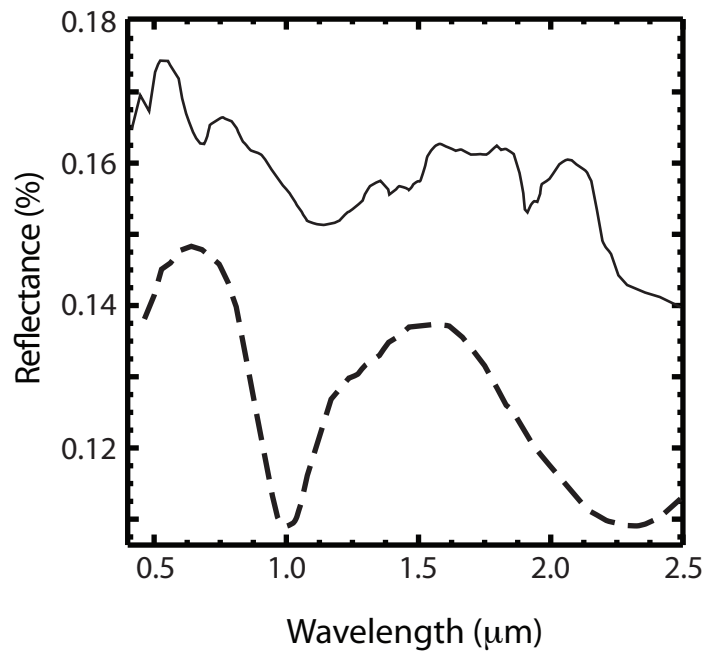


Figure 3: Reflectance spectra of basalt (dashed line) and anorthosite (solid line) samples (Salisbury et al., 1991). The 1- μm absorption that we measure in this work is formed by a charge transfer between ferric and ferrous iron (Jensen, 2005). Notice the increased depth in the 1- μm absorption depth. Mare basalts with varying 1- μm absorption depths will indicate varying ilmenite abundances.

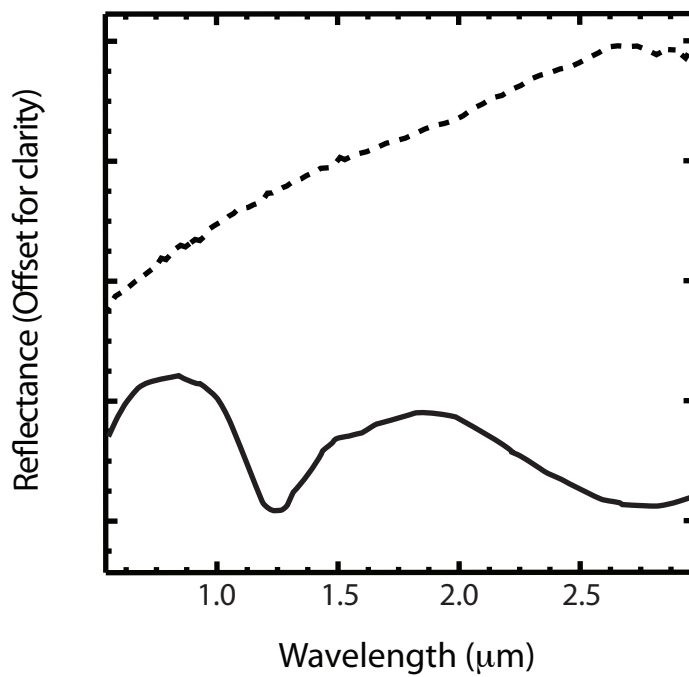


Figure 4: M³ reflectance spectra from Mare Imbrium basalts on the nearside. Solid line represents mare basalt spectrum without “reddening” effect. Dashed line shows mare basalt spectrum with the “reddening” effect. Notice the increased slope in the dashed spectrum, compared to the solid spectrum.

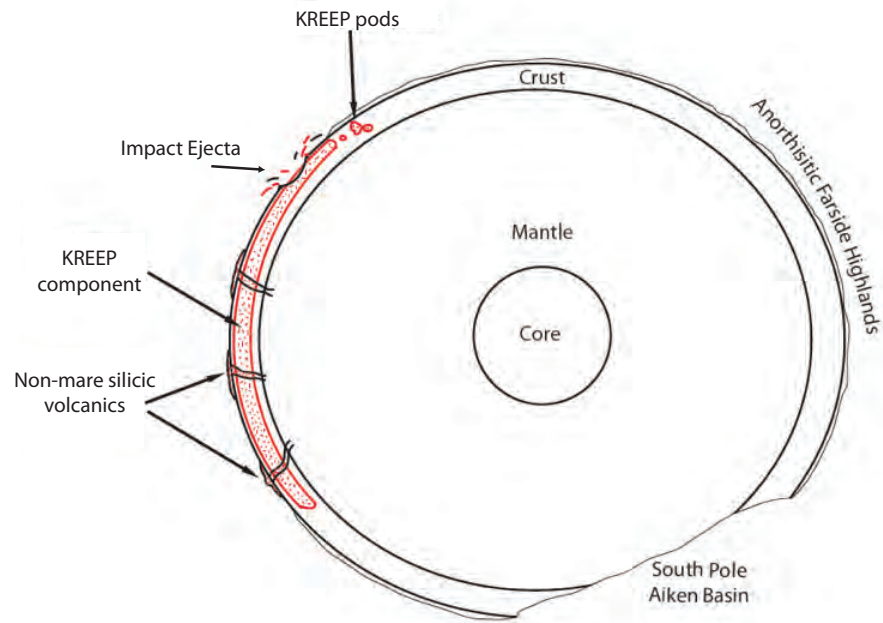


Figure 5: Schematic cross-section showing the spatial extent of KREEP within the lunar crust ~1-3 billion years ago. Mare basalts on the nearside could possibly have been enriched by KREEP as their melts were mixed with the KREEP layer. Modified from Wieczorek et al. (2006).

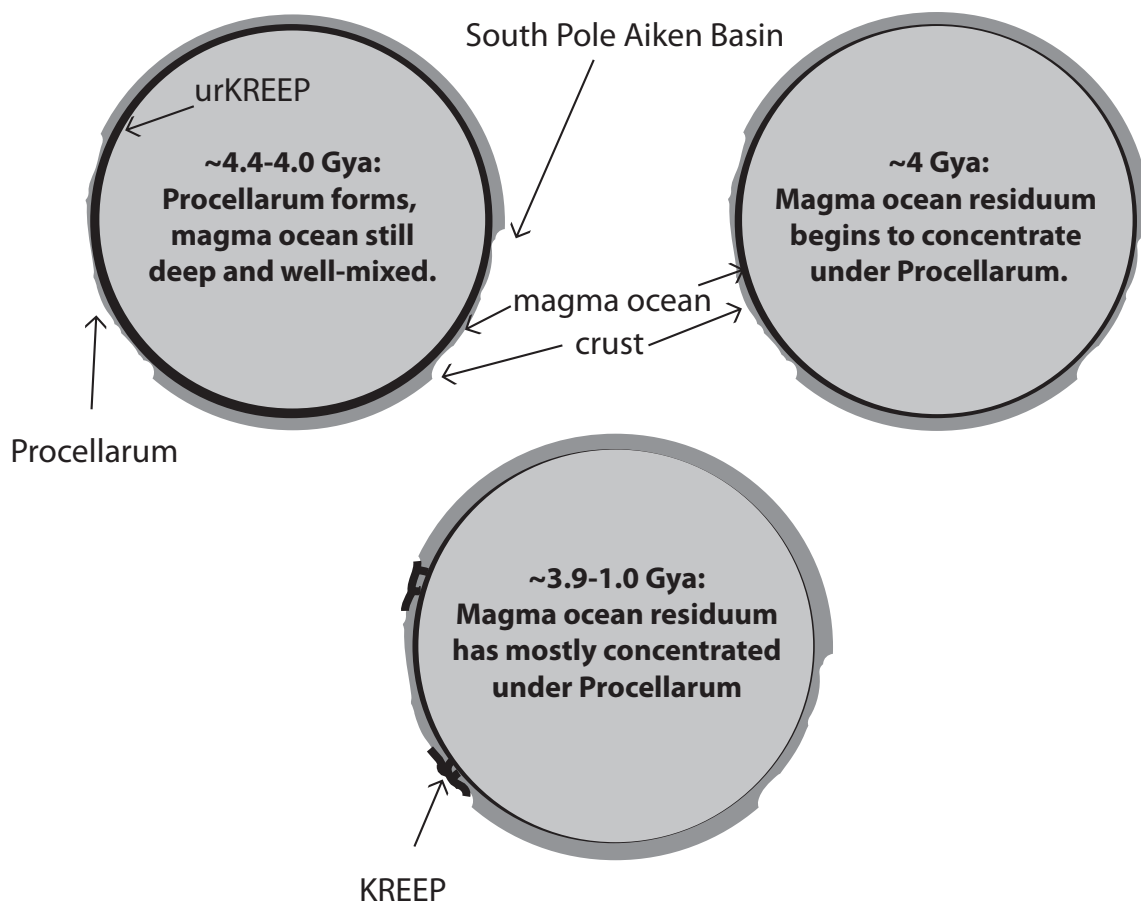


Figure 6: Progressive development of the lunar magma ocean. By the time the South Pole Aitken Basin impact occurred (Time 1), most of the lunar magma ocean had already accumulated under the thinner crust on the nearside. From Shearer et al. (2006).

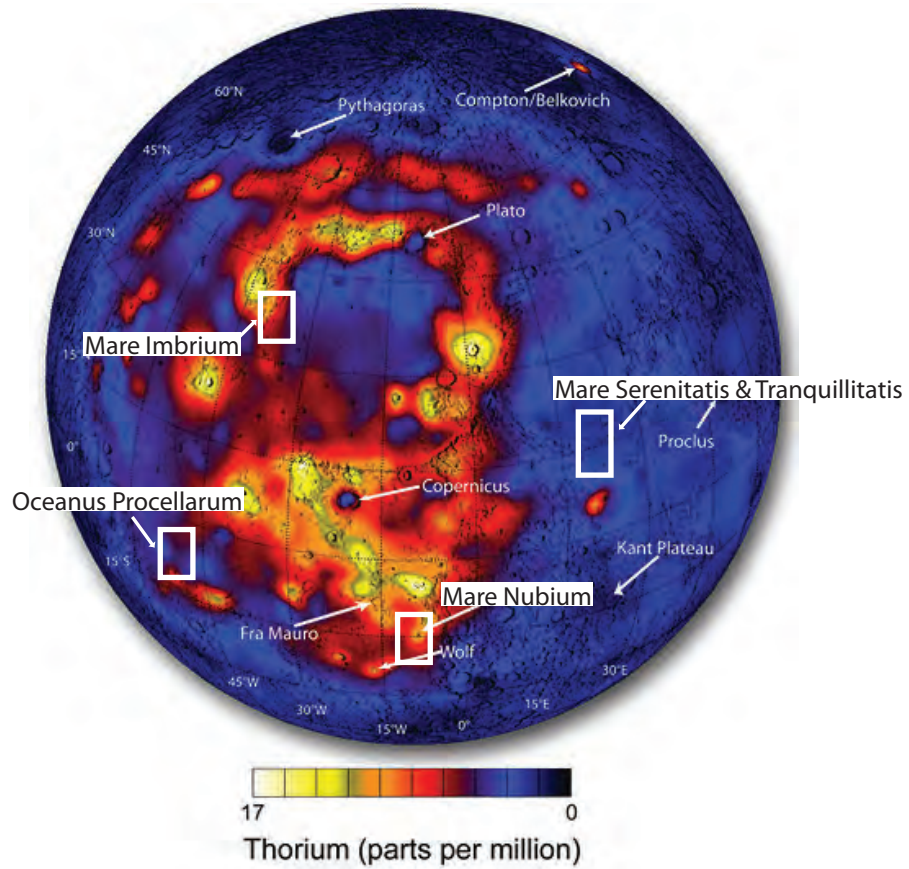


Figure 7: LP-ThGRS data showing nearside thorium concentrations. White boxes indicate target sites: Southern Oceanus Procellarum (lower left), West Mare Nubium (lower right), West Mare Imbrium (upper left), and Mare Tranquillitatis and Serenitatis (middle right). From Lawrence et al. (2007).

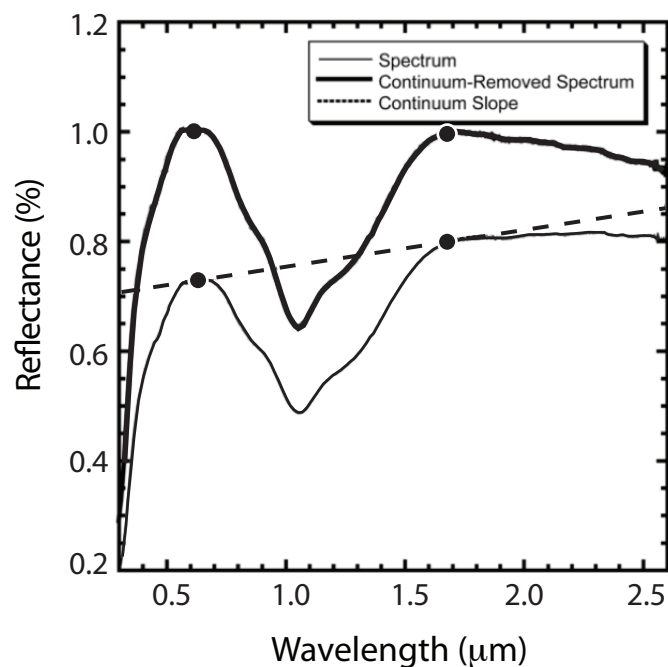


Figure 8: Continuum slope removal process. The thin, solid line shows the original spectrum of olivine before continuum removal. The dashed line is the continuum slope defined by the line connecting the band shoulders (solid dots) of the ca. 1.1 μm absorption. The continuum slope is then used to produce a continuum-removed spectrum by dividing the original spectrum by the continuum slope. The bold, solid line shows the resulting continuum-removed spectrum. Modified from Isaacson et al. (2011).

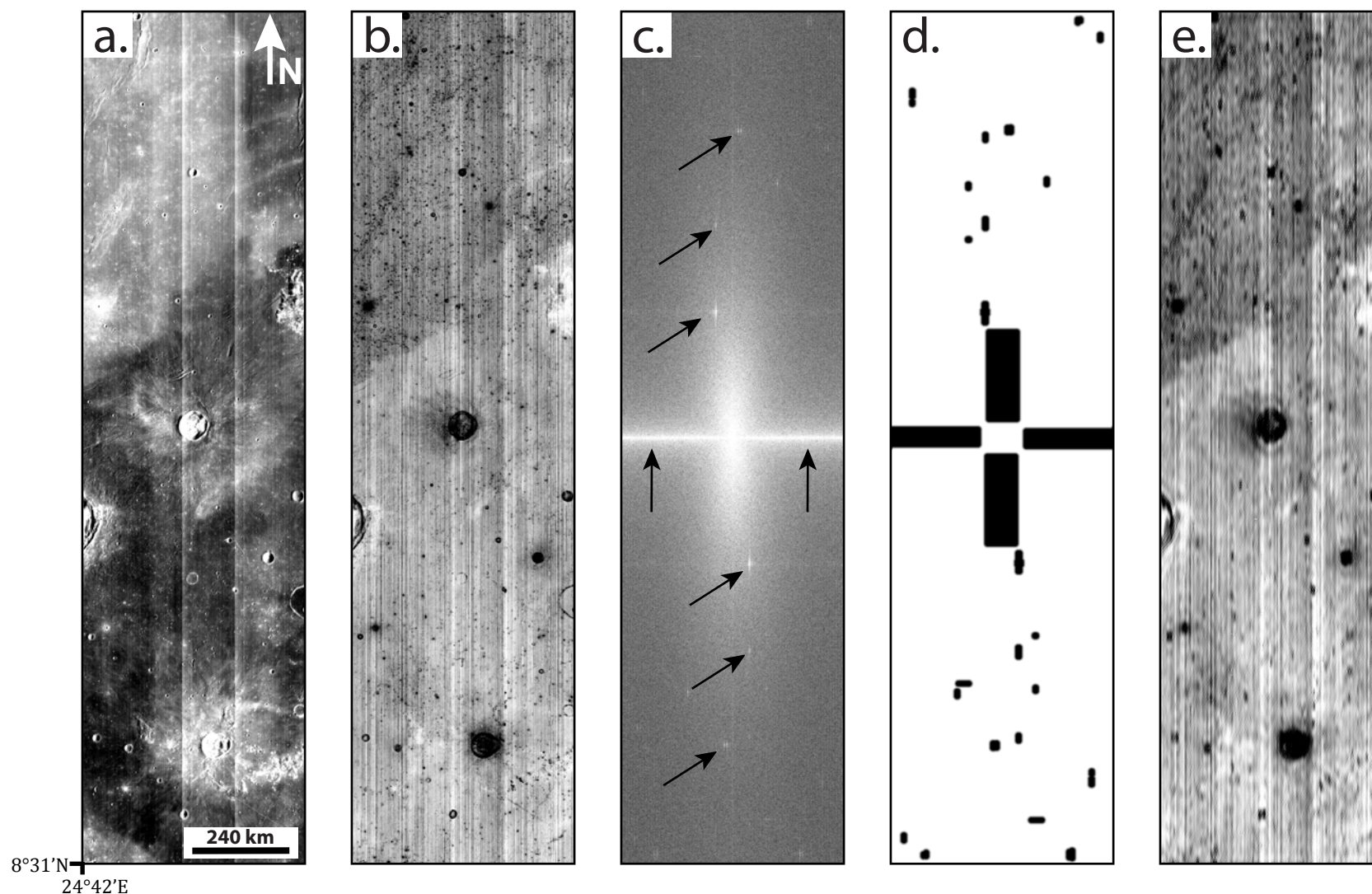


Figure 9: Example of the steps involved in the frequency filter we applied to the M^3 images. (a) Original I/F M^3 image. (b) Continuum-removed image. (c) Frequency domain image of created using the Fast Fourier transform (FFT). (d) User-defined frequency filter that masks out anomolous frequency components in (c), examples indicated by the black arrows. In addition, a 5 pixel taper is applied to the ends of each mask (black polygons) in (d). (e) The result of applying the frequency filter. (e) Final filtered M^3 image. Notice that there is less striping (e) than there is in (b). Even though striping still exists, the effects of the most closely spaced stripes in (b) has been diminished in (e).

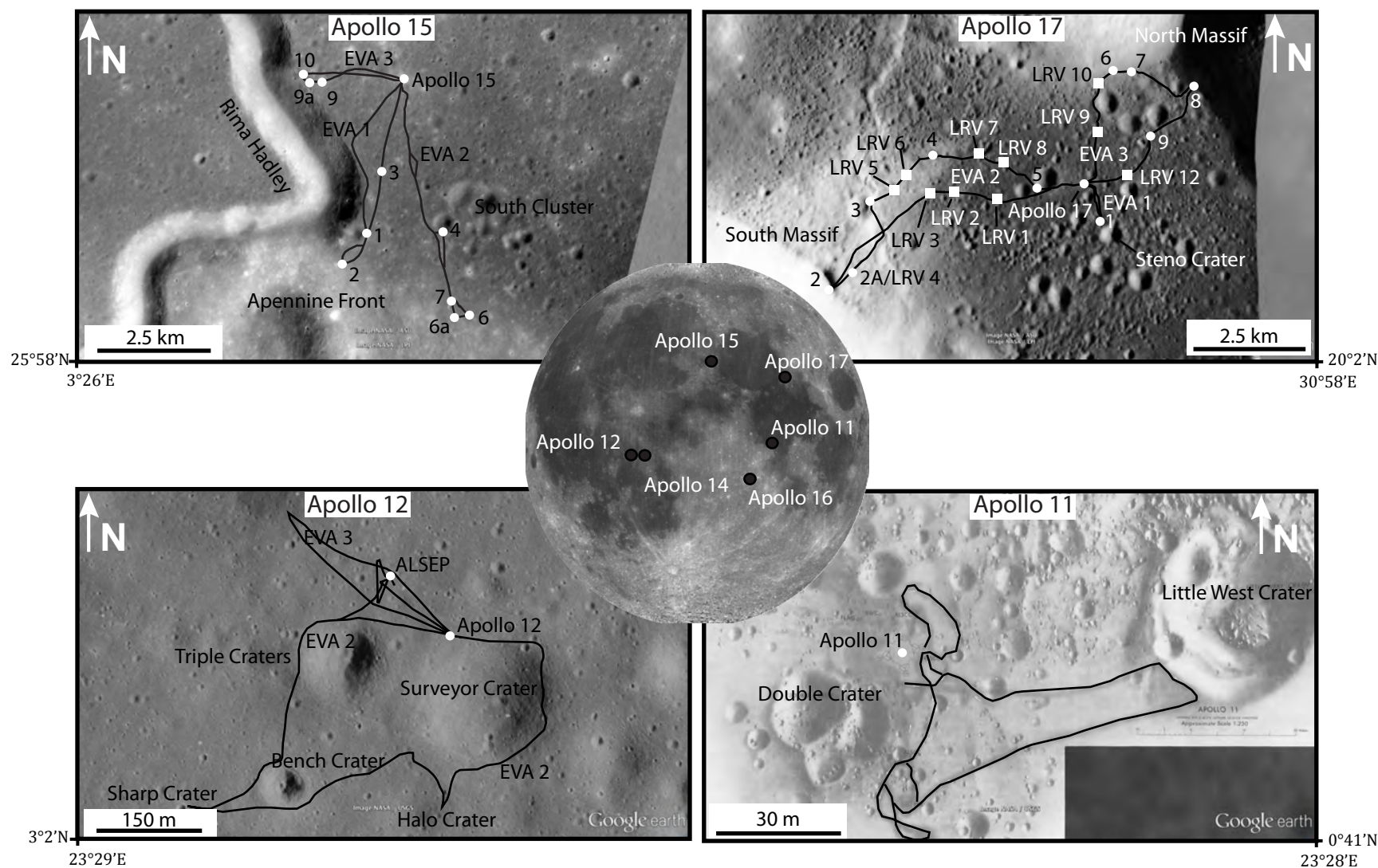


Figure 10: Clementine global albedo image (center) showing Apollo landing sites (black dots). Apollo 11, 12, 15, and 17 landing site images show extraveicular activities (EVA) traverses (black lines), Lunar Rover (LRV) traverse samples (white squares), and stations (white dots). See Table 2 for sample information. Apollo 14 and Apollo 16 samples were not used in this study because those landing sites were in anorthositic highland areas. Base imagery from Google Earth.

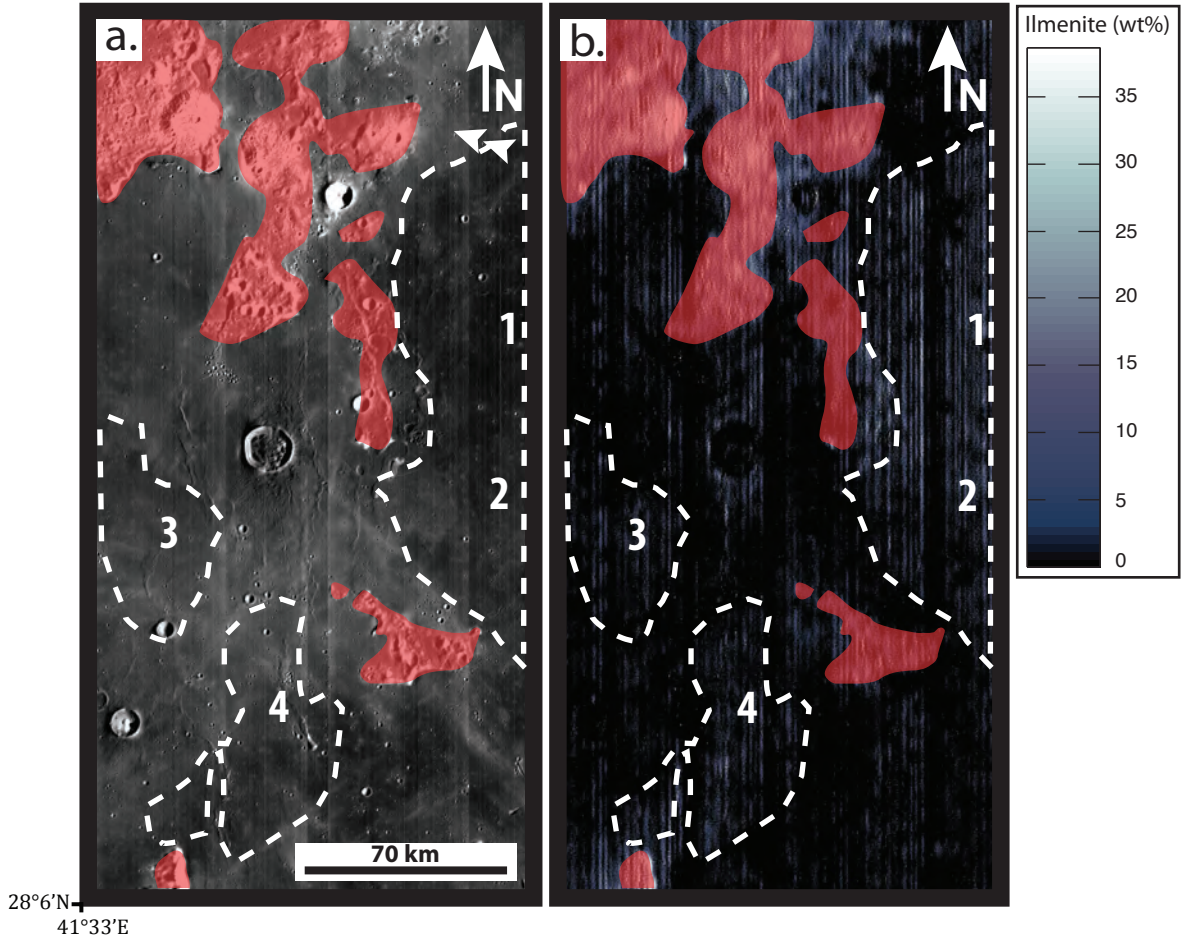


Figure 11: (a) M³ (band 7) image of W. Mare Imbrium (~36°N, 40°W). White numbers refer to sites that were measured in Table 2. White dashed polygons outline ilmenite-rich basalts. Red transparent polygons show anorthositic highland material. Double white arrows indicate illumination direction. (b) Band math ($b_{\text{shoulder}} - b_{\text{min}} = \Delta R$) image of continuum-removed and frequency-filtered M³ image showing shallow 1-μm absorptions (ilmenite-rich) in blues and white hues and deep 1-μm absorptions (ilmenite-poor) in black (see color scale).

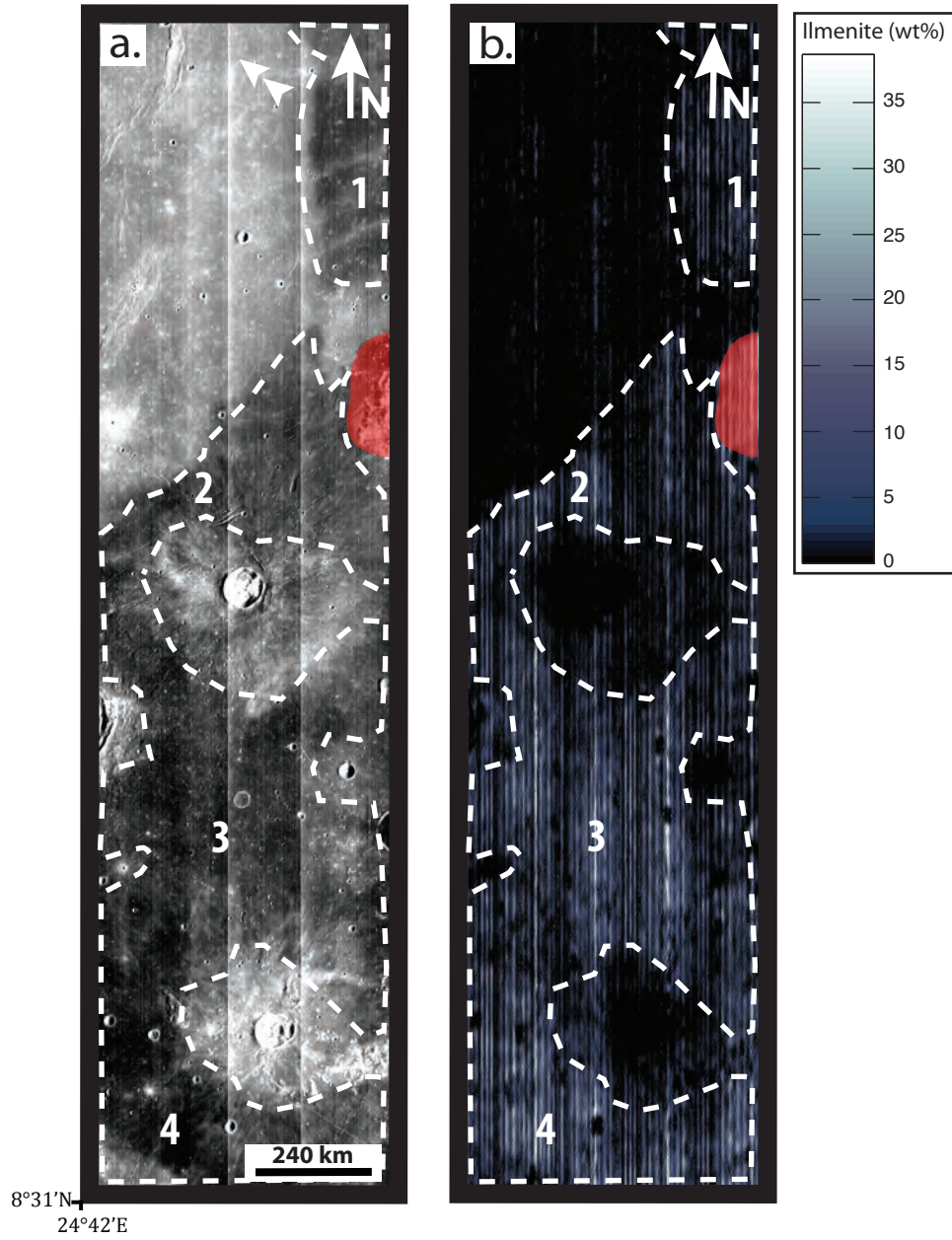


Figure 12: (a) M^3 (band 7) image of Mare Serenitatis and Tranquillitatis ($\sim 19^\circ\text{N}$, 26°E). White numbers refer to sites measured in Table 2. White dashed polygons outline ilmenite-rich basalts. Red transparent polygons show anorthositic highland material. Double white arrows indicate illumination direction. (b) Band math ($b_{\text{shoulder}} - b_{\text{min}} = \Delta R$) image of continuum-removed and frequency-filtered M^3 image showing shallow 1- μm absorptions (ilmenite-rich) in blues and white hues and deep 1- μm absorptions (ilmenite-poor) in black (see color scale).

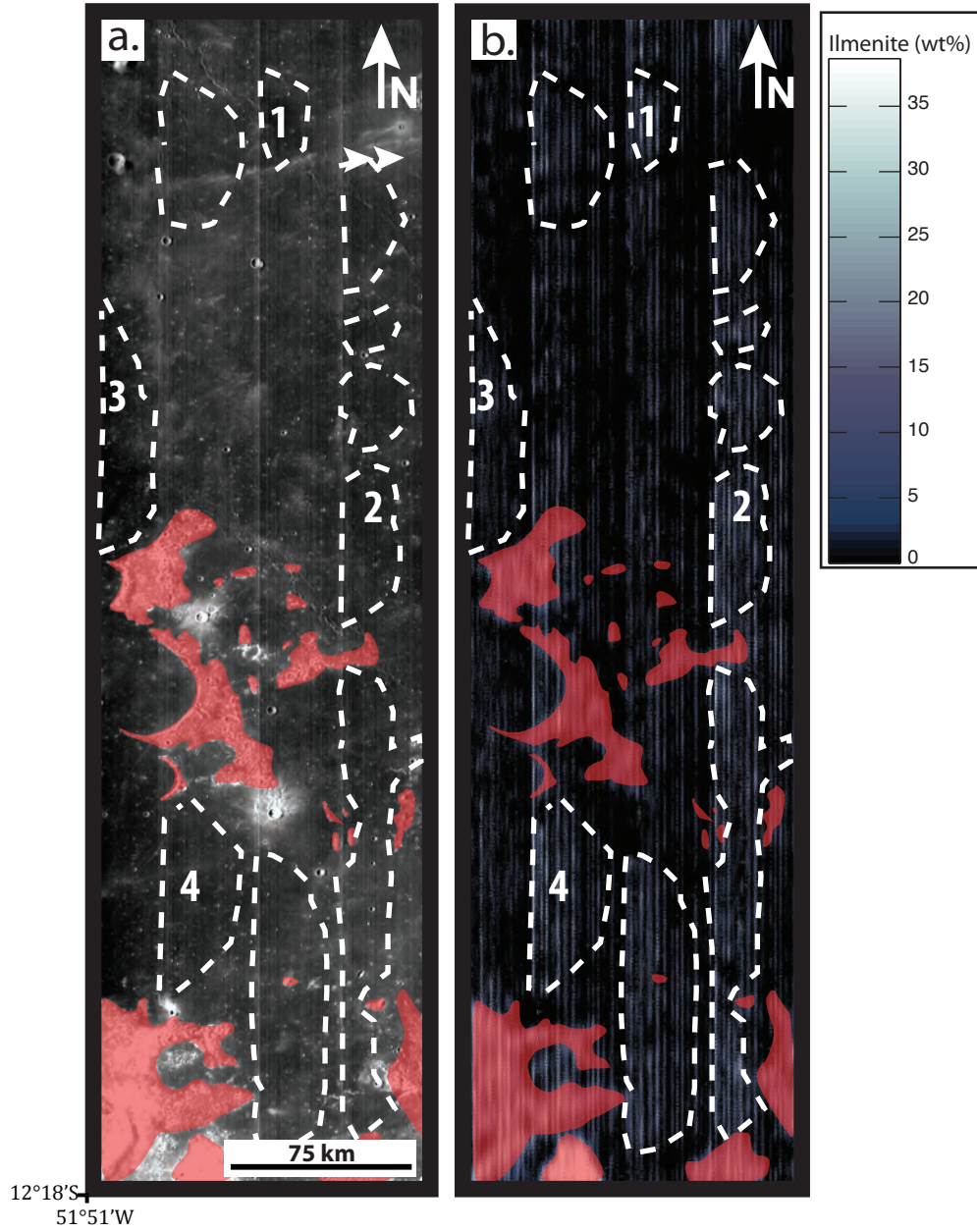


Figure 13: (a) M³ (band 7) image of S. Oceanus Procellarum (~10°S, 50°W). White numbers refer to sites measured in Table 2. White dashed polygons outline ilmenite-rich basalts. Red transparent polygons show anorthositic highland material. Double white arrows indicate illumination direction. (b) Band math ($b_{\text{shoulder}} - b_{\text{min}} = \Delta R$) image of continuum-removed and frequency-filtered M³ image showing shallow 1-μm absorptions (ilmenite-rich) in blues and white hues and deep 1-μm absorptions (ilmenite-poor) in black (see color scale).

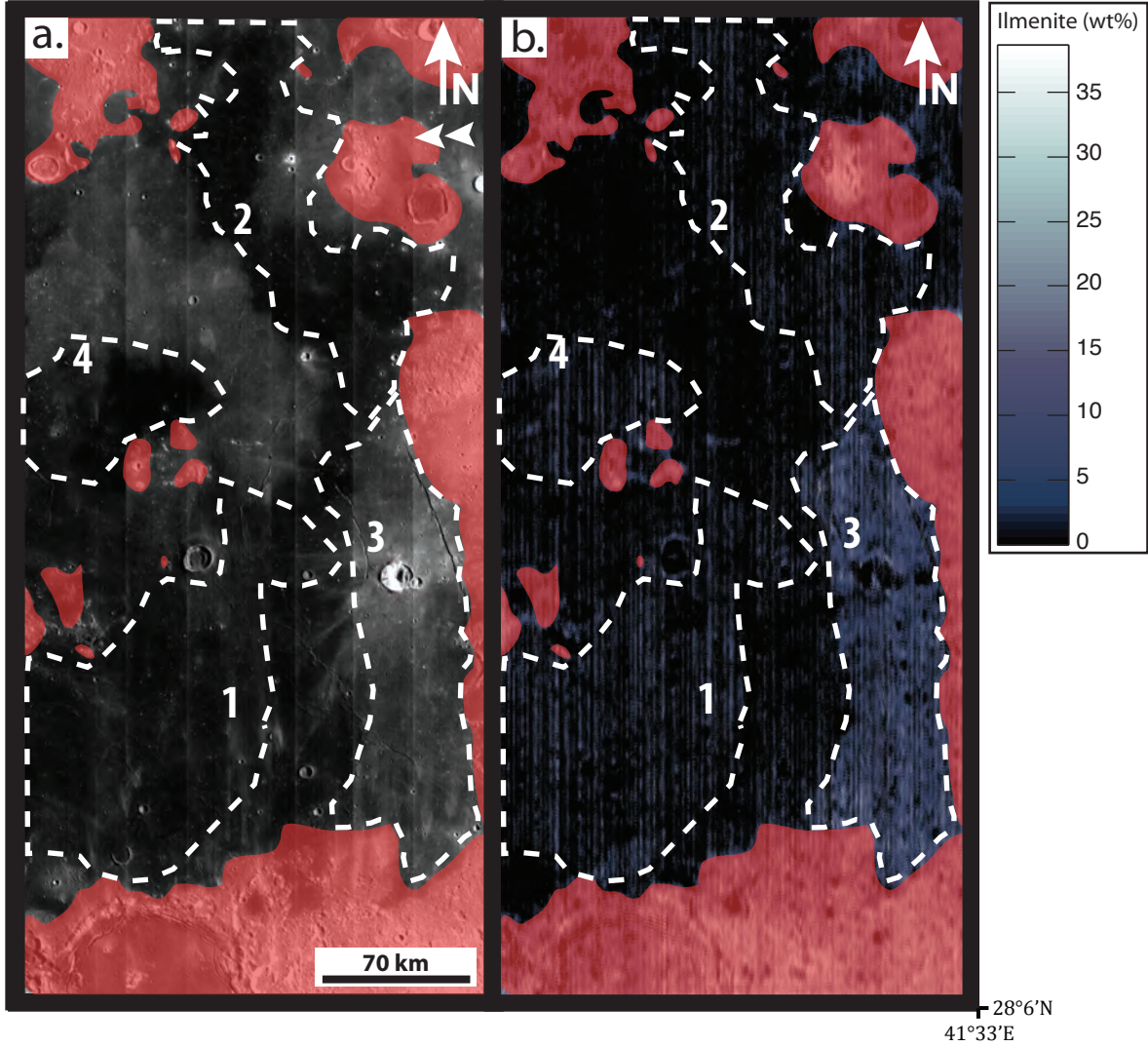


Figure 14: (a) M³ (band7) image of Mare Nubium (~15°S, 8°W). White numbers refer to sites measured in Table 2. White dashed polygons outline ilmenite-rich basalts. Red transparent polygons show anorthositic highland material. Double white arrows indicate illumination direction. (b) Band math ($b_{\text{shoulder}} - b_{\text{min}} = \Delta R$) image of continuum-removed and frequency-filtered M³ image showing shallow 1-μm absorptions (ilmenite-rich) in blues and white hues and deep 1-μm absorptions (ilmenite-poor) in black (see color scale).

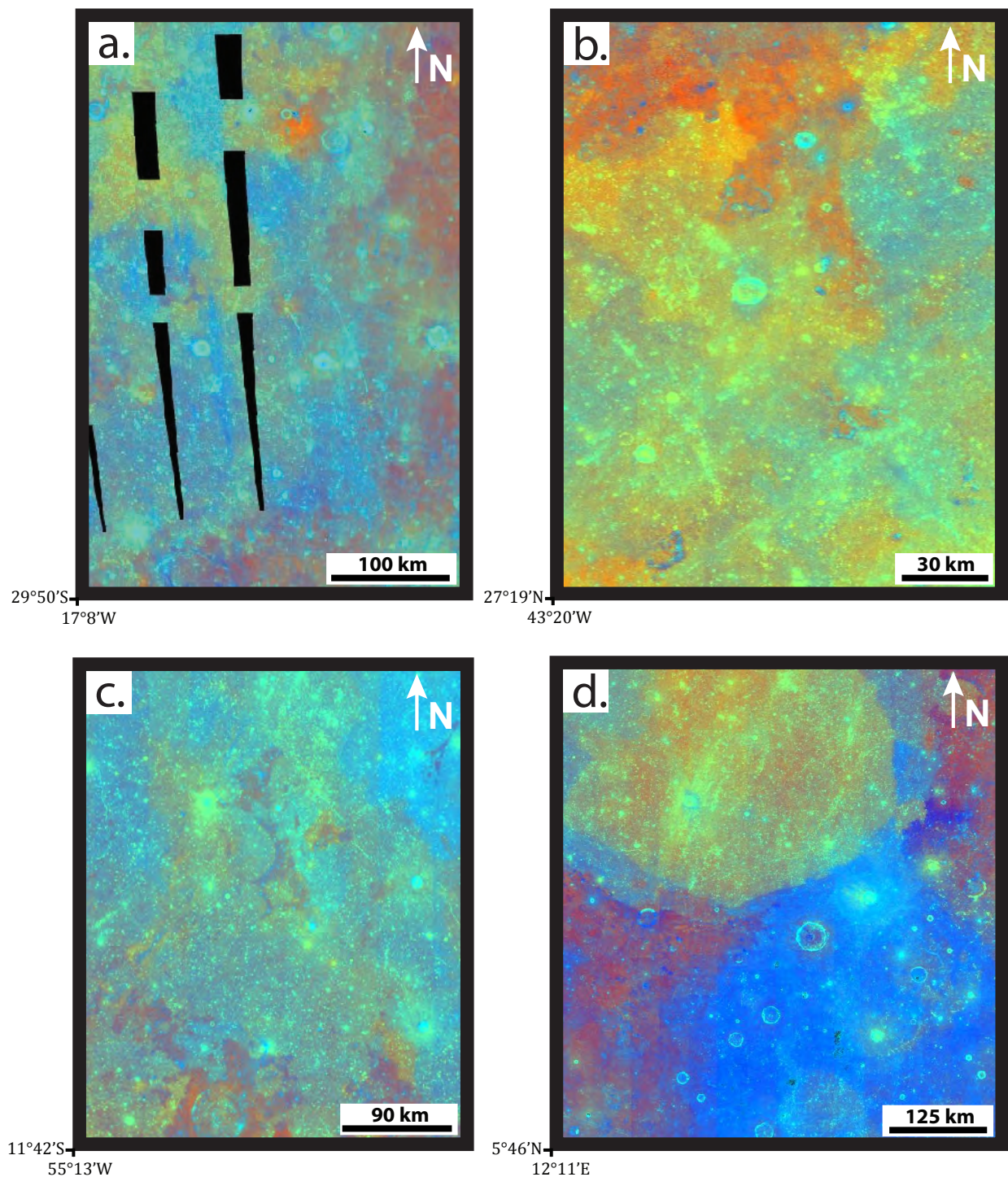


Figure 15: Clementine RGB ratio images (R: 750nm/415nm, G: 750nm/950nm, B: 414nm/750nm) showing maria that are Ti-poor in yellow/orange hues, and maria that are Ti-rich in blue hues. Optically mature highlands are in blue hues, and optically immature highlands are shown in red hues. (a) Eastern Mare Nubium; (b) Western Mare Imbrium; (c) Southern Oceanus Procellarum; and (d) Mare Serenitatis (top) and Tranquillitatis (bottom). See Figure 1 for location. From Eliason et al. (1999).

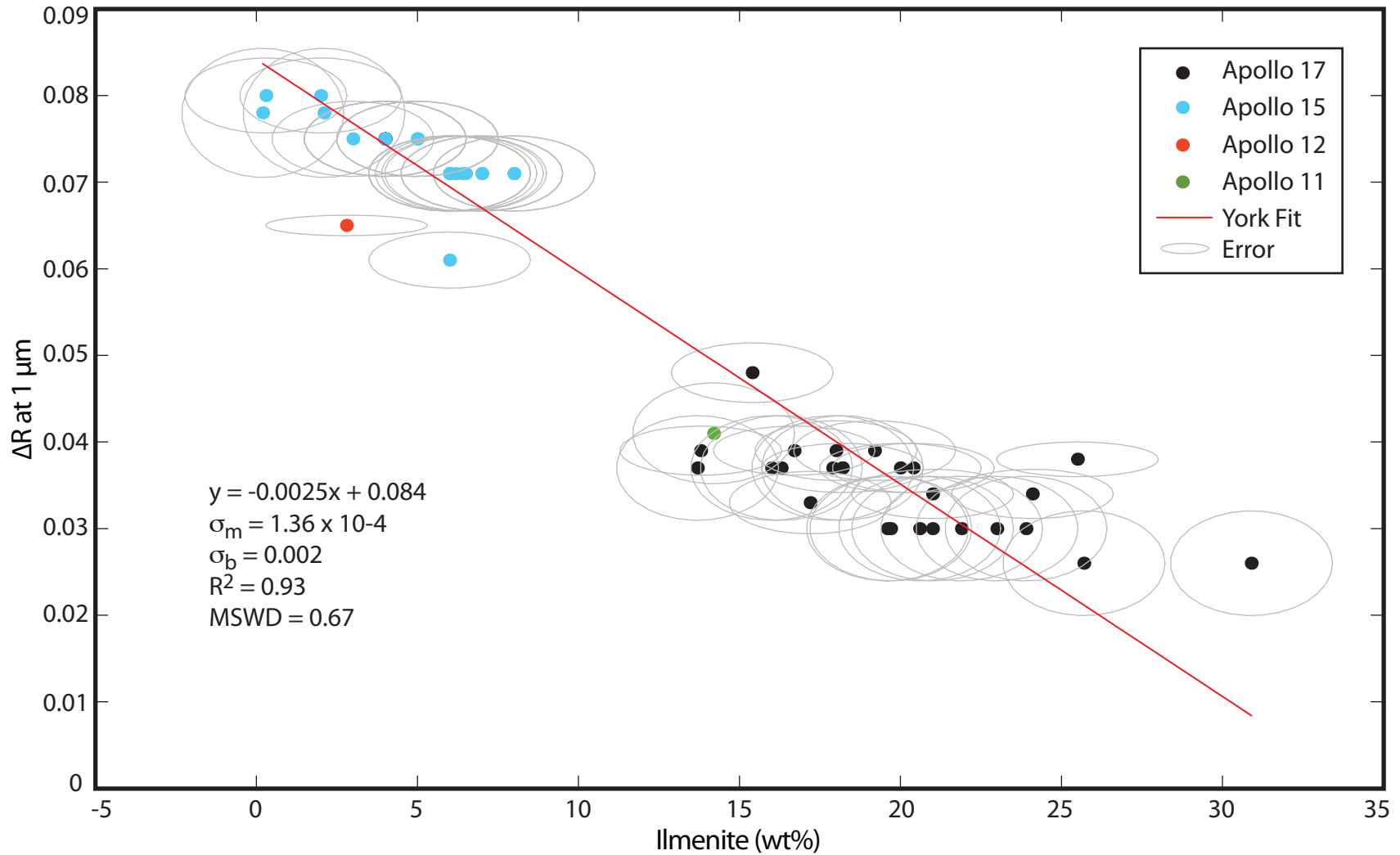


Figure 16: Ilmenite regression model showing ilmenite abundances of Apollo samples versus the 1-μm absorption depths from the remotely sensed spectra of the stations from which the samples were collected. Red line shows the lease-squares linear fit (with standard errors in x and y; York fit), which accounts for ~93% of the variance in the data. Apollo 11 samples shown in green, Apollo 12 shown in red, Apollo 15 shown in blue, and Apollo 17 shown in black (Table 2) (Meyer, 2012). Errors in X and Y for each data point are shown by the light gray ellipses.

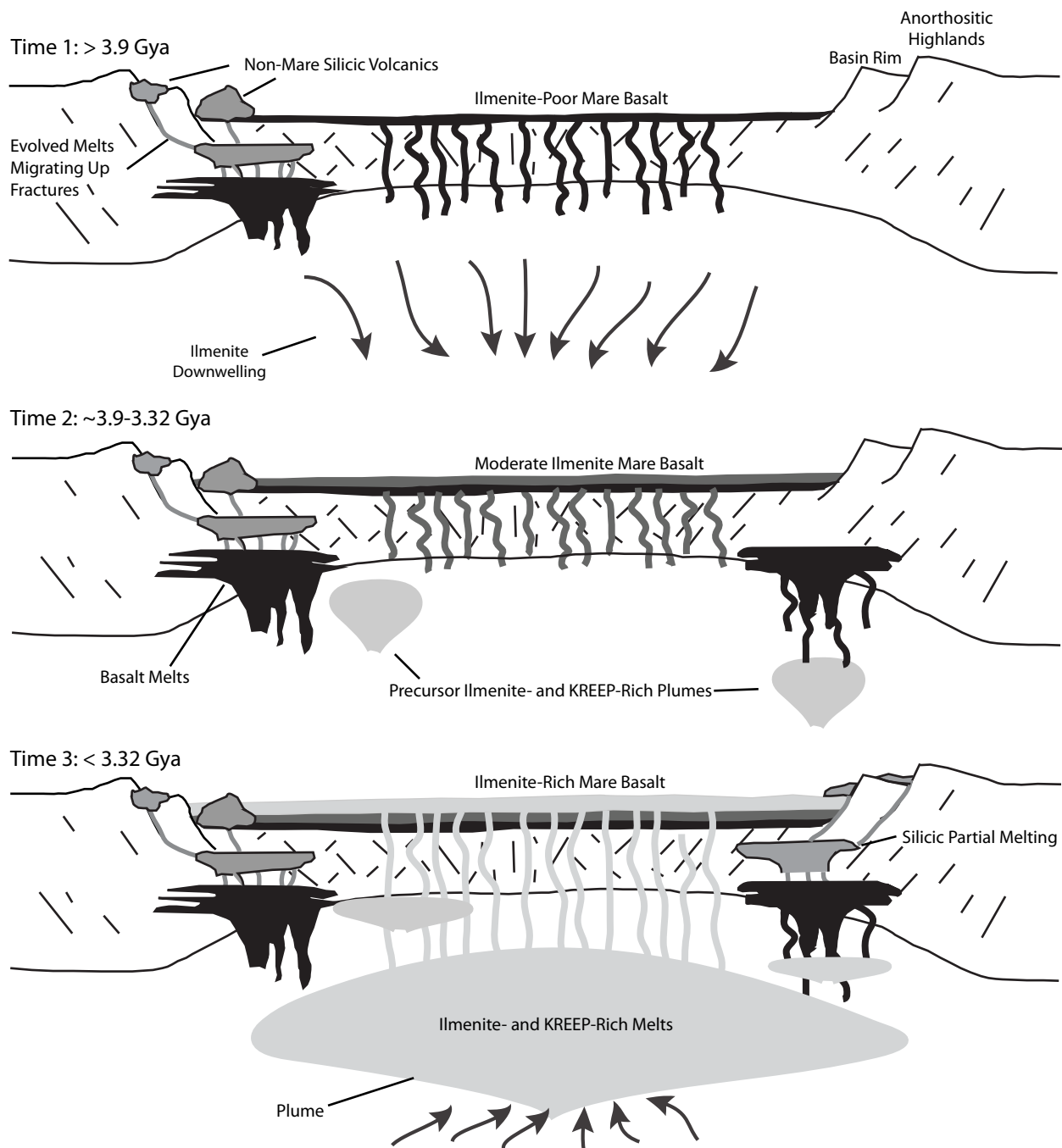


Figure 17: Schematic cross-section of nearside volcanism through time at Mare Nubium and Imbrium (~3.9-3.32 Gya). Time 1 represents the ilmenite downwelling (black arrows) that occurred early in the geologic history of the Moon. Hydrous melts may have reached the surface prior to old, ilmenite-poor mare basalts, and then were embayed by subsequent mare basalt volcanism. Time 2 represents the volcanism that occurred after the ilmenite downwelling within the PKT. Early ilmenite- and KREEP-rich plumes could have begun to arrive at ~3.32 Gya and mix with partial melts at the base of the lunar crust. Time 3 represents the arrival of the main plume of ilmenite- and KREEP-rich melts that were pulled down during the ilmenite downwelling and subsequently mixed near the core-mantle boundary. The arrival of the plume marks the beginning of widespread ilmenite- and KREEP-rich eruptions at ~3.32 Gya. Modified from Hagerty et al. (2006).

APPENDIX 1: APOLLO SAMPLE DATA

Basalt samples from Apollo 11, 12, 15, and 17 were used to create the ilmenite regression model. The locations of these samples and the traverses on which they were collected (Figure 10) are taken from the Lunar Sample Compendium (Myer, 2012). Samples from Apollo 14, which visited the Fra Mauro region (Figure 10), and Apollo 16, which visited the Descartes Highlands (Figure 10), were not used because these landing sites were in highland areas. In addition, samples collected at Apollo 17 stations 6, 7, and 8 (Figure 10) were omitted from the analysis because they might include both mare and highland rocks, which, at the resolution of the M^3 images, would yield a mixed image spectrum that is hard to reconcile with the mineralogy of the samples collected there.

Our methodology for detecting ilmenite in mare basalt uses shallowing of the $1\text{-}\mu\text{m}$ absorption as a proxy (Issacson et al., 2011). It is, however, only applicable to basalt. If we extract image spectra from an area with highland material, which has no significant $1\text{-}\mu\text{m}$ absorption (Figure 3), we could incorrectly interpret these highland materials to be mare basalts containing large concentrations of ilmenite. Therefore, we chose not to include Apollo basalt samples that were collected from stations near anorthositic highland material in our study (see Section 3.5).

Uncertainties in the ΔR values obtained from the M^3 imagery, in the ilmenite concentrations from Apollo basalt samples, and in the regression described in Section 3.5 are explicitly propagated to yield uncertainties in the ilmenite concentrations we determine from M^3 data (Appendix 2). The Apollo stations were located using M^3 images co-registered with the band-depth images, but, because of the relatively low-resolution of the M^3 data ($\sim 140\text{ m/pixel}$), it was only possible to locate individual stations for Apollo 15 and 17 to within an area (“region-

of-interest”) of 3-4 pixels. For each station, the average ΔR was calculated from the pixels in the region-of-interest, and this value was associated with the ilmenite concentration for the rocks collected at that station. We calculate the mean and the 1-sigma standard deviation ($\sigma_{\Delta R}$) of the ΔR values for the pixels extracted from the band depth image. To determine uncertainties of the ilmenite concentrations obtained from the Apollo samples we examine samples that contain several alternative modal mineralogies. Some Apollo sample reports list one modal mineralogy, but none reported ilmenite concentration uncertainty (Meyer, 2012). To determine ilmenite concentration uncertainties in Apollo samples we calculated the mean and standard deviation of the ilmenite concentrations listed for the samples with multiple modal mineralogies. We then determined the average standard deviation of the multiple ilmenite determinations and assumed this standard deviation for all the Apollo samples.

References:

Isaacson, P.J., Pieters, C.M., Hiroi, T., Liu, Y., Dhingra, D., Klima, R.L., and Taylor, L.A., 2011, Reflectance Spectroscopy of Ilmenite: New Constraints from Apollo Sample Measurements: *Proceedings of the 42nd Lunar and Planetary Science Conference*, p. 2130.

Meyer, C., 2012, *The Lunar Sample Compendium* <http://curator.jsc.nasa.gov/lunar/lsc/index.cfm>.

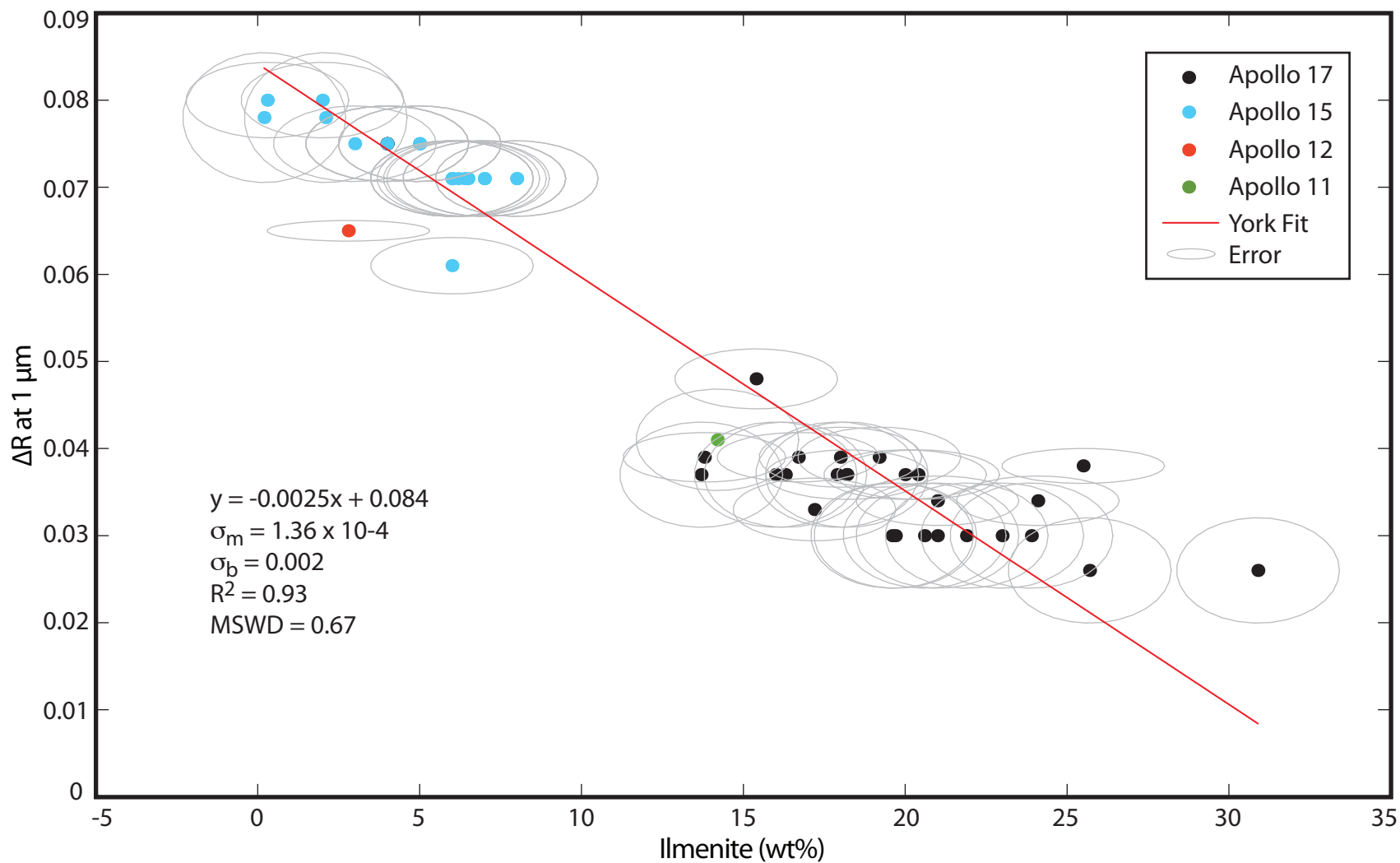


Figure A1: Ilmenite regression model showing ilmenite abundances of Apollo samples versus the 1- μm absorption depths from the remotely sensed spectra of the stations from which the samples were collected. Red line shows the least-squares linear fit (with standard errors in x and y; York fit), which accounts for ~93% of the variance in the data. Apollo 11 samples shown in green, Apollo 12 shown in red, Apollo 15 shown in blue, and Apollo 17 shown in black (Table 2) (Meyer, 2012). Errors in X and Y for each data point are shown by the light gray ellipses.

TABLE A2. APOLLO BASALT SAMPLES

Apollo Mission	Station	Sample #	Ilmenite (wt%, x)	Ilmenite Uncertainty (wt%, σ_x)	ΔR at $1\mu\text{m}$	ΔR Uncertainty ($\sigma_{\Delta R}$)	Region of Interest Size (km)
11	LM	10003	13.3	2.5	0.042	0.006	1120.000
11	LM	10017	15.1	2.5	0.035	0.006	1120.000
11	LM	10020	12.5	2.5	0.051	0.006	1120.000
11	LM	10022	14.1	2.5	0.042	0.006	1120.000
11	LM	10024	16.4	2.5	0.035	0.006	1120.000
11	LM	10029	15.8	2.5	0.035	0.006	1120.000
11	LM	10032	16.5	2.5	0.035	0.006	1120.000
11	LM	10044	12.6	2.5	0.051	0.006	1120.000
11	LM	10045	13.5	2.5	0.042	0.006	1120.000
11	LM	10047	11.2	2.5	0.051	0.006	1120.000
11	LM	10049	14.1	2.5	0.042	0.006	1120.000
11	LM	10050	14.2	2.5	0.042	0.006	1120.000
11	LM	10057	15.5	2.5	0.035	0.006	1120.000
11	LM	10058	13.0	2.5	0.051	0.006	1120.000
11	LM	10062	12.5	2.5	0.051	0.006	1120.000
11	LM	10069	16.6	2.5	0.035	0.006	1120.000
11	LM	10071	14.8	2.5	0.035	0.006	1120.000
11	LM	10072	13.2	2.5	0.042	0.006	1120.000
11	LM	10092	15.6	2.5	0.035	0.006	1120.000
12	LM	12002	0.9	2.5	0.066	0.001	980.000
12	LM	12004	1.4	2.5	0.066	0.001	980.000
12	LM	12005	1.9	2.5	0.066	0.001	980.000
12	LM	12006	1.1	2.5	0.066	0.001	980.000
12	LM	12007	2.9	2.5	0.066	0.001	980.000
12	LM	12008	4.7	2.5	0.064	0.001	980.000
12	LM	12009	1.2	2.5	0.066	0.001	980.000
12	LM	12011	2.9	2.5	0.066	0.001	980.000
12	LM	12012	1.9	2.5	0.066	0.001	980.000
12	LM	12014	0.6	2.5	0.066	0.001	980.000
12	LM	12016	4.8	2.5	0.064	0.001	980.000
12	LM	12017	1.5	2.5	0.066	0.001	980.000
12	LM	12018	0.5	2.5	0.066	0.001	980.000
12	LM	12019	3.7	2.5	0.064	0.001	980.000
12	LM	12020	0.2	2.5	0.066	0.001	980.000
12	LM	12021	1.7	2.5	0.066	0.001	980.000
12	LM	12022	9.0	2.5	0.063	0.001	980.000
12	LM	12031	3.9	2.5	0.064	0.001	980.000
12	SW	12035	0.1	2.5	0.066	0.001	980.000
12	SW	12037	6.3	2.5	0.063	0.001	980.000
12	SW	12038	3.5	2.5	0.064	0.001	980.000
12	SW	12039	2.8	2.5	0.066	0.001	980.000
12	SW	12040	2.3	2.5	0.066	0.001	980.000
12	SW	12043	3.5	2.5	0.064	0.001	980.000

TABLE A2. APOLLO BASALT SAMPLES (CONT.)

Apollo Mission	Station	Sample #	Ilmenite (wt%, x)	Ilmenite Uncertainty (wt%, σ_x)	ΔR at $1\mu m$	ΔR Uncertainty ($\sigma_{\Delta R}$)	Region of Interest Size (km)
12	SE	12046	3.4	2.5	0.064	0.001	980.000
12	SE	12047	5.3	2.5	0.064	0.001	980.000
12	SE	12051	5.3	2.5	0.064	0.001	980.000
12	SE	12052	3.5	2.5	0.064	0.001	980.000
12	SE	12053	3.9	2.5	0.064	0.001	980.000
12	SE	12054	5.2	2.5	0.064	0.001	980.000
12	SE	12055	0.4	2.5	0.066	0.001	980.000
12	SE	12056	6.8	2.5	0.063	0.001	980.000
12	SE	12062	0.3	2.5	0.066	0.001	980.000
12	SE	12063	4.6	2.5	0.064	0.001	980.000
12	SE	12064	3.9	2.5	0.064	0.001	980.000
12	SE	12065	1.6	2.5	0.066	0.001	980.000
12	LM	12072	1.4	2.5	0.066	0.001	980.000
12	LM	12075	0.6	2.5	0.066	0.001	980.000
12	LM	12076	4.0	2.5	0.064	0.001	980.000
12	LM	12077	0.4	2.5	0.066	0.001	980.000
15	3	15016	6.0	2.5	0.061	0.003	420.000
15	4	15475	2.1	2.5	0.078	0.007	1120.000
15	4	15486	0.2	2.5	0.078	0.007	1120.000
15	9	15536	4.0	2.5	0.075	0.004	560.000
15	9	15545	3.0	2.5	0.075	0.004	560.000
15	9	15555	5.0	2.5	0.075	0.004	560.000
15	9	15556	2.0	2.5	0.080	0.004	560.000
15	9	15597	0.3	2.5	0.080	0.004	560.000
15	9	15598	6.5	2.5	0.071	0.004	560.000
15	9	15605	6.4	2.5	0.071	0.004	560.000
15	9	15607	5.0	2.5	0.075	0.004	560.000
15	9	15620	4.0	2.5	0.075	0.004	560.000
15	9	15610	8.0	2.5	0.071	0.004	560.000
15	9	15633	6.0	2.5	0.071	0.004	560.000
15	9	15641	6.0	2.5	0.071	0.004	560.000
15	9	15643	4.0	2.5	0.075	0.004	560.000
15	9	15663	6.0	2.5	0.071	0.004	560.000
15	9	15636	6.2	2.5	0.071	0.004	560.000
15	9	15651	5.0	2.5	0.075	0.004	560.000
15	9	15672	6.0	2.5	0.071	0.004	560.000
15	9	15665	8.0	2.5	0.071	0.004	560.000
15	9	15669	7.0	2.5	0.071	0.004	560.000
15	9	15676	4.0	2.5	0.075	0.004	560.000
15	9	15678	7.0	2.5	0.071	0.004	560.000
15	9	15682	7.0	2.5	0.071	0.004	560.000
17	LM	70017	19.2	2.5	0.039	0.003	840.000

TABLE A2. APOLLO BASALT SAMPLES (CONT.)

Apollo Mission	Station	Sample #	Ilmenite (wt%, x)	Ilmenite Uncertainty (wt%, σ_x)	ΔR at $1\mu m$	ΔR Uncertainty ($\sigma_{\Delta R}$)	Region of Interest Size (km)
17	LM	70215	18.0	2.5	0.039	0.003	840.000
17	LM	70035	15.4	2.5	0.048	0.003	840.000
17	ALSEP	70135	21.9	2.5	0.030	0.006	420.000
17	ALSEP	70139	18.2	2.5	0.037	0.006	420.000
17	ALSEP	70147	21.0	2.5	0.030	0.006	420.000
17	ALSEP	70145	20.6	2.5	0.030	0.006	420.000
17	ALSEP	70146	19.6	2.5	0.030	0.006	420.000
17	ALSEP	70148	17.9	2.5	0.037	0.006	420.000
17	ALSEP	70149	23.0	2.5	0.030	0.006	420.000
17	ALSEP	70155	16.3	2.5	0.037	0.006	420.000
17	ALSEP	70156	19.7	2.5	0.030	0.006	420.000
17	ALSEP	70157	16.0	2.5	0.037	0.006	420.000
17	ALSEP	70165	13.7	2.5	0.037	0.006	420.000
17	ALSEP	70185	23.9	2.5	0.030	0.006	420.000
17	ALSEP	70255	30.9	2.5	0.026	0.006	420.000
17	ALSEP	70275	25.7	2.5	0.026	0.006	420.000
17	LRV 12	70315	25.5	2.5	0.038	0.002	420.000
17	5	75015	16.7	2.5	0.039	0.003	420.000
17	5	75035	13.8	2.5	0.039	0.003	420.000
17	5	75055	20.0	2.5	0.037	0.003	420.000
17	5	75065	20.4	2.5	0.037	0.003	420.000
17	5	75075	24.1	2.5	0.034	0.003	420.000
17	5	75086	18.2	2.5	0.037	0.003	420.000
17	5	75087	21.0	2.5	0.034	0.003	420.000
17	9	79265	17.2	2.5	0.033	0.004	420.000

* Obtained from modal mineralogies of returned Apollo basalt samples (Meyer, 2012).

† Extracted from M^3 band depth image. Value is related to region associated with station.

** Average ilmenite uncertainty for modal mineralogy determinations (Meyer, 2012).

†† Uncertainty of band depth values around the Apollo sample station.

APPENDIX 2: LINEAR REGRESSION ACCOUNTING FOR STANDARD ERRORS IN X AND Y

The following MATLAB code was created using MATLAB v. 7.12.0 student version. The code is designed to perform a least-squares linear regression (York, 1969; York et al., 2004) that takes into account the standard errors in ΔR and ilmenite concentrations of Apollo samples. The data points are created using ilmenite concentrations from Apollo samples (x) and 1 μm band depths (ΔR) of the Apollo sample stations, and their uncertainties σ_x and $\sigma_{\Delta R}$. The inputs (ΔR , x , σ_x and $\sigma_{\Delta R}$) are in .txt format.

The York fit function was designed by Wiens (2010) and creates a linear regression with errors in ΔR and x by following the York et al. (2004) method. After using the York fit function, our code outputs the mean square weighted difference and root mean square. The code also outputs a MATLAB plot that contains data points with error ellipses, as well as the best fit that accounts for standard error (Figure 16).

References

- Wiens, T., 2010, *Linear Regression with Errors in X and Y*: <http://www.mathworks.com/matlabcentral/fileexchange/26586-linear-regression-with-errors-in-x-and-y>. (accessed December 2014).
- York, D., 1969, Least-squares fitting of a straight line: *Earth Planetary Science Letters*, v. 5, p. 320-324.

York, D., Evenson, N., Martinez, M., and Delgado, J., 2004, Unified equations for the slope, intercept, and standard errors of the best straight line: *American Journal of Physics*. v. 72 no. 3. p. 367-375.

%linear regression takes into account the errors in X and Y. This method
 %is from D. York, N. Evenson, M. Martinez, and J. Delgado, 2004, Unified
 %equations for the slope, intercept, and standard errors of the best
 %straight line: American Journal of Physics. v. 3.

12/05/2014 Douglas L. Standart and Jose M. Hurtado, Jr.

```
clf
clc
```

```
N = 53;%number of points
Xmax = max(Ilmenite);
Xmin = min(Ilmenite);
X_range=[Xmin Xmax];%range of X values
```

```
sigma_X_max= max(delIlemnite);%maximum std error in X
sigma_Y_max= max(SigmadelR);%maximum std error in Y
```

```
%assign known variables
X = Ilmenite'; %ilmenite concentrations from Apollo samples
Y = delR'; %?R at 1  $\mu$ m from Apollo sample stations
sigma_X=delIlemnite'; %ilmenite concentration uncertainty
sigma_Y= SigmadelR'; %?R uncertainty
r=0*ones(1,N);%correlation coefficient between errors in X and Y
```

```
[a_york, b_york, sigma_ayork, sigma_byork] =...
    york_fit(X,Y,sigma_X,sigma_Y, r);%estimate parameters
```

```
tmp=Y/[X; ones(1,N)];%find least squares line fit
```

```
N_plot=N;
X_plot=linspace(X_range(1),X_range(2),N_plot);
Y_plotyork=a_york+b_york*X_plot;
```

```
fprintf('lse: a=%0.3f b=%0.3f\n',a_lse,b_lse);
```

```
fprintf('york: a=%0.3f+/-%0.3f b=%0.3f+/-
%0.3f\n',a_york,sigma_ayork,b_york,sigma_byork);
```

```
%plot the data points
```

```
figure(1)
h=zeros(1,1);
plot(X,Y,'k.')
hold on
```

```
%plot error ellipse for each point
```

```
for i=1:N
    [Xe Ye] = ellipse(X(i),Y(i),sigma_X(i),sigma_Y(i),32);
    plot(Xe,Ye,'color',[0.7 0.7 0.7])
end
```

```
%plot the york fit trendline
```

```

h(1)=plot(X_plot,Y_plotyork,'r');
hold off
legend(h,'york')
xlabel('Ilmenite (Wt%)')
ylabel('?R at 1  $\mu$ m')

%calculate the mean square weighted difference

f = N-2; %degrees of freedom

for i= 1:N;
    numer = ((Y(i)-a_york-(b_york*X(i))) .* (Y(i)-a_york-(b_york .*X(i))));
    denom = ((sigma_Y(i) .* sigma_Y(i)) + ((b_york .* b_york) .* (sigma_X(i)
.* sigma_X(i))));
    thingsum(i) = numer ./ denom;
end

mswd = sum(thingsum) ./ f

mswd_ideal= 1 + (sqrt(2 ./ f))

%calculate the root mean square (rsq)
numerator = (Y - Y_plotyork) .* (Y - Y_plotyork);

denominator = (Y .* Y);

sumnum = sum(numerator);
sumdenom = sum(denominator);

rsq= 1 - (sumnum ./ sumdenom)

slope = b_york
uncertainty_slope = sigma_byork

yintercept = a_york
uncertainty_yintercept = sigma_ayork

```



```

function [a, b, sigma_a, sigma_b, b_save] = york_fit(X,Y,sigma_X,sigma_Y, r)
[a, b, sigma_a, sigma_b, b_save] = york_fit(X,Y,sigma_X,sigma_Y, r)
%Performs linear regression for data with errors in both X and Y, following
%the method in York et al.
%X,Y are row vectors of regression data.
%sigma_X and sigma_Y are row vectors or single values for the error in X
%and Y.
%r is a row vector or signal value for the correlation coefficeints
%between the errors.
%
%References:
%D. York, N. Evensen, M. Martinez, J. Delgado "Unified equations for the
%slope, intercept, and standard errors of the best straight line" Am. J.
%Phys. 72 (3) March 2004.

%Copyright Travis Wiens 2010 travis.mlfx@nutaksas.com

N_itermax=10;%maximum number of iterations
tol=1e-15;%relative tolerance to stop at

N=numel(X);

if nargin<5;
    r=0;
end

if numel(sigma_X)==1
    sigma_X=sigma_X*ones(1,N);
end

if numel(sigma_Y)==1
    sigma_Y=sigma_Y*ones(1,N);
end

if numel(r)==1
    r=r*ones(1,N);
end

%make initial guess at b using linear squares
tmp=Y/[X; ones(1,N)];
b_lse=tmp(1);
%a_lse=tmp(2);

b=b_lse;%initial guess

omega_X=1./sigma_X.^2;
omega_Y=1./sigma_Y.^2;

alpha=sqrt(omega_X.*omega_Y);

b_save=zeros(1,N_itermax+1);%vector to save b iterations in
b_save(1)=b;

for i=1:N_itermax
    W=omega_X.*omega_Y./(omega_X+b^2*omega_Y-2*b*r.*alpha);

```

```

X_bar=sum(W.*X)/sum(W);
Y_bar=sum(W.*Y)/sum(W);

U=X-X_bar;
V=Y-Y_bar;

beta=W.*(U./omega_Y+b*V./omega_X-(b*U+V).*r./alpha);

b=sum(W.*beta.*V)/sum(W.*beta.*U);
b_save(i+1)=b;
if abs((b_save(i+1)-b_save(i))/b_save(i+1))<tol
    break
end
end

a=Y_bar-b*X_bar;

x=X_bar+beta;
%y=Y_bar+b*beta;

x_bar=sum(W.*x)/sum(W);
%y_bar=sum(W.*y)/sum(W);

u=x-x_bar;
%v=y-y_bar;

sigma_b=sqrt(1/sum(W.*u.^2));
sigma_a=sqrt(1./sum(W)+x_bar^2*sigma_b^2);

```

APPENDIX 3: CONVERTING BAND DEPTH IMAGES INTO ILMENITE MAPS

The code was designed using MATLAB version 7.12.0. The code is designed to convert a band depth image (ΔR) to a map showing ilmenite concentrations (ilmenite wt%) using the linear regression model (Equation 4). The input is an ENVI image containing ΔR values (i.e. band depth image). The output is a MATLAB plot containing ilmenite concentrations. The MATLAB plot is subsequently saved as a TIFF file.

```
%Code designed to convert a band depth image ( $\Delta R$ ) from M3 to an ilmenite
%map (ilmenite wt%). The conversion is done using the linear equation from
%the linear regression model that was derived by plotting Apollo basalt
%ilmenite concentrations against the  $\Delta R$  values for the locations the
%samples were taken.
```

```
%updated 11/19/2014 Douglas L. Standart
```

```
clear
clc
clf
```

```
%DATA PREPARATION
```

```
columns = 966;
rows = 1922;
```

```
% load ENVI band-depth image
fid1 = fopen( 'BandDepthImage_XXXXX' , 'r' , 'l' ) ;
imagecontour = fread( fid1 , [ columns , rows ] , 'float' ) ;
fclose( fid1 ) ;
imagecontour = imagecontour' ;
```

```
ilmenitemap = zeros (rows, columns);
```

```
%create ilmenite map using linear regression equation, but without huge
%values from the anomalous striping values and non-mare material.
```

```
for m = 1 : rows
    for n = 1 : columns
        %solve for x( $\Delta R$ ) for the linear equation  $y = -0.0025x + 0.084$ 
        x = (imagecontour(m, n) - 0.084)/-0.0025;
        %assign 0% ilmenite values (xmax) for negative values
        if x < 0;
            ilmenitemap (m, n) = 0;
        else
            %set a max on ilmenite concentration based on y values from
            %linear equation that would be attributed to reflections
            %and therefore not a mare basalt. when y = 0 xmin =
            %38.6842105
            ilmenitemap (m, n) = x;
            if x > 33.7;
                ilmenitemap (m,n) = 0;
            else
                ilmenitemap (m,n) = x;
            end
        end
    end
end
```

```
% plot ilmenitemap
figure( 3 )
colormap( jet )
hold off
imagesc( ilmenitemap( : , : ) )
axis image
hold on
title( 'Ilmenite Map' )
colorbar( 'vert' )
```

CHAPTER 4: TARGETING ALUNITE IN EPITHERMAL AND COPPER PORPHYRY DEPOSITS USING ASTER VNIR, SWIR, AND TIR IMAGERY

Standart, D. L., Hurtado, J. M. (Jr.), and Goodell, P. C.

Department of Geological Sciences, The University of Texas at El Paso, 500 West University Avenue, El Paso, Texas 79968

Abstract: Alunite ($\text{KAl}_3(\text{SO}_4)_2(\text{OH})_6$) is a sulfate mineral that is commonly found in argillic alteration zones of porphyry and epithermal systems, and in other supergene enriched mineral deposits. Using ASTER (Advanced Spaceborne Thermal Emission and Reflection Radiometer) data, we target spectral features associated with hydroxyl (OH^-) and sulfate (SO_4^{2-}). Previous studies have used OH^- absorptions near $2.2\text{ }\mu\text{m}$ to target alunite, but their methods can confuse alunite with carbonates, detrital clays, iron oxides, and jarosite. We use a logical operator approach to increase our confidence in targeting alunite and delineate it from carbonates, detrital clays, iron oxides, and jarosite. The first logical operator targets a doublet absorption near $2.2\text{ }\mu\text{m}$ associated with OH^- in alunite, detrital clays, and carbonates. It also targets the negative spectral slope between 0.8 and $1.65\text{ }\mu\text{m}$, in order to delineate alunite from iron oxide and jarosite. We also develop a second logical operator that targets the $9\text{-}\mu\text{m}$ absorption associated with SO_4^{2-} in alunite, jarosite, and quartz. To test the effectiveness of our logical operator methodology in places where carbonates, detrital clays, limonite, and vegetation not related to porphyry and epithermal systems are present, we conduct a ground truth investigation at Cuprite Hills, Nevada. We show that the alunite identified by our alunite map is spatially correlative to the regions indicated by AVIRIS mineral maps to contain alunite. Our improved methodology for locating

alunite with ASTER data is an inexpensive, easy, and reliable method for discovering new porphyry and epithermal mineral deposits that can be applied to a variety of exploration problems.

Keywords: alunite; ASTER; copper porphyry deposits; Cuprite Hills; epithermal silver-gold deposits; remote sensing

1. Introduction

Regional mineral exploration is a critical first step for the discovery of new mineral deposits by exploration mining companies. With advances in remote sensing techniques, and as data storage and processing becomes cheaper, mineral exploration companies are finding that multispectral imagery can be a valuable resource for initial exploration mining projects. Some mineral deposits, such as epithermal silver-gold and copper porphyry deposits, leave a “footprint” at the surface in the form of hydrothermal clays (Mars and Rowan, 2006; Guilbert and Park, 2007), and previous studies have shown the ability to detect hydrothermal clays with multispectral imagery (Clark et al., 1993; Clark and Swayze, 1996; Rowan and Mars, 2003; Mars and Rowan, 2006). One of these clays, alunite ($\text{KAl}_3(\text{SO}_4)_2(\text{OH})_6$), is a sulfate mineral that is commonly found in argillic alteration zones of porphyry systems and has potential for use as a regional proxy to locate potential economic deposits. However, a weakness of most previous attempts to map alunite with multispectral remote sensing data (e.g., Clark et al., 1993; Clark and Swayze, 1996; Rowan and Mars, 2003; Mars and Rowan, 2006) has been the inability to reliably distinguish alunite from carbonates, detrital clays, iron oxides, jarosite ($\text{KFe}_3(\text{OH})_6(\text{SO}_4)_2$), and vegetation.

This research improves on the previous methodologies for mapping argillic alteration by targeting spectral features that are unique to alunite. Using multispectral imagery from the ASTER (Advanced Spaceborne Thermal Emission and Reflection Radiometer) instrument and with ENVI image processing software, we target alunite by examining the absorption features in reflectance spectra associated with hydroxyl (OH^-) and sulfate (SO_4^{2-}). Our approach employs a set of “logical operators” (*sensu* Mars and Rowan, 2006) that target three spectral characteristics of alunite: the 2.17-2.2- μm OH^- absorption; the 9- μm SO_4^{2-} absorption; and the negative spectral

slope between 0.8 and 1.65 μm . We test the logical operators that we develop by examining the spectra of ground samples obtained at Cuprite Hills, Nevada, a well-studied calc-alkalic porphyry system (Abrams and Ashley, 1980; Mars and Rowan, 2006). This site allows us to test the effectiveness of our logical operator methodology in places where carbonates, detrital clays, limonite, sulfates, and vegetation are co-mingled with alunite at the pixel level. We show that the resulting methodology is an inexpensive, easy to implement, and reliable method for discovering new porphyry mineral deposits that can be applied to a variety of exploration problems. Ultimately, the methodology presented here may lead to an increase in epithermal and porphyry copper ore discoveries at a time when the easily located discoveries have already been made.

2. Background

Porphyry copper and epithermal silver-gold deposits are both known as oxidized intrusion-related (OIR) deposit types (Robert et al., 2007). OIR deposits are products of large, intermediate to felsic porphyry stocks that form at continental and oceanic convergent margins (Robert et al., 2007). Porphyry copper and epithermal silver-gold deposits are known to be associated with hydrothermal clays, such as alunite (Guilbert and Park, 2007). This makes alunite a good proxy for remotely sensing OIRs with remotely-sensed, multispectral images. In this section we introduce the types of alteration zones within these deposit types, as well as the types of enrichment. In addition we explain the argillic logical operator previously developed by Mars and Rowan (2006) to detect these deposits.

2.1 Porphyry Copper Deposits

A porphyry copper deposit (PCD) is classified as either “simple” or “complex” (Guilbert and Park, 2007). The ores of a simple PCD are either located entirely within the porphyritic intrusive rocks that created the ore, or entirely within the country rock adjacent to the intrusion. Complex PCDs, on the other hand, cross in and out of the intrusion and the country rock. Beyond this, the definition of a PCD is not universally accepted. The most common description involves a large, low- to medium-grade (~0.35-2% Cu ore) deposit that formed due to a shallow, calc-alkaline porphyritic intrusion. In this deposit type, the host rock adjacent to the intrusion exhibits sulfide and silicate zoning that includes: (a) potassic-propylitic, alkali metasomatic alteration; and (b) phyllic-argillic, hydrolytic alteration (Figure 1; Mars and Rowan, 2006).

2.2 Epithermal Silver-Gold Deposits

Epithermal Silver-Gold deposits (ESGD) are hydrothermal deposits that occur at shallow depths and low temperatures (50-300°C) (Guilbert and Park, 2007). Because ESGDs occur at shallow depths in tectonically active regions, they have the tendency to be eroded. Therefore, very few ESGDs are seen in pre-Cenozoic host rocks.

ESGDs can be directly related to deep intrusive bodies, but unlike PCDs, ESGDs usually have no visible association with the intrusion. The country rocks near the conduits that aid the flow of hot meteoric fluids (i.e. epithermal veins) are usually heavily altered. The alteration can spread for long distances due to high porosity and permeability in the host rocks that allow hot meteoric fluids to flow. The primary alteration products in ESGDs are: alunite, chlorite, sericite, zeolites, clays, adularia, silica, and pyrite (Guilbert and Park, 2007). These minerals are formed by the same alteration processes that form PCDs: potassic-propylitic, alkali metasomatic alteration; and phyllic-argillic, hydrolytic alteration (Figure 1b). However, in ESGDs, these

processes occur in a different spatial pattern than in PCDs (Figure 1b). In ESGDs, phyllic-argillic alteration zones occur closer to the surface than in PCDs, whereas, potassic-propylitic alteration zones are deeper and closer to the epithermal veins in ESGDs than they are in PCDs (Figure 1b). In addition, sulfosalt ore minerals are common in ESGDs, including silver sulfantimonides and sulfarsenides, and silver and gold tellurides.

2.3 Alteration Assemblages

Two of the types of alteration that occur in PCDs and ESGDs, potassic and propylitic, are created by metasomatism (Guilbert and Park, 2007). Metasomatism chemically alters the host rock by the action of iron- and sulfur-bearing hydrothermal fluids, often resulting in potassium feldspar replacements. Potassic alteration due to metasomatism occurs when a calc-alkaline porphyritic intrusion is intruded into the host rock and produces potassium feldspar, quartz and biotite, as well as some sericite (a fine grained muscovite) and anhydrite. Propylitic alteration, on the other hand, results in feldspathic host rock being replaced with chlorite, epidote, carbonate, and albite.

Two other types of alteration that occur in PCDs and ESGDs, phyllic and argillic, are created by hydrolysis (Guilbert and Park, 2007). Hydrolysis is the process of producing hydrous silicates from anhydrous host rocks by the introduction of a hydrothermal fluid rich in hydrogen cations (i.e., acidic water). Hydrolysis is primarily responsible for producing mica and clay minerals, including alunite and kaolinite in argillic alteration zones, as well as sericite in phyllic zones. Phyllic alteration results in an abundance of sericite and pyrite. Argillic alteration converts plagioclase and amphibole into alunite, kaolinite, and montmorillonite. Argillic alteration occurs at relatively lower temperatures than metasomatic alteration. Since alunite is a

common hydrothermal mineral in ESGDs and PCDs and in secondary enrichment zones, it is an excellent multi-purpose proxy for ESGDs and PCDs in regional mineral exploration.

2.4 Hypogene and Supergene Enrichment

In both PCDs and ESGDs, there are two stages of mineral enrichment: hypogene and supergene (Guilbert and Park, 2007). The first stage of enrichment in the host rock is called hypogene enrichment, which takes place as a porphyritic intrusion rises through the country rock. This stage involves the generation of the previously mentioned potassic, propylitic, phyllic, and argillic alteration zones (see Sections 2.1 and 2.2). After this initial stage of mineralization, groundwater percolating through the mineralized host rock can produce supergene enrichment.

Supergene enrichment requires permeable host rock, abundant pyrite, acid-soluble ore-metal-bearing minerals, and a subjacent reducing environment, such as the groundwater table (Guilbert and Park, 2007). As the oxidized meteoric water seeps down to the water table, it creates a stratigraphy of weathering zones, which together are called the supergene zone (Figure 2). The uppermost zone, the leached zone, typically shows honeycomb patterns of hydrous iron oxides (e.g., jarosite, limonite, goethite) marking where ore minerals were once present. The oxidized zone, which lies below the leached zone, is where dissolution of the ore-metal-bearing minerals (i.e. pyrite, chalcopyrite, sphalerite) to elemental cations in solution occurs. The cations are then transported down to the water table, where reducing conditions exist, allowing the cations in solution to reprecipitate and mineralize to form the supergene-enriched zone superimposed on the original hypogene alteration (Figure 2). It should be noted that leaching can redistribute several elements, but copper is the most common one.

2.5 Alteration Exploration Using Remote Sensing

As a result of supergene enrichment, minerals such as alunite, kaolinite, and hydrous iron oxides and sulfates are left behind in the leached and oxidized zones (Figure 2). If the leached and oxidized zones are exposed at the surface by uplift and/or erosion, they can serve as proxies for the ore enrichment below. Many of the residual minerals in the supergene zone have unique signatures in reflectance spectra that allow us to map them easily using remote sensing methods. For example, alunite and kaolinite show two unique absorptions in their reflectance spectra that are associated with OH^- and SO_4^{2-} . The OH^- produces a doublet absorption at 2.17-2.2 μm that is seen in both alunite and kaolinite (Figure 3; Mars and Rowan, 2006), while an absorption produced by SO_4^{2-} occurs at ~9 μm only in alunite (Figure 3; Bishop and Murad, 2005). Hydrous iron sulfates and silicates – e.g., limonite, hematite, goethite, and jarosite – show a positive spectral slope at ~1 μm , allowing us to differentiate them from alunite which has a negative spectral slope at ~1 μm (Figure 4).

Although we seek to target alunite associated with PCDs and ESGDs, we also need to map the phyllic zone in order to avoid including it in the argillic zone maps. For example, sericite (fine grained muscovite) is an abundant mineral in phyllic zones and, like alunite, also shows an absorption produced by OH^- at ~2.2 μm (Figure 3; Mars and Rowan, 2006). This ~2.2 μm absorption can be confused with that of alunite and kaolinite if the precise wavelength of the band center of the absorption is not measured. With this in mind, an approach to distinguishing between alunite, kaolinite, and sericite is the logical operator methodology (e.g., Mars and Rowan 2006).

2.6 Argillic Logical Operators

Mars and Rowan (2006) used a logical operator approach to regionally map hydrothermally altered rocks that are commonly found in PCDs and ESGDs. Logical operators are mathematical expressions that compare, for example, one or more band ratios to predetermined threshold values. The band ratios and the threshold values are chosen by examining the slopes and/or the absorption/reflection strengths of particular spectral features unique to the target material(s) in lab reflectance spectra. The individual band ratio-to-threshold comparisons, implemented using inequalities, are linked by a string of Boolean IF, THEN, AND, OR and NOT operators. In this way, the logical operator creates a byte image output that consists of zeros and ones. Zeros are created when a pixel fails at least one of the Boolean tests in the logical operator, and a one is assigned to the pixel if it passes all the Boolean tests in the logical operator. The zeros in the resulting byte image are also called a “mask” since those pixels are essentially removed from the output by the assignment of zero digital number to that location. The ones in the resulting byte image indicate those pixels that meet the criteria built-in to the design of the logical operator, and, hence, mark the potential locations of the target material(s). The logical operator described by Mars and Rowan (2006) is designed to mask out vegetation and shadows and to target phyllic or argillic alteration minerals, including alunite, kaolinite, and sericite.

The logical operator used by Mars and Rowan (2006) to differentiate argillic from phyllic alteration is:

$$\left(\left(\frac{band3}{band2} \leq 1.35 \right) \& (band4 > 260) \& \left(\left(\frac{band4}{band5} \right) > 1.25 \right) \right. \\ \left. \& \left(\left(\frac{band5}{band6} \right) \leq 1.05 \right) \& \left(\left(\frac{band7}{band6} \right) \geq 1.03 \right) \right) \quad (1),$$

where & is the Boolean AND. The vegetation mask is the first expression in Equation (1) and uses the ratio of ASTER band 3 to ASTER band 2 (a simple vegetation index) to target the characteristic spectral signature of vegetation in the visible-near infrared (VNIR), also known as the “red edge” (Birth and McVey, 1968; Cohen, 1991; Colombo et al., 2003; Mars and Rowan, 2006). The red edge marks a sharp increase in the reflectance of green, healthy vegetation at $\sim 0.7 \mu\text{m}$ (band 3 in ASTER data) compared to the visible red (band 2 in ASTER data). Through the analysis of spectral library and image reflectance spectra, Mars and Rowan (2006) determined that an ASTER band 3/2 ratio value of ≤ 1.35 indicates areas that contain no vegetation. The second expression in Equation (1) masks dark pixels, including shadows and mafic rocks by taking advantage of a known problem with the ASTER instrument known as “cross talk” (Rowan and Mars, 2003; Mars and Rowan, 2006). The cross-talk defect allows light to leak from the band 4 optical path into the band 5 and 9 detectors (Mars and Rowan, 2006). Cross-talk affected pixels that have low reflectance in ASTER band 4 will therefore show anomalously high reflectance values in ASTER bands 5 and 9 (Mars and Rowan, 2006). Bands 6 and 8 are not directly affected by cross-talk, but high reflectances in band 5 and 9 will erroneously deepen absorption features at bands 6 and 8 (Mars and Rowan, 2006). Mars and Rowan (2006) determined that ASTER band 4 values less than 260 indicate pixel locations whose spectra are particularly impacted by cross-talk effects.

The third, fourth, and fifth expressions in Equation (1) were used by Mars and Rowan (2006) to map the 2.17-2.2- μm absorption associated with OH^- in alunite and kaolinite and also to differentiate argillic (i.e. alunite and kaolinite) alteration zones from phyllic (i.e. sericite) alteration zones. Since the sericite OH^- absorption is within $\sim 0.05 \mu\text{m}$ of the OH^- absorption in the reflectance spectra of alunite and kaolinite (Figure 5), Mars and Rowan (2006) analyzed lab

spectra to determine the appropriate band ratio for differentiating among alunite, kaolinite, and sericite. Using ASTER spectra of alunite and kaolinite (argillic alteration) (Figure 5), Mars and Rowan (2006) determined that band 4 reflectance is 25% greater than reflectance in band 5 when argillic alteration is present. Therefore an ASTER band 4/5 ratio greater than 1.25 (third term in Equation (1)) will map the 2.17 μm feature seen in argillic alteration zones (Figure 5). Similarly Mars and Rowan (2006) determined that ASTER band 5 reflectance is 5% lower than reflectance in band 6 in argillic rocks. Therefore an ASTER band 5/6 ratio less than 1.05 (fourth term in Equation (1)) will delineate argillic from phyllic alteration (Figure 5). Mars and Rowan (2006) also determined that ASTER band 7 reflectance is 3% greater than reflectance in band 6 in argillic rocks. Therefore an ASTER band 7/6 ratio greater than or equal to 1.03 (fifth term in Equation (1)) will map the 2.2 μm feature seen in argillic alteration zones (Figure 5).

A weakness of the Mars and Rowan (2006) argillic logical operator (Equation 1) applied to mapping PCDs and ESGDs has been its inability to distinguish alunite from carbonates, detrital clays, iron oxides, iron sulfates, and vegetation (Clark et al., 1993; Clark and Swayze, 1996; Rowan and Mars, 2003; Mars and Rowan, 2006). This is because limestone and jarosite have a $\sim 2.25\text{-}\mu\text{m}$ OH^- absorption that is similar to the $2.2\text{-}\mu\text{m}$ OH^- absorption exhibited by alunite (Rowan and Mars, 2003; Bishop and Murad, 2005). In addition to jarosite and limestone, detrital clays with $2.2\text{-}\mu\text{m}$ absorptions (i.e. illite and montmorillonite), common in alluvium but not associated with alunite, may also be inadvertently mapped by the argillic operator.

With this in mind, an alternative might be to use a logical operator that also targets the $9\text{-}\mu\text{m}$ absorption associated with SO_4^{2-} in alunite (Bishop and Murad, 2005). However, because quartz and carbonate also have a significant $9\text{-}\mu\text{m}$ absorption (Figure 3) (Rowan and Mars, 2003), they may be erroneously included in alunite maps based on the $9\text{-}\mu\text{m}$ absorption. Another

possibility is to target the spectral slope between 0.8 μm and 1.65 μm (Figures 3 and 5). Hydrous iron sulfates and silicates – e.g., limonite, hematite, goethite, and jarosite – show a positive spectral slope between 0.8 and 1.65 μm , whereas alunite shows a negative slope (Figure 4). The best strategy, however, may be to use a combination of all the spectral features unique to alunite (OH^- and SO_4^{2-} absorptions and spectral slope) to limit the potential for misidentification.

2.7 Mineral Mapping Using Hyperspectral Data

The application of hyperspectral data to mineral exploration is promising but has so far been limited to due poor spatial coverage, and complicated and computationally extensive processing. In this study we compare our results to maps of alunite-rich regions built by the Airborne Visible/Infrared Imaging Spectrometer (AVIRIS). AVIRIS is a hyperspectral imager that flew aboard a Twin Otter aircraft 4 km above ground level to acquire the data used by Swayze et al. (2014). AVIRIS measures wavelengths from 0.4 to 2.5 μm in 224 bands, with a spatial resolution of 4-6 m and a spectral resolution of 0.01 μm (Green et al., 1998; Swayze et al., 2014). Swayze et al. (2014) used AVIRIS data to map OH^- absorptions associated with clays (kaolinite and alunite), micas, sulfates and carbonates in Cuprite Hills (Swayze et al., 2014). The resulting map shows the spectrally dominant materials (clays, micas, sulfates, and carbonates) with strong spectral features at 1.3-2.5 μm (Figure 6). Swayze et al. (2014) verified their map using: (1) comparisons to published maps and reports; (2) field observations; (3) mineralogical analyses of field samples (i.e. X-ray diffraction, X-ray fluorescence, electron probe microanalysis, and scanning electron microscopy); and (4) comparison of AVIRIS spectra to laboratory spectra (Swayze et al., 2014).

3. Cuprite Hills, Nevada

Cuprite Hills, Nevada is a well-studied area that contains an abundance of hydrothermally-altered rocks that include the minerals we are concerned with in this study: alunite, kaolinite, calcite, quartz and sericite (Ashley and Abram, 1980; Rowan and Mars, 2003; Mars and Rowan, 2006; Swayze et al., 2014). Cuprite Hills is located ~15 km south of Goldfield in southwestern Nevada (Figure 7). Highway 95 passes through the area making it easy to access, and its low relief makes field work easy. In addition, the low relief reduces the need to apply illumination and topographic shadowing corrections to remotely-sensed imagery.

The host rocks in the Cuprite Hills belong to the Cambrian Harkless (~1000 m thick), Mule Spring (~140 m thick), and Emigrant (~1700 m thick) Formations, all of which are exposed in the eastern portion of Cuprite Hills (Figure 8) (McKee, 1968; Ashley and Abrams, 1980; Swayze et al., 2014). The Harkless Formation consists of phyllitic siltstone with some sandy limestone, and includes muscovite, chlorite, biotite, and quartz (Swayze et al., 2014). The Mule Spring Formation consists of thinly-bedded limestone and siltstone, and the Emigrant Formation consists of thinly-bedded limestones and chert (Swayze et al., 2014). The Mule Spring and Emigrant Formations, therefore, primarily include the minerals quartz and calcite.

Tertiary volcanics overlie the Cambrian section in the area. There are four Tertiary volcanic units (in stratigraphic order from oldest to youngest): the Siebert Tuff (85-160 m thick); an unnamed porphyritic basalt (0-10 m thick); the Thirsty Canyon Tuff (18-30 m thick); and the Pediment Basalt (3 m thick) (Ashley and Abrams, 1980; Swayze et al., 2014). The two tuff formations consist of quartz latitic felsite, rhyolite, and latite tuff, all interbedded with conglomerate and sandstone (Figure 8; Ashley and Abrams, 1980; Swayze et al., 2014). As a

whole, the Tertiary volcanic units contain the following minerals: quartz, plagioclase, limonite, alkali feldspar, and scarce amounts of biotite and hornblende.

The Siebert Tuff is a coarse-grained ash flow tuff with pumice lapilli and a basal volcanoclastic conglomerate and sandstone (Figure 8; Ashley and Abrams, 1980; Swayze et al., 2014). It covers most of the eastern portion of Cuprite Hills except where the younger Thirsty Canyon Tuff overlies it (Figure 8). The western portion of the Siebert Tuff is exposed as a sliver adjacent to the Cambrian rock units (Figure 8). A small, un-named porphyritic, plagioclase- and olivine-bearing basalt of Miocene age overlies the Siebert Tuff and is exposed in the eastern part of the study area (Figure 8). The overlying Thirsty Canyon Tuff consists of sodic rhyolite ash-flow tuff that has been dated to be ca. 7.6 Ma (Figure 8) (Ashley and Abrams, 1980; Swayze et al., 2014). This unit is largely exposed in the northeast and overlies both the Siebert Tuff and the un-named basalt (Figure 8). The youngest (upper Miocene; Ashley and Abrams, 1980; Swayze et al., 2014) Tertiary unit is the Pediment Basalt, which has a minor outcrop in the western part of the study area (Figure 8).

Three types of hydrothermal alteration, caused by hydrolysis and metasomatism, are exposed in the Cuprite Hills: silicification, opalization, and argillization. These occurred as hydrothermal fluids passed through the country rock before 7.6 Ma, prior to the eruption of the Thirsty Canyon Tuff, therefore leaving it devoid of mineralization (Ashley and Abrams, 1980; Swayze et al., 2014). Silicification produced abundant quartz, calcite, kaolinite, and alunite that are seen in veins and disseminated in the Siebert Tuff and parts of the Harkless Formation (Figure 9; Ashley and Abrams, 1980; Swayze et al., 2014). Opalization, which is the mineralization of largest extent in the Cuprite Hills, produced alunite, kaolinite, opal, dickite, pyrophyllite, calcite, buddingtonite, muscovite, montmorillonite, and jarosite within most of the

Siebert Tuff and parts of the Harkless and Mule Springs formations (Figure 9) (Ashley and Abrams, 1980; Swayze et al., 2014). Argillization, the least abundant type of hydrothermal alteration in the Cuprite Hills, produced kaolinite, bleached biotite, opal, montmorillonite, and abundant limonite in the Siebert Tuff (Figure 9) (Ashley and Abrams, 1980; Swayze et al., 2014).

4. Data

We use data from the Advanced Spaceborne Thermal Emission and Reflection Radiometer (ASTER), an instrument on board the Terra satellite (Abrams, 2002). Unlike a hyperspectral instrument, like AVIRIS, that collects data in tens or hundreds of closely-spaced spectral bands, ASTER is a multispectral instrument with lower spectral resolution, collecting data in 14 bands distributed amongst 3 subsystems: the visible and near-infrared (VNIR); the shortwave infrared (SWIR), and the thermal infrared (TIR) (Abrams, 2002; Mars and Rowan, 2006). The VNIR subsystem consists of 3 bands ranging from 0.52-0.86 μm with a spatial resolution of 15 m per pixel (Table 1). The SWIR consists of 6 bands ranging from 1.6-2.43 μm with a spatial resolution of 30 m per pixel (Table 1). The TIR consists of 5 bands ranging from 8.125-11.65 μm with a spatial resolution of 90 m per pixel (Table 1).

Because of the relatively low spatial resolution and much greater swath width of ASTER compared to hyperspectral instruments like AVIRIS, only one ASTER scene was required to cover the entire Cuprite Hills area (Table 1). It was acquired August 24, 2001 (ID#: 00308242001185220). The georeferenced ASTER surface reflectance and emissivity data products used in this study were generated on-demand and downloaded from the NASA Earth Observing System Data and Information System (EOSDIS; <http://reverb.echo.nasa.gov>). The

Level 2 data products we used, AST_07XT and AST_05 (Table 1), were generated from the raw Level 1A data of the Cuprite Hills scene. The AST_07XT product is surface reflectance in the both VNIR and SWIR that has been atmospherically corrected (Thome et al., 1999) as well as crosstalk-corrected (Thome et al., 1999; Iwasaki et al., 2002). The AST_07XT product comprises two data files with different spatial resolutions, one for surface reflectance in the VNIR (3 bands; 15 m/pixel) and the other for surface reflectance in the SWIR (6 bands; 30 m/pixel) (Table 1). The AST_05 product is surface emissivity in the TIR obtained by performing both an atmospheric correction as well as temperature-emissivity separation (Gillespie et al., 1999) (Table 1). The AST_05 product is a single image file with a different spatial resolution (5 bands; 90 m/pixel) than either of the two AST_07XT image files.

5. Methods

The method for targeting alunite that we present builds on the Mars and Rowan (2006) argillic logical operator (Equation 1). We improve on the previous work by seeking to reduce the influence that the presence of iron oxides, iron sulfates, carbonates, and detrital clays have on the reliable identification of alunite. To do this, we modify the Mars and Rowan (2006) logical operator to take into account the slope between 0.8 and 1.65 μm , and we also develop a separate SO_4^{2-} logical operator that targets the 9- μm absorption present in alunite (Bishop and Murad, 2005). With the combined results of these two logical operators, we can find pixels that exhibit spectral features unique to alunite. We implement our technique using the ENVI image processing software and ArcGIS.

5.1 ASTER Preprocessing

Before the logical operator processing could be done, the AST_05 and AST_07XT images had to be “layer stacked”. This preprocessing was required because the Level-2 VNIR, SWIR and TIR image files have different spatial resolutions (15 m/pixel, 30 m/pixel, and 90 m/pixel, respectively), and, as a result, they cannot be mathematically combined (i.e. band ratioed, etc.) without spatial resampling to a common resolution. Layer stacking produces a single, multi-band image, with a single user-defined pixel size and projection, from georeferenced input images with different spatial resolutions. The resulting composite data file can then be used for further processing. We chose to resample the AST_07XT SWIR bands and the AST_05 TIR bands to match the 15-m resolution of the AST_07XT VNIR bands with the nearest neighbor resampling method. Doing so preserves the native spatial resolution of the VNIR bands and reduces the pixel size of the SWIR and TIR pixels to 15-m, without losing any information. After layer stacking, we spatially subset the image data so as to only include the area immediately surrounding the Cuprite Hills in order to minimize the amount of data to process and store.

5.2 SO₄²⁻ Logical Operator

A deep and broad absorption feature associated with SO₄²⁻ in alunite is present in the TIR at 9 μm (Figure 3). Since detrital clays do not exhibit a 9-μm absorption, this absorption can be used to distinguish alunite from detrital clays. However, quartz and carbonates also have 9-μm absorptions. Carbonates exhibit a smaller 9 μm absorption compared to quartz and alunite (Figure 3) (Rowan and Mars, 2003), therefore a band ratio targeting deep 9 μm SO₄²⁻ absorptions can be used to avoid mapping carbonate.

To map SO_4^{2-} , we use ASTER bands 12 (9.1 μm) and 13 (10.6 μm), which straddle the center wavelength (9 μm) of the SO_4^{2-} absorption. With these bands, we implement the following logical operator (the “ SO_4^{2-} operator”) in ENVI using the “band math” function:

$$\left(\left(\frac{\text{band3}}{\text{band2}} \right) \leq 1.35 \right) \& (\text{band4} > 260) \& \left(\left(\frac{\text{band13}}{\text{band12}} \right) \geq 1.08 \right) \quad (2),$$

where the first two terms are the vegetation mask and dark pixel mask, respectively, used by Mars and Rowan (2006) (c.f. Equation 1). Using the AVIRIS mineral maps produced by Swayze et al. (2014) (Figure 6) as a guide, we extracted ASTER TIR spectra from several regions indicated by Swayze et al. (2014) to host alunite-bearing rocks (Figure 6). We determined that ASTER band 13 reflectance is $\sim 8\%$ greater than reflectance in band 12 for pixels that contain alunite (Figure 6). Therefore an ASTER band 13/12 ratio greater than 1.08 should delineate sulfate-bearing rocks from carbonate and quartz (Mars and Rowan, 2006). However the SO_4^{2-} logical operator will still map silicified rocks in addition to alunite because quartz also contains a 9 μm absorption.

5.3 OH^- -FeO Logical Operator

In order to avoid mapping quartz, iron oxides, and iron-sulfates (i.e. jarosite, hematite, limonite), we modify the argillic logical operator of Mars and Rowan (2006) (Equation 1) to include another term that delineates alunite from quartz, iron oxides, and iron-sulfates. We call this modified logical operator the “ OH^- -FeO logical operator” and implement it in ENVI using the “band math” function:

$$\left(\left(\frac{\text{band3}}{\text{band2}} \right) \leq 1.35 \right) \& (\text{band4} > 260) \& \left(\left(\frac{\text{band4}}{\text{band3}} \right) \leq 1 \right) \& \left(\left(\frac{\text{band4}}{\text{band5}} \right) > 1.25 \right) \& \left(\left(\frac{\text{band5}}{\text{band6}} \right) \leq 1.05 \right) \& \left(\left(\frac{\text{band7}}{\text{band6}} \right) \geq 1.03 \right) \quad (3),$$

where the ASTER band 4/3 ratio in the third term differentiates alunite from both iron oxides and sulfates by their spectral slope between $\sim 1.65\ \mu\text{m}$ and $\sim 0.8\ \mu\text{m}$ (Figure 4). The spectra of iron oxides and iron sulfates have positive slopes between band 3 ($0.8\ \mu\text{m}$) and 4 ($1.65\ \mu\text{m}$) (Figure 4) (Mars and Rowan, 2006). Alunite, however, has a negative slope between band 3 ($0.8\ \mu\text{m}$) and 4 ($1.65\ \mu\text{m}$) (Figure 4). Therefore, pixels for which the ASTER band 4/3 ratio is less than or equal to 1 will have a spectral slope consistent with alunite.

5.4 Alunite Map

We combine the SO_4^{2-} and OH^- -FeO logical operator maps to produce an “alunite map” that will more accurately depict alunite-rich rocks than previous attempts to map alunite. This is done by exporting the SO_4^{2-} and OH^- -FeO logical operator map byte images from ENVI as TIFF image files. The TIFF-format files are then imported to ArcGIS, and the resulting rasters are converted to shapefiles. The shapefiles preserve the locations that have binary 1 assignments in the SO_4^{2-} and OH^- -FeO logical operator maps. The shapefiles are then logically combined with the ArcGIS intersection tool to produce a single shapefile that shows the most probable locations of alunite.

5.5 Cuprite Hills Field Work

To validate and verify the performance of our logical operator approach to mapping alunite, we did a ground truth field investigation at Cuprite Hills in January 2013. For this test, we collected ~ 35 samples from the eastside portion of Cuprite Hills for the purpose of making reflectance spectral measurements and the construction of a library of laboratory spectra. We aimed to sample the areas indicated by the OH^- and SO_4^{2-} logical operator maps to contain

alunite, kaolinite, quartz, and sulfates. The logical operator maps were generated prior to the fieldwork. Sample locations are shown in Figure 10. We chose not to gather samples in the western portion of Cuprite Hills since the altered units in that area have been covered by alluvium (i.e. detrital clay, carbonates, and iron oxides) that have been shed off the Cambrian sedimentary units. This alluvium is dominated by detrital clays and carbonates, which exhibit spectra that contain $\sim 2.2\text{-}2.3\text{ }\mu\text{m}$ absorptions (see section 2.5) and will cause ASTER spectra obtained from this area to exhibit a $2.2\text{-}2.3\text{ }\mu\text{m}$ absorption that is not associated with alunite.

At each site, we collected at least 1 kg of representative material to ensure enough sample was available to perform multiple laboratory measurements, if necessary. Most of the samples were of loose, rocky soil taken from colluvial units covering the hillsides. Outcrops that were large enough to be seen in ASTER imagery ($>30\text{ m}$ in extent) were sampled using a rock hammer. Samples were collected in separate gallon-sized zippered plastic bags. In order to ensure the integrity of the bag and reduce the risk of sample contamination, we doubled-bagged each sample. Each sample was assigned a CHxxx code, where the CH stands for Cuprite Hills, and xxx is unique a three-digit sample number (Table 2).

5.6 Reflectance Spectroscopy of Cuprite Hills Samples

The Cuprite Hills samples were processed and analyzed at The University of Texas at El Paso (UTEP). Each sample was crushed with a jaw crusher and then sieved to 1-mm and 500- μm mesh sizes. Care was taken to reduce contamination between samples, and all tools were thoroughly cleaned and inspected for contamination between sample preparations. We used the 500- μm size fraction for consistency in our further analyses of the samples.

All samples were analyzed using the GER 3700 VNIR-SWIR spectroradiometer (Table 3) at UTEP. This instrument measures radiance in 645 bands between 0.3 μm and 2.5 μm , with a spectral resolution of 0.0015 μm in the 0.3-1.05 μm range, 0.0065 μm in the 1.5-1.9 μm range, and 0.0095 in the 1.9-2.5 μm range (Table 3). The GER 3700 does not measure radiance in the TIR. The spectroradiometer was periodically calibrated (every four measurements) using a standard white reflectance target plate. Radiance values obtained from the calibration target were used to normalize the radiance values from the measured samples in order to obtain reflectance. All the laboratory reflectance spectra we obtained from the Cuprite Hills samples were then compiled into a spectral library (Appendix 1).

5.7 Analysis of Laboratory Spectra

The Cuprite Hills laboratory spectra were compared to the USGS laboratory spectrum (Clark et al., 1993) of alunite (AL706; 15 μm grain size). The larger grain size in our samples could cause the 2.17-2.2 OH^- absorption to shift and widen relative to the laboratory spectrum of alunite. However, the shifted and widened 2.17-2.2 μm absorption did not affect our ability to determine if alunite was present in the samples. By doing this comparison we can determine whether the Cuprite Hills sample spectra are consistent with spectral features attributed to alunite. For example, a sample collected in regions indicated by the OH^- -FeO logical operator map to exhibit OH^- absorptions would be expected to contain both the 2.17-2.2 μm absorption due to OH^- , as well as the negative slope between 0.8 μm and 1.65 μm .

6. Results

6.1 SO_4^{2-} Logical Operator

The SO_4^{2-} logical operator identifies a majority, but not all, of the Siebert Tuff formation in the Cuprite Hills scene as containing alunite, quartz, or jarosite (Figure 8 and 11). Since the Siebert Tuff contains abundant quartz, it is important to understand why the entire Siebert Tuff is not mapped as quartz by the SO_4^{2-} logical operator (Figure 11). Three possible reasons for why the entire Siebert Tuff is not mapped as sulfate or quartz are: (1) vegetation coverage; (2) shadowing; and/or (3) spectral mixing with materials that do not exhibit a 9 μm absorption, such as detrital clays or iron oxides, and that reduce the 9- μm absorption associated with quartz and sulfate.

The SO_4^{2-} logical operator also identifies pixels in some areas within the Cambrian sedimentary units and the alluvium east of the Cambrian outcrops as containing alunite, quartz, or jarosite (Figures 8 and 11). The identified pixels within the Cambrian sedimentary units are likely sandstone (quartz). The SO_4^{2-} logical operator, however, does not map any pixels associated with the Thirsty Canyon Tuff as quartz, possibly due to the lack of silicification or alteration (i.e. argillic-phyllitic, potassic-propylitic) in this unit (Figure 8 and 11).

When we compare the results of the SO_4^{2-} logical operator (Equation 2) to the Mars and Rowan (2006) argillic logical operator (Equation 1) we see that they are very similar (Figures 11 and 12). However, the Mars and Rowan (2006) argillic logical operator maps a larger area in the alluvium as argillic-rich compared to what is mapped as either alunite, quartz, or jarosite by the SO_4^{2-} logical operator (Figures 11 and 12).

6.2 OH^- -FeO Logical Operator

The OH⁻-FeO logical operator identifies pixels within the Siebert Tuff formation as alunite, kaolinite, and/or detrital clays (Figures 8 and 11). The OH⁻-FeO logical operator map (Figure 11) does not indicate the presence of alunite, kaolinite, and/or detrital clays in the center of the altered Siebert Tuff, in the eastern portion of Cuprite Hills (Figures 9 and 11), indicating argillic minerals (kaolinite and alunite) are not present in the center of the Siebert Tuff.

6.3 Alunite Map

The alunite map (Figure 13) shows alunite in the same regions of argillic alteration as shown by the alteration map produced by Ashley and Abrams (1980) (Figure 9 and 13). The alunite map (~112 km²) (Figure 13) contains ~95% (2170 km²) fewer pixels that are potentially alunite than does the Mars and Rowan (2006) argillic operator map (~2282 km²) (Figure 12). The reduction in area in our alunite map, compared to the Mars and Rowan (2006) argillic operator map, illustrates the effectiveness of our alunite map to specifically target alunite and not detrital clays, quartz, carbonates, iron oxides, or jarosite. The alunite map does not map any of the Cambrian sedimentary units nor the alluvium in the Cuprite Hills scene as alunite (Figure 13). In addition, when compared to the AVIRIS mineral map (Figure 6) (Swayze et al., 2014), we see that regions mapped as alunite by our alunite map are spatially correlative to alunite regions within the AVIRIS mineral map (Figure 6) (Swayze et al., 2014).

6.4 Cuprite Hills Samples

Samples CH008, CH018, CH020, and CH021 were collected from areas that, according to our ASTER-derived maps, show neither the OH⁻ (Figure 14) nor SO₄²⁻ signatures that would be consistent with alunite, quartz, or jarosite (Figure 5 and 11). However, the lab spectra for

CH008, CH018, and CH021 exhibit both the $\sim 2.15\ \mu\text{m}$ absorptions and negative slopes between $0.8\ \mu\text{m}$ and $1.65\ \mu\text{m}$ that are consistent with alunite (Appendix 1). The $2.17\text{-}2.2\text{-}\mu\text{m}$ OH^- absorption associated with alunite is shifted to the left (to shorter wavelengths) by $\sim 0.02\ \mu\text{m}$ in the lab spectra of samples CH008, CH018, and CH021 (Appendix 1). The lab spectrum for sample CH020, only exhibits the negative slope between $0.8\ \mu\text{m}$ and $1.65\ \mu\text{m}$, and no $\sim 2.15\ \mu\text{m}$ absorption.

Samples CH005, CH006, CH007, and CH019 were collected from areas that, according to the OH^- map (Figure 11), have OH^- signatures consistent with alunite, detrital clays, and carbonate (Figure 5 and 11). According to the SO_4^{2-} map (Figure 11), these samples should also not exhibit significant $9\text{-}\mu\text{m}$ absorptions in TIR emissivity spectra. The lab spectra of each of these samples has both the $\sim 2.15\ \mu\text{m}$ OH^- absorption and the negative slope between $0.8\ \mu\text{m}$ and $1.65\ \mu\text{m}$, consistent with alunite (Appendix 1). The $2.17\text{-}2.2\text{-}\mu\text{m}$ OH^- absorption associated with alunite is shifted to the left (to shorter wavelengths) by $\sim 0.02\ \mu\text{m}$ in the lab spectra of samples CH005, CH006, CH007, and CH019 (Appendix 1). However, the $\sim 2.15\ \mu\text{m}$ absorptions in the lab spectra of CH005 and CH019 may be questionable since their right shoulders are very shallow (Figure 14; Appendix 1).

Samples CH010, CH011, CH012, CH013, CH014, CH017, CH025, CH029, CH030, CH032, and CH033 were collected from areas that, according to the SO_4^{2-} map (Figure 11), should exhibit $9\text{-}\mu\text{m}$ absorptions in TIR emissivity spectra (Figure 3 and 11). According to the OH^- map, these samples should not have signatures consistent with alunite, detrital clays, and carbonate (Figure 11). However, the lab spectra for each of these samples shows both the $\sim 2.15\ \mu\text{m}$ OH^- absorption and the negative slope between $0.8\ \mu\text{m}$ and $1.65\ \mu\text{m}$, consistent with alunite (Appendix 1). The $2.17\text{-}2.2\text{-}\mu\text{m}$ OH^- absorption associated with alunite is shifted to the left (to

shorter wavelengths) by $\sim 0.02\ \mu\text{m}$ in the lab spectra of samples CH010, CH011, CH012, CH013, CH014, CH017, CH025, CH029, CH030, CH032, and CH033 (Appendix 1). The lab spectra for CH017, CH025, and CH032, however, exhibit questionable $\sim 2.15\ \mu\text{m}$ absorptions since their right shoulders are very shallow (Figure 14; Appendix 1).

Samples CH002, CH003, CH004, CH009, CH016, CH023, CH026, CH027, and CH035 were collected within the regions identified as alunite in our alunite map (Figure 13) (i.e. both the OH^- and SO_4^{2-} logical operators are satisfied). Their lab spectra show the two VNIR-SWIR spectral features that are consistent with alunite (i.e. the $2.17\text{-}2.2\text{-}\mu\text{m}$ OH^- absorption and the negative slope between $0.8\ \mu\text{m}$ and $1.65\ \mu\text{m}$) (Figure 15). The $2.17\text{-}2.2\text{-}\mu\text{m}$ OH^- absorption associated with alunite is shifted to the left (to shorter wavelengths) by $\sim 0.02\ \mu\text{m}$ in the lab spectra for samples CH002, CH003, CH004, CH009, CH016, CH023, CH026, CH027, and CH035 (Figure 15).

7. Discussion

Our logical operators primarily map alunite, kaolinite, quartz, jarosite and iron oxides in the Siebert Tuff formation. However, when used together, they effectively map alunite, which is consistent with the alteration maps presented by Ashley and Abrams (1980) (Figures 8, 9, and 11). In the OH^- and SO_4^{2-} logical operator maps, the silicified-rock in the Siebert Tuff clearly delineates the contact between the unaltered Thirsty Canyon Tuff and the heavily mineralized Siebert Tuff (Figure 11). In addition we show that our maps are consistent with alunite mapped by hyperspectral datasets, indicating that we can use ASTER to map alunite with high confidence and low cost.

7.1 Logical Operator Assssment Using Cuprite Hills Ground Truth

The lab spectra of 20 out of 28 (~71%) analyzed samples (CH003, CH004 CH005, CH006, CH007, CH009, CH010, CH011, CH012, CH013, CH014, CH016, CH019, CH020, CH023, CH027, CH029, CH030, CH033, CH035) are consistent with the alunite map (Figure 11). However, we were unable to determine if the samples predicted to exhibit the 9- μm SO_4^{2-} absorption actually do have the 9- μm absorption because the GER 3700 spectroradiometer cannot measure TIR wavelengths. The locations of all of the alunite-bearing samples (CH002, CH003, CH004, CH009, CH016, CH023, CH026, CH027, and CH035) (Figure 11 and 15) spatially correlate with pixels identified as alunite in the alunite map (Figure 11 and 13).

For all samples with an OH⁻ absorption feature, the lab spectra show this feature shifted ~0.02 μm to the left (to shorter wavelengths) so that it is centered at ~2.15 μm . Mars and Rowan (2006) have shown that such a shift in the OH⁻ absorption can be due to mixing of alunite with kaolinite (Figure 16). The fact that we see a shift in our lab spectra suggests that our samples contain mixtures of alunite and kaolinite. This is expected in argillic alteration zones (see Section 2.3), and is consitent with the argillic alteration pattern mapped by Ashley and Abrams (1980) (Figure 9). The presence of kaolinite and alunite in our samples is also consistent with the AVIRIS mineral map produced by Swayze et al. (2014) (Figure 17). Their map shows that the eastern Cuprite Hills region we sampled is dominated by mixed kaolinite and alunite (Figure 17).

Some of the Cuprite Hills samples were collected from areas that failed the OH⁻-FeO operator, but had lab spectra inconsistent with the remote sensing results (CH008, CH010, CH011, CH012, CHO13, CH014, CH017, CH018, CH021, CH025, CH029, CH030, CH032, and CH033; Appendix 1). Because they failed the OH⁻-FeO operator, these samples either have

positive spectral slopes between 0.8 and 1.65 μm or they lack the OH^- absorption features. The lab spectra for all these samples have the OH^- absorption, which suggests that the problem lies in the ASTER 4/3 band ratio in Equation (3) and spectral mixing of alunite with iron oxides and iron sulfates. Such mixing would cause the spectral slope between 0.8 and 1.65 μm to be positive, rather than the negative slope expected for alunite. If we were to increase the band 4/3 ratio threshold in Equation (3), by just 5%, from 1 to 1.05, the number of pixels identified as alunite, kaolinite, detrital clays, or carbonate by the OH^- -FeO logical operator would increase by 60%, from 10,889 to 17,428 pixels. Some of these additional pixels also pass the SO_4^{2-} logical operator, which would increase the number of pixels identified as alunite by 225%, from 111 km^2 to 250 km^2 .

The degree to which we increase the ASTER 4/3 band ratio depends on how conservative we want the resulting map to be. A small ratio (<1) increases the chances that identified pixels are enriched in alunite more so than iron oxides and jarosite, whereas a larger ratio (>1) may result in a less conservative map that includes increasing amounts of iron oxides and jarosite. While the terms in Equation (3) that identify OH^- will be able to discriminate against iron oxides, jarosite will remain in the resulting map because, like alunite, it contains OH^- .

Given the low spatial and spectral resolution of ASTER, we expect a certain amount of spectral mixing in our alunite map. With the semi-conservative choice of ASTER 4/3 band ratio threshold used here ($=1$), small alunite-bearing outcrops may have been overlooked in the Cuprite Hills, but we are confident that the larger alunite deposits were not. Comparison with previous mapping (Mars and Rowan, 2006.), demonstrates that this is the case (Figures 12 and 13).

Two of the Cuprite Hills samples (CH002 and CH026; Appendix 1) do not appear to contain alunite, even though they were collected from areas that were mapped as alunite-bearing. The reason for this is likely to also be related to spectral resolution and mixing. At the pixel level (15 m/pixel), these areas, which are generally going to contain mixtures of materials, may have spectra consistent with abundant alunite, but, in the field, we may have a relatively high probability of picking samples that are not alunite. A potential way of mitigating against this misfortune would be a sampling strategy where multiple samples are collected per pixel-equivalent area. The disadvantage to this approach would be the large number of samples required.

7.2 Logical Operator Assessment Using Other Datasets

With the issues discussed in the previous section in mind, an alternative way of validating the logical operator approach for mapping alunite with ASTER that we present here is to use other remotely-sensed datasets as points of comparison. For example we can qualitatively compare our alunite map to the Abrams and Ashley (1980) argillic alteration map. The region within the Siebert Tuff that is identified as alunite in the northeast portion of our alunite map (Figure 13) coincides with the northernmost, prominent zones of argillic alteration mapped by Abrams and Ashley (1980) (Figure 9). More quantitatively, we can compare our results to those of Mars and Rowan (2006). Whereas they map 2,282 km² of argillic (kaolinite + alunite) alteration (Figure 12), we map an area of 118 km² as being consistent with abundant alunite (Figure 13). The decrease in area is the result of the SO_4^{2-} operator and the ASTER band 4/3 ratio in our methodology, and all areas identified as containing alunite using our method are included in the argillic zone mapped by Mars and Rowan (2006).

More importantly, the areas indicated by our alunite map to be consistent with alunite spatially correlate with the areas mapped as alunite by Swayze et al. (2014) using AVIRIS hyperspectral data (Figure 17). Swayze et al. (2014) show a circular pattern of alunite-rich outcrops in the center of the eastern portion of the Siebert Tuff (Figure 17). In our alunite map, we see a similar circular pattern of pixels with abundant alunite in the same location (Figure 17). Swayze et al. (2014) also show abundant alunite at the “Alunite Hills” in the western part of the study area (Figure 17). The Alunite Hills are similarly mapped as being abundant in alunite using our logical operator approach, although the area is smaller (3.2 km^2 vs. 13.4 km^2) than that identified by Swayze et al. (2014). The difference in area is likely the result of our choice of ASTER band 4/3 threshold. The spatial correlation between our alunite map and the AVIRIS mineral map (Figure 6 and 13) indicates that the OH^- and SO_4^{2-} logical operators that we employ in this study are reliable.

7.3 Implications for Exploration Geology

Remote sensing is becoming increasingly important for mineral exploration (Toovey, 2011). However, the cost of remotely-sensed data of sufficient quality and quantity may be a financial barrier for some, particularly junior mining companies. In addition, the costs of acquiring and processing of large volumes of remotely-sensed data may be a logistical barrier for even the largest of mining companies. In all cases, the perceived expertise required to integrate remote sensing into an exploration program may be a deterrent. Our methodology using ASTER is sufficiently rapid, inexpensive, simple, yet reliable enough, to solve these problems.

Hyperspectral instruments such as AVIRIS afford the user with tens to hundreds of spectral bands, sufficient to do true spectroscopy, and, in the case of airborne datasets, provides

those at high spatial resolution. However we argue that, for exploration purposes, high spatial and spectral resolution may not be necessary. We have shown that our method using relatively coarse spatial resolution ASTER multispectral data yields reliable results that are similar to those obtained from hyperspectral data. While the logical operator method with ASTER may miss small (or poorly exposed) features at the surface, and while it may be subject to the limitations set by spatial mixing and simple band ratio techniques, our method can be used to process images covering areas in a relatively short amount of time. The possibility of creating regional reconnaissance maps may more than outweigh the lack of detail that hyperspectral data could provide. This is particularly important given the fact that hyperspectral data to date is not widely available, and, when it is, because of the large data volume (i.e. number of pixels and number of bands), it is cumbersome and computationally-expensive to process, especially for regional studies. ASTER scenes, on the other hand have close to global coverage and much larger swaths (60 x 60 km) than any hyperspectral instrument (c.f. AVIRIS swath of a few km for just a handful of places on earth). The larger coverage and smaller volume of data (e.g., ASTER with 14 bands vs. AVIRIS with 224 bands) in multispectral datasets allows for faster processing of larger regions. In addition, ASTER scenes are cheap and easy to obtain, whereas hyperspectral imagery may not even exist in certain areas, regardless of price.

A regional mineral exploration project would start with acquiring ASTER scenes that cover the region of interest, such as the Sierra Madre of Mexico. After applying the remote sensing methodology for targeting alunite described in this study, ESGD and PCD prospects can be identified for further examination. At this point two options are available to further examine the prospects. The more conservative option involves acquiring more data, such as geophysical measurements and/or hyperspectral imagery, prior to acquiring ground samples from the

prospects. The objective of acquiring more data would be confirm that a large deposit exists in the subsurface. Spectroscopy is great for finding minerals at the surface, but it is impossible to quantify how large the deposit is and whether it is economical without other types of data. The riskier option involves sending geologists out to sample each prospect. The second option has more risk because it could cost more money in the long run if the prospects returned samples that do not contain alunite. Time and man-power could be saved by the conservative option. The conservative option increases the chance of success of a given prospect by increasing the amount of information available to make an interpretation before committing significant resources to a field campaign.

Since we have shown our method for mapping alunite with ASTER imagery to be reliable, and comparable to the results obtained using AVIRIS but at a fraction of the time and cost we expect exploration companies to boost exploration efforts of PCDs and ESGDs given the ease and accessibility of ASTER data processing. Even though AVIRIS has better spatial and spectral resolutions than ASTER, it still does not have the coverage that ASTER has, which is nearly global. Furthermore, if an area that a company is exploring is not covered by hyperspectral imagery, it could take months to acquire and process the imagery to begin mapping alunite. In that amount of time, one could map, for example, the entire Sierra Madre of Mexico using ASTER data and our method for targeting alunite and have exploration prospects in line for field work. The benefits of ASTER imagery (i.e. global coverage, cheap, and readily available) make is more economically and logistically viable for use by junior mining companies facing millions of dollars in exploration costs. With our method for targeting alunite, junior and major mining companies will be able to easily explore large regions without risking large economic loss.

8. Conclusions

Alunite is a hydrothermal clay sulfate that is a key target in PCD and ESGD exploration (Guilbert and Park, 2007). Its presence in both the hypogene and supergene enrichment phases makes it a good proxy for remotely targeting these deposits. However, previous studies (e.g., Mars and Rowan, 2006) that have attempted to map alunite with remotely-sensed multispectral data have been unable to adequately exclude the spectral signature of detrital clays, carbonates, and iron oxides. We have described an improved methodology that focuses on three spectral features unique to alunite: 2.17-2.2- μm OH^- absorptions; 9- μm SO_4^{2-} absorption; and a negative slope between 0.8 and 1.65 μm . By modifying the argillic logical operator of Mars and Rowan (2006) to reduce the spectral signature of iron oxides, we have been able to create more accurate maps of OH^- -bearing rocks. Similarly, we use a SO_4^{2-} logical operator that targets significant 9- μm SO_4^{2-} absorptions attributed to alunite, jarosite and quartz, in order to reduce the spectral signature of detrital clays and carbonates and ultimately produce maps depicting alunite, jarosite, and quartz. Including the SO_4^{2-} logical operator in our methodology, as well as modifying the Mars and Rowan (2006) argillic logical operator, was key in reducing the spectral signatures of unwanted materials. The combination of modifying the argillic operator and adding a logical operator that targets SO_4^{2-} allows us to create maps that show where alunite-bearing outcrops are present.

By testing OH^- and SO_4^{2-} logical operators at the well-studied calc-alkalic porphyry deposit at Cuprite Hills, we were able to ensure our alunite map was accurate. We found indications that the threshold value used with the ASTER 4/3 band ratio in our OH^- -FeO logical operator may overlook some small alunite-bearing outcrops, and that, as a result, it can

mistakenly mask out pixels that actually contain alunite. However, a small ASTER 4/3 band ratio threshold is necessary in order to reduce the spectral signal of jarosite, carbonates, and detrital clays. Increasing the ASTER 4/3 band ratio threshold will increase the number of pixels indicated by the OH⁻-FeO logical operator to have alunite. However, due to the increased spectral mixing caused by low spatial and spectral resolution of ASTER data, the increased area indicated by the OH⁻ map to contain alunite will also contain unwanted materials (i.e. alluvium, carbonates, and iron oxides).

We have shown that our alunite maps spatially correlate with alunite-rich regions in the AVIRIS mineral map of Swayze et al. (2014). This is important for junior and major mining companies since ASTER is cheap and widely available dataset, and hyperspectral datasets comparable to AVIRIS can be expensive and have limited availability. Our method for using ASTER data to target alunite would encourage regional exploration for PCD and ESGD deposits using remote sensing methods. Our improved method for targeting alunite should lead to more discoveries of ESGDs and PCDs, as a result of increased regional exploration efforts enabled by new remote-sensing techniques such as ours. Our methodology may prove useful in mining districts such as the Sierra Madre of Mexico where topography and vegetation limit access to certain areas. In addition, it will allow users to weigh the “above-ground risk” (e.g. political instability, taxes, security, etc.) against the economic value of prospects identified using the method developed in this study. Using ASTER imagery and the method for finding alunite presented here as an initial platform for exploration projects will help junior and major mining companies alike plan sampling missions that may lead to the discovery of the next major PCD or ESGD deposit.

References

- Abrams, M., 2002, *ASTER User Handbook (Vol.1)*: Jet Propulsion Laboratory/California Institute of Technology, 135 p..
- Ashley, R. P. and Abrams, M. J., 1980, *Alteration Mapping Using Multispectral Images – Cuprite Mining District, Esmeralda County, Nevada* (USGS, Open-File Report 80-367), 26 p..
- Birth, G. S. and G. McVey, 1968, Measuring the Color of Growing Turf with a Reflectance Spectroradiometer: *Agronomy Journal*, vol. 60, p. 640-643.
- Bishop, J.L. and Murad, E., 2005, The visible and infrared spectral properties of jarosite and alunite: *American Mineralogist*, v. 90, no. 7, p. 1100-1107, doi: 10.2138/am.2005.1700.
- Clark, R.N., Swayze, G.A., Gallagher, A.J., King, T.V.V., and Calvin, W.M., 1993, *The USGS, Digital Spectral Library Version 1: 0.2 to 3.0 microns*(United States Geological Survey, Open-File Report 93-592), 1340 p, (<http://speclab.cr.usgs.gov>).
- Clark, R. N. and Swayze, G. A., 1996, Evolution in imaging spectroscopy analysis and sensor signal-to-noise: An examination of how far we have come: *6th Annual Jet Propulsion Laboratory Airborne Earth Science Workshop*, p. 49-53.

Cohen, W. B., 1991, Response of Vegetation Indices to Changes in Three Measures of Leaf Water Stress: *Photogrammetric Engineering & Remote Sensing*, vol. 36, no. 1, p. 298-300.

Colombo, R., Bellingeri, D., Fasolini, D., and C. M. Marino, 2003, Retrieval of Leaf Area Index in Different Vegetation Types Using High Resolution Satellite Data: *Remote Sensing of Environment*, vol. 86, p. 120-131.

Gillespie, A.R., Rokugawa, S., Hook, S.J., Matsunaga, T., and Kahle, A.B., 1999, *Temperature/Emissivity Separation Algorithm Theoretical Basis Document (Version 2.4)*. National Aeronautics and Space Administration, 64 p..

Green, R.O., Eastwood, M.L., Sarture, C.M., Chrien, T.G., Aronsson, M., Chippendale, B.J., Faust, J.A., Pavri, B.E., Chovit, C.J., Solis, J., Olah, M.R., and Williams, O., 1998, Imaging spectroscopy and the Airborne Visible/Infrared Imaging Spectrometer (AVIRIS): *Remote Sensing of Environment*, v. 65, p. 227-248.

Guilbert, J. M. and Park, C. F., 2007, *The Geology of Ore Deposits*: Waveland Press Inc (Illinois), 985 p.

Iwasaki, A., Fujisada, H., Akao, H. Shindou, O., and Akagi, S., 2002, Enhancement of Spectral Separation Performance for ASTER/SWIR: *SPIE Proceedings*, v. 4486, p. 42-50.

Mars, J.C. and Rowan, L.C., 2006, Regional mapping of phyllic- and argillic-altered rocks in the Zagros magmatic arc, Iran, using Advanced Spaceborne Thermal Emission and Reflection Radiometer (ASTER) data and logical operator algorithms: *Geosphere*, v. 2, no. 3, p. 161-186, doi: 10.1130/GES00044.1.

McKee, E.H., 1968, Geology of the Magruder Mountain area, Nevada-California: *Geological Society of America Bulletin*, v. 1251-H. p. 1-40.

Robert, F., Brommecker, R., Bourne, B.T., Dobak, P.J., McEwan, C.J., Rowe, R.R., and Zhou, X., 2007, Models and Exploration Methods for Major Gold Deposit Types: *Ore Deposits and Exploration Technology*, v. 48, p. 691-711.

Rowan, L.C. and Mars, J.C., 2003, Lithologic mapping in the Mountain Pass, California area using Advanced Spaceborne Thermal Emission and Reflection Radiometer (ASTER) data: *Remote Sensing of Environment*, v. 84, no. 3, p. 350-366, doi:10.1016/S0034-4257(02)00127-X.

Swayze, G.A., R.N. Clark, A.F.H. Goetz, K.E. Livo, G.N. Breit, F.A. Kruse, S.J. Stutley, L.W. Snee, H.A. Lowers, J.L. Post, R.E. Stoffregen, and R.P. Ashley, 2014, Mapping advanced argillic alteration at Cuprite, Nevada using imaging spectroscopy: *Economic Geology*, v. 109, no. 5, p. 1179-1221. doi:10.2113/econgeo.109.5.1179

Thome, K., Biggar, S., and Takashima, T., 1999, *Algorithm Theoretical Basis Document for ASTER Level 2B1 (Surface Radiance) and ASTER Level 2B5 (Surface Reflectance)*:

Remote Sensing Group of the Optical Sciences Center, 45 p.

Toovey, L.M., 2011, *Introduction to Remote Sensing and Mineral Exploration*:

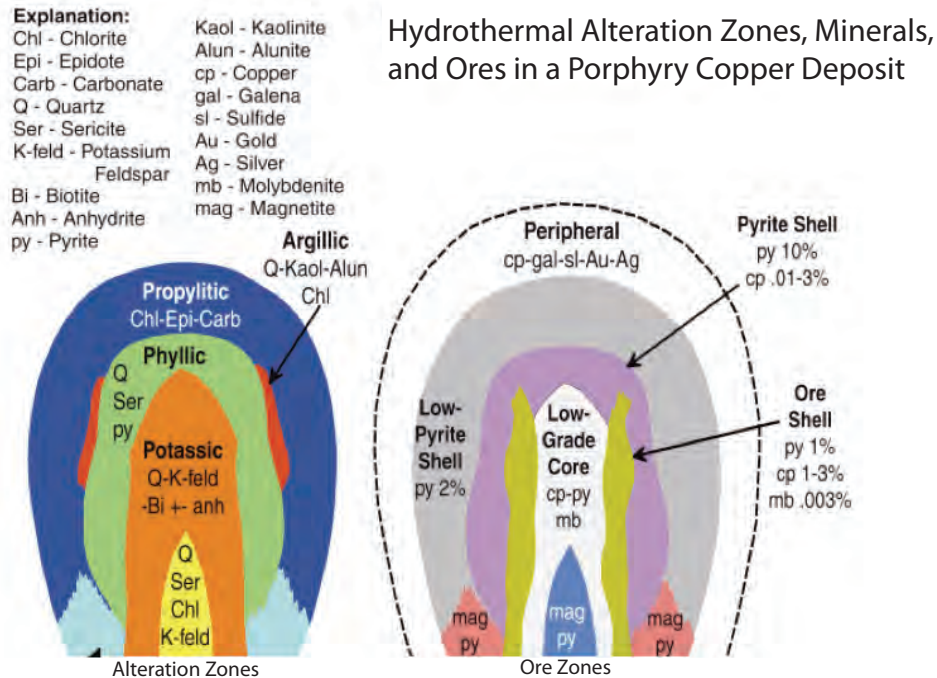
<http://goldinvestingnews.com/14571/introduction-to-remote-sensing-and-mineral-exploration.html> (accessed November, 2014).

Table 1. ASTER Instrument Characteristics				
Spectrometer		Band Number	Spectral Range (μm)	Spatial Resolution (m)
AST 7XT	VNIR	1	0.52-0.60	15
		2	0.63-0.69	15
		3N	0.78-0.86	15
		3B	0.78-0.86	15
	SWIR	4	1.6-1.7	30
		5	2.145-2.185	30
		6	2.185-2.225	30
		7	2.235-2.285	30
		8	2.295-2.365	30
		9	2.360-2.430	30
AST 05	TIR	10	8.125-8.475	90
		11	8.475-8.825	90
		12	8.925-9.275	90
		13	10.25-10.95	90
		14	10.95-11.65	90
		Abrams, 2002		

Table 2. Cuprite Hills Samples			
Sample*	UTM E	UTM N	Description
CH002	485019.27	4154606.01	white, low density, porous, opalized, fractured
CH003	485101.74	4154653.99	white volcanic rock
CH004	485110.35	4154731.15	brecciated, white volcanic rock
CH005	485063.75	4154826.79	red (oxidized), soil and porous volcanic rock
CH006	485077.52	4154849.77	mixed soil
CH007	485111.67	4154879.43	mixed soil
CH008	485089.95	4154918.52	red volcanic rock outcrop, vesicular
CH009	484844.96	4155009.76	half white brecciated volcanics, half red (oxidized)
CH010	484702.37	4154954.12	White silicified volcanic rock, large phenocrysts
CH011	484319.06	4154795.09	loose white and yellow tinged material
CH012	484271.42	4154734.47	white porous volcanic rock
CH013	484194.45	4154715.49	soil, red stained clasts and glassy white volcanics
CH014	484214.7	4154659.88	highly silicified material
CH015	484238.47	4154594.56	highly silicified material
CH016	484239.43	4154550	highly silicified material
CH017	484087.55	4154482.96	opalized material
CH018	483915.98	4154498.18	white volcanic, weathering rind, varnish, lichen
CH019	483841.05	4154532.13	red, fine-grained volcanoclastic, sandstone ??
CH020	483519.04	4154502.97	light gray/purple porphyritic felsic volcanic
CH021	483820.64	4154309	red tailings pile
CH022	483853.37	4154302.14	white, massive, abundant sulfur
CH023	484054.25	4154248.55	silicified, white, lithic volcanic
CH024	484076.21	4154207.18	red, smells of sulfur, volcanoclastic, rounded clasts
CH025	484192.42	4154122.04	red soil, sulfur smell
CH026	484337.73	4154108.04	extremely vesicular and silicified rock
CH027	484356.69	4154098.07	extremely vesicular and silicified rock
CH028	484521.25	4154099.67	extremely vesicular and silicified rock
CH029	484633.38	4154202.72	extremely vesicular and silicified rock
CH030	484723.98	4154108.82	surface cover
CH031	484781.11	4154120.85	surface cover
CH032	484808.99	4154119.17	surface cover
CH033	484868.83	4154131.32	white/brown soil
CH034	484903.12	4154121.66	surface cover
CH035	485060.34	4154190.37	surface cover
*Samples collected within Siebert Tuff Fm. (see figure 9). CH001, CH028, and CH034 discarded due to sample bags breaking and risking contamination. Projected coordinate system: NAD 1927 Zone 11N			

Table 3. GER 3700 Instrument Characteristics	
Spectral Range	350 nm to 2500 nm
Channels	704
Bandwidth	0.0015 μm : 0.35 μm to 1.05 μm 0.0065 μm : 1.5 μm to 1.9 μm 0.0095 μm : 1.9 μm to 2500 μm
Sighting	Laser

a.



b.

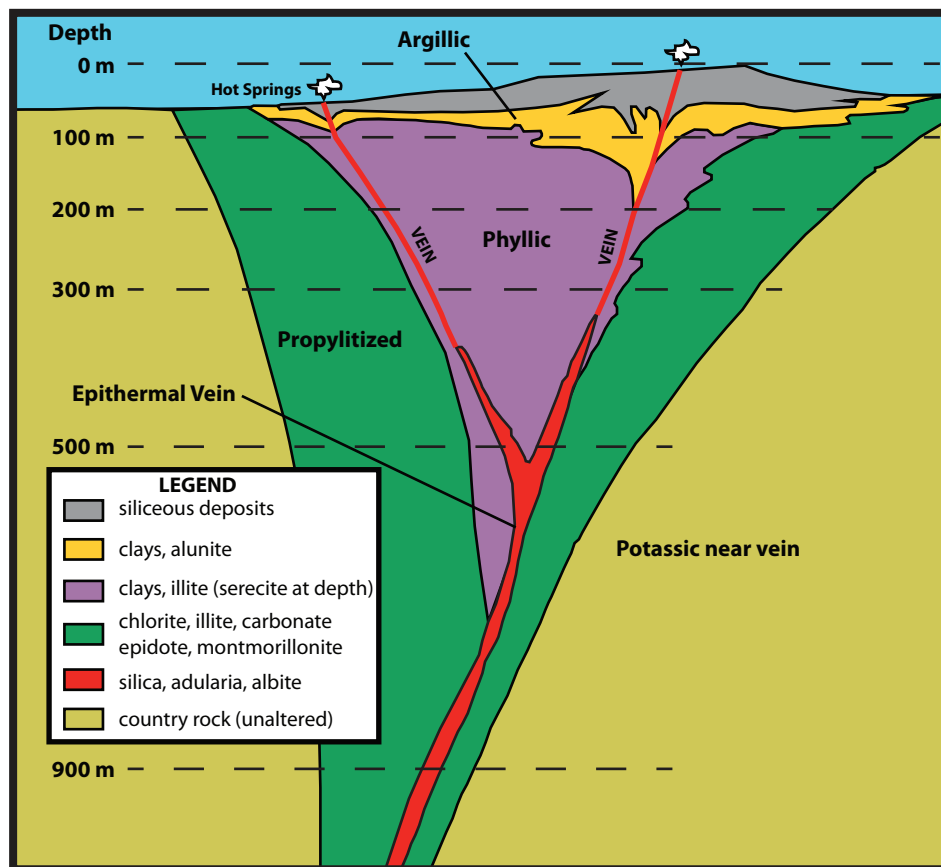


Figure 1: (a) Cross section of ores (right) associated with alteration zones (left) in a porphyry copper deposit (PCD) (Mars and Rowan, 2006). (b) Cross section of epithermal deposit showing hydrothermal alteration minerals and types, including propylitic, phyllic, argillic, and potassic (modified from Buchanan, 1981).

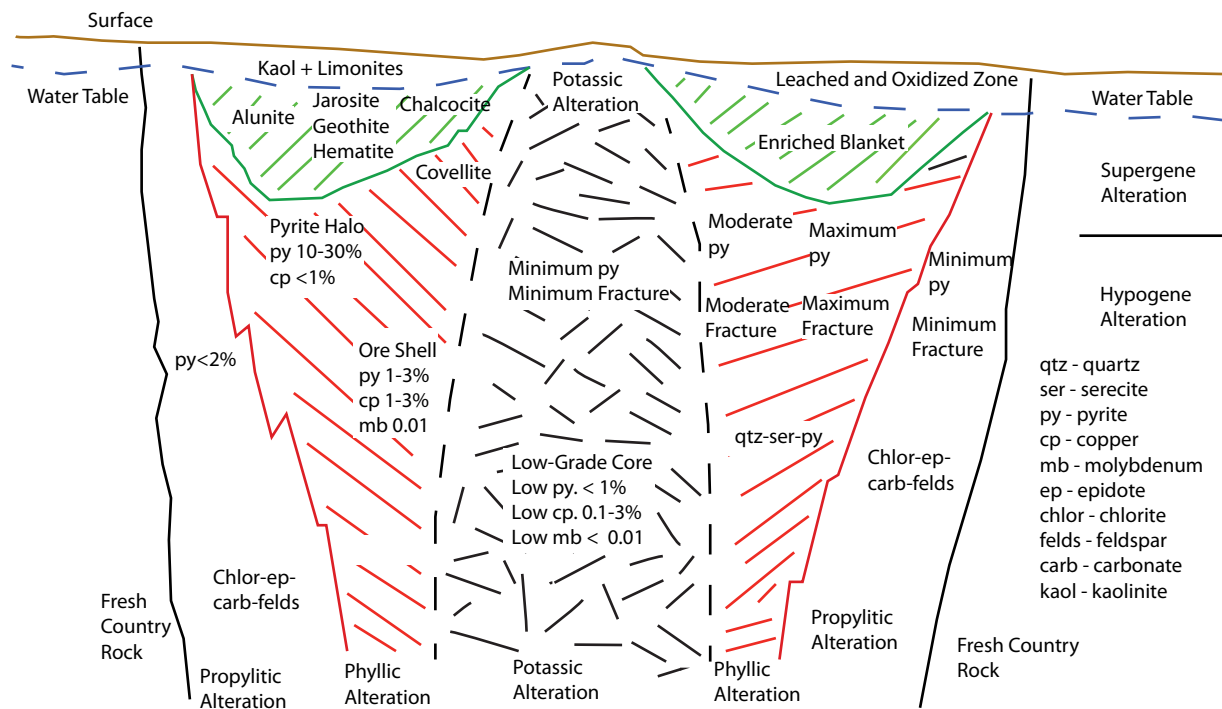


Figure 2: Cross section of a typical copper porphyry system showing hypogene and supergene alteration. Alteration, mineralization, and structure are repeated symmetrically around the potassic core (Guilbert and Park, 2007).

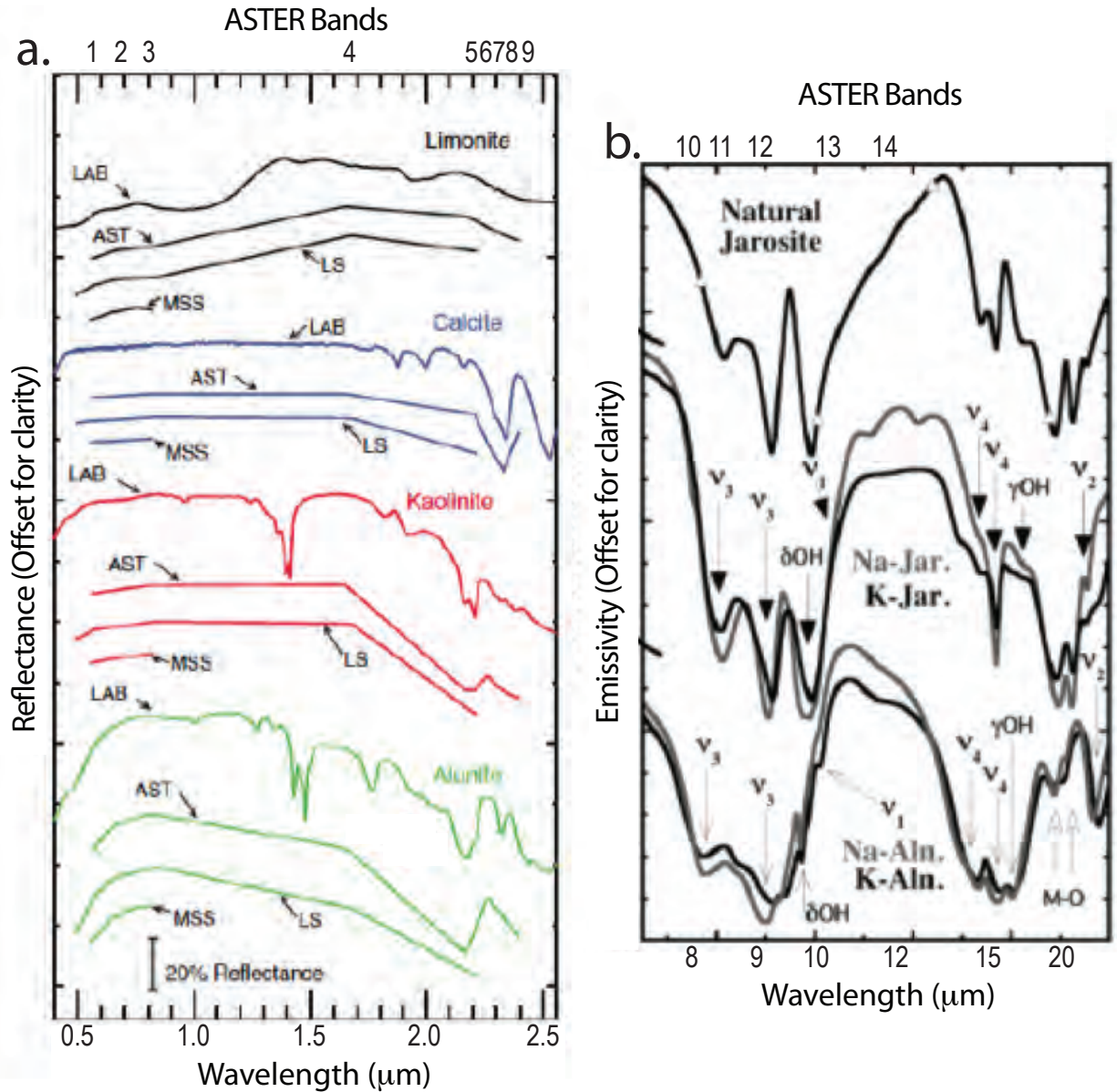


Figure 3: (a) USGS laboratory reflectance spectra (LAB) of key minerals within the study area (Mars and Rowan, 2006). The doublet feature at 2.2 μm in alunite and kaolinite is used to distinguish it from other hydrous minerals. The spectra shown have been resampled to ASTER (AST), Landsat Thematic Mapper (LS), and Landsat Multispectral Scanner (MSS) bandpasses. The numbers across the top indicate ASTER band center positions. From Mars and Rowan (2006). (b) Transmittance spectra of jarosite and alunite. SO_4^{2-} modes (ν_1 , ν_2 , ν_3 , and ν_4) and OH^- modes are displayed. From Bishop (2005).

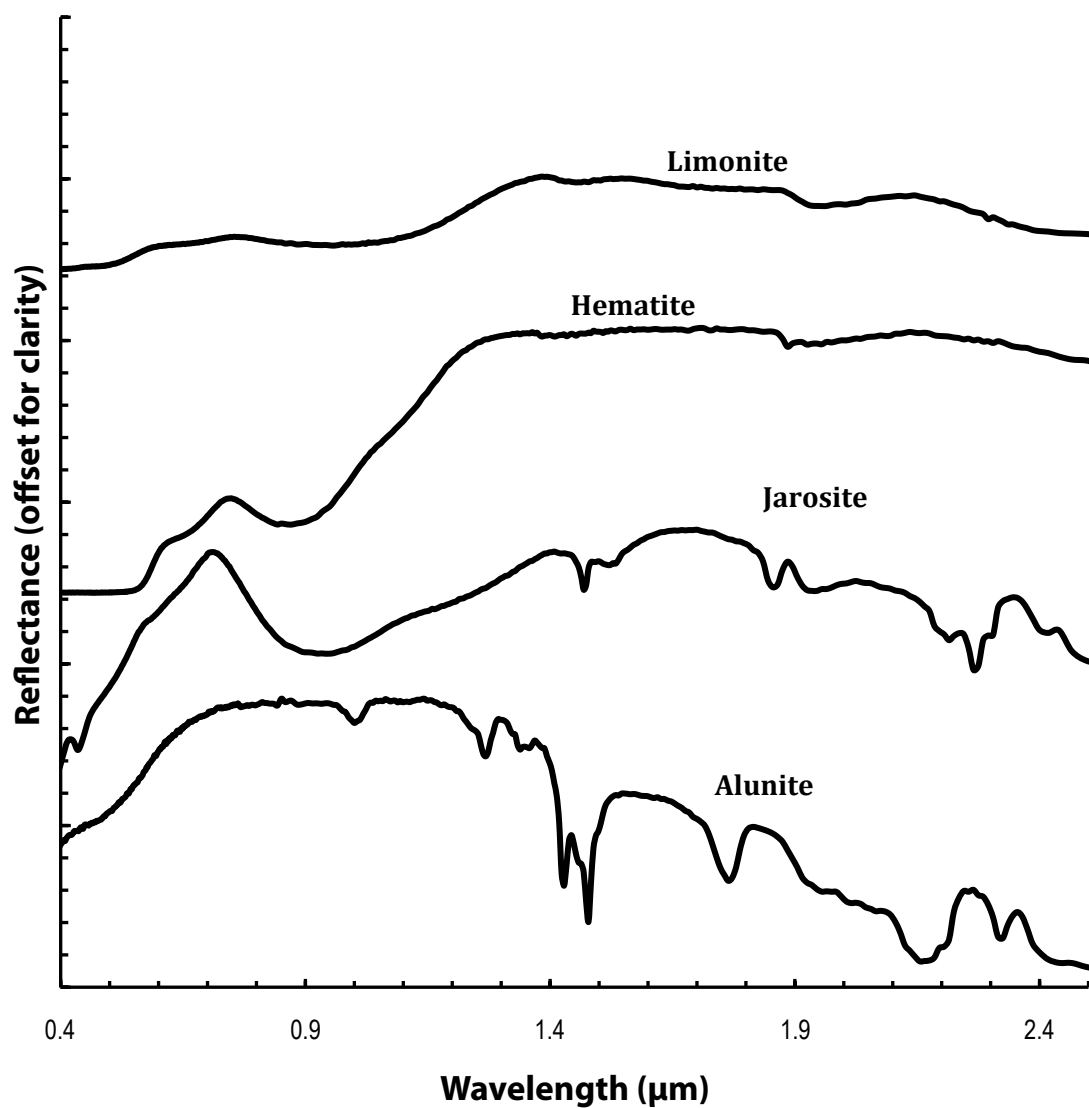


Figure 4: Spectra of alunite, jarosite, hematite, and limonite from the USGS spectral library (Clark et al., 1993). Notice the negative slope in alunite between $\sim 0.8 \mu\text{m}$ (ASTER band 3) and $\sim 1.65 \mu\text{m}$ (ASTER band 4) compared to the positive slope in jarosite, hematite, and limonite.

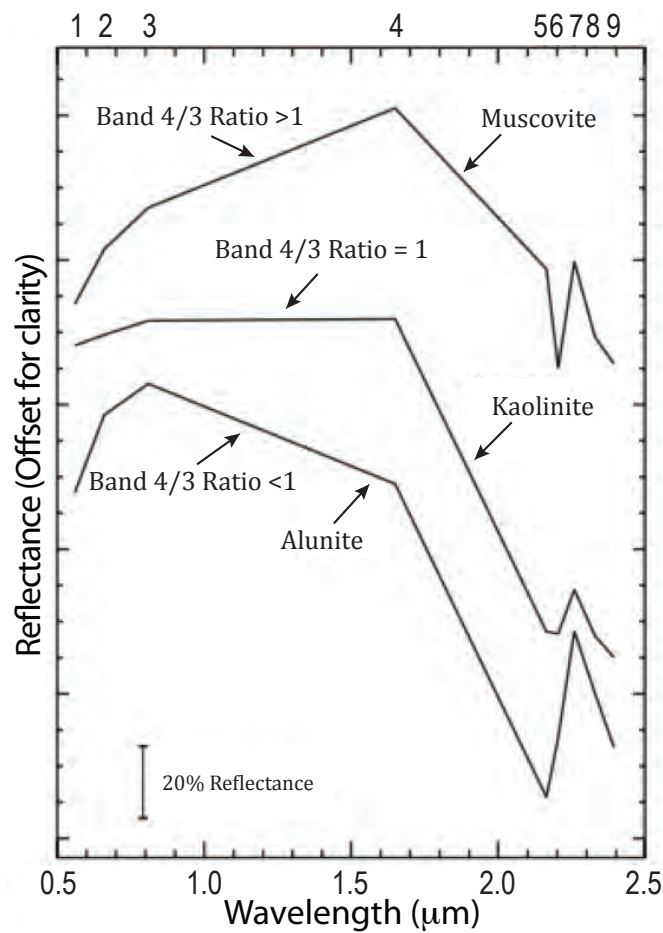


Figure 5: Laboratory reflectance spectra of alunite, kaolinite, and muscovite. The spectra have been resampled to ASTER bandpasses. Numbers across the top indicate ASTER band center positions. The spectral slopes estimated using the ASTER band 4/3 ratio shows how a band threshold can be determined from ASTER spectra. These spectral slopes allow us to distinguish minerals from one another. Modified from Mars and Rowan (2006).

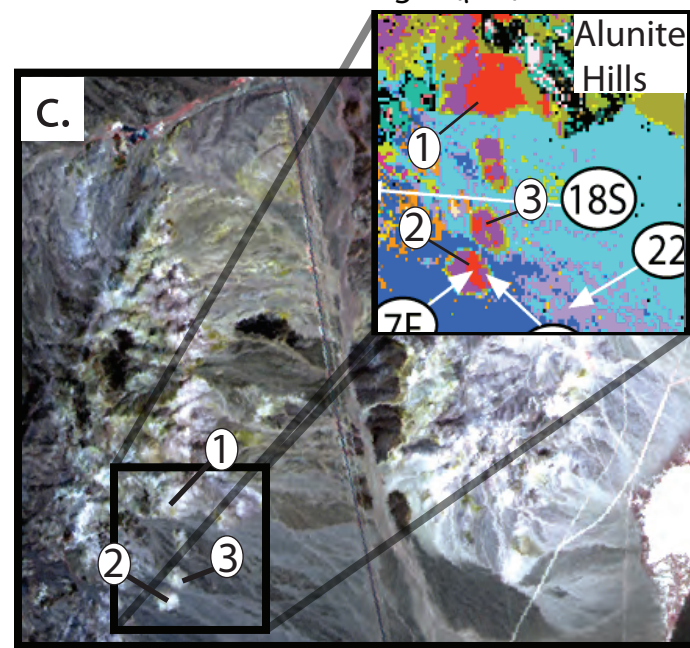
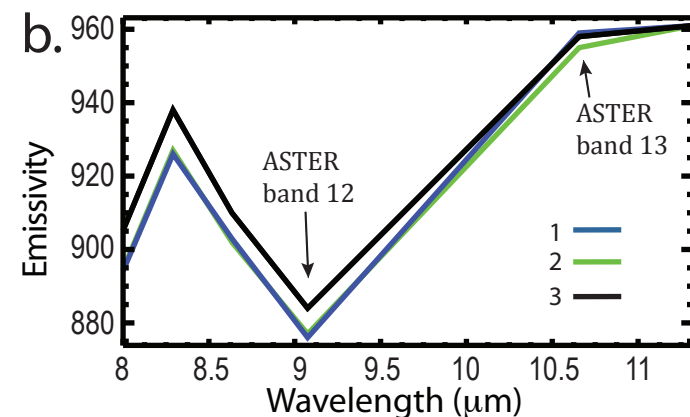
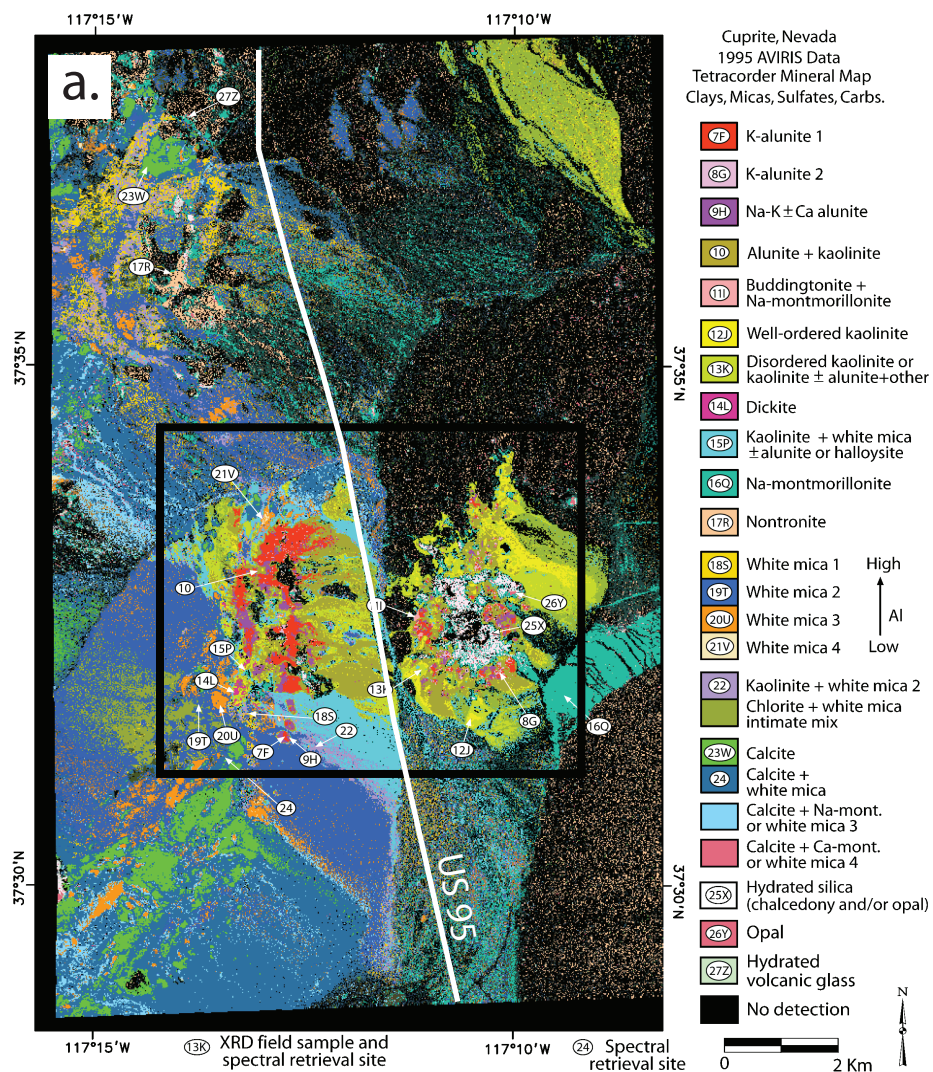


Figure 6: (a) AVIRIS mineral map of clays, micras, sulfates, silicates, and carbonates at Cuprite Hills. Number-letter combinations indicate where samples were collected and analyzed with x-ray diffraction (XRD) (from Swayze et al., 2014). Black box indicates the area shown in (b) (Swayze et al., 2014). (b) ASTER TIR emissivity spectra from (b), shown by numbers 1-3. Band 13/12 ratio was estimated from the ASTER TIR spectra. The emissivity in band 13 is 8% greater than band in 12. (c) ASTER RGB image (R: band 3, G: band 2, B: band 1) of Cuprite Hills. The inset is the AVIRIS mineral map associated with the black box in the ASTER image. Numbers indicate where ASTER TIR emissivity spectra were taken. The AVIRIS mineral map is used to verify the effectiveness of our logical operator maps to map alunite.

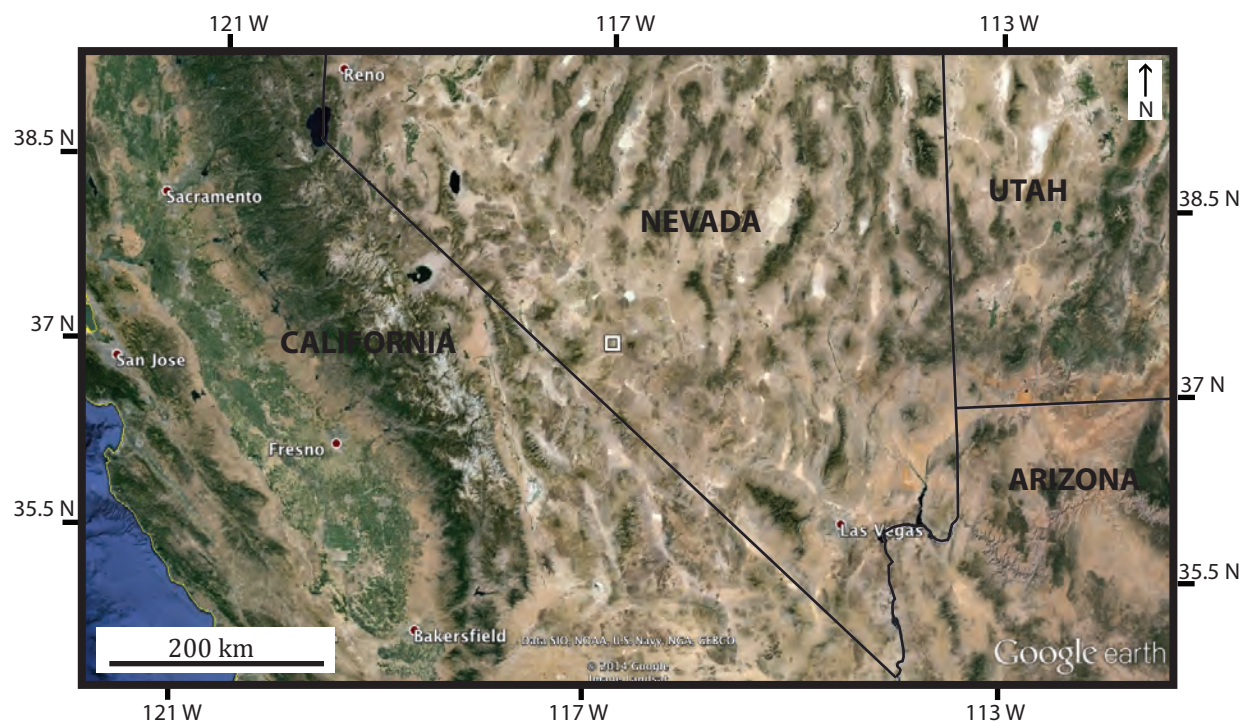


Figure 7: Regional map showing location of Cuprite Hills, NV (white box) within the Cordilleran mobile belt. Imagery from Google Earth. Black lines are state boundaries.

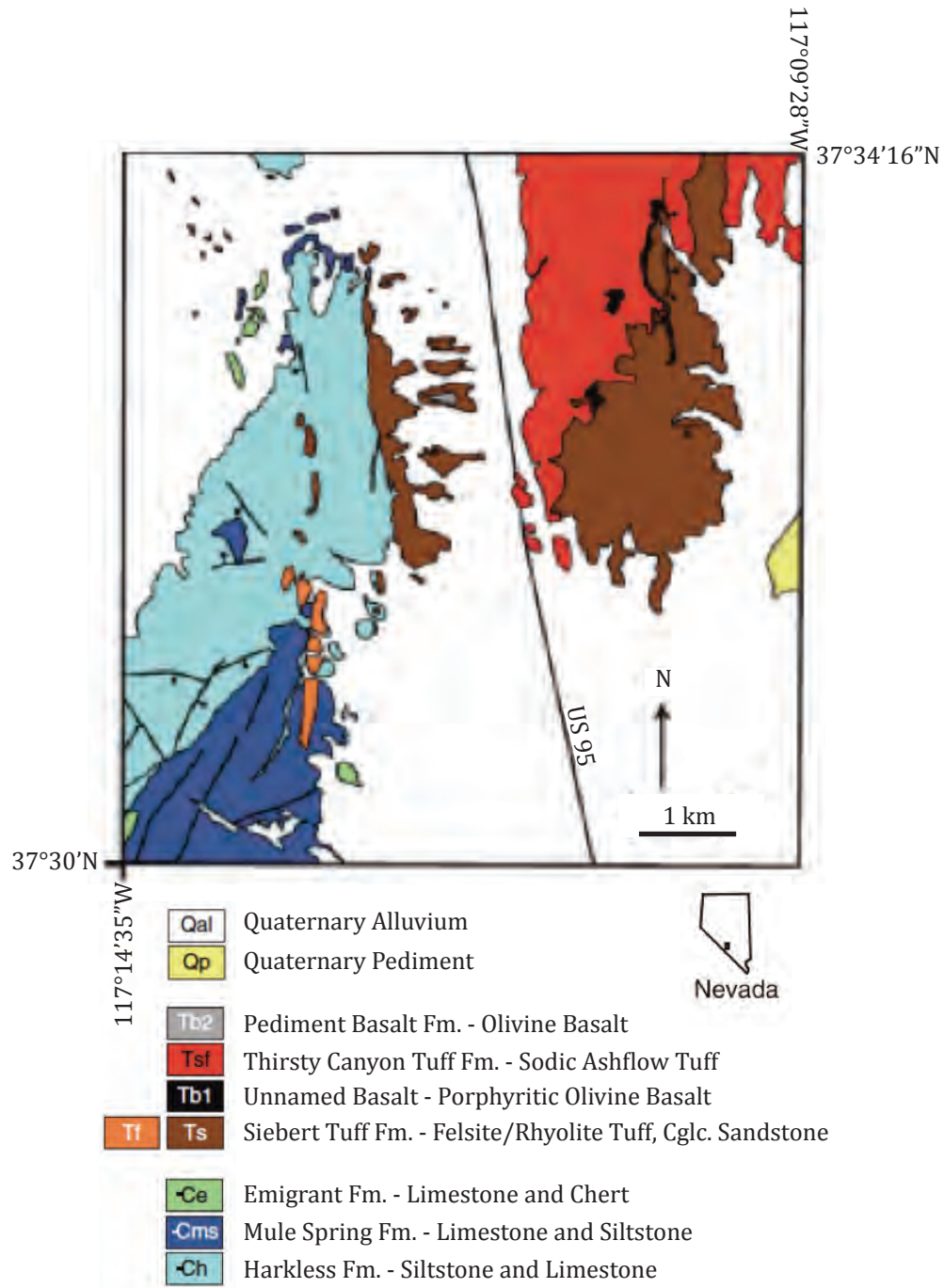


Figure 8: Geologic Map of the Cuprite Hills, Nevada. From Mars and Rowan (2006).

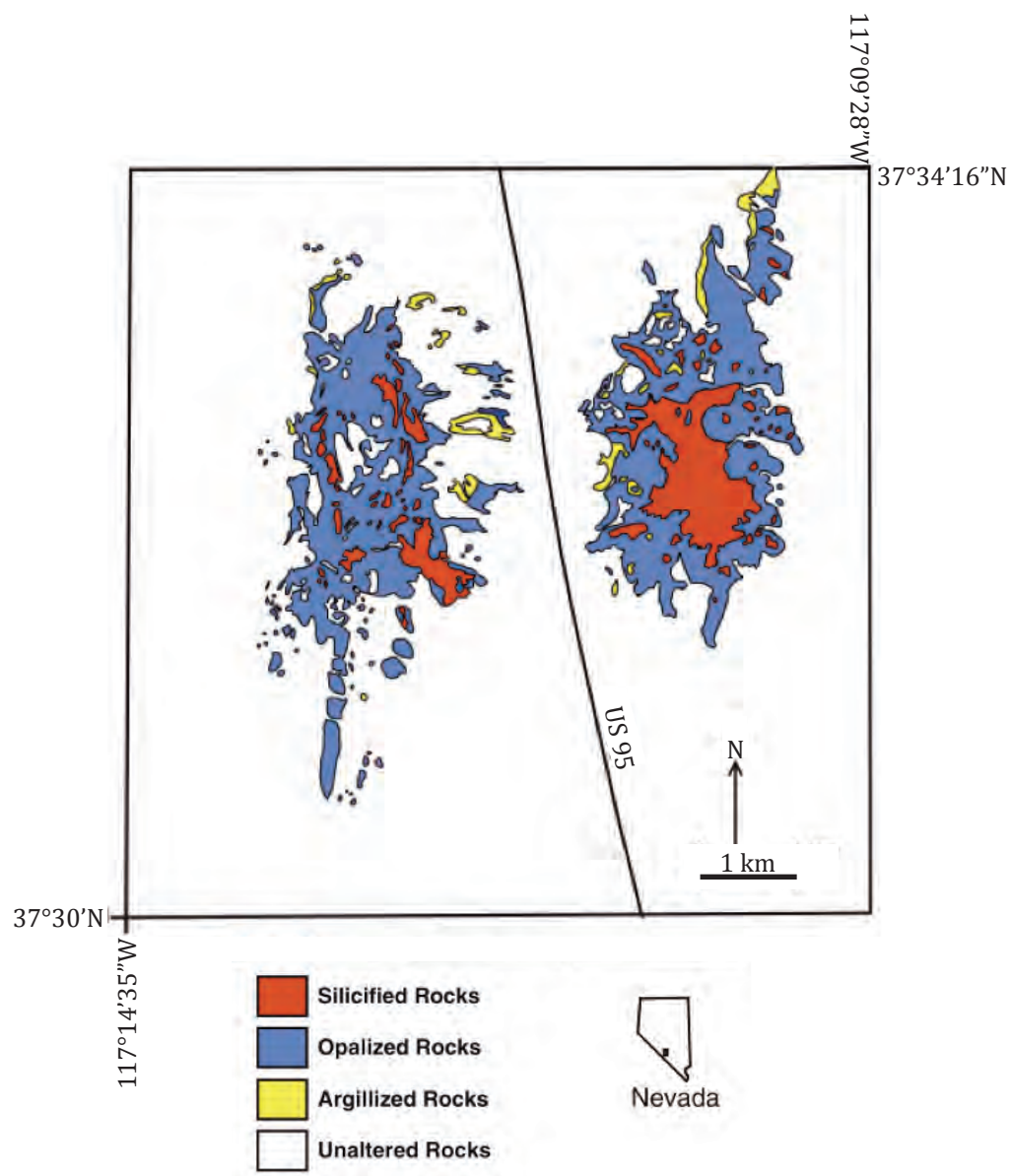


Figure 9: Map showing the distribution of altered rocks in the Cuprite Hills, NV. Area shown is the same as figure 8 From Ashley and Abrams (1980) and Mars and Rowan (2006).

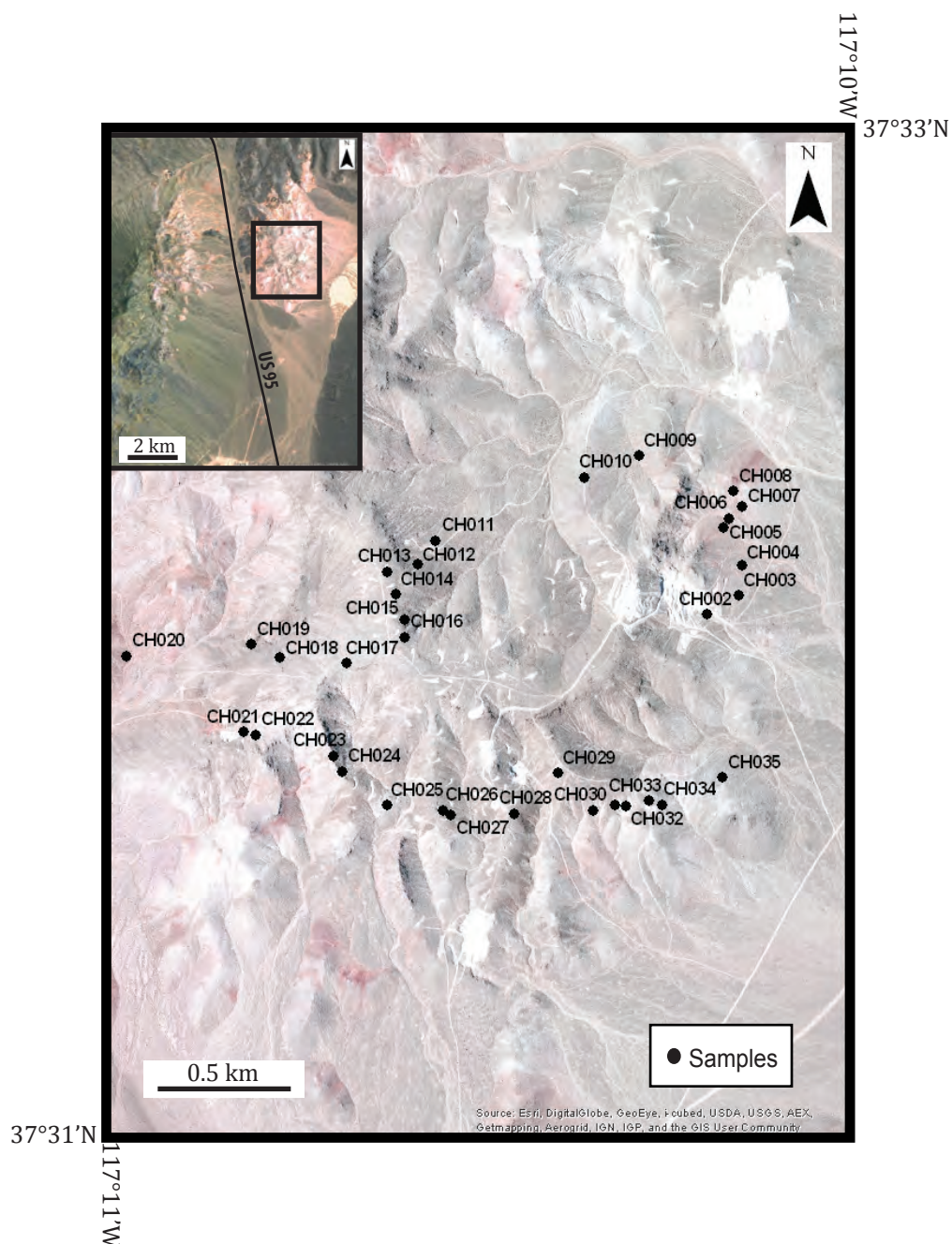


Figure 10: Map of eastern Cuprite Hills showing locations of samples (black dots). Inset map in the upper left corner shows location within Cuprite Hills. Inset is the same location as figures 8 and 9. Black line running through inset map marks location of US Highway 95. Basemap from Esri, DigitalGlobe, Geoeye.

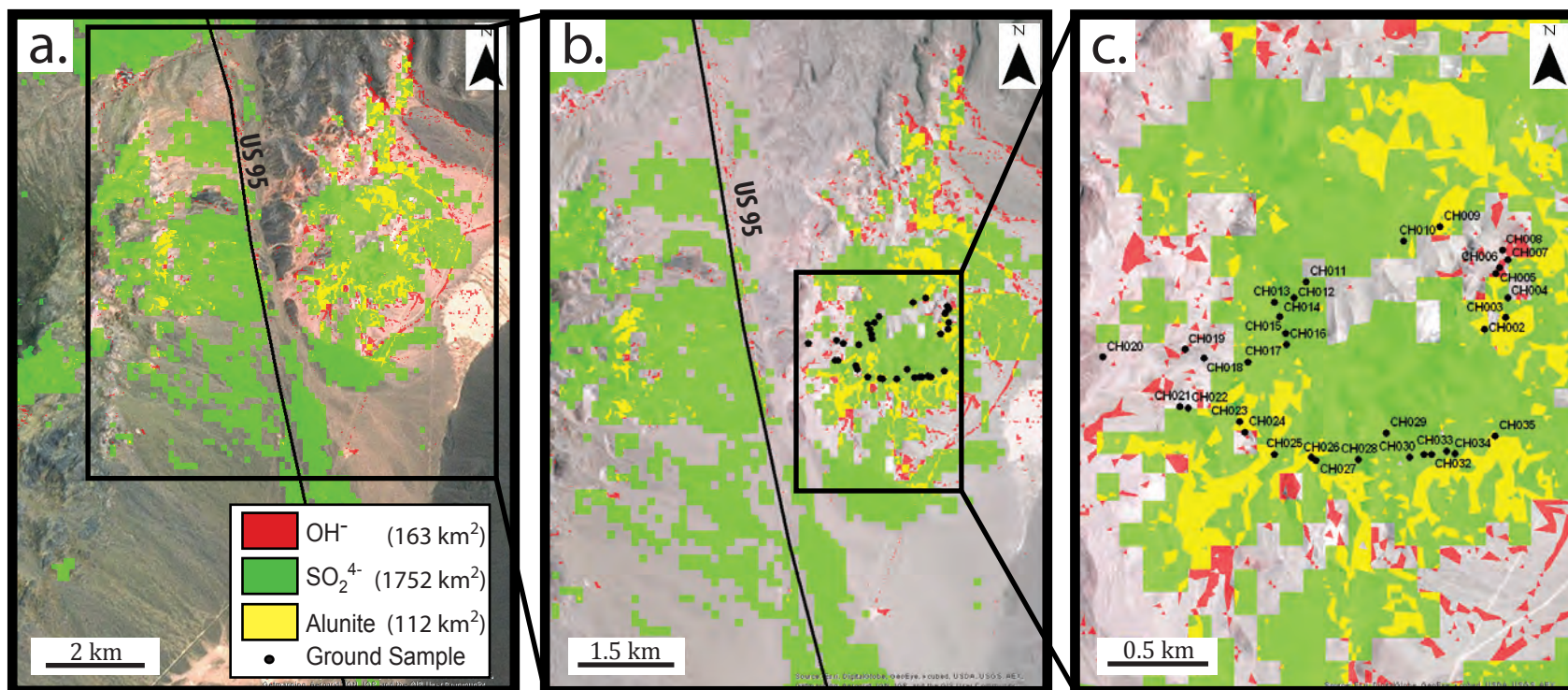


Figure 11: (a) Cuprite Hills aerial photo with logical operator results overlain. Sulfate logical operator results in green, hydroxyl logical operator results in red, and alunite results in yellow. The area covered by each map is shown in the legend. This panel covers the same area as figures 8 and 9. (b) Zoomed-in version of (a) showing locations of the samples (black dots) that were collected in the field (see Appendix 1 for lab spectra of field samples). (c) Close-up of samples on the eastern side of Cuprite Hills. Black line running through (a) and (b) marks US Highway 95. Black boxes show the location of panels (b) and (c). Basemaps from Esri, DigitalGlobe, Geoeye.

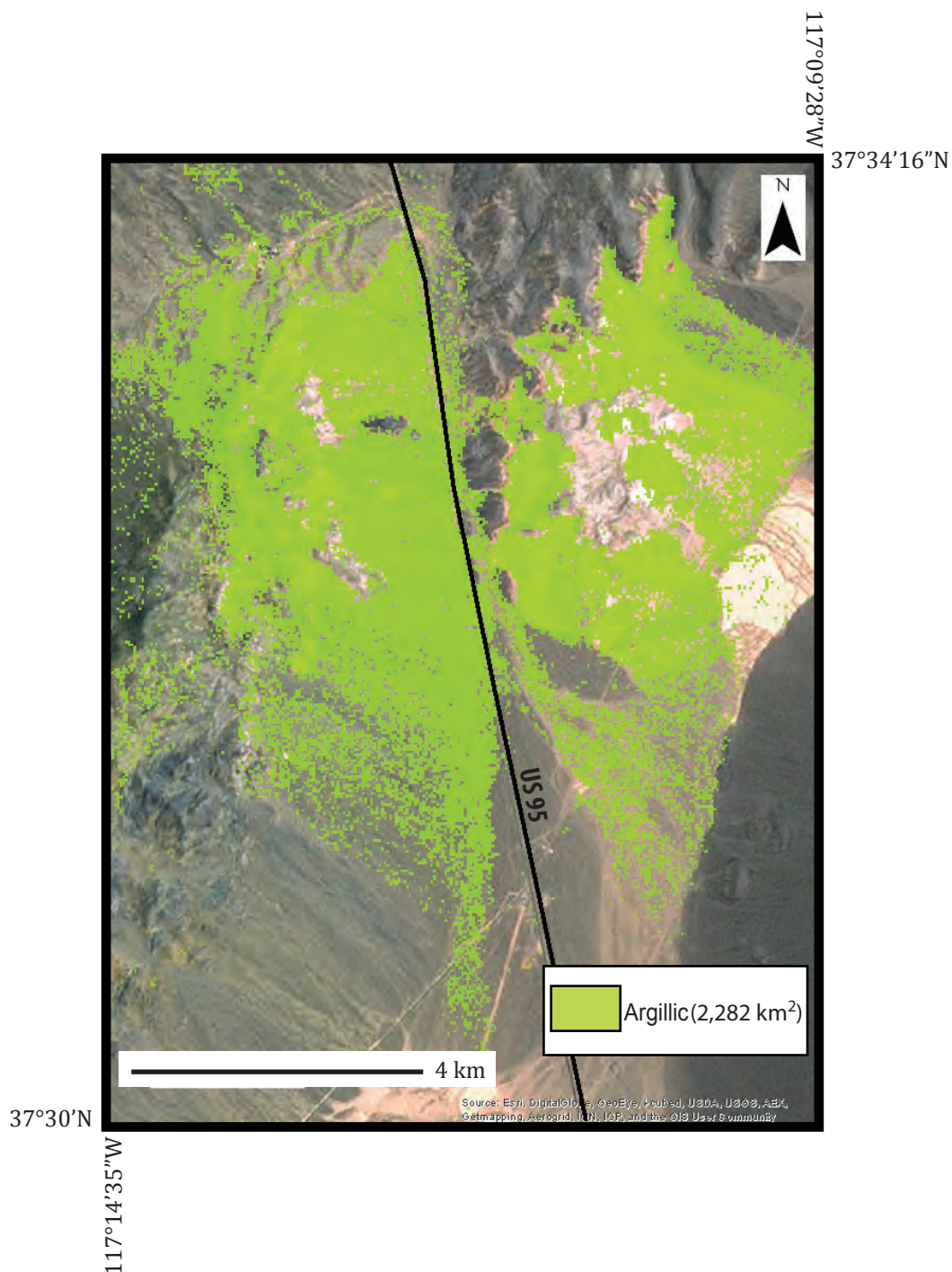


Figure 12: Cuprite Hills aerial photo showing the result of the Mars and Rowan (2006) argillic logical operator designed to target OH⁻ absorptions within alunite and kaolinite. Total area of argillic logical operator is shown in the legend. Covers the same area as figures 8, 9, and 11a. Black line running though figure marks US Highway 95. Basemap from Esri, DigitalGlobe, Geoeye.

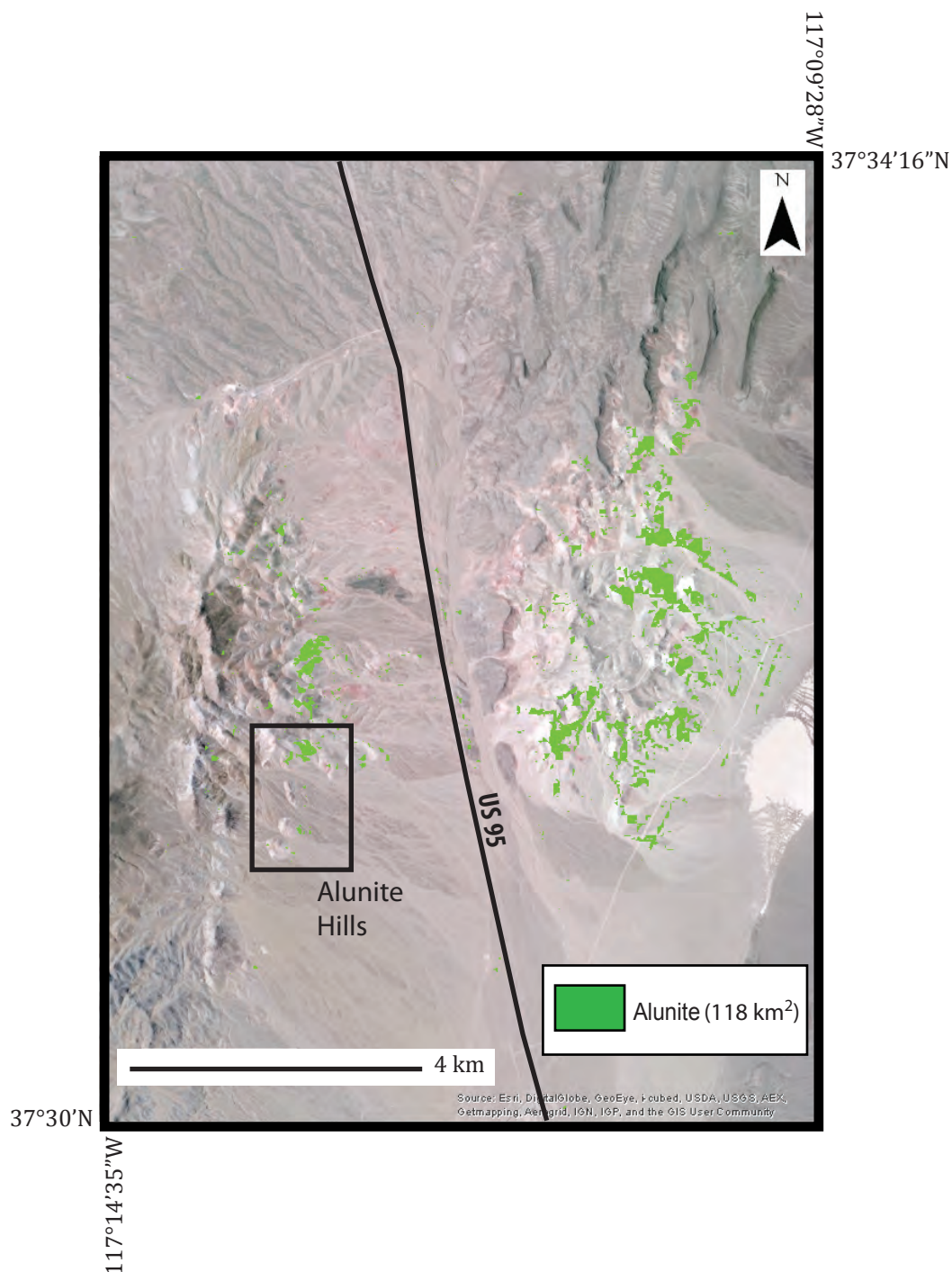


Figure 13: Cuprite Hills aerial photo showing the result of the alunite map designed to target OH^- and SO_4^{2-} absorptions within alunite. Black box indicates Alunite Hills region from figure 6. Total area of alunite map is shown in the legend. Covers the same area as figures 8, 9, 11a, and 12. Black line running through figure marks US Highway 95. Basemap from Esri, DigitalGlobe, Geoeye.

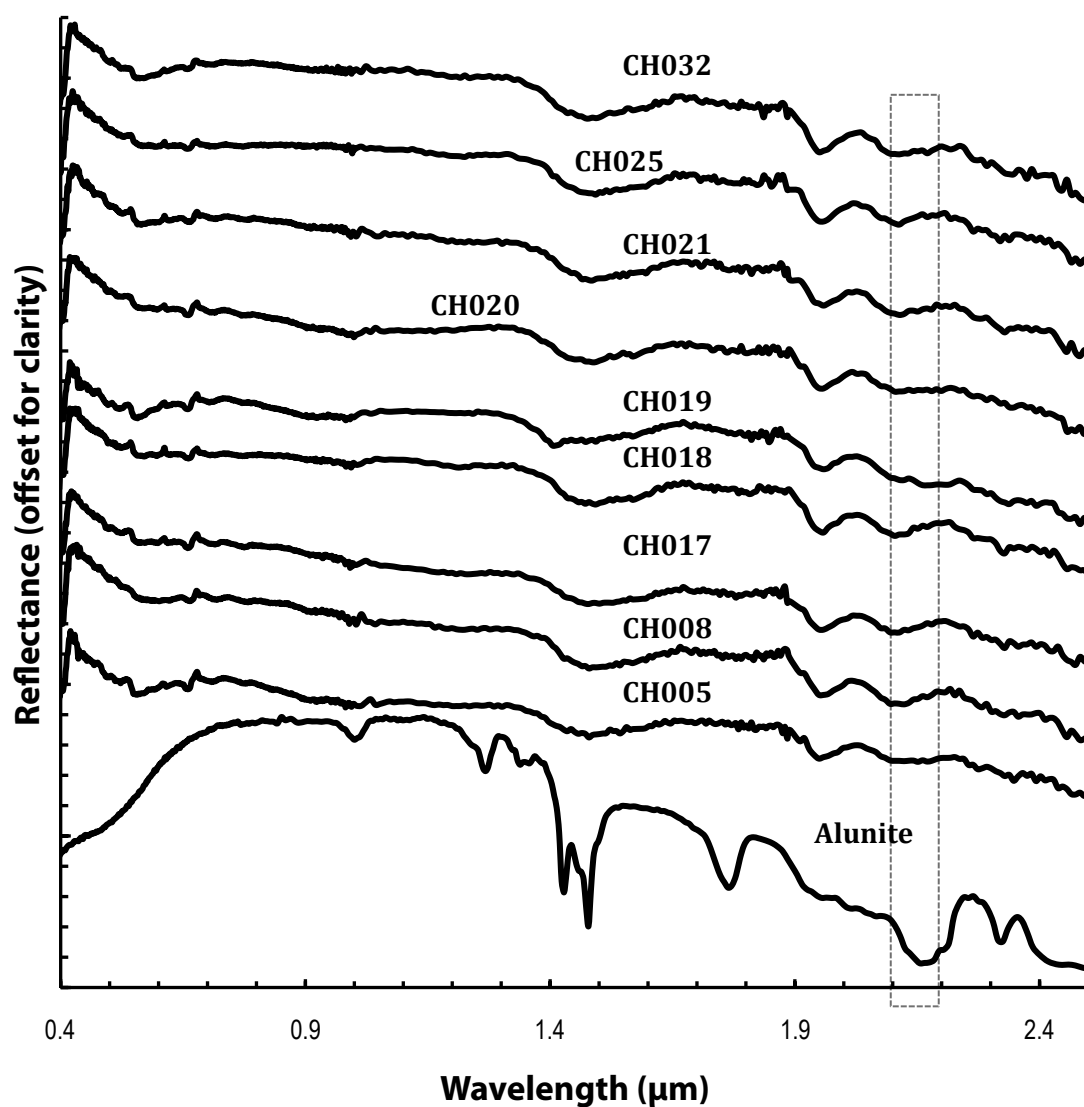


Figure 14: Spectra of Cuprite Hills samples that exhibit shallow $\sim 2.15 \mu\text{m}$ OH^- absorptions. The USGS alunite spectrum (AL706; Clark et al., 1993) is shown at the bottom for comparison. Samples CH005 and CH019 were sampled from areas that are predicted to contain $2.17\text{--}2.2 \mu\text{m}$ OH^- absorptions according to the OH^- map (Figures 9 and 10). Samples CH008, CH018, CH020, and CH021 were sampled from areas that were predicted to not contain OH^- or SO_4^{2-} according to the OH^- and SO_4^{2-} maps (Figures 9 and 10). Samples CH017, CH025, and CH032 were sampled from areas that were predicted to contain $9 \mu\text{m}$ SO_4^{2-} absorptions according to the SO_4^{2-} map (Figures 9 and 10). Dashed rectangle indicates the region between 2.1 and $2.2 \mu\text{m}$.

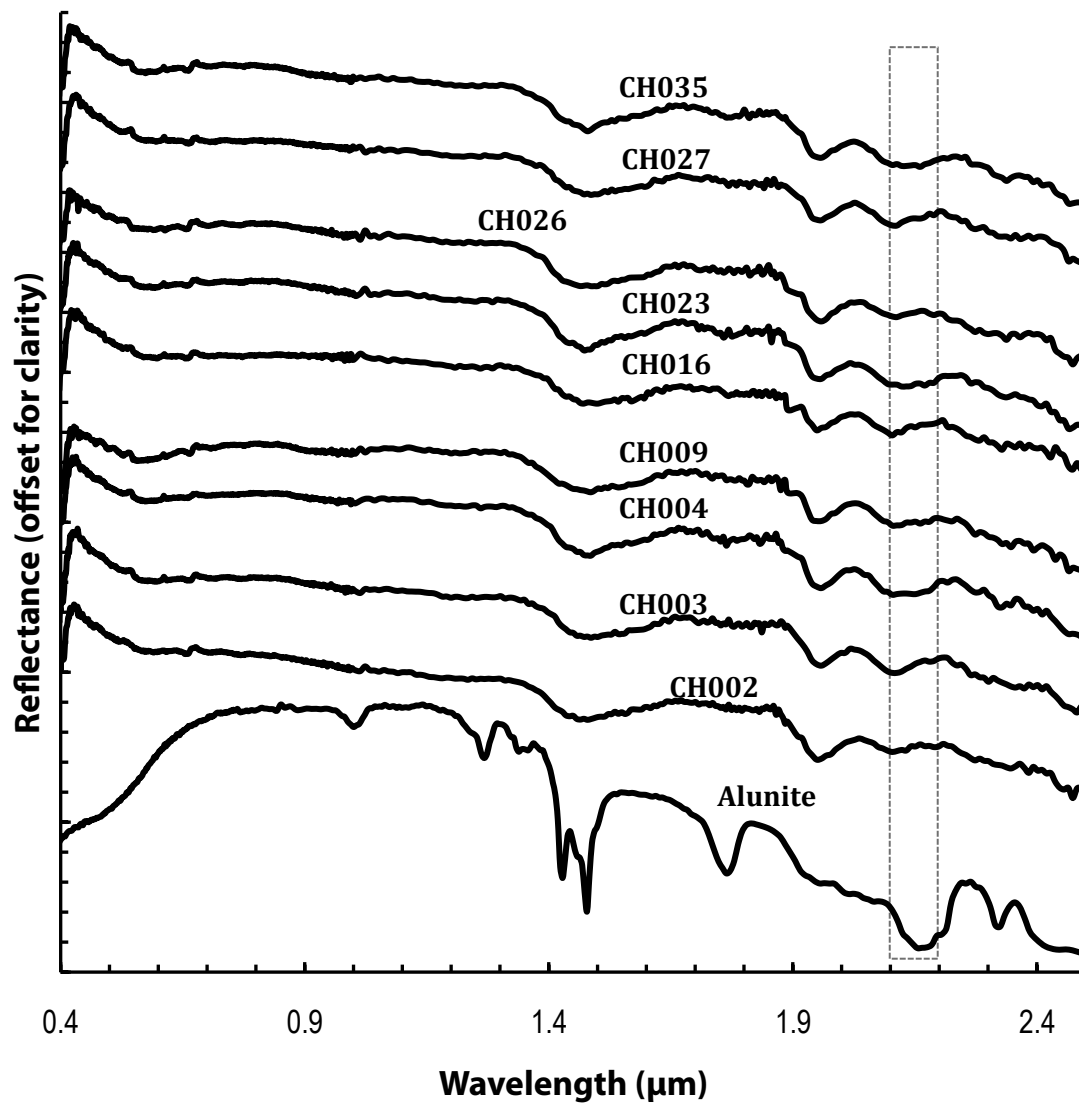


Figure 15: Spectra of Cuprite Hills samples collected from areas predicted to contain alunite according to the alunite map (Figure 11 and 13). The USGS alunite spectrum (AL706; Clark et al., 1993) is shown at the bottom for comparison. Notice the flat slope in alunite between $\sim 0.8 \mu\text{m}$ and $\sim 1.65 \mu\text{m}$. In addition, a $\sim 2.15 \mu\text{m}$ OH^- absorption is present in the Cuprite Hills samples. Dashed rectangle indicates the region between 2.1 and $2.2 \mu\text{m}$. These two spectral features in the Cuprite Hills samples are consistent with spectral features seen in alunite.

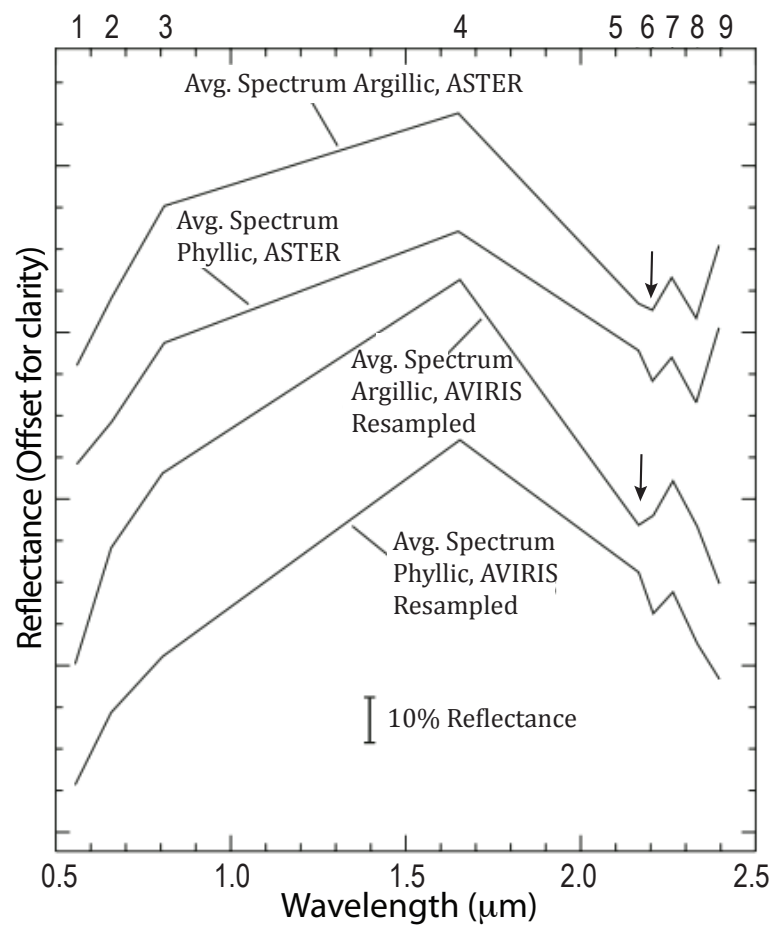


Figure 16: Average spectra of argillic and phyllic spectral units for ASTER and ASTER-simulated (AVIRIS resampled to ASTER bandpasses) data. Notice the $\sim 2.2 \mu\text{m}$ OH^- absorption has shifted in the AVIRIS resampled spectra to $\sim 2.15 \mu\text{m}$ (black arrows). This is caused by the mixing of kaolinite and alunite (from Mars and Rowan, 2006).

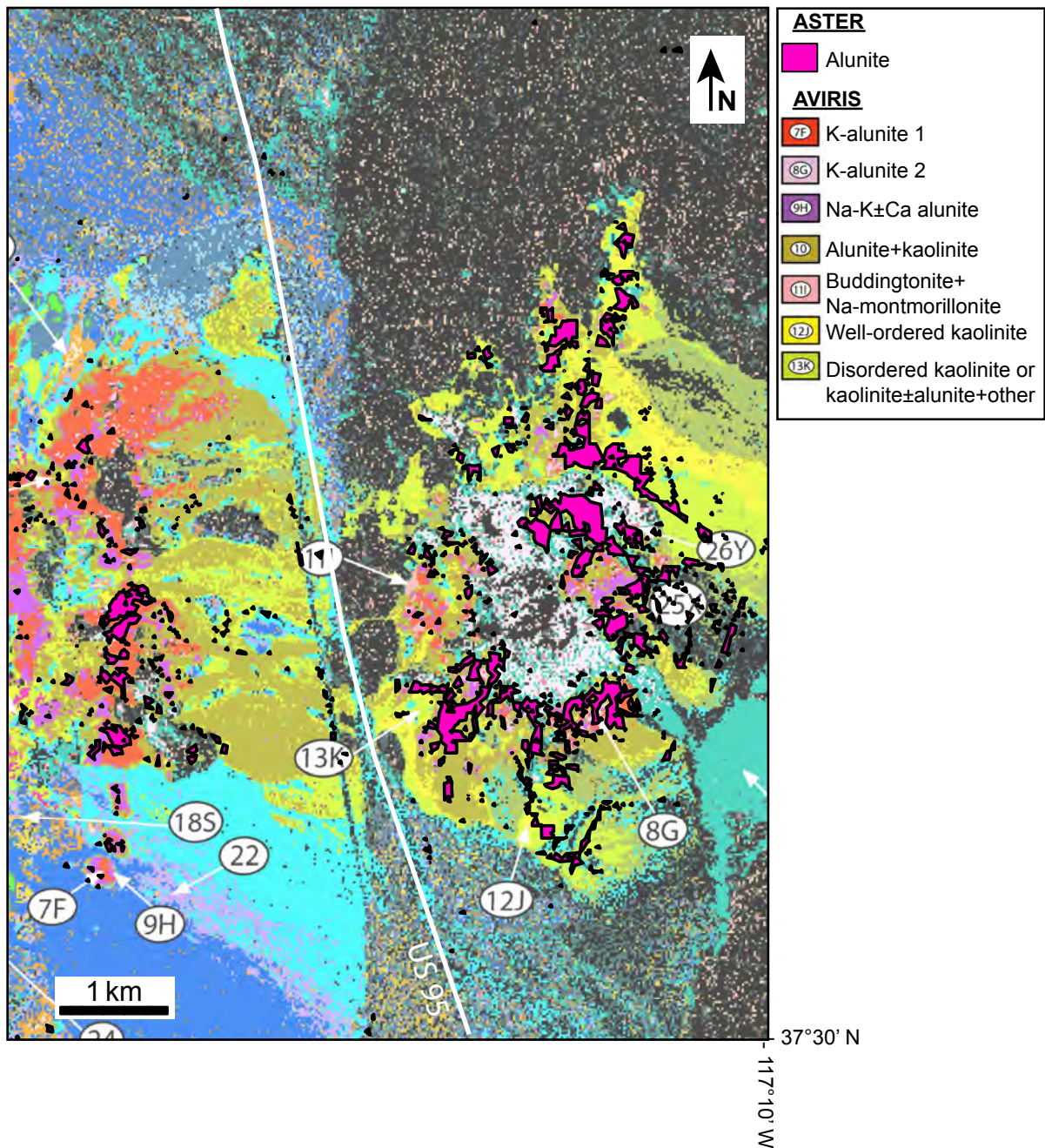


Figure 17: AVIRIS mineral map showing pixels exhibiting spectra consistent with alunite (Swayze et al., 2014). The results from our alunite map, which was developed using ASTER scenes and the OH--FeO and SO42- logical operators, are overlain on the AVIRIS mineral map to show how well the alunite map correlates with the high spatial and spectral resolution of AVIRIS.

APPENDIX 1: CUPRITE HILLS LABORATORY SPECTRA

The Cuprite Hills samples were processed and analyzed at The University of Texas at El Paso (UTEP). Each sample was crushed with a jaw crusher and then sieved to 1-mm and 500- μm mesh sizes. Care was taken to reduce contamination between samples, and all tools were thoroughly cleaned and inspected for contamination between sample preparations. We used the 500- μm size fraction for consistency in our further analyses of the samples.

All samples were analyzed using the GER 3700 VNIR-SWIR spectroradiometer at UTEP. This instrument measures radiance in 645 bands between 0.3 μm and 2.5 μm , with a spectral resolution of 0.0015 μm in the 0.3-1.05 μm range, 0.0065 μm in the 1.5-1.9 μm range, and 0.0095 in the 1.9-2.5 μm range (Table 3). The GER 3700 does not measure radiance in the TIR. The spectroradiometer was periodically calibrated (every four measurements) using a standard white reflectance target plate. Radiance values obtained from the calibration target were used to normalize the radiance values from the measured samples in order to obtain reflectance.

The Cuprite Hills laboratory spectra were compared to the USGS laboratory spectrum (Clark et al., 1993) of alunite (AL706; 15 μm grain size). The larger grain size in our samples could cause the 2.17-2.2 OH^- absorption to shift and widen relative to the laboratory spectrum of alunite. By doing this comparison we can determine whether the Cuprite Hills sample spectra are consistent with spectral features attributed to alunite. For example, a sample collected in regions indicated by the OH^- logical operator map to exhibit OH^- absorptions would be expected to contain both the 2.17-2.2 μm absorption due to OH^- , as well as the negative slope between 0.8 μm and 1.65 μm .

The following figures contain the sample spectra (solid black line) plotted with USGS

alunite spectrum (AL706; Clark et al., 1993), which is shown as a dotted line in all the spectra plots.

References

Clark, R.N., Swayze, G.A., Gallagher, A.J., King, T.V.V., and Calvin, W.M., 1993, The USGS, Digital Spectral Library Version 1: 0.2 to 3.0 microns(United States Geological Survey, Open-File Report 93-592), 1340 p, (<http://speclab.cr.usgs.gov>).

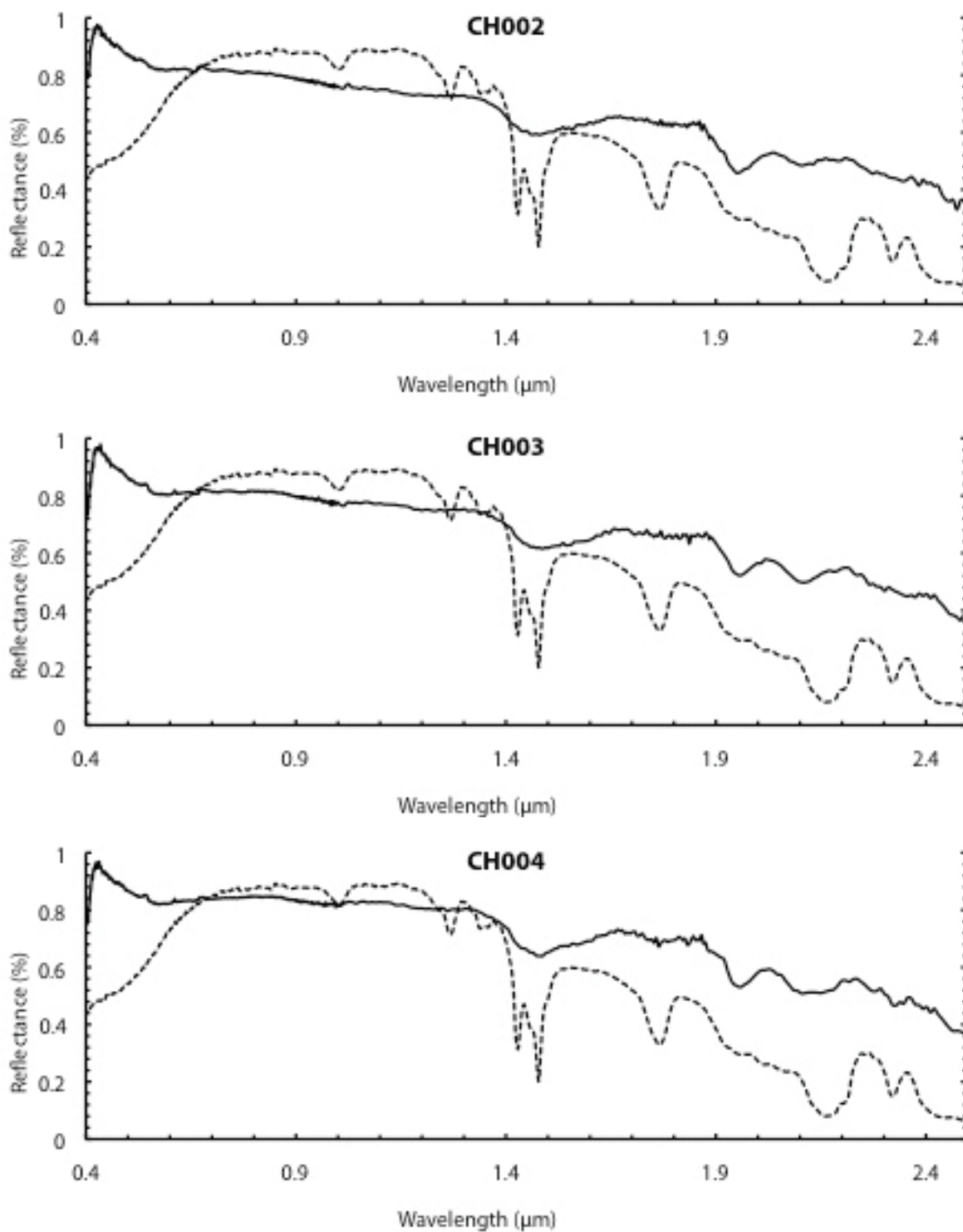


Figure A1: Ground spectra from Cuprite Hills, NV (solid black). USGS alunite spectrum (AL706; Clark et al., 1993).

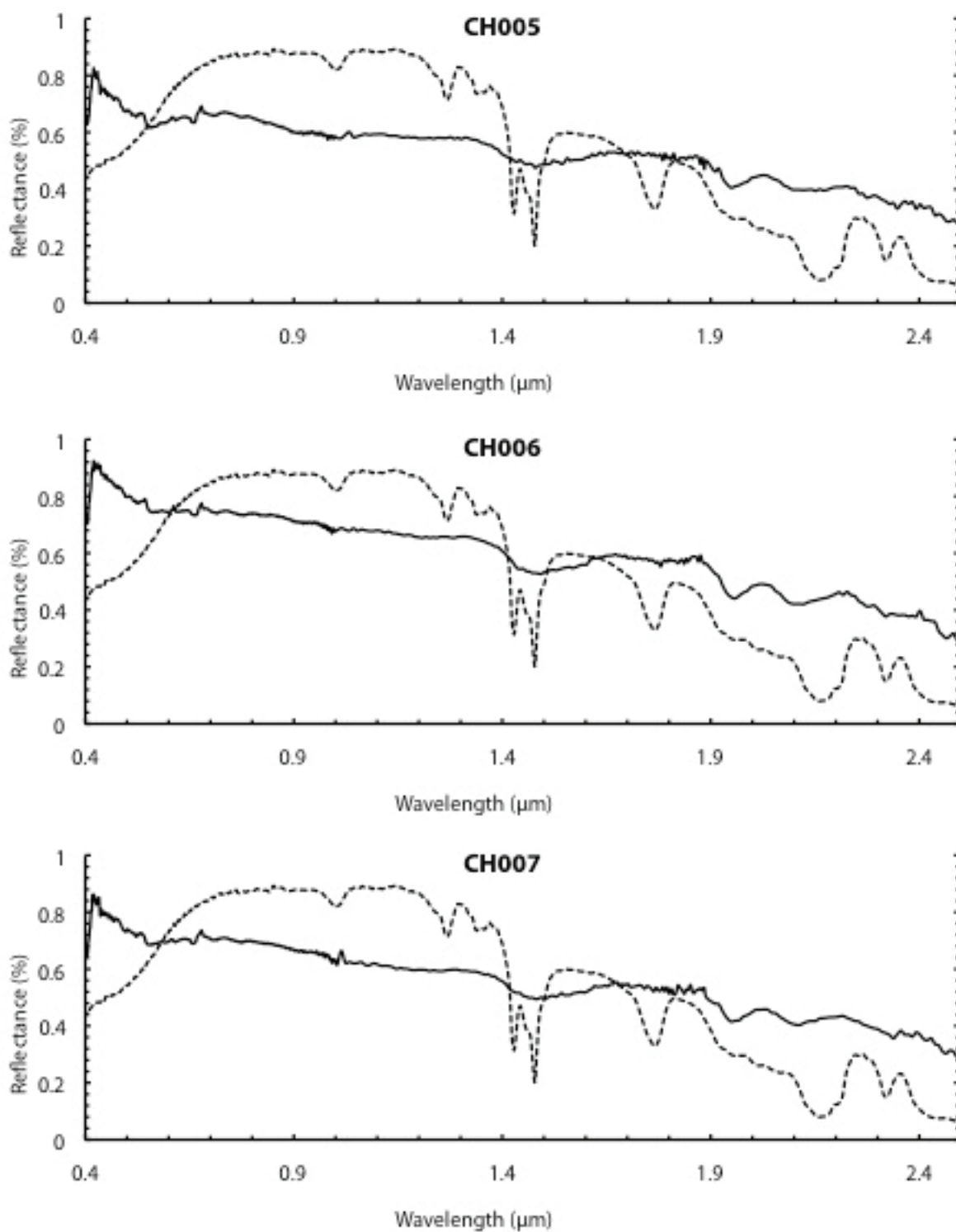


Figure A2: Ground spectra from Cuprite Hills, NV (solid black). USGS alunite spectrum (AL706; Clark et al., 1993).

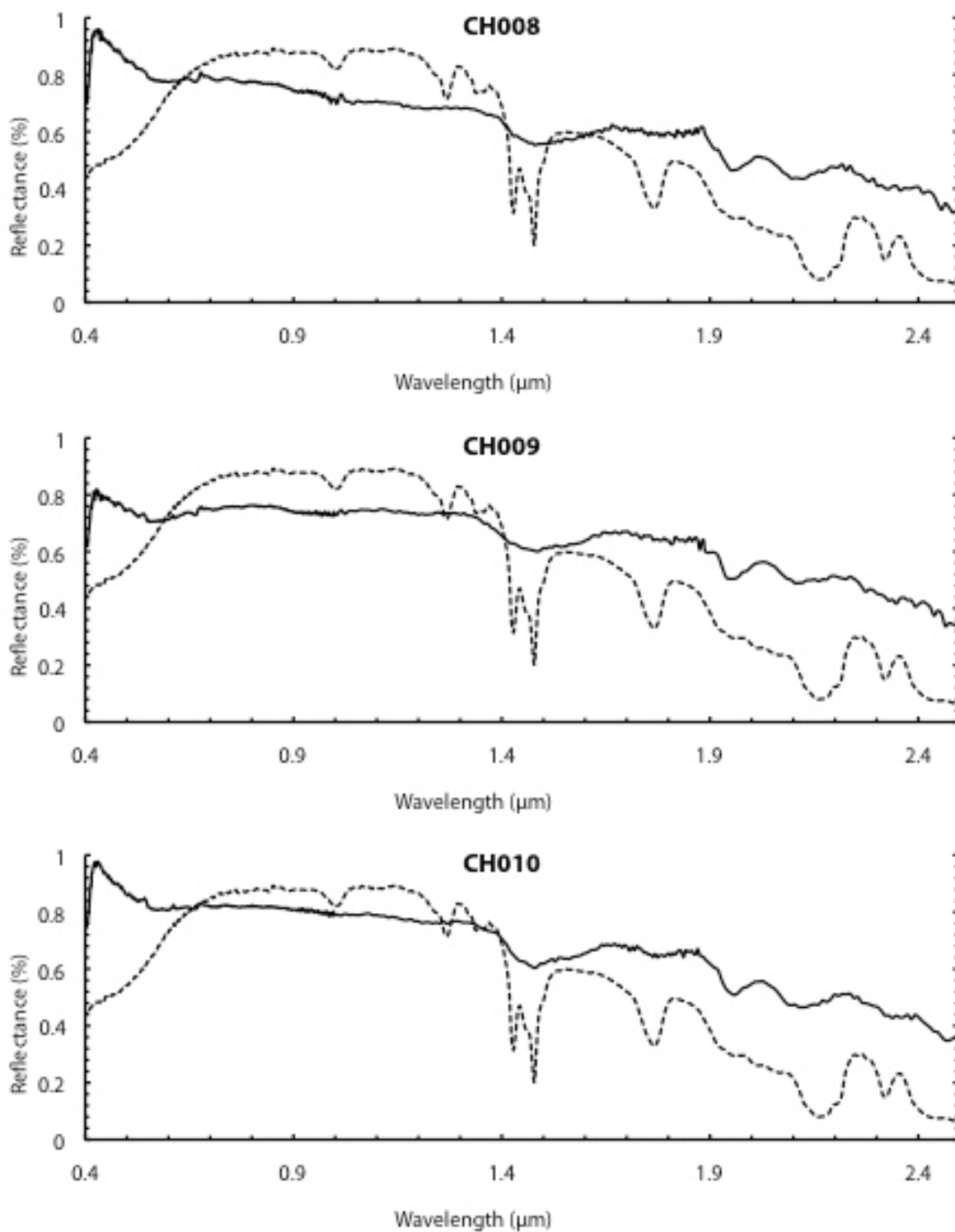


Figure A3: Ground spectra from Cuprite Hills, NV (solid black). USGS alunite spectrum (AL706; Clark et al., 1993).

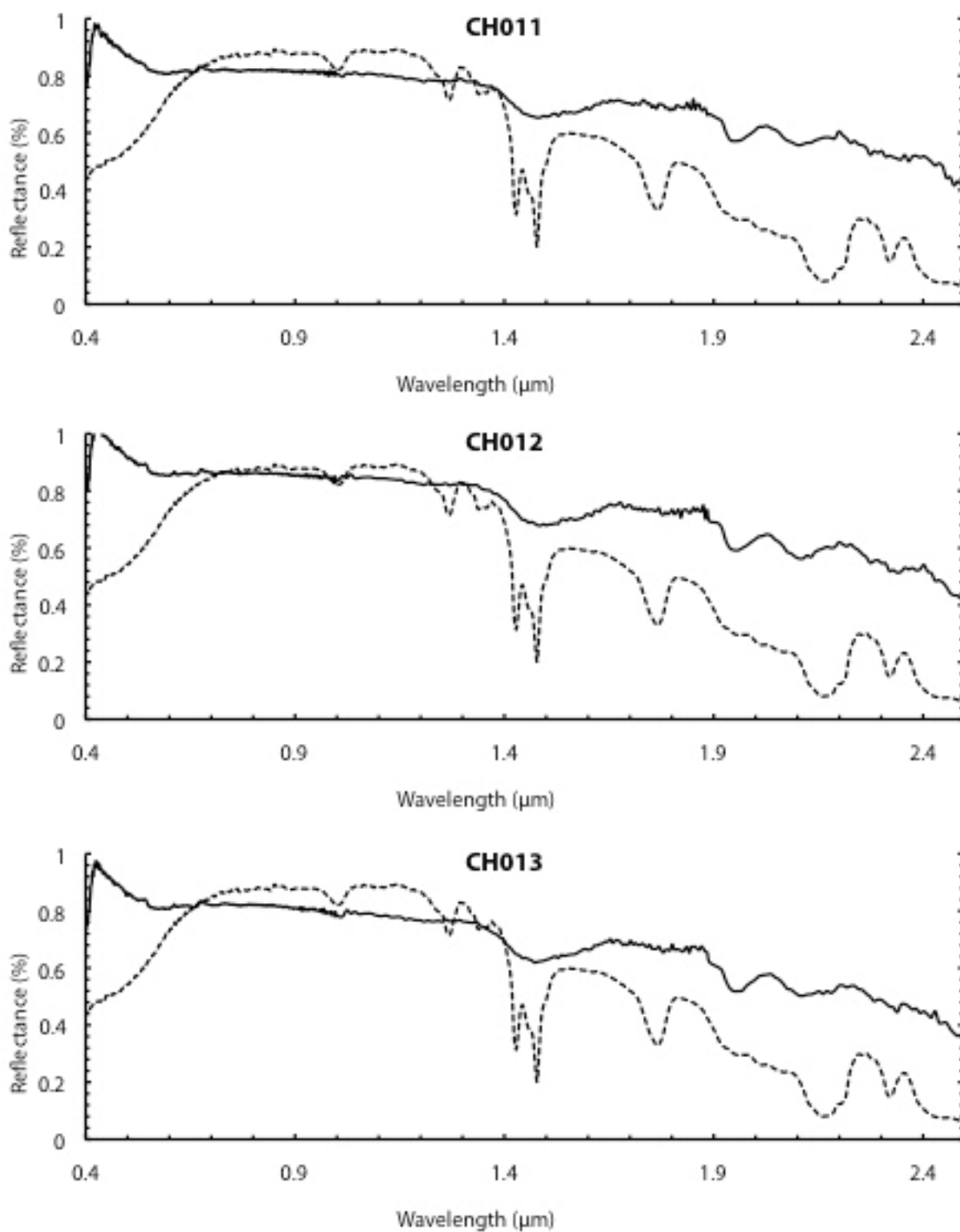


Figure A4: Ground spectra from Cuprite Hills, NV (solid black). USGS alunite spectrum (AL706; Clark et al., 1993).

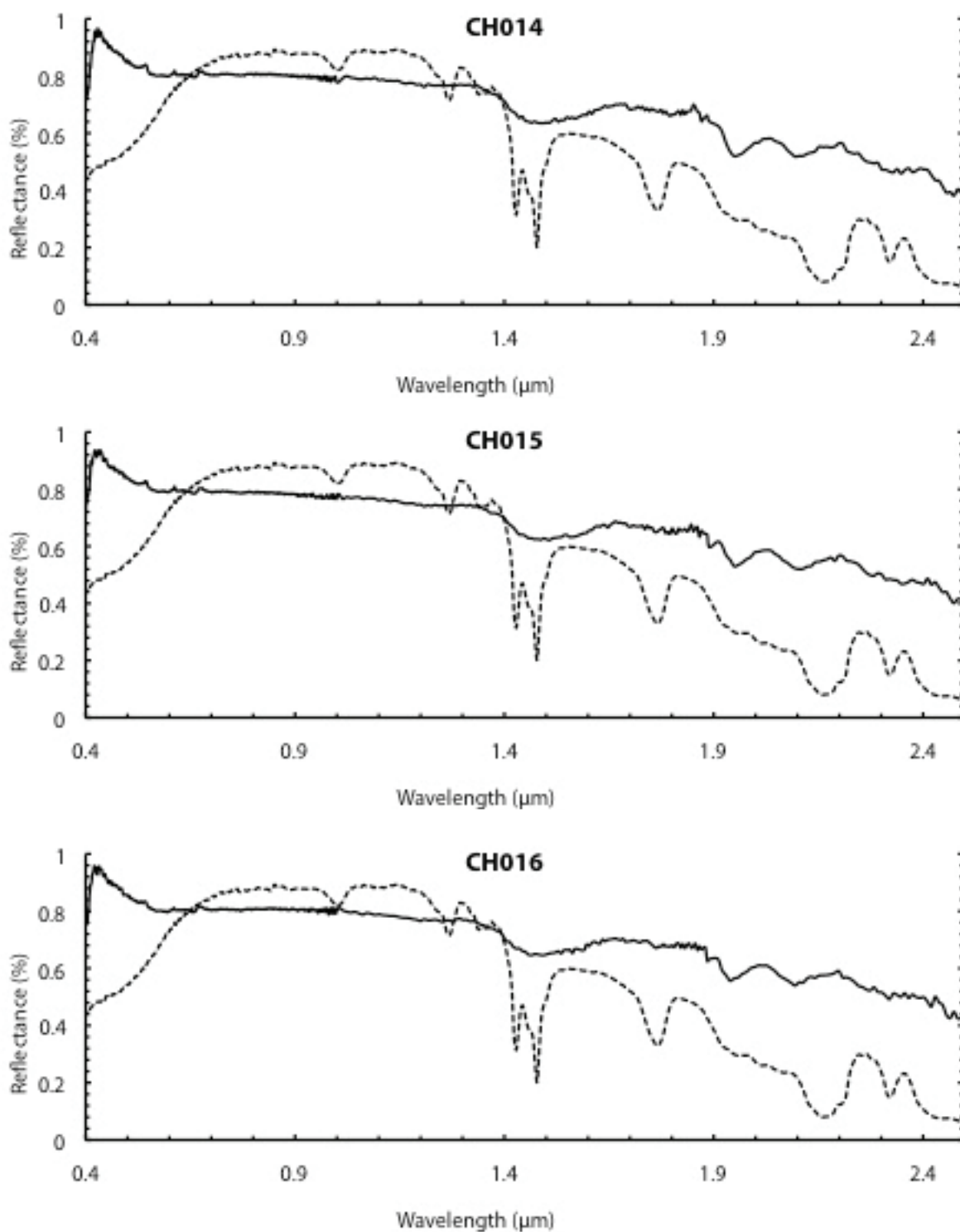


Figure A5: Ground spectra from Cuprite Hills, NV (solid black). USGS alunite spectrum (AL706; Clark et al., 1993).

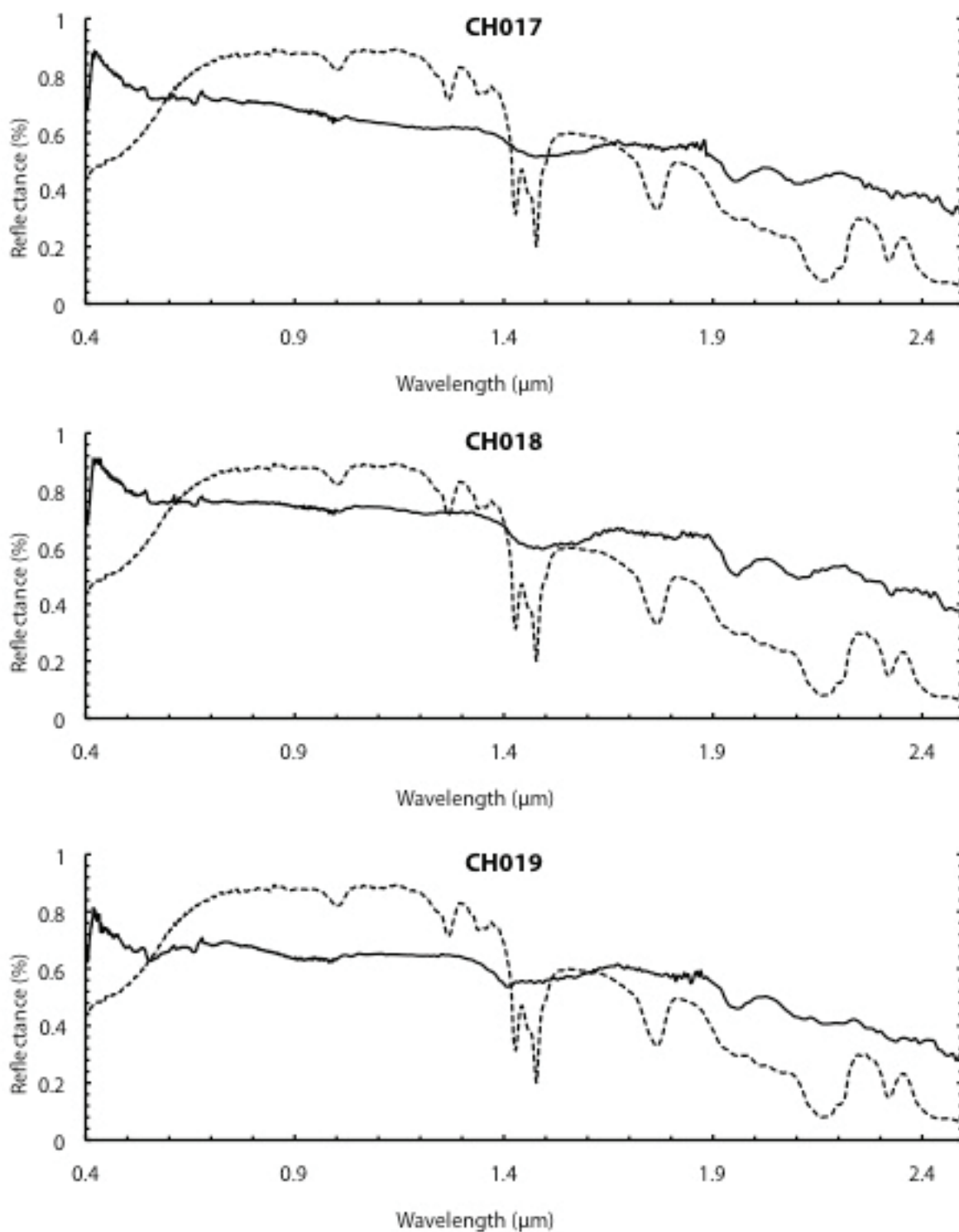


Figure A6: Ground spectra from Cuprite Hills, NV (solid black). USGS alunite spectrum (AL706; Clark et al., 1993).

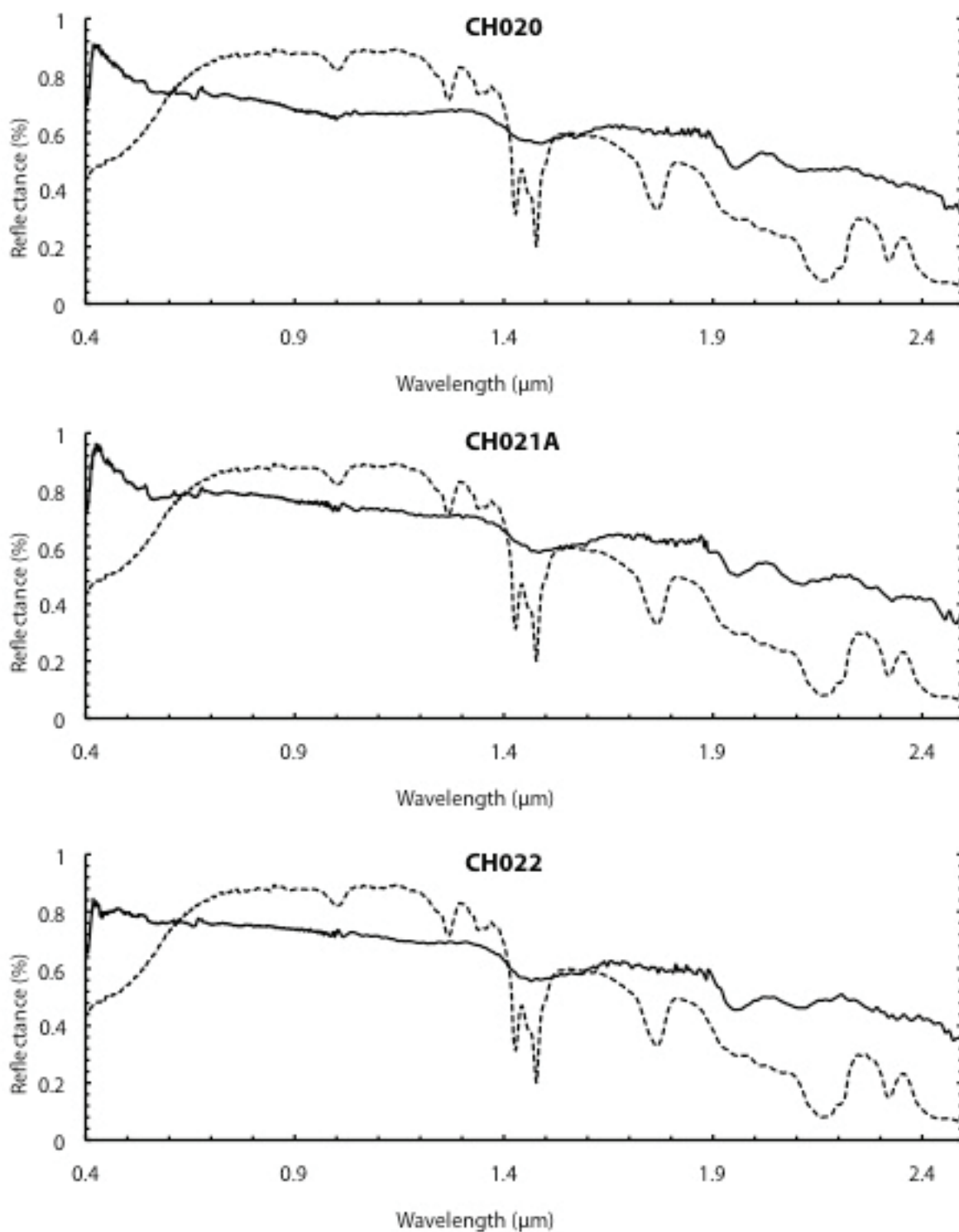


Figure A7: Ground spectra from Cuprite Hills, NV (solid black). USGS alunite spectrum (AL706; Clark et al., 1993).

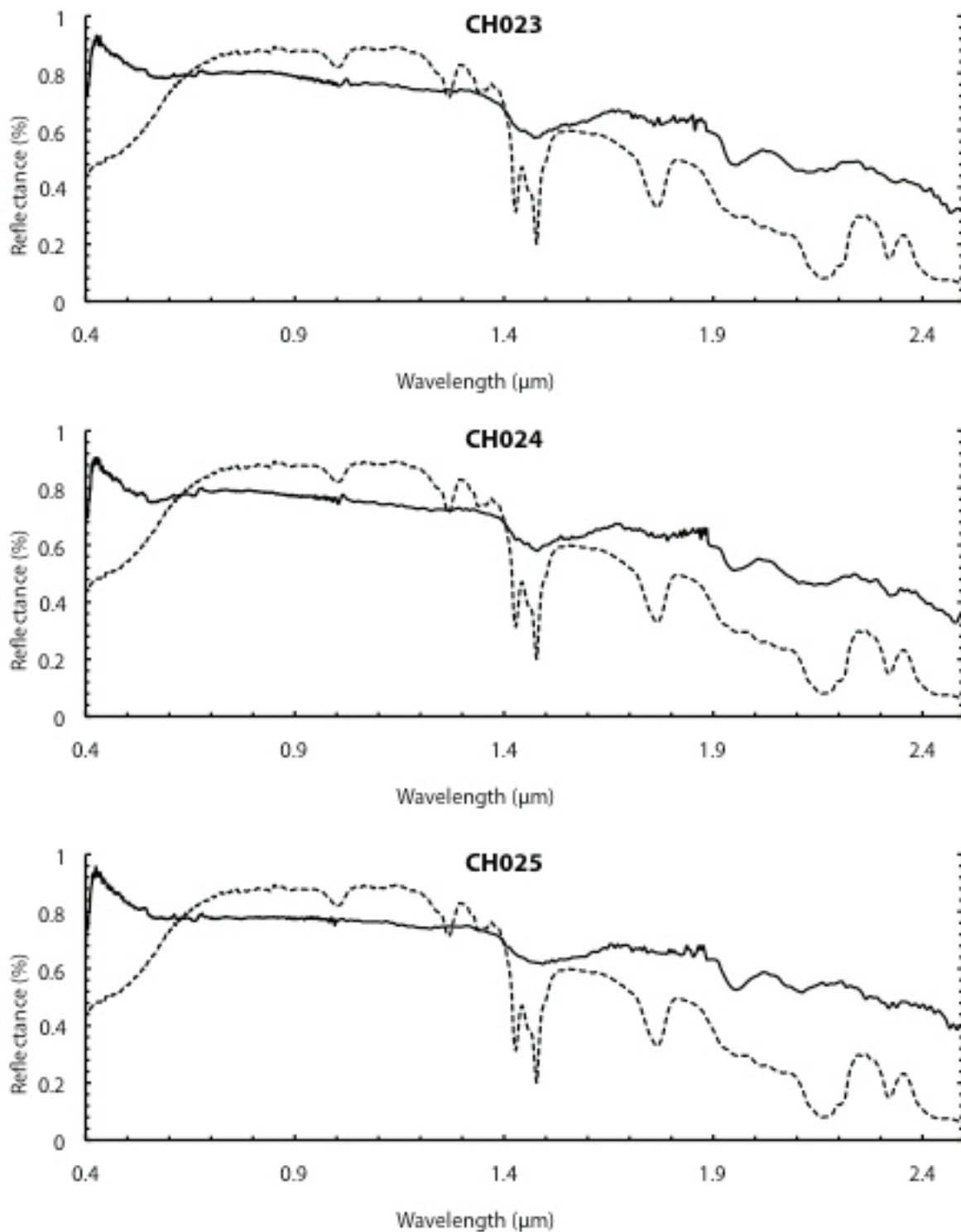


Figure A8: Ground spectra from Cuprite Hills, NV (solid black). USGS alunite spectrum (AL706; Clark et al., 1993).

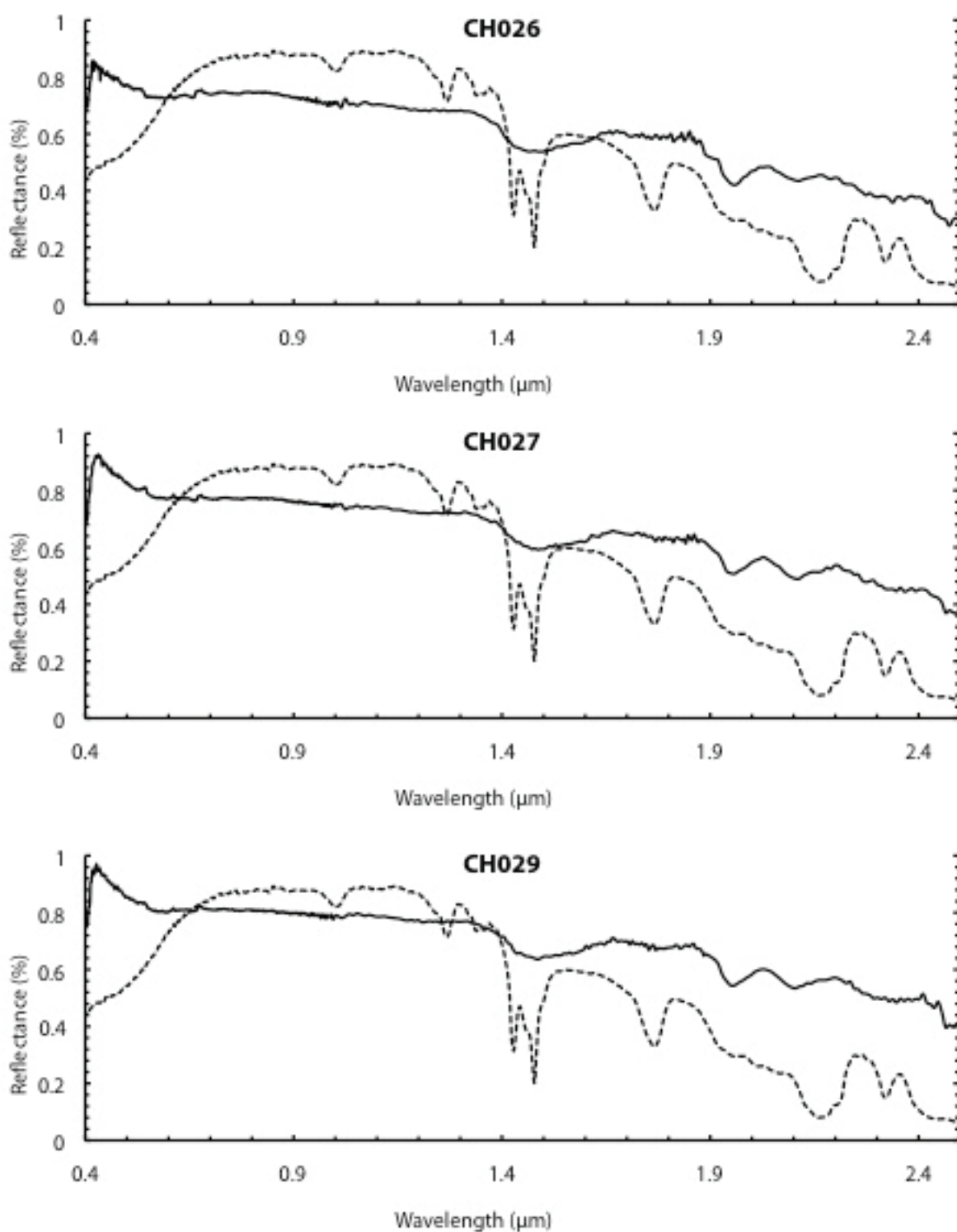


Figure A9: Ground spectra from Cuprite Hills, NV (solid black). USGS alunite spectrum (AL706; Clark et al., 1993).

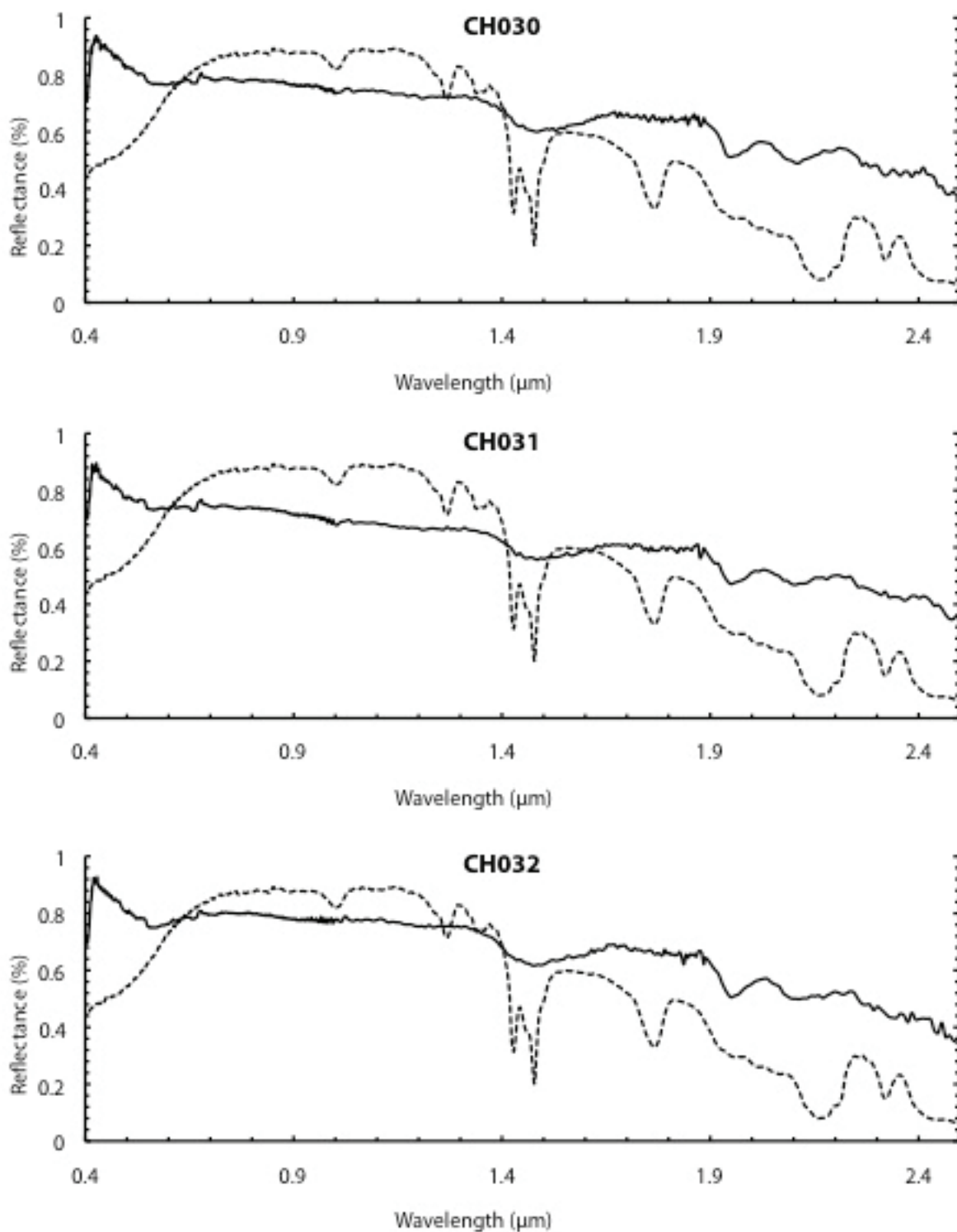


Figure A10: Ground spectra from Cuprite Hills, NV (solid black). USGS alunite spectrum (AL706; Clark et al., 1993).

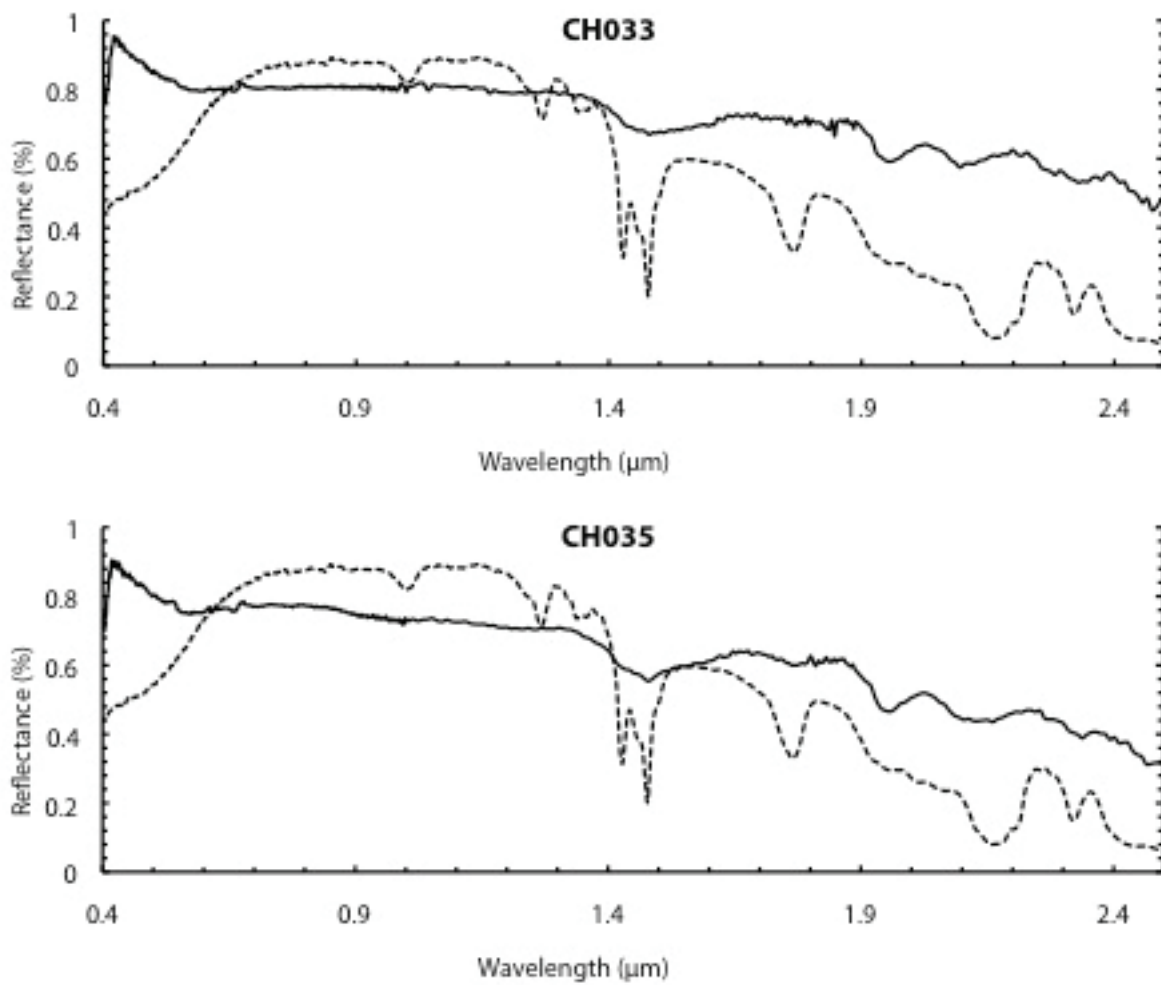


Figure A11: Ground spectra from Cuprite Hills, NV (solid black). USGS alunite spectrum (AL706; Clark et al., 1993).

CHAPTER 5: SYNTHESIS

My methods for targeting lunar water (Chapter 2) and ilmenite-rich mare basalts (Chapter 3) will enable future research that could lead to an expanded understanding of the lunar dichotomy and the formation of non-mare silicic features. The methods I developed for mapping ilmenite and water on the lunar surface could one day be used to find ideal locations for a lunar outpost that would rely on nearby mineral-rich material for sustainability. The methodology that I develop to detect terrestrial alunite (Chapter 4) is nearly as accurate for detecting alunite as high-spatial resolution hyperspectral platforms. This improved methodology can lead to cheap and reliable terrestrial mineral exploration, especially in limited access areas, such as the Sierra Madre of Mexico.

1. Lunar Geologic Exploration

1.1 Key Research Findings

The work in Chapters 2 and 3 answer the questions I posited in Chapter 1. I was able to develop an effective tool for mapping ilmenite that helped show three stages of basaltic eruptions within the Procellarum KREEP Terrane (PKT), as well as identify large concentrations of water on the nearside and farside and suggested what mechanism may be responsible for the formation of non-mare silicic features. I suggest that M^3 can be effective for placing constraints on the evolution of the lunar crust.

Chapter 2 shows that silicic volcanic features on the nearside and the farside of the Moon are heavily enriched in water (Figure 1). I was able to confidently estimate water concentrations as high as 127 ± 21 ppm, the largest water concentrations seen at non-polar latitudes, at Hansteen

Alpha on the nearside. In addition, I estimated water concentrations of 274 ± 47 ppm at CBTA on the farside. The water concentrations are over twice as high as any known feature on the nearside. The high water concentrations within urKREEP may have led to lower melting points of material at the base of the crust and partial melt generation sooner than anhydrous material, since increased volatile content (i.e. water or carbon dioxide) will lower the melting point of rocks. At Hansteen Alpha, mare basalts superimpose non-mare silicic features, demonstrating that Hansteen Alpha erupted prior to the southern Oceanus Procellarum mare basalts adjacent to it (Hawke et al., 2003). Hydrous melts associated with non-mare silicic features suggests that most, if not all, of the non-mare silicic features on the Moon may have been generated via basaltic underplating. This is because the alternative, silicate liquid immiscibility (SLI), predicts that basaltic magmas would have formed before silica-rich magmas (Hagerty et al., 2006). Basaltic underplating involves the emplacement of basaltic magmas under the crust (Hagerty et al., 2006). The basaltic magmas melt the crustal country rock, potentially yielding silicic partial melts. The presence of water in the basaltic underplating magmas would encourage them to melt sooner. The resulting silicic melts are less dense than the country rock, which leads to the rise of magmas that are enriched in water prior to the eruption of denser basaltic melts (Hagerty et al., 2006). In addition, I was able to show that KREEP-like material may be located outside of the PKT, for example at CBTA. The presence of KREEP at CBTA suggests that other places on the farside, with similar geochemistry, could exist. The lack of KREEP-enriched lithologies exposed at the surface on the farside may be related to the thicker crust that would restrict eruptions from occurring.

Chapter 3 shows that a series of magmatic phases occurred on the lunar nearside, each of which had different geochemical signatures. The early magmatic stage (Stage 1) consisted of

ilmenite-poor mare basalts. This was followed by a transition magmatic stage (Stage 2) consisting of mare basalts with moderate ilmenite concentrations. The third and final magmatic stage (Stage 3) erupted ilmenite-rich mare basalts. Stage 1 and stage 3 are consistent with the ilmenite-poor to ilmenite-rich mare basalts proposed by Staid et al., (2011). Melts erupted during Stage 2 were potentially influenced by a KREEP- and Ti-rich plume that rose to the base of the lunar crust after the ilmenite downwelling (Figure 2). This transition can be seen in the eruption of basalts with moderate ilmenite concentrations at ~3.32 Gya at Mare Nubium and Ibrum, just before ilmenite- and KREEP-rich basaltic eruptions become more common within the PKT.

We propose two possible scenarios to explain why areas outside of PKT, such as Tranquillitatis and Serenatatis, do not exhibit both high KREEP and ilmenite concentrations.. In the first, the Ti-rich but Th-poor mare basalts would have erupted after (or during) the degree-1 downwelling (Zhong et al., 2000; Parmentier et al., 2002; Khan et al., 2014) that affected the nearby PKT. In this case, the Ti originated from interaction with Ti-rich material that was not completely removed by the downwelling and that remained at the base of the crust. The KREEP may have never existed at Mare Tranquillitatis and Serenitatis, or it was removed by the degree-1 downwelling, redistributing that material and concentrating it at the PKT. In the second scenario, the Ti-rich but Th-poor mare basalts would have erupted prior to the degree-1 downwelling. In this case, while the Ti-rich material may eventually have been partially or completely removed by the downwelling, it existed in the subsurface at the time of melt generation. However, the lack of Th would imply that KREEP did not exist at all at Tranquillitatis and eastern Serenitatis. These hypotheses are testable if both the timing of mare

basalt volcanism and the degree-1 downwelling can be constrained. While the former is known (3.9-1 Gya; Hiesinger et al., 2000; Hiesinger et al., 2003), the latter is not.

The ilmenite regression model that I have developed (Chapter 3) is a powerful tool for mapping ilmenite-rich basalts, with the ability to map ilmenite concentration between 0 and $\sim 33.7 \pm 1.8$ wt%. However, the model has limitations. The ilmenite regression model indicates that mare basalts with >33.7 wt% ilmenite are indistinguishable from both anorthositic highland material or non-mare silicic features. This is because ilmenite concentrations higher than 33.7 ± 1.8 wt% are associated with a 1- μm -reflection feature rather than a 1- μm absorption feature in reflectance spectra from M^3 images. Anorthositic highland material and non-mare silicic features lack 1- μm absorption features, and therefore could be incorrectly mapped as ilmenite-rich mare basalts.

1.2 Broader Implications

The work I have done here supports the hypothesis of a potential ilmenite downwelling occurring on the nearside of the Moon. Recently, Khan et al. (2014) have shown, using data from the Gravity Recovery and Interior Laboratory (GRAIL) that an ilmenite-rich layer is present at the core-mantle boundary of the Moon, which suggests that an ilmenite downwelling did occur early in lunar history. My results suggest that the ilmenite downwelling occurred sometime between 3.9 and 3.32 Gya, when moderate ilmenite basalts were beginning to erupt within the PKT (Figure 2). In addition Andrews-Hanna et al. (2014) have recently shown that a plume could have been responsible for mare volcanism on the nearside. They support this by noting the presence of a quasi-rectangular array of fractures in the lunar subsurface seen by

GRAIL (Andrews-Hanna et al., 2014). The rectangular spatial pattern is consistent with a plume. An impact would form ring fractures in the shape of an ellipse (Andrews-Hanna et al., 2014). My suggestion of 3 magmatic stages of basaltic eruptions on the nearside suggests that a KREEP- and Ti-rich plume was located on the nearside between 3.32 and 1 Gya.

The basaltic eruption episodes presented in Chapter 3 and the process of forming hydrous non-mare volcanics presented in Chapter 2 can occur together without the basaltic eruptions affecting the occurrence of hydrous non-mare silicic features (Figure 2). The hydrous melts would have formed prior to the mafic melts, due to the lower melting point of hydrous KREEP material in the subsurface.

The age of non-mare silicic features formed from partial melts created by the ilmenite- and KREEP-rich plume could be verified by another study that focuses on the cross cutting relationships between old mare basalts; hydrous, non-mare, silicic features; and ilmenite- and KREEP-rich mare basalts. If hydrous, non-mare silicic features overlie mare basalts, but are themselves superimposed by younger, ilmenite- and KREEP-rich mare basalts, then it would suggest that hydrous non-mare silicic features were emplaced before the arrival of an ilmenite- and KREEP-rich plume. A non-mare silicic feature that is adjacent to older basalts as well as younger mare basalts would be needed to test this hypothesis. The Mairan Domes (Glitch et al., 2011) could be a candidate for a study. The Mairan Domes are adjacent to very young Th-rich mare basalts (~1.3 Gya; Hiesinger et al., 2003), and with more detailed geochronologic analysis of adjacent mare basalts, older mare basalts could be identified near the Marian Domes.

Given the results of Chapters 2 and 3, there are several areas that would be worth exploring for a potential lunar outpost. Ideally, sites for a lunar outpost would have high *in-situ* resource utilization (ISRU) potential, and also high exploration (i.e. scientific) potential.

Western Mare Nubium would be ideal due to the abundance of ilmenite- and Th-rich basalts, as well as the nearby Lassell Massif, which is a hydrous non-mare silicic feature. Lassell Massif would be of particular interest for two reasons: Lassell Massif would increase our scientific knowledge of non-mare silicic features; and the water that is potentially present there could supply oxygen and fuel to a lunar outpost. Eastern Mare Imbrium is another location that would be worth exploring. Like western Mare Nubium, this location contains ilmenite- and KREEP-rich basalts as well as the non-mare silicic features at Gruithuisen Domes.

A robotic mission could be sent to the Moon in advance of a human mission with the objective of gathering resources from these ISRU sites. While humans prepare for the mission ahead, robots could utilize the ilmenite-rich basalts to build structures and even break the ilmenite (FeTiO_3) down to oxygen and Ti (Duke et al., 2006), where Ti could be used to make strong, lightweight alloys for building structures. In addition, the Th in the basalts could be used as a power source, if thorium-fueled reactors are practical at that time (Duke et al., 2006). By the time humans arrive, most of the work building their habitat would be complete, and they would have a surplus of necessary materials. The robots could then be sent to roam and explore nearby geology when not being used to harvest oxygen or other materials.

1.3 Future Research Priorities

To further support the exploration of water-enriched lithologies on the Moon, and the idea of basaltic underplating as the primary mechanism for creating non-mare silicic features, future work could examine additional known non-mare silicic features (i.e. Aristarchus Plateau, Mairan Domes, etc.) to determine how much water, if any, is present. If mare basalts superimpose these other non-mare silicic features, that would suggest that the silica-rich melts

erupted before the mare basalts. Since I suggest non-mare silicic features are younger than mare basalts, they may have been given more time to reach the surface due to lower melting points induced by the presence of water. Mare basalts superimposed on non-mare silicic features is consistent with what is predicted by basaltic underplating, where silicic melts could form prior to the formation of mafic melts.

Future research could also be directed towards developing ilmenite maps that cover the entire nearside of the Moon. Such a study could locate ilmenite-rich eruptions on the nearside and determine when they erupted using geochronologic studies that constrain the ages of the mare basalts (e.g., Hiesinger et al., 2000; Hiesinger et al., 2003). The study could then determine if a geochemical relationship exists between mare basalts of similar ages. Such a study could potentially verify my hypothesis of a transition eruption stage (~3.32 Gya) (Figure 2) between the high-Ti and low-Ti stages of Staid et al. (2011).

The methods I present here could also be applied to the South Pole Aiken Basin (SPAB). Using my method at SPAB would allow future studies to locate ilmenite-rich mare basalts on the farside of the Moon. Because KREEP and ilmenite appear to occur together in late stage basaltic eruptions on the lunar nearside, the presence of ilmenite-rich basalts at SPAB could indicate the presence of KREEP there as well. The presence of KREEP at SPAB would suggest that KREEP is not just restricted to the PKT. Instead, it would suggest that a continuous layer of KREEP is present throughout the lunar subsurface or that it exists as pods, dikes, or sills throughout the lunar subsurface.

2. Terrestrial Mineral Exploration

2.1 Key Research Findings

In Chapter 4, I have shown that Advanced Spaceborne Thermal Emission and Reflection Radiometer (ASTER) multispectral data can be used to target alunite with results that are comparable in accuracy to those obtained from mineral maps derived from high spatial resolution Airborne Visible/Infrared Imaging Spectrometer (AVIRIS) hyperspectral data (Figure 3). When compared to the Mars and Rowan (2006) argillic map, my alunite map is much more effective at accurately targeting alunite-rich regions. However, it does appear that the alunite detection methodology using ASTER data may be affected by mixing with kaolinite and some iron oxides, but not nearly as many non-alunite materials are mapped as the Mars and Rowan (2006) argillic map (Figure 3).

2.2 Broader Implications

My improved method for targeting alunite should lead to more discoveries of ESGDs and PCDs as a result of increased regional exploration efforts encouraged by the new remote-sensing techniques. High spatial and spectral resolution datasets, such as AVIRIS, are expensive to acquire and have sparse coverage compared to ASTER data. In the time that it would take to acquire data from a high-resolution platform I could map a large portion of the Sierra Madre of Mexico and possibly have several prospective deposits mapped.

The method for mapping alunite that I have developed in Chapter 4 is nearly as accurate as AVIRIS (Figure 3). Using ASTER imagery and the method for finding alunite presented in Chapter 4 as an initial platform for exploration projects will help junior and major mining

companies alike plan sampling missions that may lead to the discovery of the next major PCD or ESGD deposit.

2.3 Future Research Priorities

Swayze et al. (2014) recently published an AVIRIS mineral map that I did not have prior to the sampling mission to Cuprite Hills. If I possessed the AVIRIS mineral map prior to my sampling mission to Cuprite Hills, I would have sampled more of the western side of Cuprite Hills due to the abundance of alunite in that region. The AVIRIS mineral map indicates a region called “Alunite Hills” that has spectral signatures consistent with alunite (Figure 3) (Swayze et al., 2014). A second sampling mission to Cuprite Hills would focus on sampling in this region in order to further verify the accuracy of my alunite map in that area (Figure 3).

Another avenue of future work is direct analytical determination of the presence and amount of alunite in samples from Cuprite Hills. While the reflectance spectroscopy results yield spectra consistent with the presence of alunite, X-ray diffraction (XRD) would allow us to characterize the samples in more detail, including assessing the degree of mixing between alunite and other minerals. The resulting data would be of great use in further validating the alunite detection technique as well as provide a basis for potentially including methods to account for spectral mixing.

Ultimately, the techniques presented in Chapter 4 will need to be tested, including ground truth validation, in unexplored localities. Ideally, a portable X-ray fluorescence (XRF) analyzer and a portable hyperspectral imager could be used in the field to confirm the presence of alunite suggested by the alunite map produced by my new method. Understanding the sensitivity of the logical operators would allow me to refine them and make even more accurate alunite maps.

If given the resources for exploring for mineral deposits, as well as more time to test the method for mapping alunite developed in chapter 4, I would identify several prospective deposits and plan sampling missions over time in order to see if I can make a discovery of my own, outside of Cuprite Hills. Given the proximity to El Paso, and the expansive history of mineral deposits found there (Coulson, 2012), the Sierra Madre of Mexico would be an ideal candidate for regional mineral exploration.

References

- Andrews-Hanna, J.C., Besserer, J., Head III, J.W., Howett, C.J.A., Kiefer, W.S., Lucey, P.J., McGovern, P.J., Melosh, H.J., Neumann, G.A., Phillips, R.J., Schenk, P.M., Smith, D.E., Solomon, S.C., and Zuber, M.T., 2014, Structure and evolution of the lunar Procellarum region as revealed by GRAIL gravity data: *Nature*, v. 514, no. 7520, p. 68-71.
- Coulson, M., 2012, *The History of Mining: The events, technology, and people involved in the industry that forged the modern world*: Harriman House. 488 p.
- Duke, M.B., Gaddis, L.R., Taylor, J.T., and Schmitt, H.H., 2006, Development of the Moon: *Reviews in Mineralogy and Geochemistry*, v. 60, p. 597-656, doi: 10.2138/rmg.2006.60.6.
- Glotch, T.D., Hagerty, J.J., Lucey, P.G., Hawke, B.R., Giguere, T.A., Arnold, J.A., Williams, J.-P., Jolliff, B.L., and Paige, D.A., 2011, The Mairan domes: Silicic volcanic constructs on the Moon: *Geophysical Research Letters*, v. 38, no. 21, doi: 10.1029/2011GL049548.
- Hagerty, J.J., Lawrence, D.J., and Hawke, B.R., 2011, Thorium abundances of basalt ponds in South Pole-Aitken basin: Insights into the composition and evolution of the far side lunar mantle: *Journal of Geophysical Research*, v. 116, no. 6, doi: 10.1029/2010JE003723.

Hawke, B.R., Lawrence, D.J., Blewett, D.T., Lucey, P.G., Smith, G.A., Spudis, P.D., and Taylor, G.J., 2003, Hansteen Alpha: A volcanic construct in the lunar highlands: *Journal of Geophysical Research*, v. 108, no. E7, doi: 10.1029/2002JE002013.

Hiesinger, H., Jaumann, R., Neukum, G., and Head III, J.W., 2000, Ages of mare basalts on the lunar nearside: *Journal of Geophysical Research*, v. 105, p. 239-275.

Hiesinger, H., Head III, J.W., Wolf, U., Jaumann, R., and Neukum, G., 2003, Ages and stratigraphy of mare basalts in Oceanus Procellarum, Mare Nubium, Mare Cognitum, and Mare Insularum: *Journal of Geophysical Research*, v. 108, no. E7, doi: 10.1029/2002JE001985.

Khan, A., Connolly, A.D., Pommier, A., and Noir, J., 2014, Geophysical evidence for melt in the deep lunar interior and implications for lunar evolution: *Journal of Geophysical Research Planets*, v. 119, doi:10.1002/2014JE004661.

Klima, R., Cahill, J., Hagerty, J., and Lawrence, D., 2013, Remote detection of magmatic water in Bullialdus Crater on the Moon: *Nature Geoscience*, v. 6, no. 9, p. 737-741, doi: 10.1038/ngeo1909.

Mars, J.C. and Rowan, L.C., 2006, Regional mapping of phyllic- and argillic-altered rocks in the Zagros magmatic arc, Iran, using Advanced Spaceborne Thermal Emission and Reflection Radiometer (ASTER) data and logical operator algorithms: *Geosphere*, v. 2, no. 3, p. 161-186, doi: 10.1130/GES00044.1.

Parmentier, E.M., Zhong, S., and Zuber, M.T., 2002, Gravitational differentiation due to initial chemical stratification: origin of lunar asymmetry by the creep of dense KREEP?: *Earth and Planetary Science Letters*, v. 201, p. 473-480.

Staid, M.I., Pieters, C.M., Besse, S., Boardman, J., Dhingra, D., Green, R., Head, J.W., Isaacson, P., Klima, R., Kramer, G., Mustard, J.M., Runyon, C., Sunshine, J., and Taylor, L.A., 2011, The mineralogy of late stage lunar volcanism as observed by the Moon Mineralogy Mapper on Chandrayaan-1: *Journal of Geophysical Research*, v. 116, p. 1-15, doi: 10.1029/2010JE003735.

Swayze, G.A., R.N. Clark, A.F.H. Goetz, K.E. Livo, G.N. Breit, F.A. Kruse, S.J. Stutley, L.W. Snee, H.A. Lowers, J.L. Post, R.E. Stoffregen, and R.P. Ashley, 2014, Mapping advanced argillic alteration at Cuprite, Nevada using imaging spectroscopy: *Economic Geology*, v. 109, no. 5, p. 1179-1221. doi:10.2113/econgeo.109.5.1179

Zhong, S., Parmentier, E.M., and Zuber, M.T., 2000, A dynamic origin for the global asymmetry of lunar mare basalts: *Earth and Planetary Science Letters*, v. 177, no. 3-4, p. 131-140, doi: 10.1016/S0012-821X(00)00041-8.

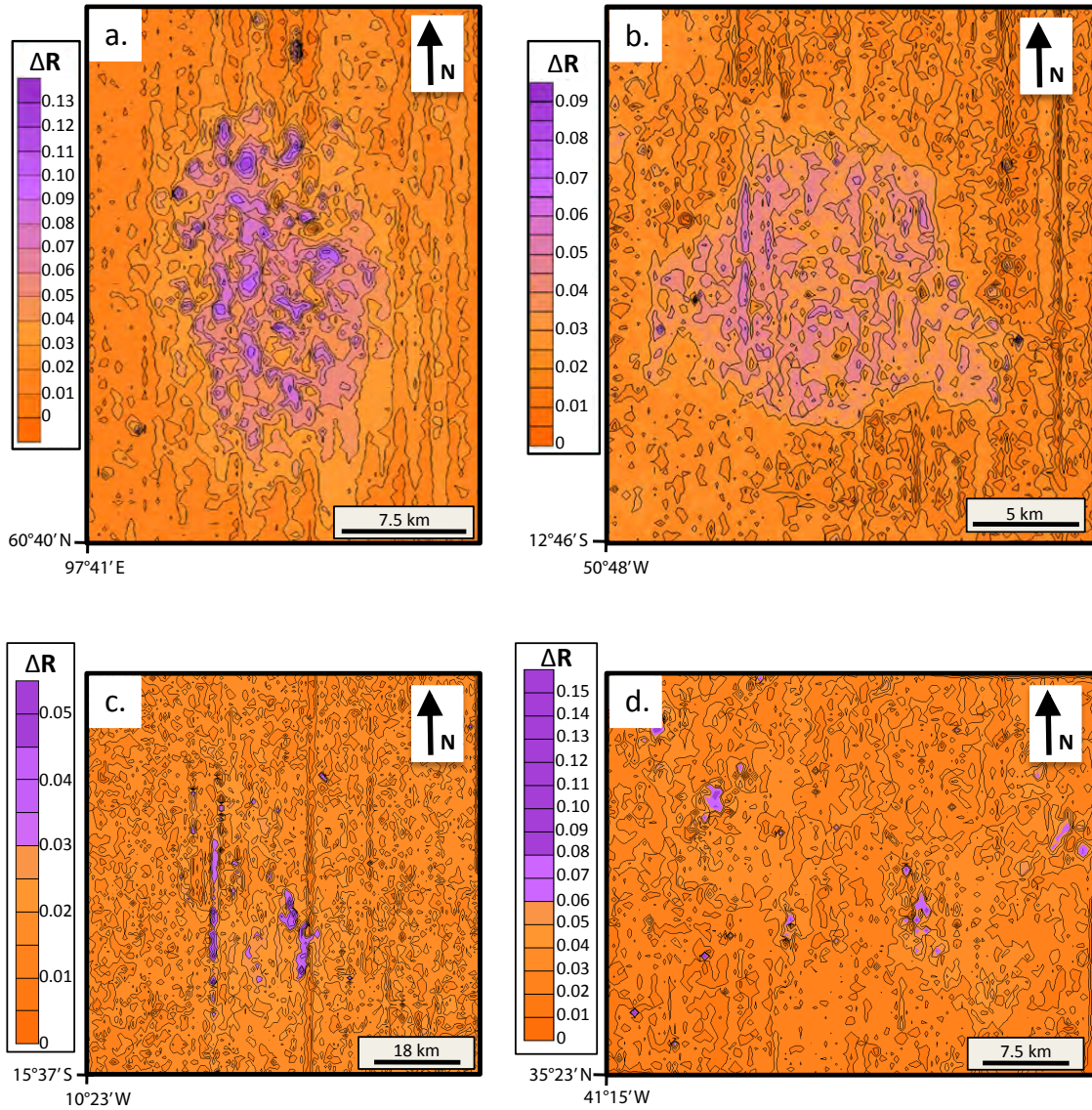


Figure 1: Contoured M³ band depth images showing absorption depths (ΔR). Purples mark locations with large 2.8- μ m absorptions. Oranges indicate small absorptions. (a) Compton Belkovich Thorium Anomaly (CBTA), (b) Hansteen Alpha (HAN), (c) Lassell Massif (LASS), (d) Gruithuisen Domes (GRUITH).

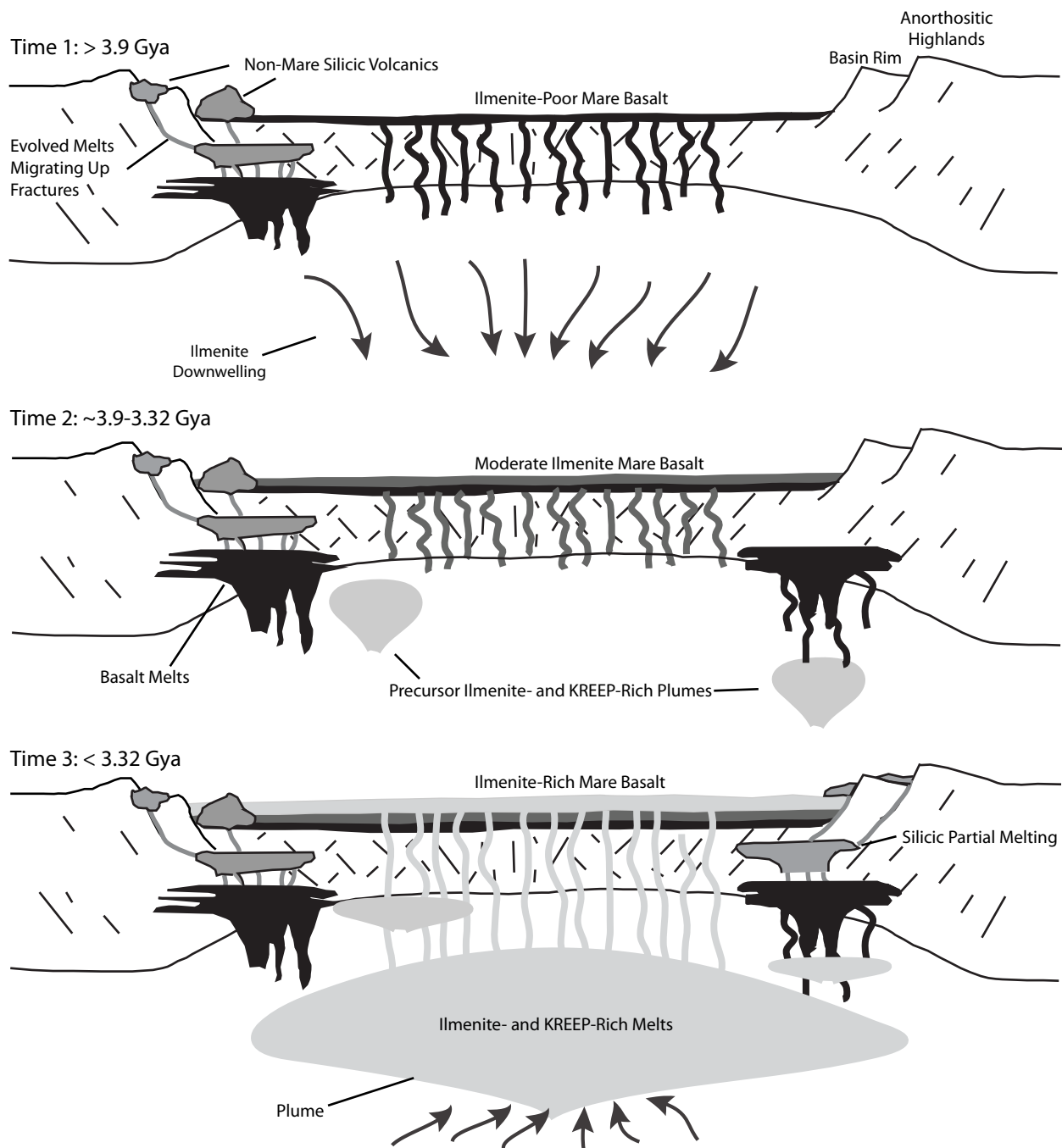


Figure 2: Schematic cross-section of nearside volcanism through time at Mare Nubium and Imbrium (~3.9-3.32 Gya). Time 1 represents the ilmenite downwelling (black arrows) that occurred early in the geologic history of the Moon. Hydrous melts may have reached the surface prior to old, ilmenite-poor mare basalts, and then were embayed by subsequent mare basalt volcanism. Time 2 represents the volcanism that occurred after the ilmenite downwelling within the PKT. Early ilmenite- and KREEP-rich plumes could have begun to arrive at ~3.32 Gya and mix with partial melts at the base of the lunar crust. Time 3 represents the arrival of the main plume of ilmenite- and KREEP-rich melts that were pulled down during the ilmenite downwelling and subsequently mixed near the core-mantle boundary. The arrival of the plume marks the beginning of widespread ilmenite- and KREEP-rich eruptions at ~3.32 Gya. Modified from Hagerty et al. (2006).

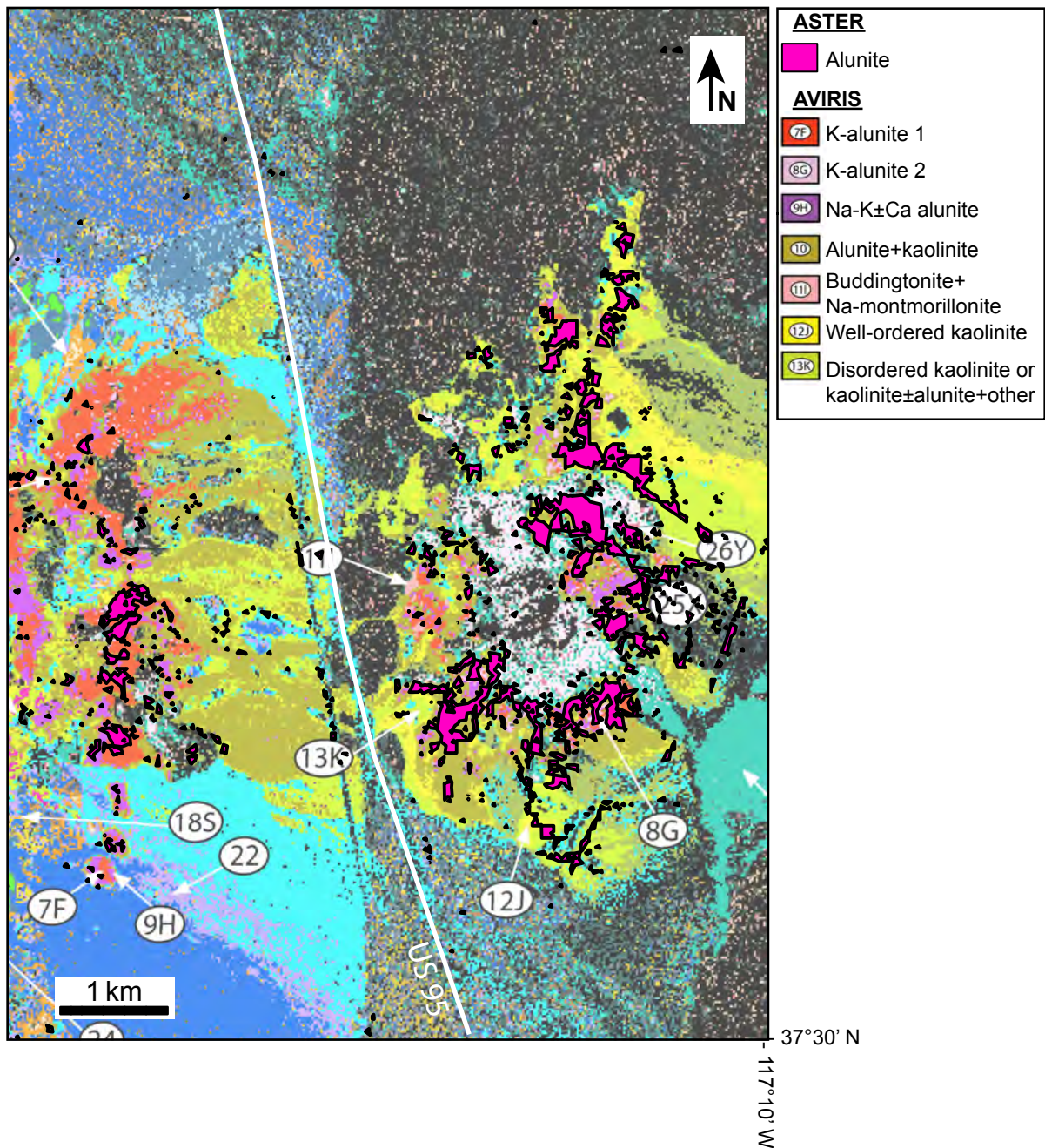


Figure 3: AVIRIS mineral map showing pixels exhibiting spectra consistent with alunite (Swayze et al., 2014). The results from our alunite map, which was developed using ASTER scenes and the OH--FeO and SO42-logical operators, are overlain on the AVIRIS mineral map to show how well the alunite map correlates with the high spatial and spectral resolution of AVIRIS.

VITA

Douglas L. Standart was born in National City, CA. He was raised in a military family in Idaho Falls, ID, where he graduated from Skyline High School in 2004. After graduation, he moved to Logan, UT to attend Utah State University, where he received a Bachelor of Science in Geology in 2010. In 2011, he came to El Paso to pursue a M.S. in geology under the supervision of Dr. Jose M. Hurtado Jr. After a successful start to his graduate career, Douglas decided to apply for the accelerated Ph.D. program at UTEP. During Douglas' time at UTEP he has participated in Desert Research and Technology Studies with NASA, acted as co-chair of the UTEP Geological Science Department's 2013 Colloquium committee, and was a teaching assistant for Introduction to Earth Science, Geoscience Processes, and Geology Field Camp I and II. He also mentored several undergraduate students, working with them on remote sensing projects related to lunar mineralogy and terrestrial economic geology. Douglas was also very active in extracurricular activities and was awarded the Bruce Davidson Award for his devotion to the UTEP Geological Sciences department and El Paso community. In addition, Douglas has also worked with companies outside of UTEP, such as consulting for junior mining companies in the El Paso area, and interning with Marathon Oil Company, where he will be working full-time after leaving UTEP.

Permanent address: 473 Spruce St

Idaho Falls, Idaho, 83401

Email address: douglstandart@gmail.com

This dissertation was typed by and all figures were prepared by Douglas L. Standart.